Universidade do Minho
Escola de Engenharia

Rajendra Kumar Varma

Numerical models for the simulation of the cyclic behaviour of RC structures incorporating new advanced materials

Julho de 2012

Numerical models for the simulation of the cyclic behaviour of RC structures incorporating new advanced materials
Rajendra Kumar Varma
UMinho | 2012

Universidade do Minho
Escola de Engenharia

Rajendra Kumar Varma

Numerical models for the simulation of the cyclic behaviour of RC structures incorporating new advanced materials

Tese de Doutoramento
Estrutural Engenharia

Trabalho efectuado sob a orientação de
Professor Doutor Joaquim António Oliveira de Barros
Professor Doutor José Manuel de Sena Cruz

Julho de 2012

ACKNOWLEDGEMENTS

This research was carried out at the Department of Civil Engineering of the University of Minho, Portugal, under the supervision of Prof. Joaquim António Oliveira de Barros and Prof Jose Manuel de Sena-cruz.

Foremost, I would like to express my sincere gratitude to Prof. Joaquim Barros for his continuous support, encouragement, advice and enthusiasm. His guidance and motivation helped me in all the time of research and writing of this thesis.

I am deeply grateful to Prof. Sena-Cruz for his detailed and constructive comments, and for his important support throughout this work. His input during the numerical implementation has been very useful.

I would also like to express my deep regards to Prof Daniel Oliveira, Prof Sujith Das, Prof Arbind Kumar Singh and Prof Alvaro Azevedo in helping me to acquire FCT grant.

The financial support provided by the Portuguese Foundation for the Science and Technology (FCT, grant number SFRH/BD/61677/2009), are gratefully acknowledged.

I would also like to thank Prof. Naim for the friendly discussion and chats we had during last few years, and the encouragement is deeply acknowledged.

I would also to thank Esmaeel for his support and being a great companion. It was a great time and I will cherish it forever. I would also like to thank Subramani in last minute help of thesis.

To all my friends, Ajoy, Ayoushma, Ajaya, Claudio, Glaucia, Kuili, Konrad, Hadi, Hamid, Mahsha, Mohammad, Silvia, Sohel, Vaibhav, Vincenzo, Wesley that always supported and encouraged me during the development of the present work I would like to express my gratitude.

The support and friendship of the colleagues from the Civil Engineering Department of the School of Engineering are gratefully valued.

Finally, my gratitude to all my family, in particular to my mother Smt Sushila Varma and my father Shri Roadmal ji Varma, my family members, Jitendra-Manisha and my wife, Monila: this work was only possible because of their unconditional support, love and friendship. Thanks for your patience.

To my Parents.

ABSTRACT

This work deals with material modelling and numerical implementation for nonlinear finite element analysis of reinforced concrete (RC) structures. Since the behaviour of concrete and steel being crucial for any RC structure under loading, uniaxial cyclic constitutive models for both were implemented in FEMIX, finite element software.

Various advanced materials have been developed with specific purposes, like fibre reinforced concrete (FRC) to improve the resistance to cracking and crack propagation, carbon fibre reinforced polymer (CFRP) for strengthening and retrofitting. The post cracking behaviour of FRC can range from strain-softening to strain-hardening. A parametric study was undertaken to study the effect of post-cracking behaviour of FRC sections, with the aim of proposing design methodology using DOCROS, software for design of cross-sections. In the ambit of parametric study, DOCROS and post-processing software to estimate force-deflection relationship of the beams failing in flexure were developed further.

To improve the confinement of RC columns, embracing them with wet lay-up CFRP sheets is one of the modern and superior techniques. The analytical relationship was proposed for uniaxial constitutive model of CFRP confined concrete under monotonic and cyclic loading. For this analytical approach, an extensive database derived from experiments carried out by various researchers was used, and the proposed cyclic constitutive law was implemented in FEMIX and validated with experimental tests carried by independent research.

The uniaxial constitutive laws of concrete, steel and CFRP confined concrete were implemented in FEMIX under fibre model, which is based on Timoshenko beam theory. The fibre model assumes that the cross-section can be divided into longitudinal fibres of steel, concrete, CFRP confined concrete etc, and perfect bind exist among fibres. However, perfect bond between concrete and steel cannot be guaranteed always, hence to idealize such material interface, bond-slip laws are developed. Special procedure is followed to simulate interface behaviour in combination with fibre approach, which is critical to simulate bar-slippage and pinching of columns.

A biaxial concrete model under the framework of the fracture mechanics was developed, to simulate the RC elements under plane stress field. The concrete response is described by a nonlinear orthotropic model, whose axes of orthotropy are parallel to the principal strain directions. Equivalent uniaxial stress-strain relationships of the concrete are used in orthogonal direction in scope of rotating crack model. To supplement it, a smeared reinforcement model for steel bars is also developed, in context of plane stress elements/Mindlin shells. All the implemented models were validated with experimental results.

RESUMO

O presente trabalho encontra-se contextualizado na modelação de leis constitutivas materiais e na implementação de modelos numéricos na análise não linear de estruturas de betão armado. Em virtude do comportamento do betão e do aço serem cruciais na resposta de estruturas de betão armado sob carregamento, leis uniaxiais cíclicas destes materiais foram implementas no software de elementos finitos FEMIX.

Vários tipos de materiais têm vindo a ser desenvolvidos com propósitos específicos, tal como o betão reforçado com fibras (FRC – *fiber reinforced concrete*) para aumentar a resistência à fendilhação e sua propagação, polímeros reforçados com fibras (FRP – *fiber reinforced polymer*) no reforço e reabilitação de estruturas. O comportamento pós-fendilhado do FRP pode variar de *strain-softening* até *strain-hardening*. Um estudo paramétrico foi realizado para avaliar o efeito do comportamento pós-fendilhado de seções de FRC, com o objetivo de propor uma metodologia de dimensionamento com recurso ao software de seções planas DOCROS. No âmbito deste estudo paramétrico, para além do DOCROS foi também usado um software de pós-processamento para a estimativa da relação força-deslocamento de vigas com rotura por flexão.

Para aumentar o confinamento de pilares de betão armado, o recurso ao encamisamento destes com recurso a mantas de CFRP constitui uma das técnicas atualmente mais promissora. Uma expressão analítica foi proposta na previsão do comportamento uniaxial de estruturas de betão confinadas com mantas de CFRP sob carregamentos monotónicos e cíclicos. Na definição desta lei constitutiva, alguns dos seus parâmetros foram calibrados com recurso a uma extensa base de dados com resultados experimentais; posteriormente a lei foi implementada no FEMIX tendo sido validada com recurso a investigação independente.

As leis constitutivas uniaxiais para o betão, aço e betão confinado com CFRP, implementadas no FEMIX, foram também usadas num modelo de fibras no âmbito do elemento finito de viga (formulação de Timoshenko). O modelo de fibras assume que a seção transversal pode ser dividida em fibras longitudinais de armadura, betão, betão confinado, etc., com aderência perfeita entre materiais. Contudo, a aderência perfeita entre betão e armaduras nem sempre pode ser garantida, sendo por isso necessário

idealizar um elemento de interface, para o qual foi desenvolvida uma lei tensão de aderência *versus* deslizamento. Procedimentos especiais foram adotados na simulação do comportamento da interface combinado com o modelo de fibras, o qual é crítico na correta simulação do deslizamento de armaduras e do efeito de *pinching* em pilares.

Foi desenvolvido um modelo constitutivo biaxial para o betão baseado na mecânica da fratura com intuito de simular estruturas submetidas a estados planos de tensão. A resposta do betão é descrita por um modelo não linear ortotrópico, nos quais os eixos de ortotropia são paralelos às direções das extensões principais. Relações uniaxiais tensão-extensão equivalentes para o betão foram usadas nas direções de ortotropia no âmbito do *rotating crack model*. Complementarmente, um modelo de reforço distribuído para a simulação de armaduras foi desenvolvido no contexto da simulação de estruturas laminares (estado plano de tensão e cascas). Todos os modelos foram validados com recurso a resultados experimentais.

INDEXES

CHAPTER SIX - MATERIAL NONLINEAR BEHAVIOUR OF LAMINAR RC STRUCTURES SUBJECTED TO CYCLIC LOADING

CHAPTER SEVEN - CONCLUSION AND POSSIBLE FUTURE WORK

CHAPTER 1

Introduction

1.1 INTRODUCTION

Almost all the reinforced concrete (RC) frames can be considered as a combination of beams, columns, shear-walls and slabs. They are expected to withstand strong earthquake motions and should deform well into the inelastic range with stable hysteretic behaviour. It has been observed that the inelastic deformations are mostly concentrated at certain critical regions, like joints, which lead to failure of the structure (Bertero & Mahin 1975, Bertero & Popov 1975). The failure mode, deflection and ductility of structure and its structural components are significantly affected by mechanisms such as confinement effect, tension stiffening, bond slip, rebar buckling, creep, etc (CEB-FIB, 2008). For each of them, researchers have proposed diverse formulations. Moreover, the application of such theories are mostly not used by structural engineers, because of either complicated formulations or parameters they require to know in advance, in some cases of difficult physical interpretation by designers. Hence the guidelines are based on simplified formulations, primarily those that involve very few parameters that can be estimated in real practical situations. One of the cases being the seismic analysis of multistorey building, where each floor is assigned one degree of freedom for simplification, in which the results does not give significant insight into the accurate structural component behaviour. In these analyses, each storey is lumped at floors to simplify the analysis, but this approach cannot predict the response of its sub-elements like beams and columns (Fajfar, 2000). In this case of multistorey frame, beams, columns, beam-column joints and slabs need to be analysed independently for the purpose of detailing, as well as with other structural components inside a complete structure, for the over all response of structure to seismic loads.

In last decades researchers have proposed several ways of analysing these type of structures. The non linear finite element analysis (NLFEA) is the one of most well accepted. By using computational tools of acceptable time consuming, the structural analysis problems which used to take very long time when using models of high sophistication, sometimes even days, can now be solved in just few minutes on personal computers. The evolution of NLFEA has been so stunning that it is not limited to just researchers, but is exercised as everyday tool by structural engineers and designers. Several types of computing tools have been made in last few decades, and moreover due to easy availability of these computing tools, NLFEA is almost becoming a compulsory design tool for current structures, mainly those in zones of medium-high seismic risk. The state-of-the-art report by CEB (1996a-b) has very well documented the significance of these tools and has also pointed out these tools need to be used judiciously as slight changes in loading pattern, constitutive material or analytical models can bring huge variation in results. For example, the reinforced concrete columns and beams can be analysed by frame type of finite elements, while shear walls and slabs can be analysed by plane stress and Mindlin shell finite elements, respectively. However, to address specific issues, for example to analyse a joint for detailing, 3D solid element are better suited compared to 2D plane stress element. A 3D model can simulate the 3D confinement by stirrups and the crack width at corners (CEB-FIB, 2008), effectively. At the same time it has to be noted that the computing time taken by solid elements is much higher than when using 2D finite elements. Sometime the finite element are modified to suit the purpose of analysis. As the transverse section of structural elements is, in general, not homogenous in terms of materials and arrangement of reinforcement, hence researchers have proposed fibre element method (Taucer *et* al. 1991, Spacone *et* al. 1992) and layered model (Ugural 1981, Huang 1989, Barros 1989) for beams and shells, respectively.

Once a type of finite element is assumed, the next question is what type of material (constitutive) models should be used. A wrong choice of constitutive model may generate useless results. The constitutive models are generally based on nonlinear elasticity, plasticity, fracture mechanics, damage continuum mechanics etc. Some approaches are based on empirical solutions, while some of them use classical mechanics formulation. Each approach has its own drawback and advantage; hence it cannot be used for all types of structures.

Concrete and steel are the two most widely used material. The behaviour of concrete changes significantly based on uniaxial, biaxial or triaxial load condition. However, the uniaxial behaviour is the most simplified, and has been subject of research from last few decades. The concrete has been exploited for its high performance in compression. However, concrete has much reduced strength in tension, and its post cracking behaviour remains one of the important phenomenons in context of cracking, which also governs the failure of a structure (Vechio 1999, Mansour *et* al. 2001, Palermo and Vecchio 2003, Kwak and Kim 2004). During its service life, a structure is subjected to various kinds of loading conditions, therefore a probability of cracking formation is quite high. The crack pattern can be obtained by constitutive models based on smeared and discrete crack concepts. Smeared crack models are better choice when the diffuse cracking can be assumed, while discrete crack models are important when few major cracks play critical role in the structure. The smeared crack approach can also be divided in two categories, namely, rotating and fixed crack approach. In rotating crack approach the shear stress is a consequence of principal stress and easy to implement in softwares. However, in case of fixed crack approach the shear is modelled explicitly.

Other than steel and concrete, various innovative materials have been developed or deliberated with specific focus being of retrofitting and strengthening, like Carbon Fibre Reinforced Polymers (CFRP), Fibre Reinforced Concrete (FRC) etc. To avoid discrete cracks, FRC has been investigated due to its ability to generate multiple and disperse cracks (Naaman and Shah 1979, Shah *et.* al 2004). The FRC has been applied to structures where corrosion can be minimised, for example sluice-ways, navigational locks and bridge piers. Even a thin FRC layer can have the equivalent strength of thicker plain concrete sections. CFRP has been projected as a lightweight material for strengthening and retrofitting, however nowadays some newly built structures are also using them (Sena-Cruz 2004, Teng & Lam 2006, Motavalli & Czaderski 2007). The use of CFRP sheets for the confinement of concrete columns is one of the most promising applications of this composite (Toutanji 1999, Barros *et al.* 2001, Barros and Ferreira, 2005a), since the load carrying and the energy dissipation capacities can increase significantly.

The constitutive modelling of all the building materials is one of the key factors in achieving the estimated behaviour of structure accurately and reliably under repeated

inelastic, varying and irregular load cycles. In some of constitutive models, huge number of iterations are required, which in turn evaluates the stresses from constitutive laws as their basic step, for NLFEA of large concrete structures. It is intended to simulate the structures, based on the algorithms which are not time consuming and can reproduce the critical behaviour with acceptable error. However, to improve the predictive performance of the simulations, the constitutive models for the materials should also consider the behaviour of the interface between the constituent materials. The interface behaviour is mostly used to incorporate the effects like bar-slippage, pinching etc. The interface concept has been used in context of development of crack pattern, too.

Despite the very high sophisticated tools, the users should be cautious while adopting the solution and should verify how accurately and reliably the reinforced concrete behaviour is predicted. For example, an informal competition was organised by ASCE-ACI Committee 447 to simulate the results of large scale test carried out at University of California at San Diego. The predictions of strength and pre peak were acceptable, while the post peak response predicted by the researchers showed appreciable deviation from the real behaviour. It should be noted that the researchers were able to adjust parameters, optimize their models and improve analyses. Hence the ability to estimate the reinforced concrete behaviour has improved significantly, but still it needs more degree of confidence.

1.2 RESEARCH SIGNIFICANCE

The thesis is proposed to address the issues of design and analysis of reinforced concrete structures and, at the same time, with a special contribution on the simulation of CFRP-based strengthened RC structures, and FRC structures.

Numerous constitutive models exist, which have been successfully tested and applied to various experimental investigations, as summarized by CEB-FIB(2008) they still are not robust enough to predict the RC response under cyclic loading condition.

The nonlinear behaviour of concrete, reinforcing steel, CFRP laminates are modelled, as well as their interaction through bond-slip constitutive models. The models implemented provide a rational framework for NLFEA, and will be accompanied by discussions on their advantages and limitations.

Some of the modification and proposals implemented, like section under axial load and bending and, prestressing of section in phases, were primarily to improve DOCROS, software based on design of cross-section. The proposal of design curves for Fibre reinforced concrete was carried in order to initiate the steps which can be accepted for rational and sound design of structures based on these advanced materials.

A brief resume of the tests performed at University of Minho are also reported and validated by the numerical tools made during the research. The numerical models were also validated to reproduce the relevant aspects demonstrated of experimental tests performed by other researchers.

1.3 OBJECTIVE

The main objectives of the present work are to develop constitutive and numerical approaches for the estimation of nonlinear response of concrete structures. The main goals of the present work are:

- To propose and develop a cyclic constitutive model for the simulation of CFRP confined concrete elements, and verify the predictive performance of the model by simulating experimental tests carried out at the University of Minho and by other independent researchers;

- Implement into FEMIX, a finite element software, constitutive models for modelling the uniaxial cyclic behaviour of concrete (confined and unconfined), steel rebars, and the behaviour of concrete-reinforcement interface;

- Develop an uniaxial cyclic constitutive model for FRC and propose suitable characteristic curves, with the aim to propose design guidelines for these advanced materials;

- Develop a fibre model according to 3D Timoshenko beam theory. Steel rebars are also simulated, as well the concrete/steel interface, in order to be possible the analysis of a RC frame structure following the NLFEA strategy;

- Develop a biaxial constitutive model for concrete, and a smeared reinforcement model for steel. These models were implemented in plane stress type structures and then were extended to 3D shell type structures formulated according to the Reissner-Mindlin theory;

- Add new functionalities into DOCROS, which is a computational tool for the design of cross sections namely, the possibility of applying axial loads; reinforcements with a certain prestress level. Using the flexural stiffness derived from the moment-curvature relationship derived from Docros, the force-deflection of beams failing in bending can be estimated by using another computational tool: DefDocros.

1.4 THESIS OUTLINE

The Chapter 2 will underscore the fundamental requirement for structural modelling by describing the mechanical behaviour of materials. The uniaxial cyclic models for nonlinear behaviour of concrete, steel and CFRP will be described in detail. The next advance step in structural modelling is the interaction between these materials and hence nonlinear interface behaviour for concrete and steel will be described by suitable constitutive bond-slip laws.

The Chapter 3 will describe numerical software developed for the analysis and design of cross sections in bending and axial load, designated as DOCROS. It will emphasize on prestressing, retrofitting and strengthening of section in phases. DOCROS will be applied to parametric study based on the post-cracking characteristic of FRC, to generate the design curves for strain softening and strain hardening FRC. Using the moment-curvature relationship generated from DOCROS, the force-deflection response of a statically determinate element failing in bending can be determined using DefDOCROS. Practical examples are analysed by DOCROS and DefDOCROS to explore the possibility of replacing longitudinal reinforcement by FRC material.

The Chapter 4 present a brief resume of the experimental program of wet lay up CFRP sheets confined concrete columns carried at University of Minho, highlighting the confinement and discussion of results with aim to evaluate the important characteristics of

these tests. An extensive database of experiments carried by several other researchers is used to propose the cyclic constitutive models for CFRP confined concrete. Finally the constitutive laws are appraised by experimental data at material and structural level, for experimental data of University of Minho researchers (Barros and Ferreira 2005b) and independent researchers.

In Chapter 5 the nonlinear analysis of Timoshenko beam element by fibre approach is presented. The fibre element approach is concluded with practical example of deficiently designed building analysis, with and without strengthening intervention. Experimental campaign carried at University of Minho in collaboration with other researchers (Perrone *et* al. 2009) is also described briefly to study the effect of bar slippage and results are simulated using combination of interface and fibre element.

In Chapter 6, the developed numerical model, whose objective is to simulate concrete structures subjected to plane stress, is presented. The developed rotating crack model follows equivalent uniaxial stress-strain relations in orthogonal direction. The implementation of biaxial concrete constitutive laws in context of smeared rotating and fixed cracks will be described in detail. The performance and the accuracy of the developed numerical model are appraised by experimental results using Mindlin shell in combination with smeared reinforcement and Plane stress element with discrete reinforcement.

A brief resume of conclusions is presented in Chapter 7; an extended summary of the present thesis is also presented. The suggestions for future research are illustrated.

CHAPTER 2

Constitutive models to simulate the monotonic and cyclic behaviour of concrete, steel and FRP materials and their interfaces

2.1 MATERIALS

With easy access to computing, most of the structures can be analysed and designed by nonlinear finite element method, but the major part is being designed by assuming the materials have linear-elastic behaviour for the evaluation of the internal forces. The evolution of computing models and constitutive laws has been significant in last few decades. To achieve acceptable accuracy in any analysis, the fundamentals governing the analysis should be well defined. In case of structural analysis, the material constitutive modelling is one of the significant steps toward a successful and accepted solution. Concrete and steel are the most widely used materials in construction industry. Other materials that have recently found place in construction are the fiber reinforced polymers (FRP). The FRP materials have been mainly used in repairing and strengthening existing structures, as well as in innovative structural systems. FRP can be divided in three major categories depending on the type of fibres used: Aramid (AFRP), Carbon (CFRP) and Glass (GFRP). The CFRP and GRRP composites are more popular in reinforcing concrete and masonry structures, while aramid has been mostly used for timber. The current chapter is dedicated to the description of the cyclic constitutive models for concrete, steel and FRP that were implemented in FEMIX for the simulation of the uniaxial behaviour of these materials.

2.1.1 Concrete

The first research that attempted the characterization of the cyclic behaviour of concrete was published by Sinha *et* al. (1964). Some of the important models available in literature

are Sinha *et* al. (1964), Karsan and Jirsa (1969), Yankelevsky and Reinhardt (1987), Mander, Priestley and Park (1988a), Bahn and Hsu (1998), Chang and Mander (1994), Mansour and Hsu (2005), Palermo and Vecchio (2003). However, most of these studies focused on compressive cyclic response, only a few, Reinhardt (1984) and Reinhardt *et* al. (1986) considered cyclic tension behaviour. Some of the critical results of the experimental tests are described with focus to develop the cyclic constitutive model.

Figure 2.1, which is derived from tests conducted by Desayi *et* al. (1964) on cylindrical concrete specimen, illustrates monotonic tests results overlapping with cyclic tests results of homologous specimen. The monotonic curve approximately envelops the cyclic curves and provides an external boundary to the cycles. Hence the virgin loading of concrete specimen can be assumed as an envelope to derive the concrete material behaviour. The equation of Desai and Krishnan, discussed by Saenz (1964), was adopted by ECC (European Concrete Committee) for the compressive behaviour. The constitutive law proposed by Popovics (1973), and modified by Tsai (1988), has also quite successfully described the behaviour of monotonic concrete compressive behaviour. However, the monotonic concrete envelope has been studied by various researchers (Karsan and Jirsa, 1969, Yankelevsky and Reinhardt 1987, Bahn and Hsu 1998, Hognestand *et* al. 1955, Popovics 1973). However, none of them suitably represented the complete behaviour of concrete in compression. In fact, the proposed equations were suitable for only certain part of the compressive behaviour and failed to predict either the ascending or the post peak behaviour.

The proposed laws should fulfil the important characteristics, like the initial slope should be equal to initial modulus of deformation, should be able to predict effectively both the ascending and the post peak descending branches. At the same time the post peak behaviour should be adjustable. To simulate concretes of different brittleness, a new point can be established, designated as *critical strain point* on the post peak branch (see Figure 2.2). Moreover, use of single equation to define complete monotonic behaviour of concrete does not allow the adjustment of the softening branch to experimental results, especially the behaviour of advanced cement based materials. The location of this point can very well increase or decrease the area under the curve. The control over descending branch is important because it define the energy capacity of concrete, which in turn is

related to confinement and strength of concrete. Experiments have shown that the post peak stress decay is as smaller as larger is the degree of confinement (see Figure 2.2) (Iyengar *et* al. 1970, Scott *et* al. 1982, Mander *et* al. 1988a-b). Unconfined concrete has a much abrupt post-peak stress decay, which depends on the brittleness of the concrete (Saenz 1964). It has been observed that the transverse reinforcement provides confinement to concrete, which in turn can increase the strength and the ductility of concrete elements subjected to axial compressive loads and bending moments (Sheikh and Uzumeri 1980). Hence it was established empirically, that confined and unconfined concrete can be described by two separate models. Mostly, the effect of transverse confinement is incorporated in models by modifying the peak strength and the post peak stress-strain envelope that simulates the behaviour of confined concrete (see Figure 2.2). The stress-strain softening diagram also depends on the geometry of the specimen and testing particularities (Kotsovos 1983).

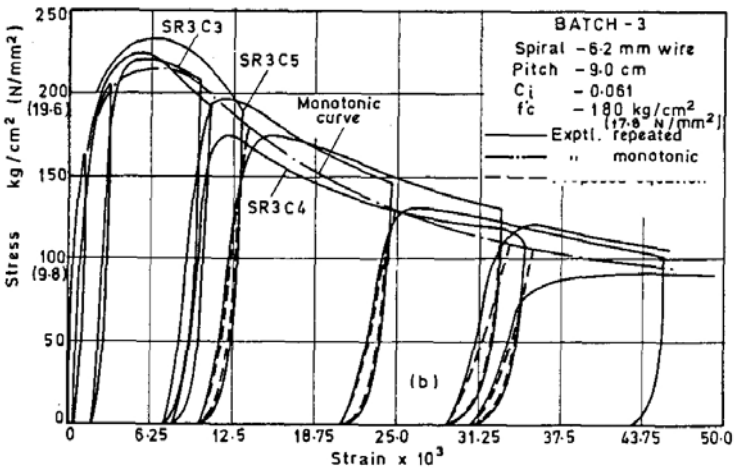

Figure 2.1: Experimental compressive behaviour of concrete (Desayi and Krishnan 1964).

Most of the typical cyclic tests carried by researchers constitute loading the concrete specimen up to a certain strain level and then unloading to a zero stress level (see Figure 2.3). The starting of unloading curve is characterized by high stiffness and gradually the stiffness decreases and become almost flat at low stress levels. As the curve become flat the plastic strain also reduces considerably. During reloading from zero stress up to envelope curve, the curve is similar to a line until the unloading strain is reached and soon after this point a pronounced non-linearity is observed. From the point of view of

damage accumulation and energy dissipation, an accurate prediction of complete cycle is utmost important. From the Figure 2.3, it is also observed that reloading curve does not return to the envelope curve at the previous maximum unloading location, hence further straining is required to take up again the envelope curve. At the same time the reloading stiffness is continuously decreasing with maximum unloading strain.

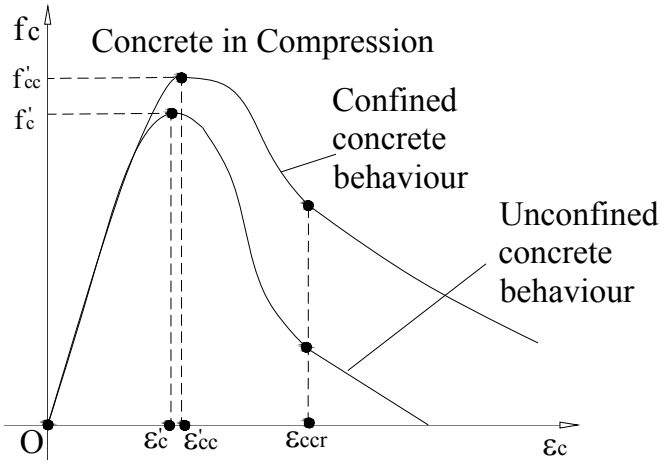

Figure 2.2: Uniaxial compressive behaviour of concrete.

Mostly the issue of partial unloading and partial reloading has been either simplified or not considered by many authors. The other reason is also being lack of experimental data available. The test results by Bahn and Hsu (1998) who developed a series of tests in order to study the response of concrete under random load cycles is used by various authors to validate the proposed models.

Very few researchers (Reinhardt, 1984 and Reinhardt *et* al., 1986, Ramtani *et* al., 1992) have studied the response of concrete under cyclic tension in detail. Several models have been proposed to represent the tensile behaviour, using straight lines (Bazant and Oh, 1983), polylinear curves (Rots *et* al., 1985), exponential curves (Gopalaratman and Shah, 1985), polynomial curves (Lin and Scordelis, 1975) or combinations of them (Cornelissen *et* al., 1985). Yankelevsky and Reinhardt (1987) have shown that the general profile of tension hysteresis is similar to hysteresis in compression, hence the same curves of compression have been modified and used for tensile loading.

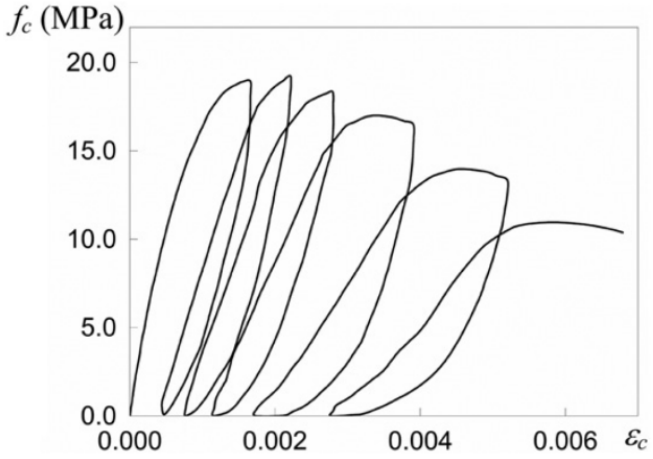

Figure 2.3: Typical cyclic compression test from Karsan and Jirsa (1964)

Based on loading loops, the uniaxial cyclic constitutive model of concrete can be fully described by three types of curves. However, based on type of mathematical equations, the complete hysteretic model can be divided in two types namely, envelope curve and connecting curves (see Figure 2.4). By decreasing the area enclosed by these curves or shifting them, the level of material degradation can be simulated. Connecting curves (e.g., BCDE, NOPQ, Figure 2.5(a)) are those curves that are used to connect the envelope curves. To simulate the phenomenon like crack opening and closing, softening or hardening, the cyclic curves are composed of several inflection points. (e.g., C, D, I, J, L). The transition curves (e.g. HI, IL, ST, TU etc) are used to connect a reversal from a connecting curve to another connecting curve, rather to an envelope curve. As reported by Chang and Mander (1994), if a transition curve is preceded directly to an envelope, the model can generate unwanted shifting under local loops. The curves follow a systematic approach that is described in Figure 2.5(b) to highlight the direction of loading and reversal if occurs. The white arrows used in Figure 2.5(b) represents a continuous excursion in the same direction, while tail of grey arrows represent the reversal point from specified curve, and tip of arrow represent the destination after reversal. In Figure 2.5(a), compression and tension envelope is assumed to be negative and positive envelope corresponding to Figure 2.5(b), respectively. Any transition or connecting curve that will lead to compression envelope, will be corresponding to negative transition (branch IL, RS, TU) and positive connecting curve (GH, NOPQ), respectively. Similarly, the positive transition

curves are PR, ST etc, and positive connecting curves are BCDE, FG etc, respectively. Figure 2.5(a) and Figure 2.5(b) reveal that a reversal from positive transition curve (for e.g., HI) will lead to negative transition curve (for e.g., IL), and if after reaching it the direction of loading remains same, it will lead to negative connecting curve (for e.g., LM), which will further lead to negative envelope curve (for e.g., MQV).

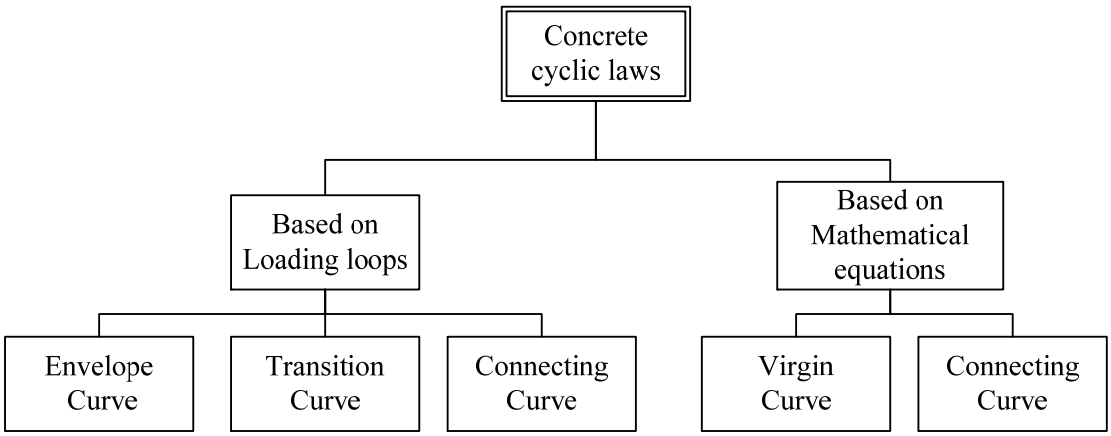

Figure 2.4: Concrete laws based on physical and mathematical properties.

From the uniaxial monotonic loading test with a concrete cylinder, an envelope stress-deformation curve can be generated, which can also be described as virgin loading of the specimen. All the hysteretic branches will be enclosed by tension and compression envelope (see Figure 2.5(a)).

Mathematically describing (see Figure 2.4), virgin curve is same as envelope curve; while the connecting curve is used to connect two points that are characterised by distinct physical phenomenon, which involve a continuous and steady change in stiffness of material, either in loading or unloading. The model uses Ramberg-Osgood equation (1935), detailed in Appendix A, for all the curves (described below), except envelope curves. The model is composed of two types of curves: monotonic envelope and hysteretic curves. As the monotonic curves form the backbone of the cyclic scheme, they are separated from other hysteretic curves; moreover all the hysteretic curves have similar equation. The complete cyclic model adopted in this work is described by fifteen rules; four rules define the monotonic envelope, while the others are used to define the hysteretic scheme.

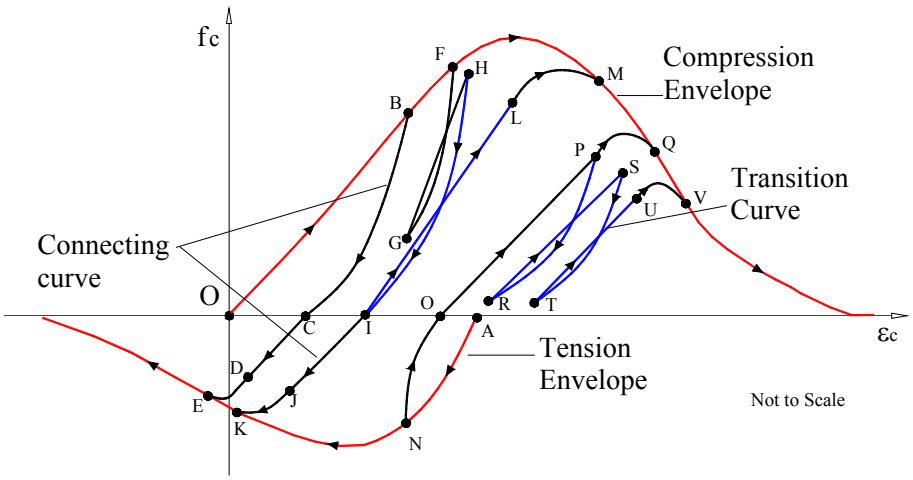

(a)

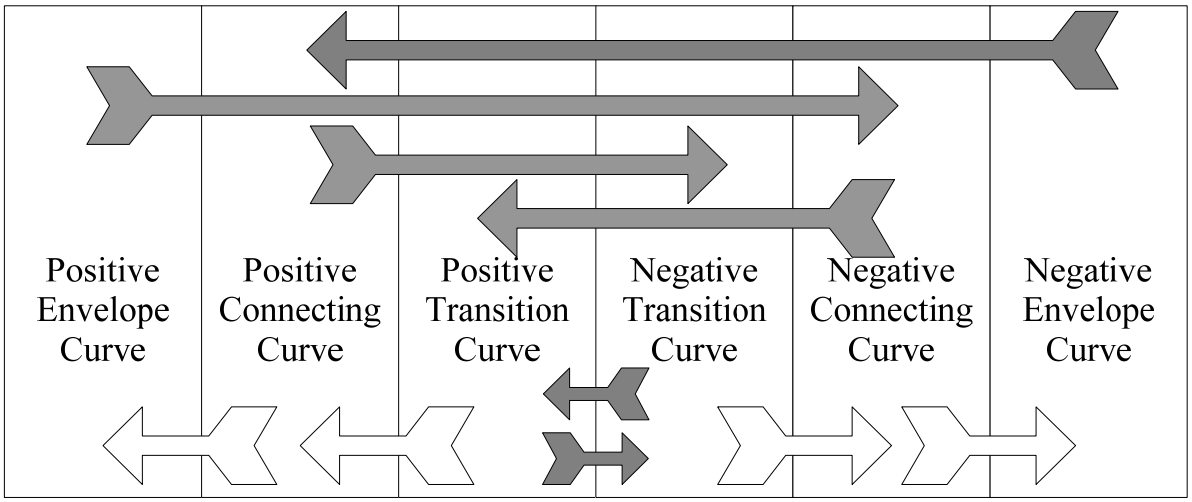

(b)

Figure 2.5: Schematic representation of type of curves based on loading and unloading.

2.1.1.1 Monotonic envelope

Figure 2.6 represents the stress-strain diagram (ε_c, f_c) of envelope curves for the simulation of uniaxial behaviour of concrete under compression and tension. The superscript + and – indicates that the parameter corresponds to a tensile and compressive state, respectively. However, it is to be noted that the stress entities of compression and tension envelope is on positive and negative ordinate side, respectively. Figure 2.6

illustrates the following entities: ε_{co} = shift strain in tension envelope; ε_{ccr}^{+} (ε_{ccr}^{-})= critical strain on tension (compressive) envelope; ε_{csp} = spalling strain; ε_{ctu} = ultimate tensile strain; E_c = concrete initial Young's modulus; (ε_{cc}, f_{cc}) = the strain and its corresponding stress at peak compression envelope; (ε_{ct}, f_{ct}) = the strain and its corresponding stress at peak tension envelope.

For compression envelope, the non-dimensional parameters are calculated from the following equations:

$$x_c^- = \varepsilon_c \Big/ \varepsilon_{cc} \tag{2.1}$$

$$n_c^- = E_c \varepsilon_{cc} \Big/ f_{cc} \tag{2.2}$$

It should be noted that for confined concrete $\varepsilon_{cc} = \varepsilon'_{cc}$ and for unconfined concrete $\varepsilon_{cc} = \varepsilon'_c$, while f'_{cc} and f'_c are the peak stress corresponding to ε'_{cc} and ε'_c, respectively.

The spalling non-dimensional strain is calculated as:

$$x_{csp} = x_{ccr}^- - \frac{y(x_{ccr}^-)}{n^- z(x_{ccr}^-)} \tag{2.3}$$

where

$$y(x_c) = \frac{n_c x_c}{D(x_c)} \tag{2.4}$$

$$z(x_c) = \frac{\left[1 - (x_c)^r\right]}{\left[D(x_c)\right]^2} \tag{2.5}$$

$$r = \frac{f_{cc}}{2.5} - 1.9 \text{, with } f_{cc} \text{ in MPa} \tag{2.6}$$

$$\begin{aligned} D(x_c) &= 1 + \left(n_c - \frac{r}{r-1}\right)x_c + \frac{(x_c)^r}{r-1} \text{ for } r \neq 1 \\ &= 1 + \left[n_c - 1 + \ln(x_c)\right]x_c \text{ for } r = 1 \end{aligned} \tag{2.7}$$

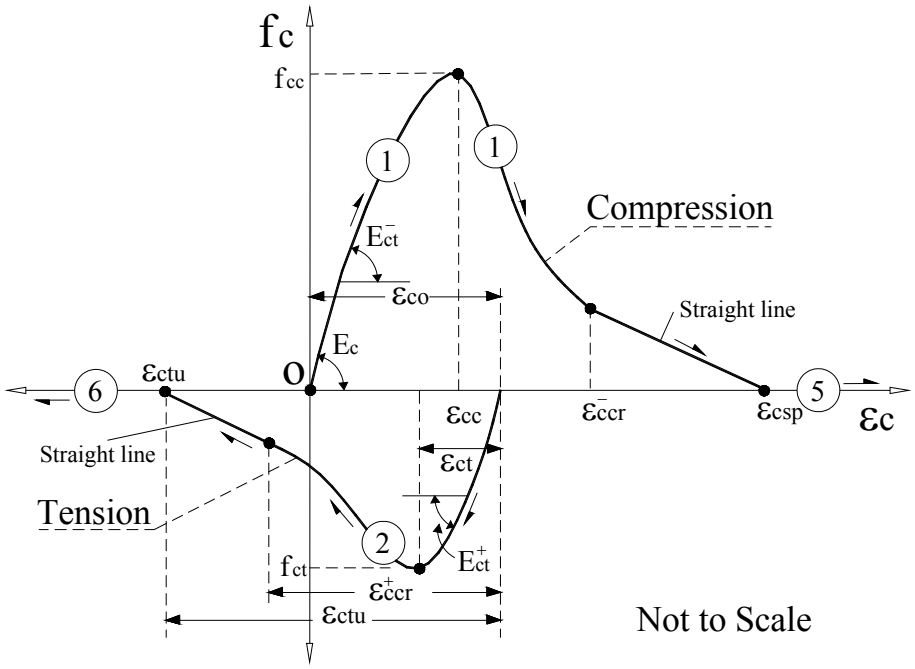

Figure 2.6: Representation of concrete envelopes in tension and compression.

Based on the derived initial parameters from Eq. (2.1) to (2.7), the non-dimensional stress-strain relationship of the envelope curve for the case of the compressive behaviour can be categorized in three zones, and written in the following manner:

for $0 < x_c^- < x_{ccr}^-$ (Tsai's equation, Rule 1)

$$f_c^- = f_{cc}\ y(x_c^-) \qquad (2.8)$$

$$E_{ct}^- = E_c\ z(x_c^-)$$

for $x_{ccr}^- \le x_c^- \le x_{csp}$ (straight line, Rule 1)

$$f_c^- = f_{cc}\ [y(x_{ccr}^-) + n_c^-\ z(x_{ccr}^-)\ (x_c^- - x_{ccr}^-)] \qquad (2.9)$$

$$E_{ccr}^- = E_c\ z(x_{ccr}^-)$$

for $x_c^- > x_{csp}$ (spalled concrete, Rule 5)

$$f_c^- = E_{ct}^- = 0 \qquad (2.10)$$

where $E_{ct}^{-(+)}$ = tangential modulus of concrete at any generic non-dimensional point $x_c^{-(+)}$, and f_c^- = concrete stress in compression side. The parameter ε_{ccr}^- represents the critical compressive strain, after which a linear stress-strain relationship is assumed for the concrete in compression (see Figure 2.6). The non-dimensional spalling strain, x_{csp}, determined according to Eq. (2.3), corresponds to the maximum compressive strain, after which, due to concrete spalling, it is assumed that the concrete residual strength is exhausted.

Eq. (2.8) and (2.9) define the Rule 1, while Eq. (2.10) defines the Rule 5. As already mentioned, the shape of the tension envelope curve is the same as that of the compression envelope curve (Chang & Mander 1994). The concrete tension envelope curve is illustrated by rule 2 (Eq. (2.11) and (2.12)) and Rule 6 (Eq. (2.13)) as follows:

for $x_c^+ < x_{ccr}^+$ (Tsai's Eq., Rule 2)

$$f_c^+ = f_{ct}\ y(x_c^+) \qquad (2.11)$$

$$E_{ct}^+ = E_c\ z(x_c^+)$$

for $x_{ccr}^+ \le x_c^+ \le x_{ctu}$ (straight line, Rule 2)

$$f_c^+ = f_{ct}\ [y(x_{ccr}^+) + n_c^+\ z(x_{ccr}^+)\ (x_c^+ - x_{ccr}^+)] \qquad (2.12)$$

$$E_{ccr}^+ = E_c\ z(x_{ccr}^+)$$

for $x_{ctu} < x_c^+$ (cracked concrete, Rule 6)

$$f_c^+ = E_{ct}^+ = 0 \qquad (2.13)$$

where f_c^+ = concrete stress in tension side, and

$$x_c^+ = \left| \frac{\varepsilon_c - \varepsilon_{co}}{\varepsilon_{ct}} \right|,\ n_c^+ = \frac{E_c\ \varepsilon_{ct}}{f_{ct}} \text{ and } x_{ctu} = x_{ccr}^+ - \frac{y(x_{ccr}^+)}{n_c^+\ z(x_{ccr}^+)} \qquad (2.14)$$

where, ε_c is a generic strain on tension envelope. It should be noted that the numerical value of ε_c can be positive or negative, depending upon ε_{co}. The evaluation of ε_{co} is described in later section.

2.1.1.2 Hysteretic laws

Whenever a reversal from envelope curve occurs, the subsequent curve is termed as unloading curve, and reversal from this later curve is termed as reloading curve. All the hysteretic rules corresponding to unloading and reloading branches are represented by a *transition curve*, which starts from an already known starting point (a subscript *a* is used to designate this point, $(\varepsilon_{ca}, f_{ca})$) and slope ($E_{ca}$) that needs to be evaluated, and ends at a target point (a subscript *b* is used to designate this point, $(\varepsilon_{cb}, f_{cb})$), whose coordinates, as well as the slope at this point (E_{cb}) need to be calculated. The transition curve is described in Appendix A and, the initial point (x_o, y_o) with slope E_o of Appendix A, are equivalent to $(\varepsilon_{ca}, f_{ca})$ with slope E_{ca}, respectively. Likewise, (x_f, y_f) and E_f of Appendix A are identical to $(\varepsilon_{cb}, f_{cb})$ and E_{cb}, respectively.

The cyclic curves will use a positive strain value, strain shift (ε_{co}), in tension envelope curve (see Figure 2.6) to simulate the realistic concrete tensile behaviour. During unloading from compression towards tension, permanent plastic strain is observed. In the concrete some part of this plastic strain will remain installed and unloading from compression will generate the tensile stresses even before any tensile strain is registered. Consequently, this effect can be modelled by shifting the tensile envelope of concrete towards compression side. It is calculated as described in the flow chart of Figure 2.7, and the variables required in calculation are shown in Figure 2.8 and Figure 2.9. In Figure 2.7, f_{cun}^{+} is calculated at envelope curve. The entities represented in Figure 2.8, (the ($\pm$) are dropped) are: $\varepsilon_{cun}^{+(-)}$ = unloading strain on tension (compressive) envelope; $\varepsilon_{cpl}^{+(-)}$ = plastic strain on tension (compressive) side; $\varepsilon_{cre}^{+(-)}$ = strain at the returning point to the tension (compression) envelope curve; $E_{cpl}^{+(-)}$ = tangential modulus at $\varepsilon_{cpl}^{+(-)}$; $E_{c\sec}^{+(-)}$ = secant modulus of concrete while unloading from envelope curve; $f_{cre}^{+(-)}$ = stress at the returning strain

($\varepsilon_{cre}^{+(-)}$); $f_{cnew}^{+(-)}$ = new stress at the unloading strain for tension (compression). The calculation of ε_{co} involves comparison of strain ductility of compression side ($x_{cu}^{-} = \left|\frac{\varepsilon_{cun}^{-}}{\varepsilon_{cc}'}\right|$) and tension side ($x_{cu}^{+} = \left|\frac{\varepsilon_{cun}^{+} - \varepsilon_{co}}{\varepsilon_{ct}}\right|$). Depending on the comparison, empirical formulas are used as shown in Figure 2.7.

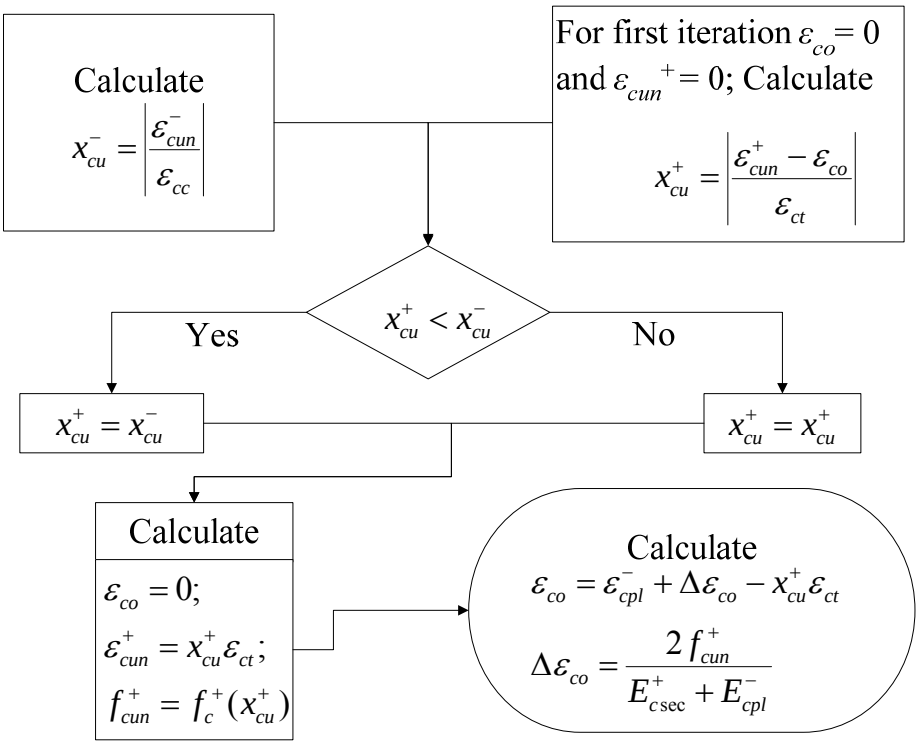

Figure 2.7: Flow chart for the calculation of shift (ε_{co}) in tension envelope curve

Chang & Mander (1994) has performed regression analysis by using experimental data from various researchers, and the equations determined for the internal parameters to define the connecting curve are included in Table 2.1.

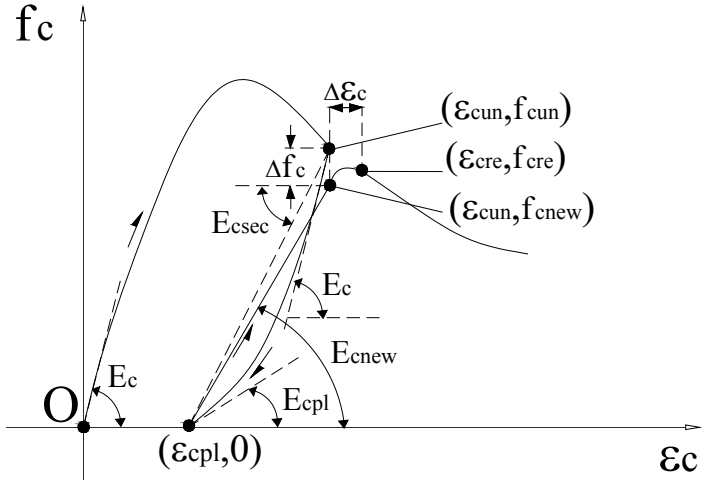

Figure 2.8: Schematic representation of unloading and reloading curve

Table 2.1: Equations to determine the internal parameters for the unloading and reloading branches of cyclic concrete constitutive model.

Parameter	(-)	(+)	
$E_{c\sec}^{+(-)}$	$E_c\left(\frac{\left\lvert\frac{f_{cun}^{-}}{E_c\varepsilon_{cc}}\right\rvert+0.57}{\left\lvert\frac{\varepsilon_{cun}^{-}}{\varepsilon_{cc}}\right\rvert+0.57}\right)$	$E_c\left(\frac{\left\lvert\frac{f_{cun}^{+}}{E_c\varepsilon_{ct}}\right\rvert+0.67}{\left\lvert\frac{\varepsilon_{cun}^{+}-\varepsilon_{co}}{\varepsilon_{ct}}\right\rvert+0.67}\right)$	(2.15)
$E_{cpl}^{+(-)}$	$0.1E_c\exp\left(-2\left\lvert\frac{\varepsilon_{cun}^{-}}{\varepsilon_{cc}}\right\rvert\right)$	$\frac{E_c}{\left\lvert\frac{\varepsilon_{cun}^{+}-\varepsilon_{co}}{\varepsilon_{ct}}\right\rvert^{1.1}+1}$	(2.16)
$\Delta\varepsilon_c^{+(-)}$	$\frac{\varepsilon_{cun}^{-}}{1.15+2.75\left\lvert\frac{\varepsilon_{cun}^{-}}{\varepsilon_{cc}}\right\rvert}$	$0.22\varepsilon_{cun}^{+}$	(2.17)
$\Delta f_c^{+(-)}$	$0.09f_{cun}^{-}\sqrt{\left\lvert\frac{\varepsilon_{cun}^{-}}{\varepsilon_{cc}}\right\rvert}$	$0.15f_{cun}^{+}$	(2.18)

The internal parameters are then used to calculate the unloading and reloading variables (see Table 2.2). A reversal from compression envelope (Rule 1, see Figure 2.9 (a)) is performed by following Rules 3, 9, 8 sequentially. Similarly, a reversal from tension envelope (Rule 2, see Figure 2.9 (b)) is performed by following Rules 4, 10 and 7 sequentially. In Figure 2.9, the virtual envelope curves are represented by dotted line and guide the incoming unloading and reloading curves to these envelopes.

Table 2.2: Unloading and reloading variables for concrete model

Variable	(-)	(+)	
$f_{cnew}^{+(-)}$	$f_{cun}^{-} - \Delta f_c^{-}$	$f_{cun}^{+} - \Delta f_c^{+}$	(2.19)
$E_{cnew}^{+(-)}$	$\dfrac{f_{cnew}^{-}}{\varepsilon_{cun}^{-} - \varepsilon_{cpl}^{-}}$	$\dfrac{f_{cnew}^{+}}{\varepsilon_{cun}^{+} - \varepsilon_{cpl}^{+}}$	(2.20)
$f_{cre}^{+(-)}$	$f_c^{-}\left(\left\|\dfrac{\varepsilon_{cre}^{-}}{\varepsilon_{cc}}\right\|\right)^{\dagger\dagger}$	$f_c^{+}\left(\left\|\dfrac{\varepsilon_{cre}^{+} - \varepsilon_{co}}{\varepsilon_{ct}}\right\|\right)^{\dagger\dagger}$	(2.21)
$\varepsilon_{cpl}^{+(-)}$	$\varepsilon_{cun}^{-} - \dfrac{f_{cun}^{-}}{E_{csec}^{-}}$	$\varepsilon_{cun}^{+} - \dfrac{f_{cun}^{+}}{E_{csec}^{+}}$	(2.22)
$\varepsilon_{cre}^{+(-)}$	$\varepsilon_{cun}^{-} + \Delta\varepsilon_c^{-}$	$\varepsilon_{cun}^{+} + \Delta\varepsilon_c^{+}$	(2.23)
$E_{cre}^{+(-)}$	$E_c^{-}\left(\left\|\dfrac{\varepsilon_{cre}^{-}}{\varepsilon_{cc}}\right\|\right)^{\dagger}$	$E_c^{+}\left(\left\|\dfrac{\varepsilon_{cre}^{+} - \varepsilon_{co}}{\varepsilon_{ct}}\right\|\right)^{\dagger}$	(2.24)

†† The stress $f_c^{+(-)}(\varepsilon_c)$ is calculated at corresponding envelope curves for generic strain ε_c.

† The tangential stiffness, $E_c^{+(-)}(\varepsilon_c)$, is calculated at corresponding envelope curves for generic strain ε_c.

The required variables to define the transition curves for reversal from compressive envelope to tension envelope and vice versa are summarized in Table 2.3 and Figure 2.9. The variables used in this table are calculated using the expressions included in Table 2.2 (see Appendix A for transition curve), which in turn use the equations included in Table 2.1.

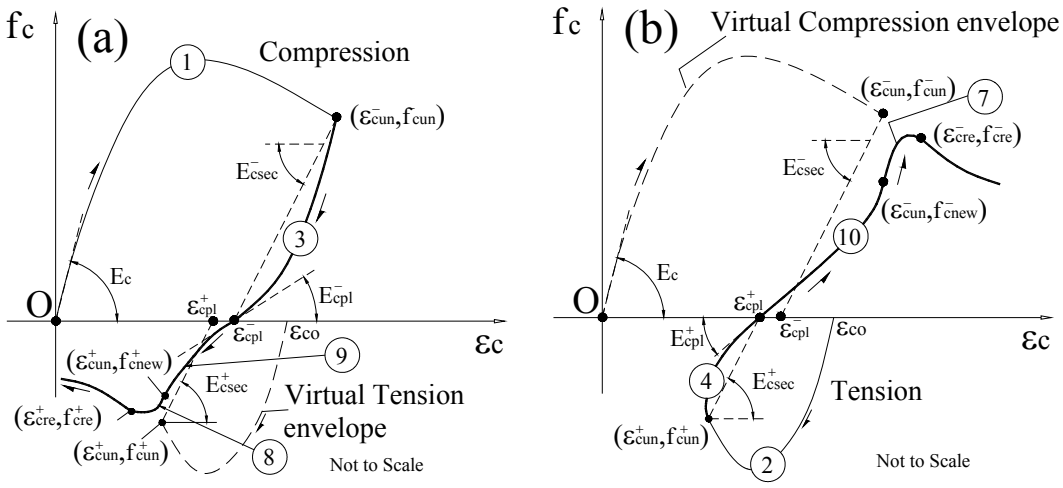

Figure 2.9: Schematic diagram for reversal from: (a) Compression envelope curve; (b) Tension envelope curve.

Table 2.3: Variables used in connecting curves for reversal from envelope curves.

Variables	Rule number					
	3	**4**	**7**	**8**	**9**	**10**
ε_{ca}	ε^{-}_{cun}	ε^{+}_{cun}	ε^{-}_{cun}	ε^{+}_{cun}	ε^{-}_{cpl}	ε^{+}_{cpl}
f_{ca}	f^{-}_{cun}	f^{+}_{cun}	f^{-}_{cnew}	f^{+}_{cnew}	0	0
E_{ca}	E_c	E_c	E^{-}_{cnew}	E^{+}_{cnew}	E^{-}_{cpl}	E^{+}_{cpl}
ε_{cb}	ε^{-}_{cpl}	ε^{+}_{cpl}	ε^{-}_{cre}	ε^{+}_{cre}	ε^{+}_{cun}	ε^{-}_{cun}
f_{cb}	0	0	f^{-}_{cre}	f^{+}_{cre}	f^{+}_{cnew}	f^{-}_{cnew}
E_{cb}	E^{-}_{cpl}	E^{+}_{cpl}	E^{-}_{cre}	E^{+}_{cre}	E^{+}_{cnew}	E^{-}_{cnew}

If during the unloading process modelled with Rule 3, a reversal from $(\varepsilon^{-}_{cro}, f^{-}_{cro})$ occurs (see Figure 2.10), it will lead to a partial unloading and reloading cycle. If the rule 3 could have been completed up to point **A** (see dotted line, Figure 2.10), a reversal from this point would have used the path shown by dotted line up to **B**. But in case of partial unloading and reloading the target point on envelope should lie between **C** and **B**, which is

represented by $(\varepsilon_{cre}^{-*}, f_{cre}^{-*})$. The parameters that define Rule 7* are obtained from the expressions of Table 2.4, corresponding to Rule 7. Similarly, if reversal from $(\varepsilon_{cro}^{+}, f_{cro}^{+})$ in Rule 4 takes place, parameters similar to Rule 8 are obtained from Table 2.4 that define the Rule 8*.

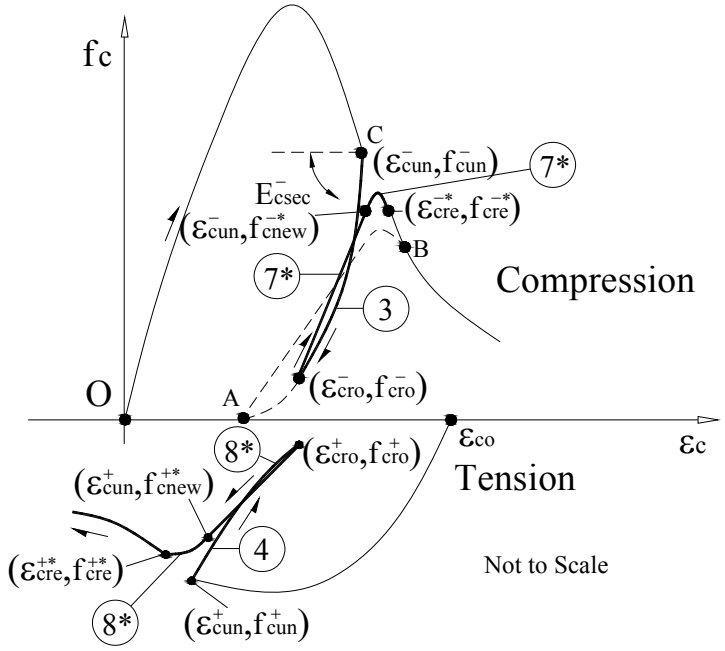

Figure 2.10: Schematic diagram of the concrete under partial unloading/reloading.

If the straining achieved in tension is more than the ultimate tensile strain (ε_{ctu}), then no tensile hysteresis is assumed to exist (see Figure 2.11). When a reversal occurs in the post-cracking phase (from Rule 6), a steady crack closure follows (Rule 13, see the corresponding variables in Table 2.6), being ε_{cr} and f_{cr} the strain and the stress components of the any general last reversal point. Moreover, in situation of no tension hysteresis, the continuation of Rule 3 will lead to rule 6 (ABC, in Figure 2.11), consequently opening of the cracks formed earlier. The opening of these cracks will not involve any tensile stresses, hence null stress (Rule 6) will continue up to maximum crack opening possible.

A reversal in Rule 9 is modelled with Rule 11, while a reversal in Rule 10 is simulated with Rule 12 (see Figure 2.12). In order to define the Rules 11 and 12, the points *a* and *b*

are assumed to be located in the branches corresponding to Rule 9 and 10, respectively (in case of Rule 12, *a* is now the target point, see Figure 2.12). Equation (2.30) is used to obtain the strain at the target point.

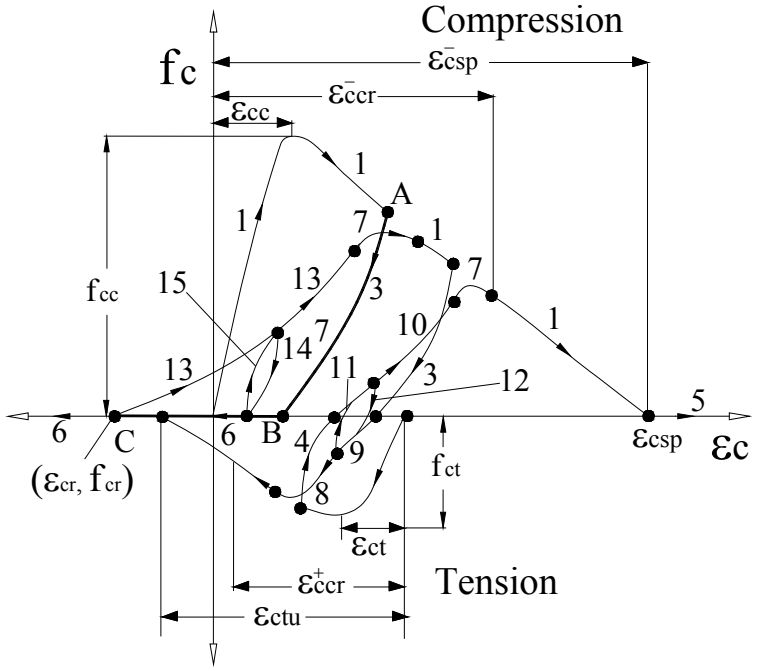

Figure 2.11: Schematic diagram of the concrete cyclic constitutive model.

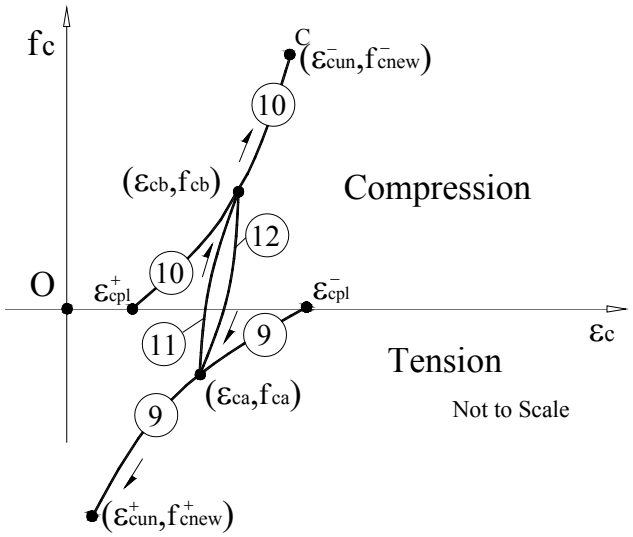

Figure 2.12: Schematic diagram for Rule 11 and Rule 12.

Table 2.4: Partial unloading and reloading variables for concrete model

Parameter	(-)	(+)	
$f_{cnew}^{+(-)}*$	$f_{cun}^{-}-\Delta f^{-}\frac{\varepsilon_{cun}^{-}-\varepsilon_{cro}^{-}}{\varepsilon_{cun}^{-}-\varepsilon_{cpl}^{-}}$	$f_{cun}^{+}-\Delta f^{+}\frac{\varepsilon_{cun}^{+}-\varepsilon_{cro}^{+}}{\varepsilon_{cun}^{+}-\varepsilon_{cpl}^{+}}$	(2.25)
$E_{cnew}^{+(-)}*$	$\frac{f_{cnew}^{-}*-f_{cro}^{-}}{\varepsilon_{cun}^{-}-\varepsilon_{cro}^{-}}$	$\frac{f_{cnew}^{+}*-f_{cro}^{+}}{\varepsilon_{cun}^{+}-\varepsilon_{cro}^{+}}$	(2.26)
$f_{cre}^{+(-)}*$	$f^{-}\left(\left\|\frac{\varepsilon_{cre}^{-}*}{\varepsilon_{cc}}\right\|\right)$	$f^{+}\left(\left\|\frac{\varepsilon_{cre}^{+}*-\varepsilon_{co}}{\varepsilon_{ct}}\right\|\right)$	(2.27)
$\varepsilon_{cre}^{+(-)}*$	$\varepsilon_{cun}^{-}+\Delta\varepsilon^{-}\frac{\varepsilon_{cun}^{-}-\varepsilon_{cro}^{-}}{\varepsilon_{cun}^{-}-\varepsilon_{cpl}^{-}}$	$\varepsilon_{cun}^{+}+\Delta\varepsilon^{+}\frac{\varepsilon_{cun}^{+}-\varepsilon_{cro}^{+}}{\varepsilon_{cun}^{+}-\varepsilon_{cpl}^{+}}$	(2.28)
$E_{cre}^{+(-)}*$	$E^{-}\left(\left\|\frac{\varepsilon_{cre}^{-}*}{\varepsilon_{cc}}\right\|\right)$	$E^{+}\left(\left\|\frac{\varepsilon_{cre}^{+}*-\varepsilon_{co}}{\varepsilon_{ct}}\right\|\right)$	(2.29)

Table 2.5: Parameters used in partial unloading and reloading.

Variables	Rule 8*		Rule 7*	
	$\left\|\varepsilon_{ro}^{+}-\varepsilon_{o}\right\|\le\left\|\varepsilon_{c}-\varepsilon_{o}\right\|$ *and* $\left\|\varepsilon_{c}-\varepsilon_{o}\right\|\le\left\|\varepsilon_{un}^{+}-\varepsilon_{o}\right\|$	$\left\|\varepsilon_{un}^{+}-\varepsilon_{o}\right\|\le\left\|\varepsilon_{c}-\varepsilon_{o}\right\|$ *and* $\left\|\varepsilon_{c}-\varepsilon_{o}\right\|\le\left\|\varepsilon_{re}^{+}*-\varepsilon_{o}\right\|$	$\left\|\varepsilon_{ro}^{-}\right\|\le\left\|\varepsilon_{c}\right\|\le\left\|\varepsilon_{un}^{-}\right\|$	$\left\|\varepsilon_{un}^{-}\right\|\le\left\|\varepsilon_{c}\right\|\le\left\|\varepsilon_{re}^{-}*\right\|$
ε_{ca}	ε_{cro}^{+}	ε_{cun}^{+}	ε_{cro}^{-}	ε_{cun}^{-}
f_{ca}	f_{cro}^{+}	$f_{cnew}^{+}*$	f_{cro}^{-}	$f_{cnew}^{-}*$
E_{ca}	E_{c}	$E_{cnew}^{+}*$	E_{c}	$E_{cnew}^{-}*$
ε_{cb}	ε_{cun}^{+}	$\varepsilon_{cre}^{+}*$	ε_{cun}^{-}	$\varepsilon_{cre}^{-}*$
f_{cb}	$f_{cnew}^{+}*$	$f_{cre}^{+}*$	$f_{cnew}^{-}*$	$f_{cre}^{-}*$
E_{cb}	$E_{cnew}^{+}*$	$E_{cre}^{+}*$	$E_{cnew}^{-}*$	$E_{cre}^{-}*$

Table 2.6: Variables used in transition curves for partial and post cracking reversals

Variables	Rule number				
	11	**12**	**13**	**14**	**15**
ε_{ca}	ε_{cr}	ε_{cr}	ε_{cr}	ε_{cr}	ε_{cr}
f_{ca}	f_{cr}	f_{cr}	0	f_{cr}	f_{cr}
E_{ca}	E_c	E_c	0	E_c	E_c
ε_{cb}	ε_{cb}	ε_{ca}	ε_{cun}^{-}	ε_{cb}	ε_{ca}
f_{cb}	f_{cb}	f_{ca}	f_{cnew}^{-}	0	f_{ca}
E_{cb}	$E_{ct,9}(\varepsilon_b)$	$E_{ct,10}(\varepsilon_a)$	E_{cnew}^{-}	0	$E_{ct,13}(\varepsilon_a)$

$$\frac{\varepsilon_{ca}-\varepsilon_{cpl}^{-}}{\varepsilon_{cun}^{+}-\varepsilon_{cpl}^{-}}=\frac{\varepsilon_{cun}^{-}-\varepsilon_{cb}}{\varepsilon_{cun}^{-}-\varepsilon_{cpl}^{+}} \tag{2.30}$$

The required variables are listed in Table 2.6, where the parameter $E_{ct,k}(\varepsilon_{ci})$ represents the tangent Young's Modulus at strain ε_{ci} for the k^{th} Rule (*i* represents the *a* or *b* point). In Table 2.6 f_{ci} represent the stress at strain ε_{ci}.

A reversal in Rule 13 is simulated with Rule 14 (see Figure 2.11), which has the *b* target point lying on the abscissa, whose strain value, ε_{cb}, can be calculated from equation (2.31)

$$\varepsilon_{cb}=\varepsilon_{ca}-\frac{f_{ca}}{E_{csec}^{-}} \tag{2.31}$$

where, E_{csec}^{-}, is obtained from Table 2.1.

Similarly a reversal from Rule 14 will generate Rule 15, which will target the starting point of Rule 14. The initial and target points required for curves of Rule 14 and Rule 15 are described in Table 2.6.

2.1.2 Steel

The cyclic model described in this section was proposed by Chang and Mander (1994) and was calibrated from the experimental data obtained from Kent and Park (1973), Ma *et* al. (1976), and Panthaki (1991). The unloading and reloading stress-strain curves were supported on the Menegotto-Pinto model (1973). Chang and Mander (1994) assumed that the form of the envelope branches should be kept intact, but when reversal occurs from them, a scale factor should be considered. This model is capable of simulating the degradation of steel under the action of local cyclic loading, which had not been proposed before. The monotonic and cyclic response of steel in tension is assumed identical to that in compression. Ten rules define the cyclic model assumed for steel bars, being five associated to the compressive state and the remaining to the tensile state, including the two envelopes.

2.1.2.1 Monotonic envelope

The monotonic envelope branches are composed of compression and tension envelope, which is the virgin loading in compression and tension, respectively. The monotonic envelope is linear-elastic until yielding is achieved, and retaining an almost constant stress until the commencement of a strain hardening phase (see Figure 2.13). In Figure 2.13, ε_{som}^{+} = point of origin of the tension envelope branch, E_s = modulus of elasticity and E_{sh}^{+} = tangent modulus at strain hardening regime. In Figure 2.13 f_{sy}^{+}, f_{sh}^{+} and f_{su}^{+} are the yield, the hardening and the ultimate (maximum) stress during tension in steel, while their corresponding strains are ε_{sy}^{+}, ε_{sh}^{+} and ε_{su}^{+}, respectively. An identical envelope and similar notation is also assumed for compressive region of steel.

The stress and the tangent elasticity modulus of the envelope curve (tension with + signal, and compression with - signal) are calculated with the Eqs (2.32)and (2.33). In these equations the tensile envelope curve (rule 1, Fig. 2.14) is described by considering the (+) version of the parameters, while the compressive envelope curve (rule 2, Fig. 2.14) is defined by considering the (-) version. Moreover, it should be noted that the numerical values of parameters on tensile side will be positive, while negative values will be assigned to parameters on compression side.

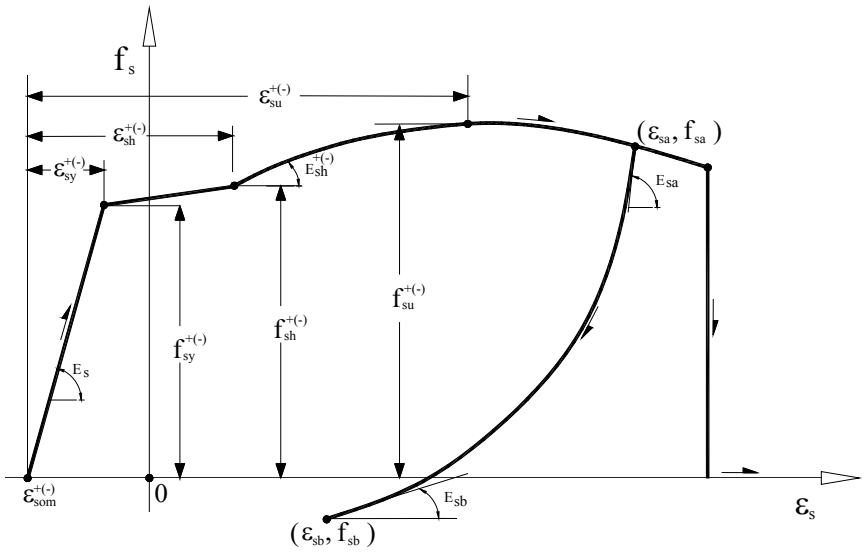

Figure 2.13: Schematic diagram of the envelope curves of the steel constitutive model.

$$f_s = \frac{E_s \varepsilon_{ss}}{\left[1+\left(\frac{E_s \varepsilon_{ss}}{f_{sy}^{\pm}}\right)^{10}\right]^{0.1}} + \frac{sign(\Delta\varepsilon_{s1})+1}{2}(f_{su}^{\pm} - f_{sy}^{\pm})\left[1-\left|\frac{\varepsilon_{su}^{\pm}-\varepsilon_{ss}^{\pm}}{\varepsilon_{su}^{\pm}-\varepsilon_{sh}^{\pm}}\right|^{p^{\pm}}\right] \tag{2.32}$$

$$E_{st} = \frac{E_s}{\left[1+\left(\frac{E_s \varepsilon_{ss}}{f_{sy}^{+(-)}}\right)^{10}\right]^{1.1}} + \frac{sign(\Delta\varepsilon_{s1})+1}{2} sign(\Delta\varepsilon_{s2}) E_{sh}^{+(-)} \left|\frac{f_{su}^{+(-)} - f_s}{f_{su}^{+(-)} - f_{sy}^{+(-)}}\right|^{\frac{p^{+(-)}-1}{p^{+(-)}}} \tag{2.33}$$

where *sign* is signum function and,

$$\varepsilon_{ss} = \varepsilon_s - \varepsilon_{so}^{+(-)};\ p^{+(-)} = E_{sh}^{+(-)} \frac{\varepsilon_{su}^{+(-)} - \varepsilon_{sh}^{+(-)}}{f_{su}^{+(-)} - f_{sy}^{+(-)}} \tag{2.34}$$

$$\Delta\varepsilon_{s1} = \varepsilon_{ss} - \varepsilon_{sh}^{+};\ \Delta\varepsilon_{s2} = \varepsilon_{su}^{+} - \varepsilon_{ss} \text{ for the case of the tensile envelope} \tag{2.35}$$

$$\Delta\varepsilon_{s1} = \varepsilon_{sh}^{-} - \varepsilon_{ss};\ \Delta\varepsilon_{s2} = \varepsilon_{ss} - \varepsilon_{su}^{-} \text{ for the case of the compressive envelope} \tag{2.36}$$

The strain parameter $\varepsilon_{som}^{+(-)}$ (Figure 2.13, derived later in next section), which is dependent on the experienced plastic excursion into the envelope curve, accounts for strain hardening during cyclic loading. Due to the shift of envelope curve, the maximum strain possible in each direction decreases, or slight premature rupture is observed (see Figure 2.14). The shift in envelope governs the maximum possible ductility is each direction (Chang and Mander 1998).

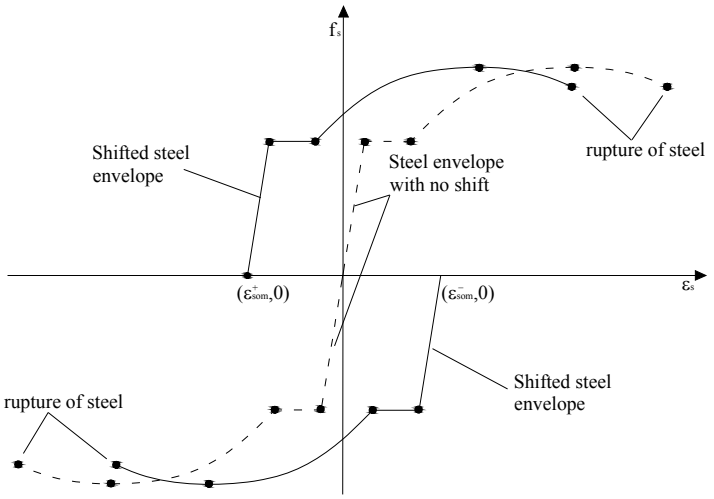

Figure 2.14: Steel envelope with and without shift of origin.

2.1.2.2 Hysteretic laws

The compression and tensile hysteretic branches are divided in four categories: Reversal, Returning, First transition and Second transition branches. Each category has two branches, one leading to compression and the other leading to tension side. The schematic diagrams for the cyclic scheme are described in Figure 2.15 and Figure 2.16. As can be seen from these figures, a reversal from the envelope generates a reversal curve (rule 3 and rule 4) that ends on the envelope of the opposite side. If a reversal occurs on reversal curves, returning branch (rule 5 and rule 6) is used to connect this reversal point and starting envelope (see Figure 2.15 and Figure 2.16). The curve that is obtained after reversal from the returning branch is called as the first transition branch (rule 7 and rule 8), while a reversal from this later one will generate first transition curves (rule 9 and rule 10). Any reversal branch is exclusively described by the two extreme points (see Figure 2.17),

i.e. maximum excursion into the tension side ($\varepsilon_{s\max}$) and compression side ($\varepsilon_{s\min}$). The Appendix B is used to obtain the strain and stress components that define the unloading and reloading branches. The following section will describe all the cyclic rules according to Figure 2.15 and will use Menegetto-Pinto (M-P) equation (1973) and the formulation detailed in Appendix B.

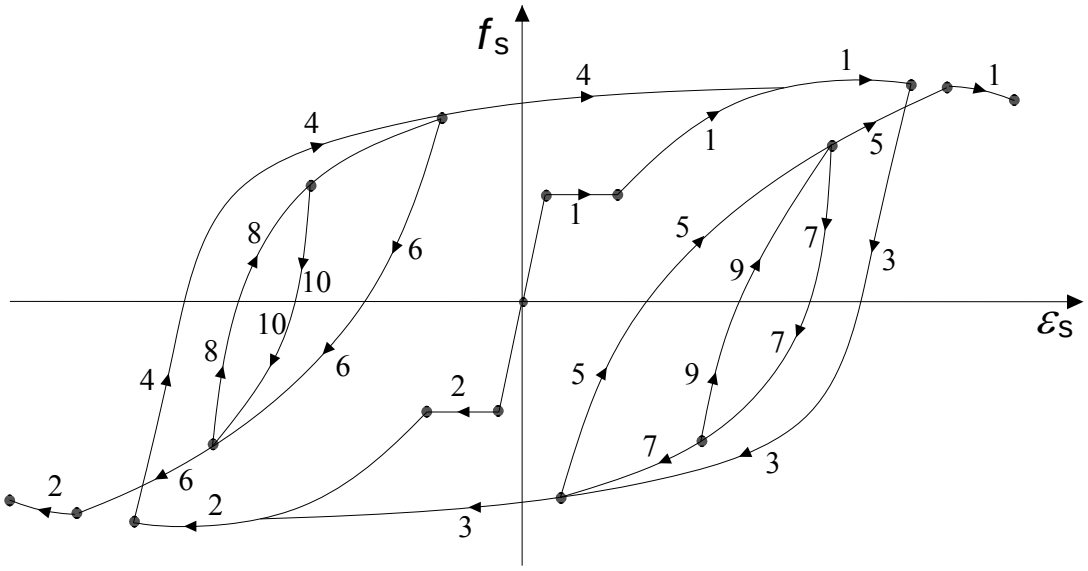

Figure 2.15: Schematic representation of the cyclic steel constitutive model.

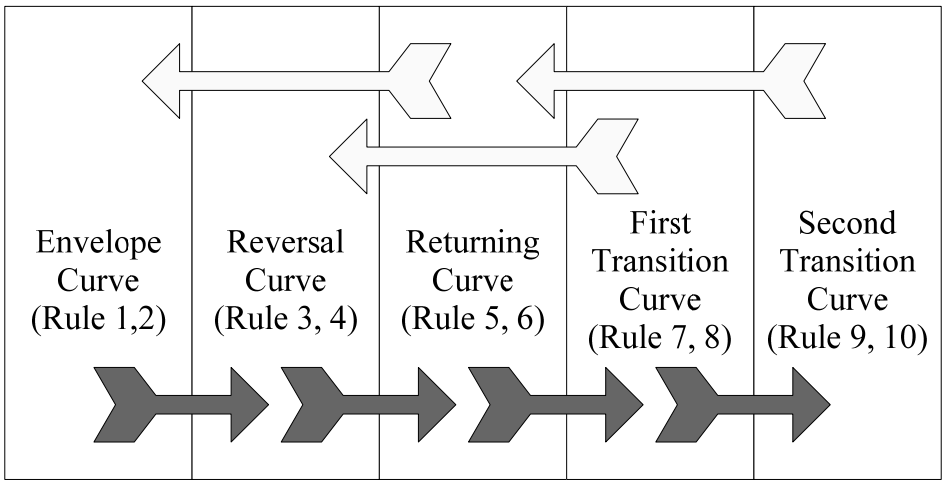

Figure 2.16: Schematic representation of type of curves based on loading and unloading.

Reversal curves (Rule 3 and Rule 4) - The reversal from envelope is categorized in two cases (see Figure 2.17) depending on the position of reversal point: a) reversal from a point within the yield plateau b) reversal from a point on the strain hardening curve. These two cases are considered separately as they are governed by different set of equations. In case of reversal from yield plateau (see Figure 2.17(a)), the internal parameters indicated in Table 2.7 are calculated, while when the unloading starts at a point on the strain hardening curve (see Figure 2.17(b)) the internal parameters included in Table 2.8 are evaluated. In Figure 2.17 the reversal from rule 1 is considered, and similar case exists for reversal from rule 2 (by + and – signs getting interchanged).

Table 2.7: Case I- Parameters for reversal branches of steel model (see Figure 2.17(a)).

Parameter	Rule 3	Rule 4
$\varepsilon_{som}^{+(-)}$	$\varepsilon_{som}^{-} = \varepsilon_{so}^{-} - \frac{f_{so}^{-}}{E_s}$	$\varepsilon_{som}^{+} = \varepsilon_{so}^{+} - \frac{f_{so}^{+}}{E_s}$
$\varepsilon_{s\max}$	$\varepsilon_{so}^{-} - \varepsilon_{som}^{+}$	$\varepsilon_{sy}^{+} + p_r(\varepsilon_{sh}^{+} - \varepsilon_{sy}^{+})$
p_r	$\frac{\varepsilon_{s\max} - \varepsilon_{sy}^{+}}{\varepsilon_{sh}^{+} - \varepsilon_{sy}^{+}}$	$\frac{\varepsilon_{s\min} - \varepsilon_{sy}^{-}}{\varepsilon_{sh}^{-} + \varepsilon_{sy}^{-}}$
$\varepsilon_{s\min}$	$\varepsilon_{sy}^{-} + p_r(\varepsilon_{sh}^{-} - \varepsilon_{sy}^{-})$	$\varepsilon_{so}^{+} - \varepsilon_{som}^{+}$
$\varepsilon_{sta}^{+(-)}$	$\varepsilon_{sta}^{-} = \varepsilon_{som}^{-} + \varepsilon_{s\min}$	$\varepsilon_{sta}^{+} = \varepsilon_{som}^{+} + \varepsilon_{s\max}$
$E_{sta}^{+(-)}$	$E_{sta}^{-} = \frac{1}{\frac{1}{E_s} + p_r\left(\frac{1}{E_{sh}^{-}} - \frac{1}{E_s}\right)}$	$E_{sta}^{+} = \frac{1}{\frac{1}{E_s} + p_r\left(\frac{1}{E_{sh}^{+}} - \frac{1}{E_s}\right)}$

For Case I and Case II, the common parameters are described in Table 2.9 and the target stress is calculated on envelope curve as $f_{sta}^{+(-)} = f_s(\varepsilon_{sta}^{+(-)})$. Once all these parameters are calculated, the Menegetto–Pinto equation (Appendix B) is followed using the Table 2.11, ε_{sai} and f_{sai} are the strain and stress components of the *a* initial point for Rule *i*, E_{sai} is the tangent elasticity modulus at this point, while ε_{sbi} and f_{sbi} are the strain and stress components of the *b* target point for Rule *i*, E_{sbi} is the tangent elasticity modulus at this

point. It is to be noted that hereon ε_{sai}, f_{sai}, E_{sai}, ε_{sbi}, f_{sbi} and E_{sbi} are equivalent to ε_o, f_o, E_o, ε_f, f_f and E_f, respectively for Appendix B.

Table 2.8: Case II-Parameters for reversal branches of steel model (see Figure 2.17(b)).

Parameter	Rule 3	Rule 4
$\varepsilon_{som}^{+(-)}$	$\varepsilon_{som}^{-} = \varepsilon_{sai}^{+} k_{rev}^{-} + \varepsilon_{sbi}^{+}(1-k_{rev}^{-})$	$\varepsilon_{som}^{+} = \varepsilon_{sai}^{-}(1-k_{rev}^{+}) + \varepsilon_{sbi}^{-} k_{rev}^{+}$
$\varepsilon_{sb}^{+(-)}$	$\varepsilon_{sb}^{+} = \varepsilon_{som}^{+} + \varepsilon_{s\max} - \frac{f_{s\max}}{E_s}$	$\varepsilon_{sb}^{-} = \varepsilon_{som}^{-} + \varepsilon_{s\min} - \frac{f_{s\min}}{E_s}$
$\varepsilon_{sa}^{+(-)}$	$\varepsilon_{sa}^{+} = \varepsilon_{som}^{+} + \varepsilon_{sh}^{+} - \frac{f_y^{+}}{E_s}$	$\varepsilon_{sa}^{-} = \varepsilon_{so}^{-} + \varepsilon_{sh}^{-} - \frac{f_y^{-}}{E_s}$
$k_{rev}^{+(-)}$	$k_{rev}^{-} = \exp\left(-\frac{\lvert\varepsilon_{s\min}\rvert}{5000(\varepsilon_{sy}^{-})^2}\right)$	$k_{rev}^{+} = \exp\left(-\frac{\lvert\varepsilon_{s\max}\rvert}{5000(\varepsilon_{sy}^{+})^2}\right)$
$\varepsilon_{sta}^{+(-)}$	$\varepsilon_{sta}^{-} = \varepsilon_{som}^{-} + \varepsilon_{s\min}$	$\varepsilon_{sta}^{+} = \varepsilon_{som}^{+} + \varepsilon_{s\max}$
$E_{sta}^{+(-)}$	$E_{sta}^{-} = E_{st}(\varepsilon_{sta}^{-})$	$E_{sta}^{+} = E_{st}(\varepsilon_{sta}^{+})$

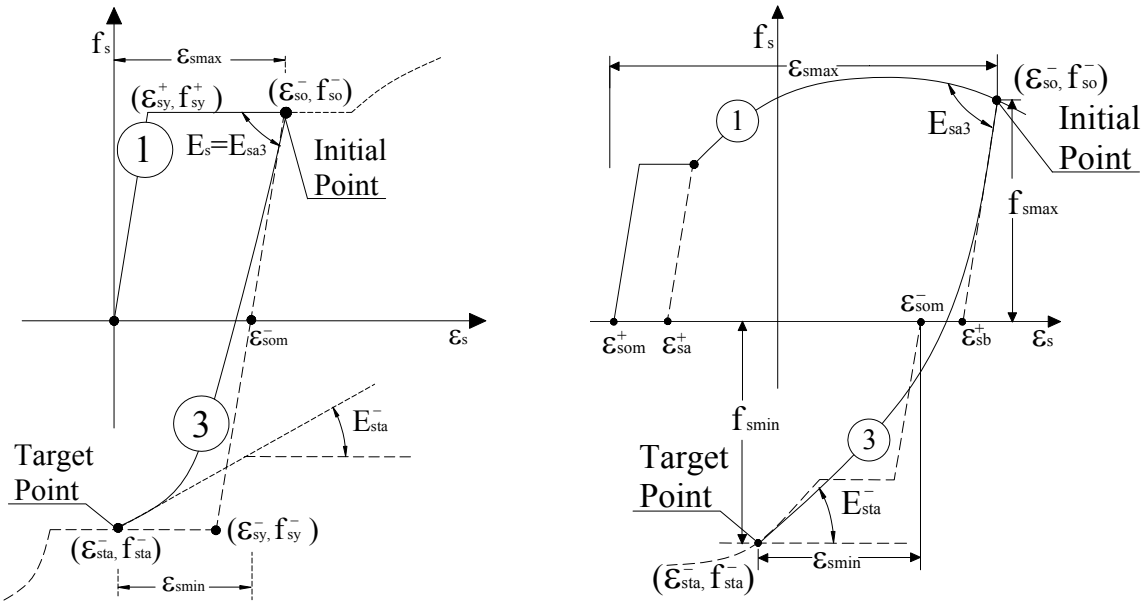

Figure 2.17: Schematic representation of type of curves based on loading and unloading.

Table 2.9 Main parameters for reversal branches of steel model.

Parameter	i = Rule 3/5/7	i =Rule 4/ 6/8
R_{si}	$20\left(\frac{f_{sy}}{E_s}\right)^{\frac{1}{3}}(1-20\Delta\varepsilon_{sai})$	$16\left(\frac{f_{sy}}{E_s}\right)^{\frac{1}{3}}(1-10\Delta\varepsilon_{sai})$
E_{sai}	$(1-\Delta\varepsilon_{sai})E_s$	$(1-3\Delta\varepsilon_{sai})E_s$

In Table 2.9 $\Delta\varepsilon_{sai} = \left|\frac{\varepsilon_{sbi}-\varepsilon_{sai}}{2}\right|$, i = Rule number; R_{si} and E_{sai} are required as curve parameters and R_{si} is designated as R in Appendix B.

Returning Branches (Rule 5 and Rule 6) - In case of reversal from envelope curve to opposite envelope is not completed (see Figure 2.18, path AB′), the reversal (B′C) from connecting curves return to previous envelope. The *returning branches*-rule 5 and rule 6, are illustrated in Figure 2.15 and corresponds to reversal from rule 3 and rule 4, respectively.

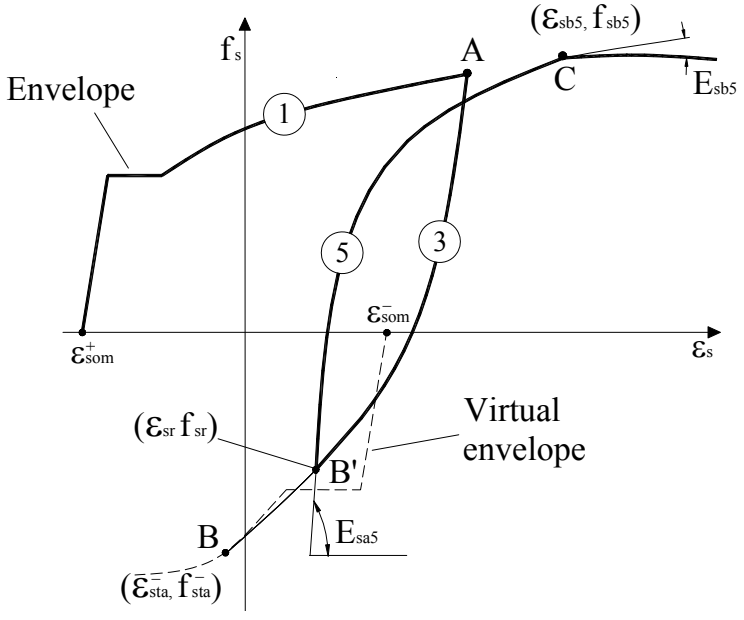

Figure 2.18: Schematic representation of rule 5.

The reversal from rule 3 (rule 4) defines the starting point of rule 5 (rule 6), and the target strain of rule 5 (rule 6) is calculated from Table 2.10. The rule 5 is illustrated in Figure 2.18, similar interpretation can be assumed for rule 6. The target stress (f_{sbi}) and slope (E_{sbi}) are calculated by Eqs. (2.32) and (2.33) for ε_{sbi}, while the starting tangential stiffness E_{sai} and R_{sai} (i =5, 6) are calculated from Table 2.9.

Table 2.10: Parameters for reversal branches of steel model.

Parameter /Condition	Rule 5	Rule 6
ε_{sbi}	$\varepsilon^{+}_{som} + \varepsilon_{s\max} + \Delta\varepsilon^{+}_{sre}$	$\varepsilon^{-}_{som} + \varepsilon_{s\min} + \Delta\varepsilon^{-}_{sre}$
$\Delta\varepsilon^{+(-)}_{sre}$	$\Delta\varepsilon^{+}_{sre} = \varepsilon_{sa3} - \varepsilon_{sa5} - \frac{f^{+}_{sy}}{1.2E_s}$	$\Delta\varepsilon^{-}_{sre} = \varepsilon_{sa4} - \varepsilon_{sa6} - \frac{f^{-}_{sy}}{1.2E_s}$
where	$0 \le \Delta\varepsilon^{+}_{sre} \le \frac{f^{+}_{sy}}{3E_s}$	$0 \ge \Delta\varepsilon^{-}_{sre} \ge \frac{f^{-}_{sy}}{3E_s}$

The initial and target coordinates for Menegetto-Pinto equation are summarized in Table 2.11. In Table 2.11 the reversal point is represented by $(\varepsilon_{sr}, f_{sr})$, it should be assumed the latest last reversal point on other curves too.

First Transition Branches (Rule 7 and Rule 8): A reversal from returning branches gives rise to first transition branches (rule 7 and rule 8). In case of reversal from rule 5 (rule 6), rule 7 (rule 8) will follow from that point onwards, rule 7 (rule 8) will target the starting point of rule 5 (rule 6), which is also the reversal from rule 3 (rule 4). The target strain (point D, see Figure 2.19) of rule 5 lies on envelope curve; however it is not the initial point (point A, see Figure 2.19) of rule 3. If rule 5 would have achieved completion, a reversal from this newly arrived point (point D) would mean reversal from envelope curve, i.e., starting of rule 3. It can be assumed that a reversal from rule 5 (partial loading), a redefined rule 3 (path D′B″) needs to be calculated. The starting strain (ε^{*}_{sa3} , point D′) of this rule needs to be between the starting strain of previous rule 3 and target strain of rule 5. From linear proportion the strain for the intermediate strain can be described by Eq (2.37):

$$\varepsilon_{sa3}^{*} = \varepsilon_{sb5}\frac{\varepsilon_{sa7}-\varepsilon_{sa5}}{\varepsilon_{sb5}-\varepsilon_{sa5}} + \varepsilon_{sb3}\frac{\varepsilon_{sb5}-\varepsilon_{sa7}}{\varepsilon_{sb5}-\varepsilon_{sa5}} \tag{2.37}$$

The Eq (2.37) will reduce to $\varepsilon_{sa3}^{*} = \varepsilon_{sb3}$, (see point F, expected end of rule 3) if the reversal happens, after rule 5 has just started ($\varepsilon_{sa7} = \varepsilon_{sa5}$), however the same expression reduces to $\varepsilon_{sa3}^{*} = \varepsilon_{sb5}$, if the reversal is suppose to happen at the end ($\varepsilon_{sa7} = \varepsilon_{sb5}$, i.e. C′ will move to D) of rule 5. After calculating the ε_{sa3}^{*}, target point parameters are calculated by rule 3, which serves as the target point for rule 7. Similarly for rule 8 an analogous expression is used to calculate the intermediate starting point of rule 4, described by Eq (2.38):

$$\varepsilon_{sa4}^{*} = \varepsilon_{sb6}\frac{\varepsilon_{sa8}-\varepsilon_{sa6}}{\varepsilon_{sb6}-\varepsilon_{sa6}} + \varepsilon_{sb4}\frac{\varepsilon_{sb6}-\varepsilon_{sa8}}{\varepsilon_{sb6}-\varepsilon_{sa6}} \tag{2.38}$$

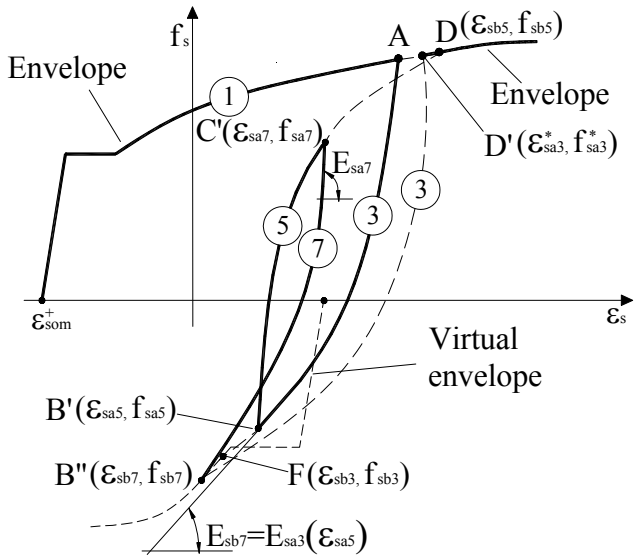

Figure 2.19: Schematic representation of rule 7.

The target point for rule 8 is same as determined by using rule 4 assuming starting point strain, ε_{sa4}^{*} The vital parameters for first transition rules are represented in tabular form (Table 2.11), where, $E_{s3}(\varepsilon_{sa5})$ is the tangential modulus calculated on rule 3 corresponding to the strain ε_{sa5}, a similar assumption is assumed for $E_{s4}(\varepsilon_{sa6})$. The equation described in Appendix-B can then be used to connect these two points of Table 2.11.

Second Transition Branches (Rule 9 and Rule 10): In case of reversal from rule 7, when partial unloading is done on rule 7, rule 9 will arise from that point onwards. The curve that follows a reversal from rule 7 is called as the second transition curve (rule 9) whose target point is defined by Eq (2.39):

$$\varepsilon_{sb9} = \varepsilon_{sa7} \tag{2.39}$$

The target stress f_{sb9} is the initial stress (f_{sa7}) of rule 7 and the target slope E_{sb9} is calculated on rule 5. Figure 2.20 represents the generation of rule 9 after reversal from rule 7, if rule 7 is not completed. The vital parameters required for rule 9 are summarized in tabular form (see Table 2.11). Using the similar analogy as used for rule 9, in case when partial loading is done on rule 8, rule 10 starts from that point onwards.

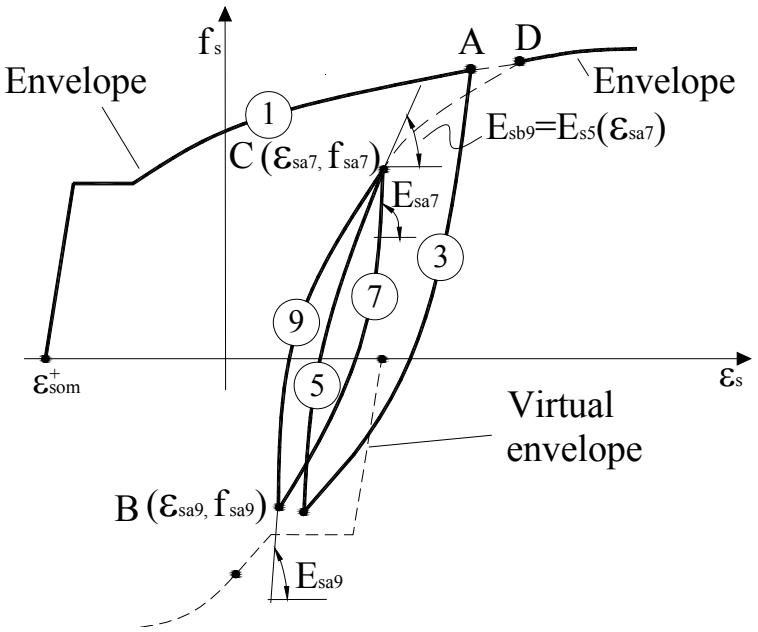

Figure 2.20: Schematic representation of rule 9.

The starting strain of rule 10 is defined by the reversal point lying on rule 8 while the target point is considered to be the starting point of rule 6. The vital parameters of the rule are summarized in tabular form (see Table 2.11). Figure 2.15 represents the generation of rule 10 after reversal from rule 8, for partial completion of rule 8.

Table 2.11. Controlling parameters used in cyclic scheme based on rule number.

Parameter	Rule number							
	3	4	5	6	7	8	9	10
ε_{sai}	$\varepsilon_{som}^{+}+\varepsilon_{s\max}$	$\varepsilon_{som}^{-}+\varepsilon_{s\min}$	ε_{sr}	ε_{sr}	ε_{sa7}	ε_{sa8}	ε_{sr}	ε_{sr}
f_{sai}	$f_{\max}$	$f_{\min}$	f_{sr}	f_{sr}	f_{sa7}	f_{sa8}	f_{sr}	f_{sr}
E_{sai} †	E_{sa3}	E_{sa4}	E_{sa5}	E_{sa6}	E_{sa7}	E_{sa8}	E_{sa9}	E_{sa10}
ε_{sbi}	$\varepsilon_{s\min}+\varepsilon_{som}^{-}$	$\varepsilon_{s\max}+\varepsilon_{som}^{+}$	$\varepsilon_{s\max}+\varepsilon_{som}^{+}+\varepsilon_{sa3}-\varepsilon_{sa5}-\frac{f_{sy}^{+}}{1.2E_s}$	$\varepsilon_{s\min}+\varepsilon_{som}^{-}+\varepsilon_{sa4}-\varepsilon_{sa6}-\frac{f_{sy}^{-}}{1.2E_s}$	ε_{sa5}	ε_{sa6}	ε_{sa7}	ε_{sa8}
f_{sbi}	$f_s(\varepsilon_{sb3})$ ††	$f_s(\varepsilon_{sb4})$ ††	$f_s(\varepsilon_{sb5})$	$f_s(\varepsilon_{sb6})$	f_{sa5}	f_{sa6}	f_{sa7}	f_{sa8}
E_{sbi}	$E_s(\varepsilon_{sb3})$ ††	$E_s(\varepsilon_{sb4})$ ††	$E_s(\varepsilon_{sb5})$	$E_s(\varepsilon_{sb6})$	$E_{s3}(\varepsilon_{sa5})$	$E_{s4}(\varepsilon_{sa6})$	$E_{s5}(\varepsilon_{sa7})$	$E_{s6}(\varepsilon_{sa8})$
R_{si} †	R_{s3}	R_{s4}	R_{s5}	R_{s6}	R_{s7}	R_{s8}	R_{s9}	R_{s10}

† Calculated from Table 2.9

†† For unloading before yielding, the parameters $E_s(\varepsilon_{sb3})$ and $E_s(\varepsilon_{sb4})$ are replaced with E_{sta}^{+} and E_{sta}^{-}, respectively.

2.1.3 CFRP

The use of Fibre Reinforced Polymer (FRP) systems has increased significantly over the past two decades mostly due to their advantageous properties like lightweight, corrosion resistance, high strength, and high stiffness compared to steel bars. These systems are found highly useful in retrofitting and strengthening, mostly to increase the load carrying capacity of concrete and masonry structures that need to be upgraded in order to support more exigent load levels. Retrofitting can save the costs of demolishing and constructing new structures, with the resulting beneficial environmental impacts. In some cases retrofitting is the unique alternative, such is the case of historical buildings or with culture relevance.

The FRP materials are available as sheets, fabrics and bars. The sheets or fabrics are available as uni-directional, multi-directional, dry sheet, laminates, plates, etc, while the

bars can have a circular, square or rectangular cross section. These polymer based materials can be reinforced with Carbon (CFRP), Aramid (AFRP), Glass (GFRP) and Basalt (BFRP) fibres. Mostly the laminates have been used as external bonding material, which uses adhesives (especially epoxies) to bond these composites to the structures. This strengthening method has shown significant advantages compared to traditional methods, because of high tensile strength of CFRP compared to steel (see Figure 2.21), easy installation and minor alterations to the geometry of the elements to be strengthened. However, special care should be taken in order to prevent premature debond, and the consequent lost of strengthening effectiveness. These composite systems can be applied using two types of techniques (ACI 2008): Externally Bonded Reinforcement (EBR), Near Surface Mounted (NSM).

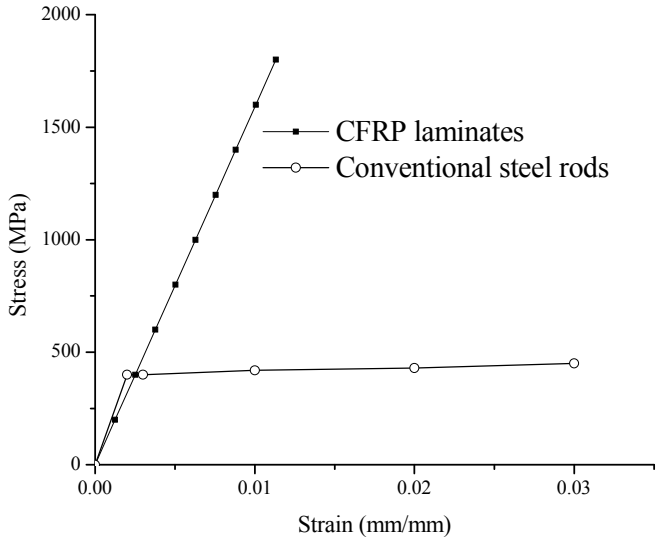

Figure 2.21: Comparison of stress-strain response of steel and CFRP laminates.

Experimental research is revealing that NSM is more effective than EBR for the flexural (Barros and Fortes 2005) and shear (Barros and Dias 2006) strengthening of concrete structures (Barros *et* al. 2007a). In the NSM technique laminate strips of CFRP are introduced into saw-cut slits opened on the concrete cover of the elements to be strengthened (Sena-Cruz 2004). EBR technique is being used for the flexural and shear strengthening, as well as for the confinement of concrete columns (Barros and Ferreira 2008). As the FRP systems behave linear elastically until failure, the constitutive equation

to model the uniaxial stress strain behaviour is assumed to be linear elastic in the numerical simulations of this work.

2.2 INTERFACE BETWEEN CONCRETE AND STEEL

An interface always exists between materials that have a distinct deformational response when subjected to the same loading conditions. Materials of different properties, like concrete, steel and FRP, have tendency to form interface transition zones in the contact areas, that are, in general, week surfaces prone to promote sliding between the materials in contact. In the computational mechanics, these interfaces zones are simulated by interface finite elements.

An interface finite element represents an imaginary zone, which is mostly considered with zero thickness, with a constitutive law that aims to simulate the sliding and separation of materials in contact. The simulations of the imperfect bond conditions, typical of the link between steel rebar and surrounding concrete, will be discussed in this section, by using a tangential stress versus sliding model in the direction of the reinforcement.

2.2.1 Perfect bond

Most of the structural analysis and design of reinforced concrete structures assume perfect bond conditions between concrete and steel rebars. This means that concrete and steel bars located at the same depth inside a section have the same deformation. In finite element modelling, common degrees of freedom are shared by different material type elements. This condition is violated in order to include the effects of bond-slip when imperfect bond is assumed.

2.2.2 Bond-slip

2.2.2.1 Survey of steel/concrete bond behaviour

One of the first experimental programs explaining the possible bond response of deformed reinforcing steel was carried by Rehm (1958). Later Lutz *et* al. (1966) also carried out similar experimental program. They did not consider all the key parameters that influence

bond response, even though the data provided the force, deformation and damage pattern associated with bond response and, hence contribute to the preliminary characterization of the concrete-steel interface.

Later, detailed investigations were conducted by Goto (1971) and several other researchers (Watstein and Mathey 1961, Lutz and Gergley 1967, Tepfers 1979). Tepfers study was focused on the prediction of bond strength for deformed reinforcement. He proposed an analytical model that considers concrete in the vicinity of reinforcing bar as a thick walled cylinder subjected to internal shear (bond stress) and pressure (radial stress). Tilantera and Rachardt (1977) had also drawn similar conclusion from an experimental investigation. An extensive research has been carried out on bond stress versus slip response by Viwathanatepa (1979a and 1979c) and Eligaushen *et* al. (1983). Viwathanatepa (1979a and 1979b) is one of the first researchers who carried out experiments focusing on the load deformation response of anchored deformed reinforcement. The experimental investigation of Hawkins *et* al. (1982) represent an extreme case of bond strength because of short anchorage length (<2 times bar diameter (Φ_b) contrary to $5\Phi_b$ as mostly reported by other researchers. The data provided by Eligaushen *et al.* (1983) shows bond slip response for deformed reinforcement subjected to monotonic tension and compression, reversed cyclic, cyclic loading in tension only, reversed cyclic loading to increasing maximum absolute slip levels etc.

This data is appropriate for the development and calibration of models. Viwathanatepa (1979b) observed that the bond strength is significantly higher for the reinforcement yielding in compression than that for reinforcement yielding in tension. This phenomenon can be explained partly on the basis of Poisson effect that causes the diameter of the reinforcing bar to shrink in case of tensile yielding and, thereby, decreasing the connectivity between steel bar and concrete surface surrounding it. In the opposite, the diameter of the reinforcing bar increases when the bar yields in compression promoting the bond conditions between steel and surrounding concrete. The results evidence a significant drop in bond strength once yielding occurs.

The interaction between steel and concrete affects significantly the behaviour of reinforced concrete structures, especially when subjected to reversed cyclic loadings (for ex.

Earthquake loading). Bond behaviour is a combination of adhesion, bearing of lugs and friction. Adhesion is related to shear strength of the steel-concrete interface and is the outcome mainly of chemical bonding. Bearing forces which are perpendicular to the lug faces and, arises to counteract the sliding of bar. Friction is generated by bearing forces on the interactional surface and, by shearing off the concrete between the lugs on the cylindrical concrete surface at the tip of lugs.

Degradation of bond strength and bond stiffness is more severe in cycles with reversed loading compared to unidirectional loading. Degradation is significantly affected by maximum slip in either direction reached previously, the number of cycles and, difference between the peak slips between which reinforcing bars is cyclically loaded. If the stress induced in either cycle does not exceed 70-80% of the monotonic bond strength, the deterioration of bond resistance is moderate. The same deterioration becomes extensive as the peak stress achieved during cycle tends to 80% or more of monotonic bond strength (τ_s).

Eligehausen *et* al. (1983) has described the interactional behaviour under cyclic loading based on physical phenomenon at microscopic scale. The variables that results in a unique definition of the bond material model are: (a) slip (b) difference in slip compared to previously achieved slip (c) peak slip in either directions (d) stress due to mechanical interaction at last slip reversal or (e) stress due to residual friction at last slip reversal. A set of eight rules defining the complete bond-slip behaviour are described in the following section, divided under monotonic envelope and hysteretic scheme. In the proposed bond model the monotonic envelopes are derived from Eligehausen *et* al. (1983) and the hyteresis scheme is derived Ciampi *et* al. (1983).

2.2.2.2 Monotonic envelope

The monotonic envelope is can be of two types, virgin envelope and reduced envelope, based on the history of loading process; however only virgin envelope is described here and the reduced envelope will be described in next section under hysteretic scheme.

Virgin Envelope: Once monotonic loading of reinforcing bar embedded in a concrete block starts, the slip versus stress is assumed to follow a monotonic envelope (Path OABCD, see

Figure 2.22). Monotonic loading up to point A results in inclined cracks generating from the tip of lugs, and their proliferation and dimension is assumed to be confined by transverse stress. If the monotonic loading is continued, it causes crushing of concrete in front of the lugs resulting in reduction of bond stiffness (tangent to the bond stress slip curve). In case the slip loading continues, inclined cracks keep start appearing from the top of lugs. When the concrete key is sheared off a cone of four times the lug height is formed, consequently peak stress (point C) and almost null bond stiffness is reached. Further increase in slip causes a decrease of the bond stress (slip-softening phase). When the bond shear crack reach the bottom of the adjacent lug, the bond stress starts falling (Point D). When the slip becomes equal to the distance between the lugs, only the frictional component remains (Point E). The experimental response described, can be analytically modeled by assuming some simplifications as described in the following section.

The envelope curve is assumed to have same shape for slip in both directions. Based on the experimental response, the bond stress-slip relationship ($\tau_b - s$) can be illustrated by the equations (2.40) to (2.43) (See Figure 2.23). In these equations + and – is used to differentiate between positive slip direction and negative slip direction, respectively.

$$\tau_b = \tau_{bp}^{+(-)} \left(s / s_{bp}^{+(-)} \right)^{\alpha} \text{ for } 0 \le s^{+(-)} < s_{bp}^{+(-)} \tag{2.40}$$

$$\tau_b = \tau_{bp}^{+(-)} \text{ for } s_{bp}^{+(-)} \le s < s_{bl}^{+(-)} \tag{2.41}$$

$$\tau_b = \tau_{bf}^{+(-)} + \left(\frac{\tau_{bp}^{+(-)} - \tau_{bf}^{+(-)}}{s_{bl}^{+(-)} - s_{bf}^{+(-)}} \right) (s - s_{bf}^{+(-)}) \text{ for } s_{bl}^{+(-)} \le s \le s_{bf}^{+(-)} \tag{2.42}$$

$$\tau_b = \tau_{bf}^{+(-)} \text{ for } s_{bf}^{+(-)} < s \tag{2.43}$$

where $\tau_{bp}^{+(-)}$ is the maximum bond stress value, $s_{bp}^{+(-)}$ is the corresponding slip, $s_{bf}^{+(-)}$ is the slip after which only frictional stress ($\tau_{bf}^{+(-)}$) remain, and $s_{bl}^{+(-)}$ represents the end of the peak stress plateau. In the Figure 2.23 the symbols ($\pm$) are dropped, while in equation it is maintained for the proposal of cyclic laws.

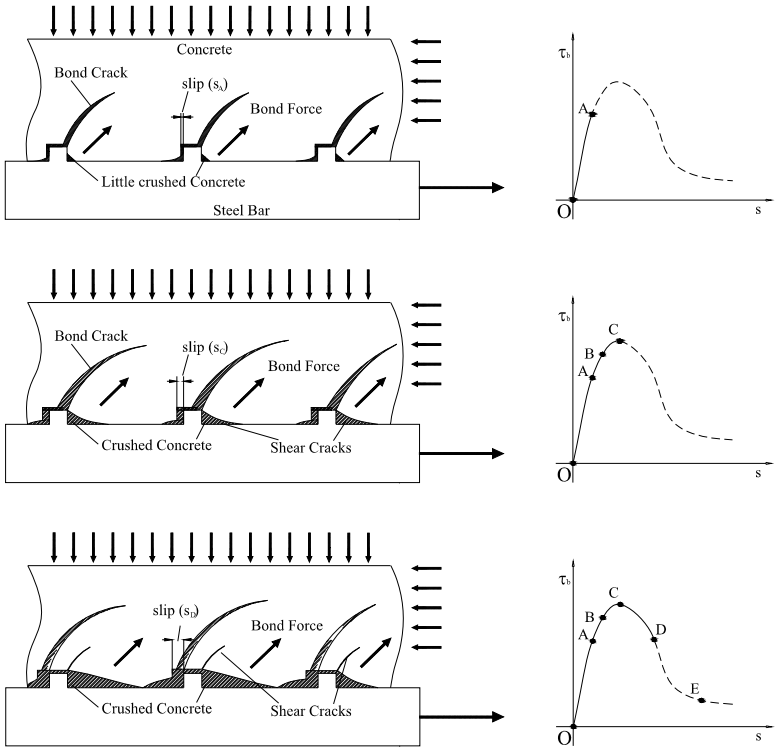

Figure 2.22: Experimental representation of bond-slip phenomenon (adapted from Eligehausen *et* al. 1983).

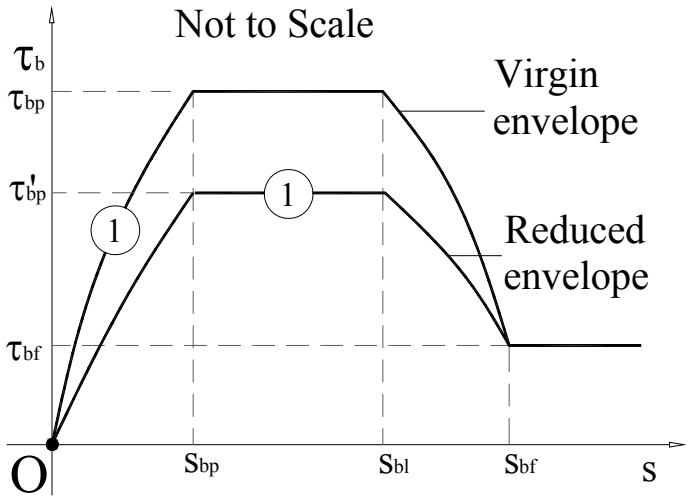

Figure 2.23: Schematic representation of bond-slip envelope for both directions

2.2.2.3 Hysteretic laws

Typical cyclic bond models include those proposed by Morita and Kaku (1973), Shipman and Gerstle (1979), Tassios (1979), and Filippou (1983). As most of the models are developed on limited experimental data, the models show variation in strength and stiffness, but the key features of the response are similar. Hence these models are acceptable for analysis of system subjected only to moderate slip reversals. More elaborate studies were conducted by Cowell (1982), Hawkins *et* al. (1982), Eligehausen *et* al. (1983), Tassios and Yannnapoulos (1983), Ciampi *et* al. (1983) and Fillipou (1983, 1986). The section will describe three important topics: cyclic experimental behaviour of concrete-steel interface, reduced envelope generation and hysteretic scheme.

As already described, hysteretic behaviour of bond slip is highly dependent on number of cycles and level of slip excursion in both directions. The unloading behaviour can be described by three key cases: unloading before reaching point A; unloading after point A but before reaching point C; and unloading from a point after C (see Figure 2.24(a)). If the unloading start before formation of inclined cracks, stiff unloading branch (AF) is resulted, and in case the slip in opposite direction is continued, the friction branch (GH) is followed. When the slip is decreased further, the stiffness increases sharply, and results in closing of cracks formed when slip corresponding to point A was reached. For the cycle to complete the reversal is considered from point I, which has slip equal to point A, but in opposite direction. A path IKL, similar to the FGH is followed (see Figure 2.24(a)). Until the slip in positive direction does not reach approximately equal to the point A, the stiffness remain almost nil, since bar slides on already crushed and cracked concrete present in front of the ribs. The full bearing capacity of lugs is reached at point M, which is assumed to be lying on the monotonic envelope.

Consider another case, if slip reversal happens near peak (see Figure 2.24(b)), then the unloading branch CF is similar to the previous case (see Figure 2.24(a)). As there is more damage so higher friction resistance is generated (point G). The cracks formed closes at higher load (point H) and generate splitting crack in other direction also. Splitting crack in addition of existing inclined crack reduces the envelope (HI). It is to be noted that this new envelope can be assumed as reduced envelope Reversal from this peak I, follows (Path IKLMN). During path LMN, the bond strength at point N is lower than C and I.

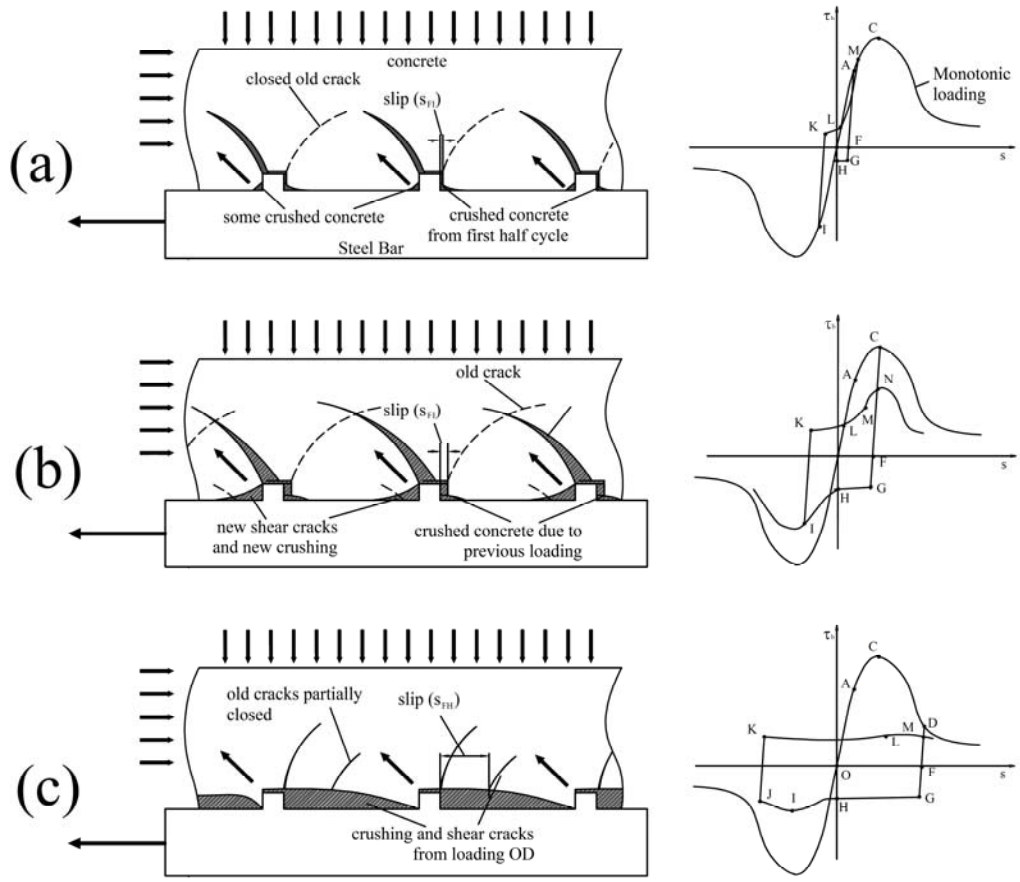

Figure 2.24: Experimental representation of cyclic bond-slip phenomenon (adapted from Eligehausen *et* al. 1983).

For the last case, when slip-reversal occurs after peak slip (point C, see Figure 2.24(c)), the bond strength is significantly less in both directions as the concrete between the lugs is sheared off. Unloading and reloading in opposite direction result in little, mostly frictional strength and almost very little bond capacity.

2.2.2.1 Reduced monotonic envelope:

To generate the effect of cyclic loading, the envelope curve (virgin) is scaled to represent the degradation in interface. To account this characteristic of response in the proposed bond model, a relationship defining the deterioration of bond strength as a function of the number of load cycles is defined. However the effect of cycles is incorporated by

calculating the energy dissipated during hysteretic cycles compared to the total available energy.

The peak bond stress $\tau_{bp}^{+(-)}$ for virgin and reduced envelope is related as:

$$\tau_{bp}^{+(-)\prime} = \tau_{bp}^{+(-)}(1-d_b) \tag{2.44}$$

where d_b is the damage factor and $\tau_{bp}^{+(-)\prime}$ is the peak stress of reduced envelope (see Figure 2.23).

Damage in the concrete surrounding the bar depends on the maximum excursion of the bar in both directions and the number of cycles. Both these parameters can be taken into account through energy dissipated, hence d_b is a function of total dissipated energy. The total energy is defined as the area under the bond-slip curve (OABC) and illustrated as:

$$P_b^{total} = \int_{s=0}^{s=s_{bf}} \tau_b s ds \tag{2.45}$$

In the Figure 2.25, for a positive envelope, the dissipated energy up to the slip reversal, s_{bun}^{+}, is calculated as:

$$P_b^{+} = \int_{s=0}^{s=s_{bun}^{+}} \tau_b s ds \tag{2.46}$$

This P_b^{+} is used for the calculation of positive reduced envelope (OJC). It is to be noted that this released energy will be used in calculation of reduced envelope, when path OADEFGH is followed.

The rules for the reversal are described in next section, however assuming if the slip in opposite direction (DEFG) continues then the dissipated energy of the other side up to slip reversal (s_{bun}^{-}) is observed, and can be calculated as:

$$P_b^{-} = \int_{s=0}^{s=s_{bun}^{-}} \tau_b s ds + 0.5 \int_{s=s_{br}^{+}}^{s=0} \tau_b s ds \tag{2.47}$$

This dissipated energy will be used in calculation of negative reduced envelope, when the slip cycle is reversed. In this case half of the energy due to the friction is assumed.

The damage factor is calculated as a function of dimensionless dissipated energy ($P_b^{+(-)} / P_b^{total}$) as described in Eqn (2.48).

$$d_b = 1 - s^{-1.2\left(P_b^{+(-)}/P_b^{total}\right)^{1.1}} \tag{2.48}$$

For d_b=0, the reduced envelope is assumed to follow monotonic envelope, while for complete damage, d_b=1, it is assumed that there will be only frictional stresses for any slip.

Some experimental investigation reveals that bond strength decrease as the number of load cycles increases. The cycles are assumed to be complete, when the same amplitude of slip is reached in opposite direction. A partial cycle assumes less degradation and hence less reduction in envelope curves. If the cycle is not completed corresponding to previously reached maximum slip then a linear interpolation is assumed, between the values valid for last slip reversal and for the complete cycle.

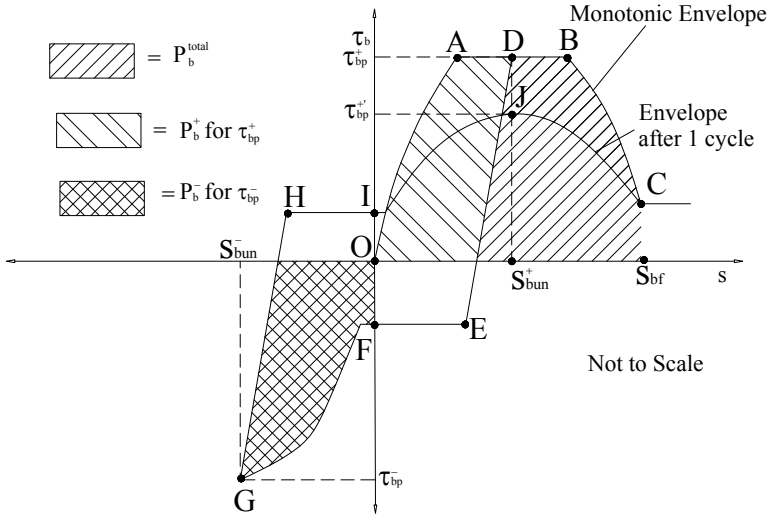

Figure 2.25: Energy dissipation of bond-slip law.

The analytical model proposed by Ciampi *et* al. (1983) is based on their extensive experimental investigation and, is represented in Figure 2.26. A slip reversal from an arbitrary point (point A $(s_{bun}^+, \tau_{bun}^+)$) on envelope will follow stiff unloading (path AB) until

frictional bond resistance (τ_{bf}^{-}) is reached. The stiff unloading is described by rule 3 (or rule 4, path DE) from positive envelope (from negative envelope) and illustrated as follows:

For $\tau_{bun}^{+} \le \tau \le \tau_{bf}^{-}$; Rule 3

$$\tau_b = \tau_{bun}^{+} + (s - s_{bun}^{+})E_b \tag{2.49}$$

For $\tau_{bun}^{-} \le \tau \le \tau_{bf}^{+}$; Rule 4

$$\tau_b = \tau_{bun}^{-} + (s - s_{bun}^{-})E_b \tag{2.50}$$

where $\tau_{bun}^{+(-)}$ is the unloading stress corresponding to unloading slip ($s_{bun}^{+(-)}$), E_b is the initial bond stiffness. Further continuation of slip in reversed direction maintains the same frictional stress, until it reaches zero slip (point C). This curve (path BC or EF) is represented by constant stress, namely the frictional stress ($\tau_{bf}^{+(-)}$), illustrated by rule 5 and 6. The rule 7 (path FG) and 8 (path CH) are similar to the connecting curve (Appendix A), where the initial point (F or C) and target point (G or H) are described in Table 2.12.

Table 2.12: Parameters used in Rule 7 and Rule 8.

Variables	Rule 7	Rule 8
s_{ba}	0	0
τ_{ba}	τ_{bf}^{-}	τ_{bf}^{+}
E_{ba}	0	0
s_{bb}	s_{bun}^{-}	s_{bun}^{+}
τ_{bb}	$\tau_b(s_{bun}^{-})^{\dagger}$	$\tau_b(s_{bun}^{+})^{\dagger}$
E_{bb}	E_b	E_b

† the parameters are calculated on reduced envelope curve.

In Table 2.12 (s_{ba},τ_{ba}), E_{ba}, (s_{bb},τ_{bb}) and E_{bb} corresponds to (x_o,y_o), E_o, (x_f,y_f) and E_f of Appendix A, respectively. In Table 2.12, $\tau_b(s_{bun}^{+(-)})$ is bond stress calculated on envelope (reduced).

A reversal from any point on rule 3 (path AB and BA, see Figure 2.27) and rule 4 (path DF and FD) will retrace the path they followed by same rule 3 (path BA) and rule 4 (path FD), respectively; however a reversal from rule 5 (path BE) and 6 (path FH) follows a path parallel to rule 3 and rule 4 respectively, represented by 3' (path CD) and 4' (path GI,). It should be noted that the rule 3' and 4' joins corresponding reduced envelope. Imposing a slip reversal from this newly reached reduced envelope will follow a similar unloading branch and then the frictional branch, assuming this reduced envelop as new virgin envelope.

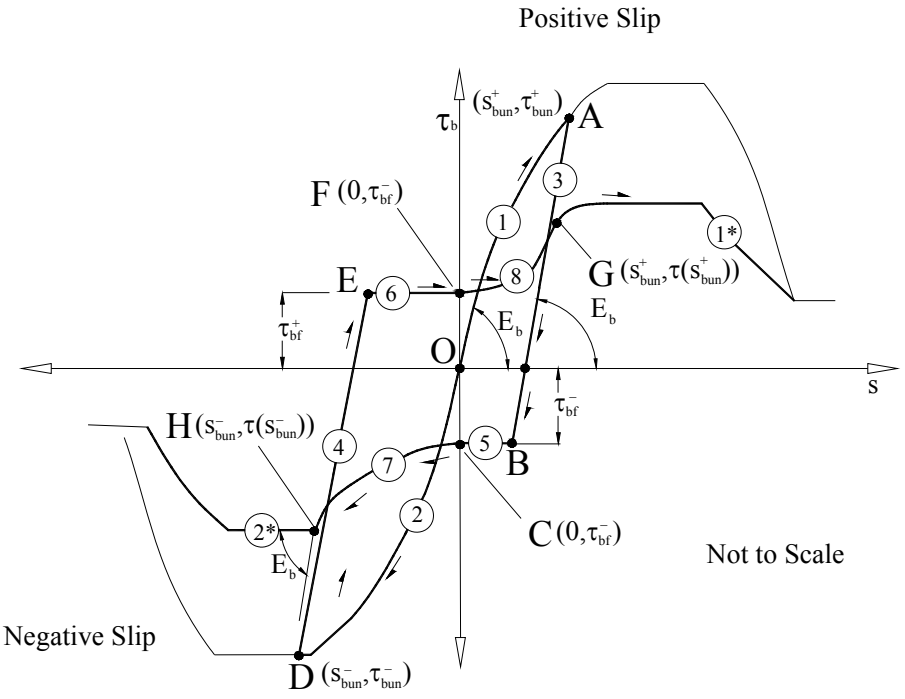

Figure 2.26: Schematic representation of bond-slip law

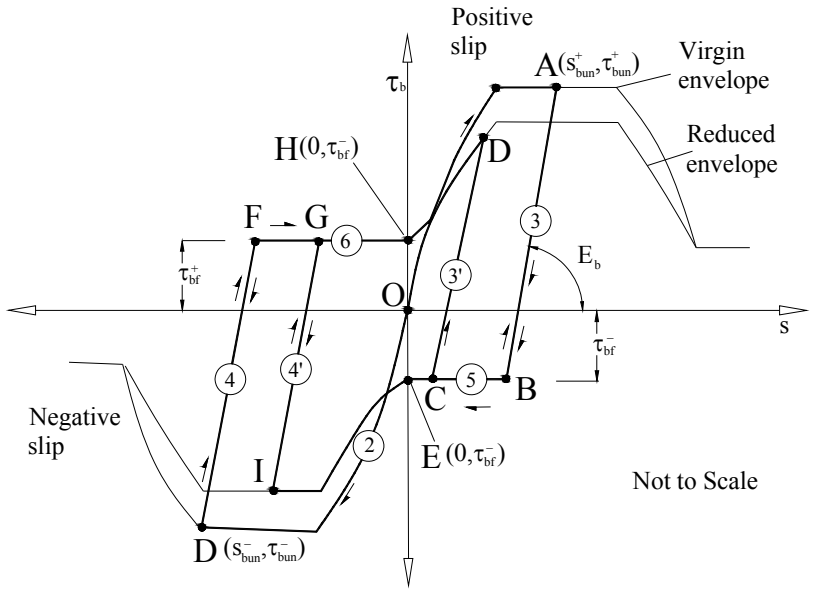

Figure 2.27: Schematic representation of partial bond –slip reversal laws

2.3 SUMMARY

The constitutive laws described in the chapter are implemented in FEMIX. The laws will be used in other chapters by referring them directly and the hysteretic scheme of concrete will be considered benchmark for proposal of laws based on CFRP-confined concrete and FRC. The proposed constitutive laws of concrete and steel are based on degradation of stiffness and corresponding strength, under cyclic loading. The constitutive laws of concrete and steel assumed the empirical equations for the estimation of degradation in strength and stiffness, however, the proposed bond laws assumed similar phenomenon based on release of energy during the cycles. The parameters of the constitutive laws that are deemed necessary to reproduce the actual experimental conditions can be adjusted suitably in the chapters dedicated to this type of analysis.

CHAPTER 3

Fibre reinforced concrete: design and application

3.1 INTRODUCTION

Romualdi and Mandel (1964) proposed for the first time the use of dispersed steel fibres for the reinforcement of concrete elements. Later various researchers (Kelly and Davis 1965, Majumdar and Ryder 1968, Majumdar 1968, Romualdi 1969, Aveston *et. al.* 1971, Kelly 1972) have used different types of fibres as dispersed reinforcement. The aim of using these fibres was to improve the resistance to cracking and crack propagation, as the dispersed fibres bridging the micro-cracks offer resistance to the degeneration into macro-cracks, contributing to enhance the behaviour of concrete structures for service and ultimate limit states. The fibre reinforcement mechanisms increase the post cracking energy absorption capacity of cement based materials. Most of the studies (Shah and Ranjan 1971, Kelly 1972, Swamy 1978, Neville 1975) conducted during the 70's highlight the increase in terms of energy absorption capacity that strain softening of Fibre Reinforced Concrete (FRC) can provide. The strain hardening behaviour of FRC in tension was reported, for the first time, by Kasperkiewickz (1978). Naaman and Shah (1973) reported inelastic response with multiple cracking and ductile failure during their experiments, which was later, correlated to strain hardening behaviour of this concrete composite. In 2006, Naaman and Reinhardt proposed the classification of FRC (see Figure 3.1) based on its tensile behaviour assessed from un-notched tensile specimens: it is classified as strain softening FRC (SSFRC) if after crack initiation the stress decreases with the increase of the strain; strain hardening FRC (SHFRC) presents a continuous increase of tensile stress after crack initiation up to its tensile failure that occurs for a strain level that in general exceeds 1%, with the formation of a diffuse crack pattern.

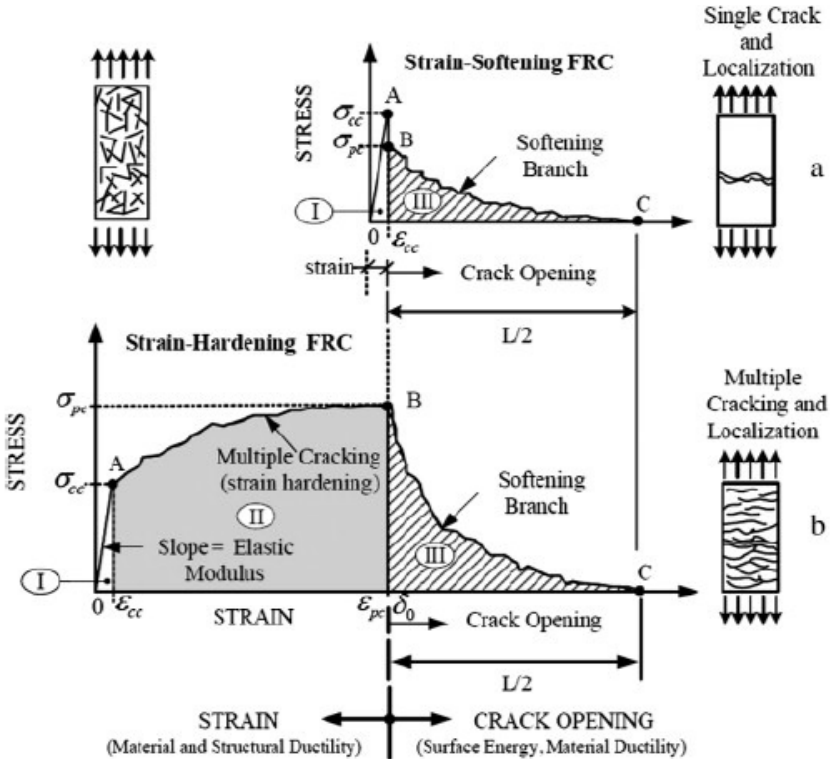

Figure 3.1: Typical stress–strain behavior of FRC: (a) Conventional strain-softening FRC composites; (b) strain-hardening FRC composites. (adapted from Naaman and Reinhardt 2006)

In last decades, several researchers have determined the mechanical tensile properties of FRC. By using these mechanical properties, innovative design formulations are being proposed for sustainable infrastructures (Mobasher, 2012). To exploit the FRC capabilities, in the present work a parametric study is presented on use of FRC as partial replacement of reinforcing steel in design of elements submitted to axial force and bending moment, based on the existing software called DOCROS, where the constitutive laws for concrete, steel and FRP, described in the previous chapter, were implemented. To better simulate the post-cracking behaviour of FRC, more suitable constitutive models were also implemented in DOCROS. These models are described in this chapter.

This chapter briefly describes the philosophy of DOCROS, its potential use in determining the moment-curvature (M-χ) relationship of a section composed by distinct materials. It also describes the algorithm implemented for the calculation of M-χ diagrams for axially loaded section and pre-stressed sections. The DefDocros program, which uses

the M-χ relationship data derived from DOCROS, predicts the force *versus* deflection (F-u) response of simply supported beams. The concrete tensile constitutive law adopted in the numerical model is presented. The residual strength ratio (α) and residual tensile strain ratio (β) of FRC (detailed in next section) are the most prominent features of the post-cracking tensile behaviour that affect the moment carrying capacity of section. For distinct mechanical steel reinforcement ratios (ω), starting from 0 up to 1 with increments of 0.2, a set of design curves are determined, taking in account the combinations of possible ductile behaviour and residual tensile strength of FRC. Finally, the performance of FRC is appraised by a set of design examples where FRC is used to replace conventional longitudinal reinforcement.

3.2 DOCROS

3.2.1 Decomposition of section in 2D

Moment-curvature diagrams of cross sections can be generated by using DOCROS, which is a software developed at the University of Minho for **D**esign **O**f **CRO**ss-**S**ections. It assumes that a plane section remains plane after deformation and perfect bond exists between distinct materials. The section is divided in horizontal layers, and the thickness and width of each one is user-defined and depend on the cross-section geometry (see Figure 3.2). DOCROS can analyze sections of irregular shape and size, composed of different types of materials subjected to an axial force (N) and variable curvature. Composite layers are used when more than one material exists at same depth of the cross section. To simulate a pre-stress effect, some of the layers can have an initial non-null stress and strain. The software can also analyze sections that have layers with distinct construction phases, such as in the case of retrofitting, where strengthening materials are activated in later phases. As the practical situation demands, the strengthening intervention is executed when the concrete elements to be rehabilitated have certain damage and internal stress and strain fields. Hence DOCROS has the capability to simulate the retrofitting in phases. Mostly, the available commercial computer programs dedicated to the structural analysis may not simulate accurately these important aspects. In DOCROS, the section is loaded and the corresponding historical data of the installed stress and strain

is stored. When new materials are added in next phases, the newly installed material contribute to the strength of structure, once the structure is further loaded.

DOCROS has a wide database of constitutive laws for the simulation of monotonic and cyclic behaviour of cement based materials, polymer based materials and steel. Any layer can be selected to control the loading process by imposing a certain incremental strain up to a defined limit. Assuming the predefined strain of control layer, curvature (χ) of the cross-section is estimated iteratively, assuming the linear strain profile along *z*-axis. The new constitutive model for the tensile behaviour of strain softening fibre reinforced concrete (SSFRC) and strain hardening FRC (SHFRC) was implemented in DOCROS, which will be described in a later section.

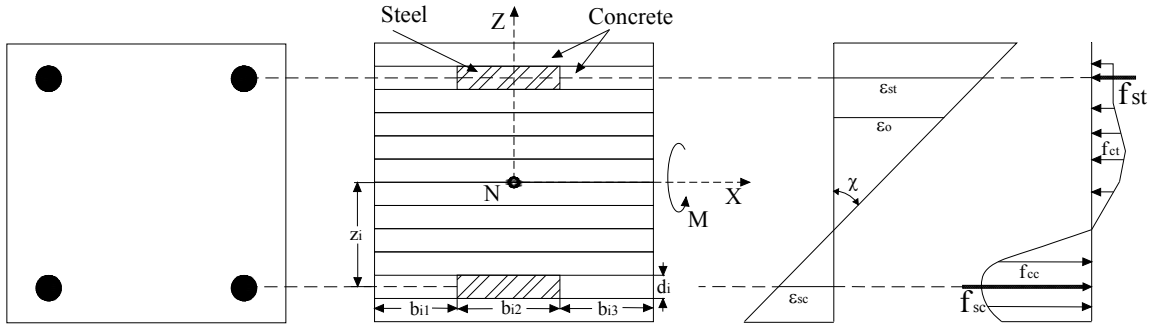

Figure 3.2: Discretization of a typical section in DOCROS.

The constitutive laws are used to calculate the stresses corresponding to the strains in the layers.The depth of neutral axis is determined itratively chnaged until the force equlibrium is reached, using Eq. (3.1). Once the equlibrium is guaranteed, the bending moment is deteremined by Eq. (3.2).

$$N = \sum_{i=1}^{n}\left(\sum_{j=1}^{m}\sigma_{ij}d_i b_{ij}\right) \tag{3.1}$$

$$M = \sum_{i=1}^{n}\left(\sum_{j=1}^{m}\sigma_{ij}d_i b_{ij} z_i d_i\right) \tag{3.2}$$

where N and M are the axial load and the bending moment, respectively, n is the number of layers along z-axis, d_i and z_i is the thickness and the position of i^{th} layer, and m is the

number of materials compositing a certain layer that can be active in the same or in distinct loading phases, which is designated as composite layer. Therefore, if a composite layer exists at z_i position (see Figure 3.2), σ_{ij} and b_{ij} represent the stress and the width of layer situated at i^{th} position along z-axis, and j^{th} is the number of segment of the set of materials along x-axis. . The stress and strain are considered positive for tension and negative for compression. The algorithm to obtain the $M-\chi$ relationship is described in detail in next section.

3.2.2 Analysis of section

The section is decomposed in layers and among one of these layers predefined strain is assigned; this strain is considered as the externally applied load condition. For this configuration of the section, internal strain should arise in diverse layers, consequently giving rise to internal forces that should balance the external loading conditions. In the following section, calculation of moment-curvature relationship is described when the section is either pre-stressed or axially loaded, in combination with preinstalled strain in layer to produce curvature.

3.2.2.1 Pre-stressing or axial load application

To take into account the effect of pre-stressing, the strain (*pre-stressing strain*) is applied to the corresponding layers. However, in case of application of axial load, the load is assumed to be applied at the geometric centre of section. In case of the section being reinforced un-symmetrically, or due to un-symmetricity about the bending axis (X) due to material type or shape, the stiffness centre may not coincide with the geometric centre of section, and an initial curvature may generate due to external axial load. The case of pre-stressing is equivalent to the application of an axial load with a certain eccentricity, except a strain (pre-stressing strain) is applied compared to relevant force (axial load). The algorithm for calculating the strain profile of a section is described in Figure 3.4, for prestressing strain application and can be changed for axial load application. The following steps describe the algorithm for calculation of the strain profile, when pre-stressing is applied:

(1) An uniform and constant strain field (ε_{int}) is applied to all the layers, until the internal axial load (N) generated is within an acceptable tolerance limit ($e_{tol} = 10^{-6}$) to external applied load (P_{ext}).

(2) The centre of application of pre-stressing force (CG_{Fe}) is calculated (when more than one layer is prestressed) and compared to the centre of internal force (CG_i) generated by equation (3.3).

$$CG_i = \sum_{i=1}^{n}\left(\sum_{j=1}^{m}\sigma_{ij}d_i b_{ij}h_i\right) \Big/ \sum_{i=1}^{n}\left(\sum_{j=1}^{m}\sigma_{ij}d_i b_{ij}\right) \tag{3.3}$$

(3) If the eccentricity (see Figure 3.4) is in tolerance limit ($=10^{-6}$), then the strain profile of the section is reached.

(4) If the eccentricity is not in tolerance limit, then the incremental strain is applied to each layer. The incremental strain for any i^{th} layer is defined by $\Delta\varepsilon_i^k$, where k is the iteration number, and is calculated from equation (3.4), where ε_1 is the strain in first layer (assumed a pivot for iteration, local ***xz*** coordinate located at layer 1), and H is the height of the section. The strain profile applied to the section is described by **A** (see Figure 3.3).

$$\Delta\varepsilon_i^k = \{(CG_{Fe} - h_i)/H\} \times \varepsilon_1 \times CG_{Fe}/H \tag{3.4}$$

(5) The total strain of each layer (ε_i^k) for the current iteration, k, is calculated by adding the incremental strain to the previous iteration strain (ε_i^{k-1}). It is to be noted that the strain profile after 1st iteration is shown by profile **B** in Figure 3.3, but during subsequent iteartion the same profile will be replaced by profile **C**.

$$\varepsilon_i^k = \varepsilon_i^{k-1} + \Delta\varepsilon_i^k \tag{3.5}$$

(6) The internal force due to this newly formed strain profile is calculated and compared to external force.

(7) If the internal force is not equal to external one, the uniform and equal strain (profile **B**, see Figure 3.3) is applied to all the layers of the section, until the equilibrium is satisfied.

(8) Now follow step (2) to achieve the strain profile of section.

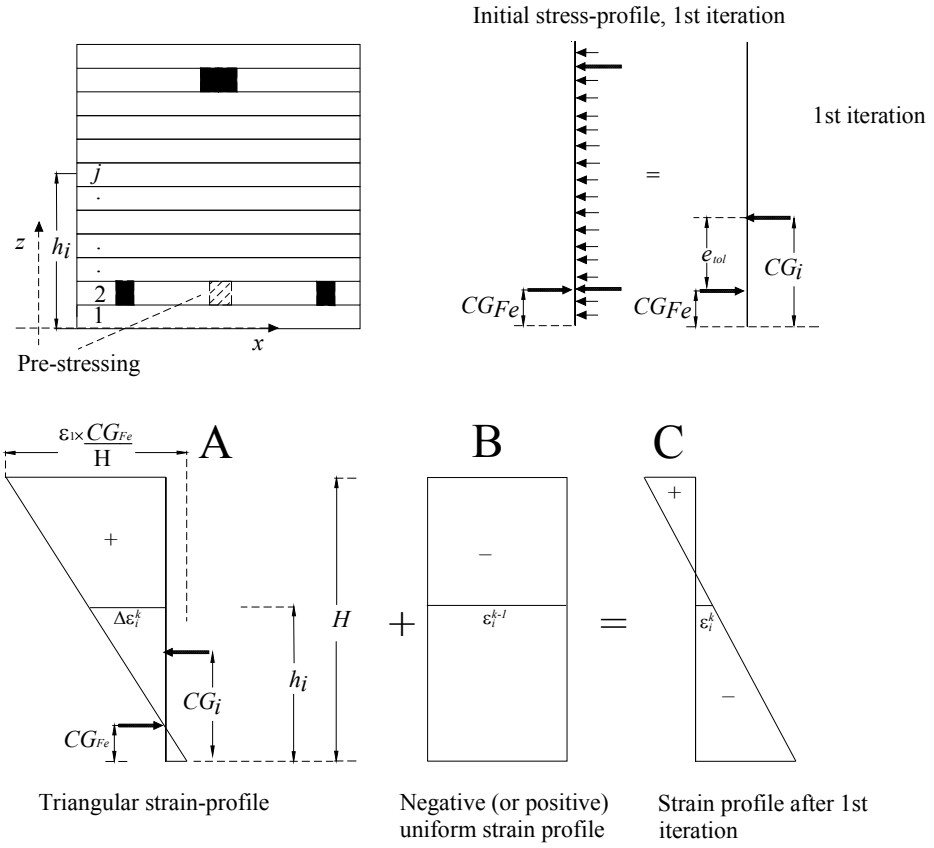

Figure 3.3: Sectional stress and strain profile corresponding to algorithm.

Once the strain profile of section is reached, the calculation of moment curvature relationship assumes an increment of strain in the predefined control layer for next combination of load case. The curvature of the section is calculated iteratively by satisfying the axial load condition using Eq. (3.1), for this newly acquired configuration. The bending moment is calculated from Eq. (3.2) using stresses of the layers reached in previous step for the calculation of axial load/pre-stress. Same steps are repeated with increasing curvature to generate the $M-\chi$ graphs for a section.

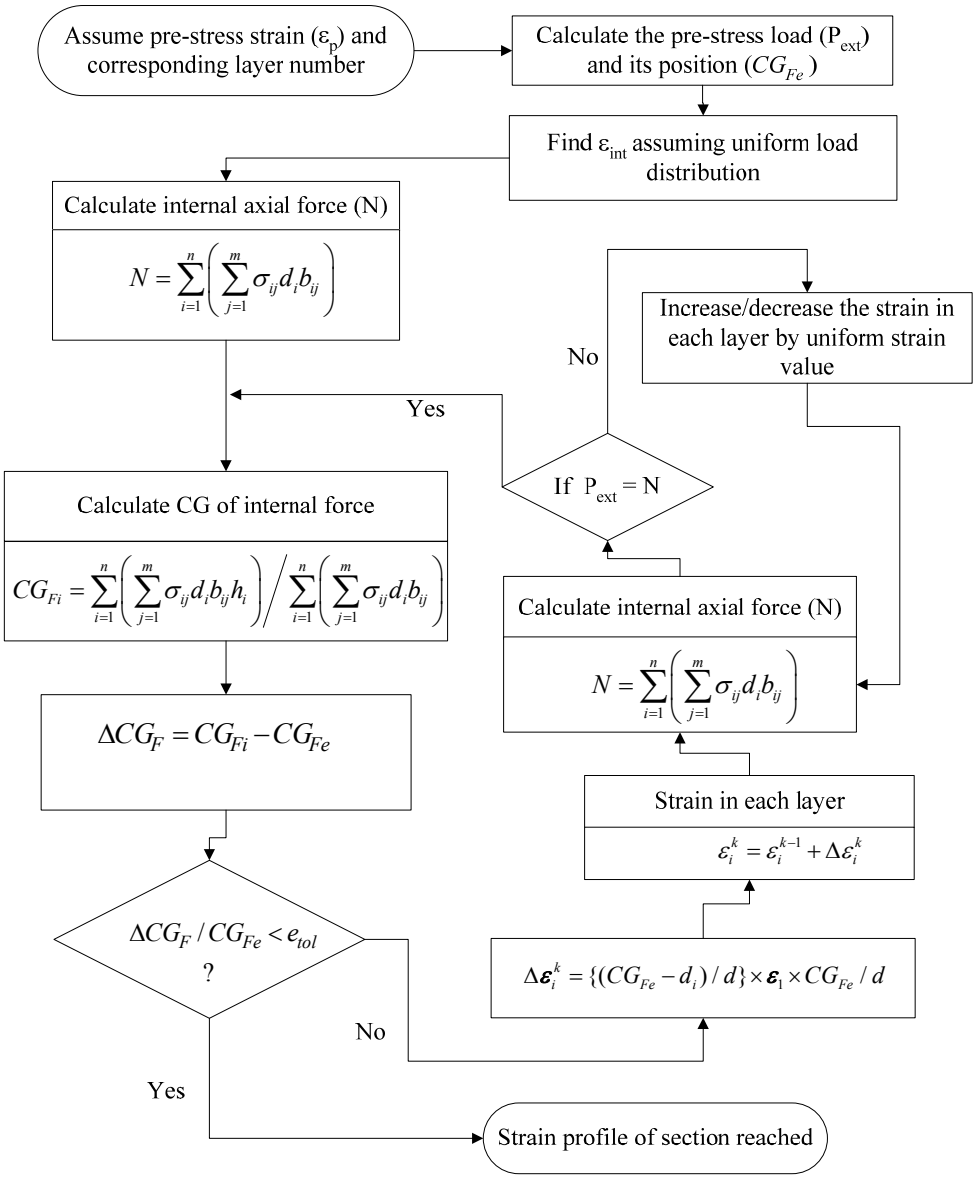

Figure 3.4: Algorithm for calculation of prestress or axial load.

3.2.3 Constitutive Laws

The envelope curves used to simulate the tensile and compressive behaviour of steel, and the compressive behaviour of concrete are described in Chapter 2. The tension envelope of FRC is simulated by the stress-strain diagram composed by multi-linear branches represented in Figure 3.5, as proposed by Soranakom and Mobasher (2007). The first branch (OA, designated Zone I) simulates the linear-elastic behaviour of FRC up to crack initiation $(\varepsilon_{ctc}, f_{ctc})$. After crack initiation, a SSFRC presents a softening phase

characterized by the branch AB′, while a SHFRC shows a hardening phase modelled by the branch AB. This phase (named Zone II) ends at a point characterized by $(\varepsilon_{ctr}, f_{ctr})$. The last phase (BC in case of SHFRC, and B′C′ for SSFRC, designated Zone III) is defined by a constant tensile stress up to the ultimate strain (ε_{ctu}). Zone I is characterized by the initial FRC Young's modulus and ends at the strain ε_{ctc} corresponding to the stress at crack initiation (f_{ctc}). In zone II the SHFRC exhibits an increase of the tensile stress with the tensile strain due to the formation of multiple cracks, while SSFRC presents a decrease of the tensile stress with the increase of tensile strain due to the formation of one macro-crack. By setting post cracking modulus (E_{cr}) to either a negative or a positive value, strain softening and strain hardening response can be simulated, respectively. Zone III is characterized by a constant stress up to a strain limit above which it is assumed that fibres cannot transfer the residual tensile stresses anymore, so the tensile capacity becomes null. The ratio between this residual stress (f_{ctr}) and (f_{ctc}) is represented by the α parameter, and the ratio between the strain at the initiation of Zone III, (ε_{ctr}) and (ε_{ctc}) is designated by β.

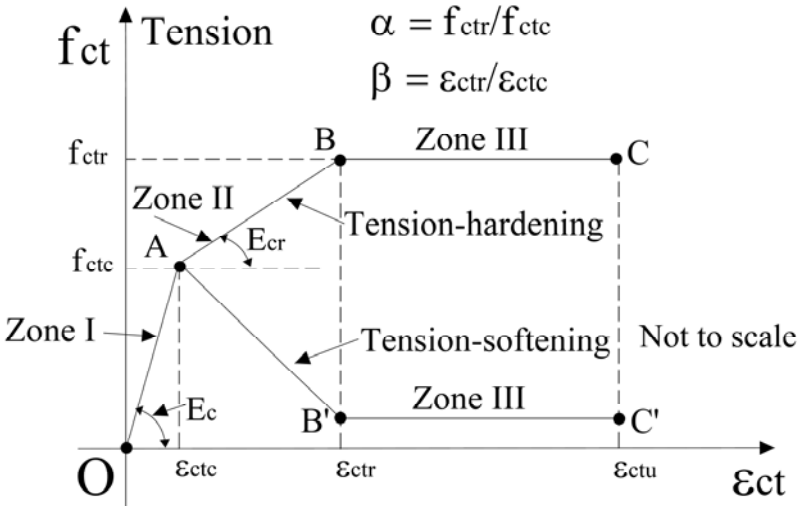

Figure 3.5: Schematic diagram of the concrete tensile envelope.

The stress-strain relationships for tension envelope are illustrated as:

$$f_c = E_c\ \varepsilon_{ct} \text{ for } 0 \le \varepsilon_{ct} \le \varepsilon_{ctc} \tag{3.6}$$

$$f_{ct} = E_c \varepsilon_{ctc} + E_{cr} \left(\varepsilon_{ct} - \varepsilon_{ctc} \right) \text{ for } \varepsilon_{ctc} \leq \varepsilon_{ct} < \varepsilon_{ctr} \quad (3.7)$$

$$f_{ct} = \alpha f_{ctc} \text{ for } \varepsilon_{ctr} \leq \varepsilon_{ct} < \varepsilon_{ctu} \quad (3.8)$$

$$f_{ct} = 0 \text{ for } \varepsilon_{ctu} \leq \varepsilon_{ct} \quad (3.9)$$

3.3 DEFDOCROS

3.3.1 Model to estimate the Force-Deflection relationship

Using the moment-curvature ($M - \chi$) relationship, the force-deflection response of a statically determinate element failing in flexure can be determined using the algorithm described in Figure 3.6. According to this model, a statically determinate beam or slab is discretized in Euler-Bernoulli beam elements of 2 nodes. The tangential or the secant flexural stiffness (the developed model has both approaches implemented) of each element, $(EI)_{Te}$ is determined from the $M - \chi$ relationship corresponding to its cross section that is stored in a data file (each element has its own $M - \chi$ file). Therefore, the present approach can simulate the deformability of a beam/slab composed of various types of cross section along the axis that can have distinct moment-curvature, enabling the model to predict with enough accuracy the force-deflection response of heterogeneous structures in terms of material constitutive laws, arrangements of the materials and geometry of cross section (Barros et *al.* 2012).

In Figure 3.6, $\underline{F}^q$ and $\underline{u}^q$ represent the total applied load vector and total displacement vector at q^{th} iteration, and the increment in these vectors are represented by $\Delta\underline{F}^q$ and $\Delta\underline{u}^q$, respectively. M_e^q represent the total moment at mid section for any element (e) and x_e represent the distance of it from left support. $\overline{\underline{K}}_{Te}^q$ and $\overline{\underline{K}}_{TE}^q$ represent the stiffness matrix at element level and assembled global stiffness matrix of beam, respectively.

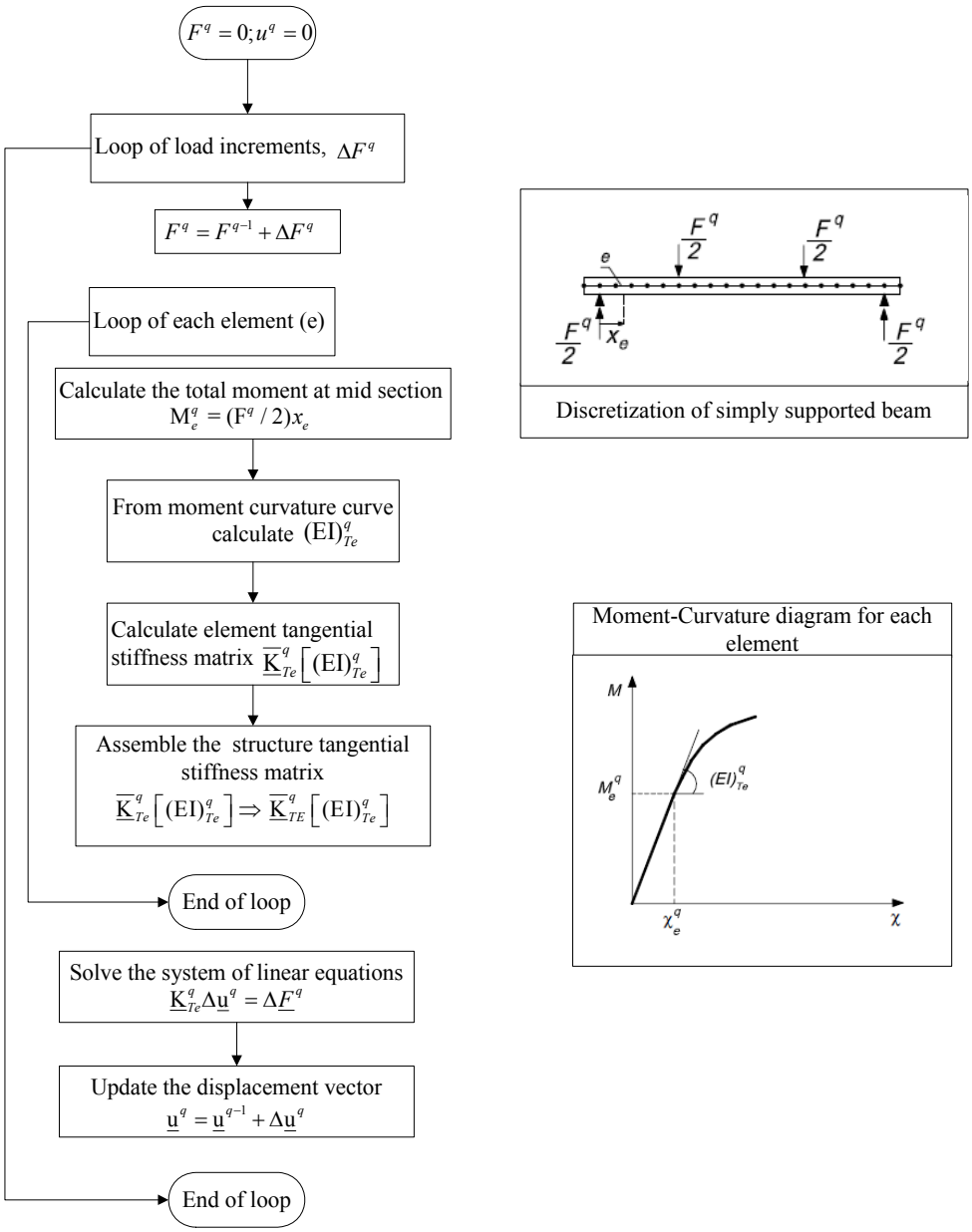

Figure 3.6: Numerical approach to simulate the deformational behavior of structural elements failing in bending (adapted from Barros and Fortes, 2005).

3.3.2 Assessment of the predictive performance of DOCROS and DefDocros

To appraise the predictive performance of DOCROS and DefDocros an independent experimental study by Badawi and Soudki (2009) on RC beams strengthened (see Figure 3.7) with pre-stressed (40% and 60%) near-surface mounted CFRP rods is considered, and the numerical results are compared with the experimental ones.

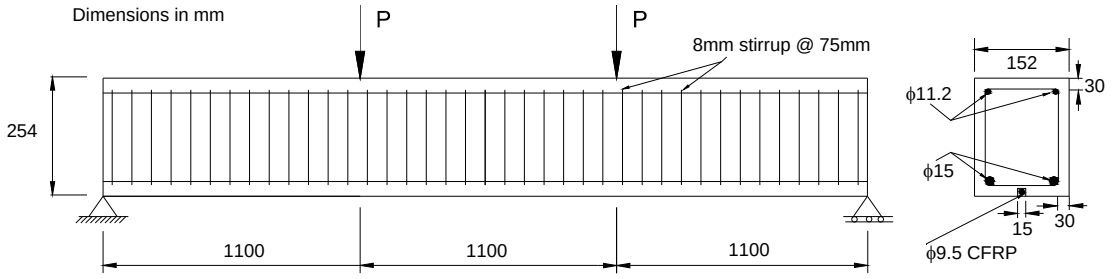

Figure 3.7: Loading and support conditions, geometry, and reinforcement details of a pre-stressed beam (Badawi and Soudki, 2009).

The loading and the support conditions are also shown in Figure 3.7. It also illustrates the specimen geometry and reinforcement details and arrangement, number and position of the CFRP rods. According to the researchers the beams were designed to fail in flexure. The beam cross-section was 152 mm × 254 mm, with distance between supports of 3300 mm, and was reinforced with 2Φ15 mm and 2Φ11.2 mm steel bars in tension and compression, respectively (see Figure 3.7). Smooth surface shear stirrups of 8 mm diameter spaced at 75 mm were provided for the shear reinforcement. The steel reinforcement had a concrete cover thickness of 30 mm. The CFRP rod of 9.5 mm diameter had an ultimate tensile strength of 1970 MPa, with an ultimate strain of 1.45%, and a modulus of elasticity of 136 GPa. The stress in the CFRP rod of 788 MPa and 1182 MPa represent 40% and 60% pre-stress level, respectively. The data corresponding to the constitutive model for concrete and reinforcing steel is included in Table 3.1 and Table 3.2, respectively. The tensile behaviour of concrete is assumed bilinear and the tensile strength was calculated according to CEB-FIB (1993). The simply supposrted beam acquires initial curvature about bending axis after the application of pre-stressing, and before application of any load.

The section of beam was divided in 27 layers along the height of 254 mm with constant width of 152 mm. The tangential flexural stiffness of the element is calculated from moment-curvature data generated from DOCROS for both the prestress situations. The beams were divided in 66 elements of 50 mm length along the longitudinal direction to take correctly into account the variation of the flexural stiffness during the loading process. Figure 3.8 compares the experimental and the numerical responses in terms of

load *versus* deflection at the mid-span. The numerical simulation predicts ultimate capacity and linear elastic branch of the experimental response satisfactorily, while it predicts higher stiffness after first cracking for 60% pre-stress.

Table 3.1: Mechanical properties of the concrete used in the simulations of the pre-stressed beams tested by Badawi and Soudki (2009).

Initial Young Modulus, E_c (GPa)	30.0
Concrete strain at peak compressive stress, ε_{ccp} (mm/mm)	2.8×10^{-3}
Concrete compressive strength, f_{ccp} (MPa)	45.0
Critical strain in compression, ε_{ccr}^{-} (mm/mm)	5.0×10^{-3}
Tensile strain at crack initiation, ε_{ctc} (mm/mm)	1.5×10^{-4}
Tensile strength at crack initiation, f_{ctc} (MPa)	4.0
Residual tensile strength, f_{ctr} (MPa)	2.0
Tensile strain corresponding to start of residual tensile strength zone, ε_{ctr} (mm/mm)	2.5×10^{-4}
Ultimate tensile strain, ε_{ctu} (mm/mm)	3.0×10^{-3}

As perfect bond condition was assumed between layers in calculation of moment curvature relationship, it predicted higher stiffness and consequently the use of it in DefDocros resulted in higher force for the displacement, once cracking initiated. In fact, it was verified from Badawi and Soudki (2009) that the slip between concrete and CFRP laminates was observed during experimental test after application of approxiamtely 50 kN until failure.

Table 3.2: Mechanical properties of the steel used in the simulations of the pre-stressed beams tested by Badawi and Soudki (2009).

Initial Young Modulus, E_s (GPa)	190
Tangent modulus at strain hardening, E_{sh} (GPa)	6.4
Yielding strain, ε_{sy} (mm/mm)	2.32×10^{-3}
Yielding stress, f_{sy} (MPa)	440.0
Hardening strain, ε_{sh} (mm/mm)	1.0×10^{-2}
Hardening stress, f_{sh} (MPa)	445.0
Strain at the ultimate stress, ε_{su} (mm/mm)	1.0×10^{-1}
Ultimate stress, f_{su} (MPa)	450.0

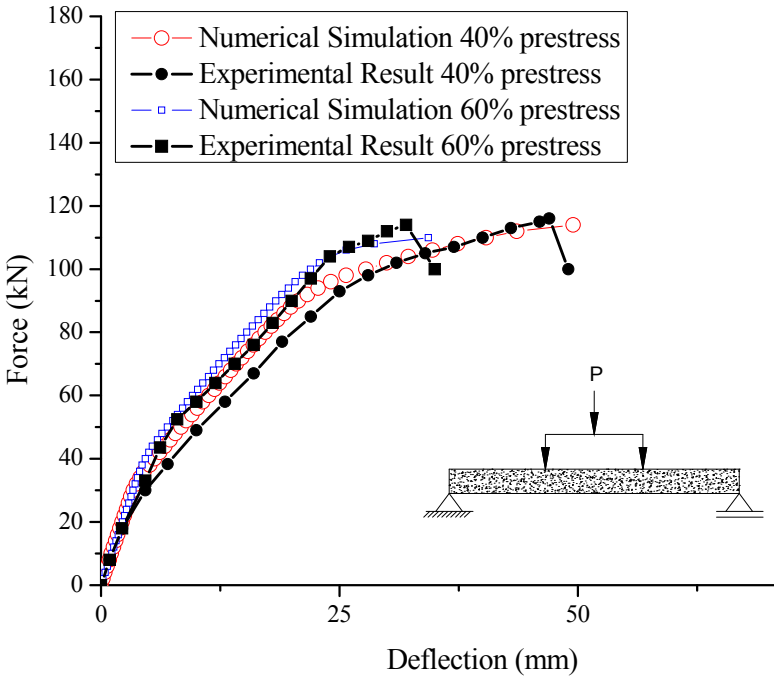

Figure 3.8: Experimental *versus* numerical load-mid span deflection curves

3.4 ANALYTICAL STUDY FOR PROPOSAL OF DESIGN GUIDELINES USING FRC CHARACTERISTIC GRAPHS

Symmetrically reinforced cross-section of 200 mm wide (b) by 400 mm height (h) with a concrete cover (c) of 20 mm (the bending moment mobilizes the larger moment of inertia of the cross section) was used to develop design curves by varying ω, α and β sequentially. Each design curve is designated by $\omega i \alpha j \beta k$, where i, j and k represent values of ω, α and β, respectively. The mechanical steel reinforcement ratio is varied from 0 to 1 with an increment of 0.2 and is calculated as:

$$\omega = A_s f_{sy} / \ bdf_{ccp} \tag{3.10}$$

where A_s is the total area (compression and tension sides) of steel reinforcement in the section, f_{sy} and f_{ccp} are yielding stress of steel and the compressive strength of the concrete, respectively, and b and d represent the width and effective depth of the section (d=h-c), respectively. As it is assumed that the residual strength can vary from negligible value to a maximum of twice the first cracking strength, hence j can vary from 0 to 2 with a step of 0.5. For the value of β, represented by k, was assigned 1, 5, 10 and 30, illustrating negligible to significant ductility.

A generic design curve $\omega i \alpha j \beta k$ is a dimensionless N-M envelope curve, built from a set of analysis with DOCROS from N_{min} (maximum compressive force) and its corresponding moment, up to N_{max} (maximum tensile force) and its corresponding moment. In this process an increment of 100 kN for N was adopted. The generated data is plotted on dimensionless force (ν) and dimensionless moment (μ), being calculated as

$$\nu \ = \ N / bdf_{ccp} \tag{3.11}$$

$$\mu \ = \ M / bd^2 f_{ccp} \tag{3.12}$$

In the generated $\nu - \mu$ curves ν is assumed positive for compressive loads. The design values included in Table 3.3 and Table 3.4 were used in the constitutive model of concrete and steel, respectively. The meaning of the parameters presented in Table 3.4 is described in detail in Chapter 2.

Table 3.3: Values of the parameters of the concrete constitutive model.

Initial Young Modulus, E_c (GPa)	29
Concrete strain at peak compressive stress, ε_{ccp} (mm/mm)	2.0×10^{-3}
Concrete compressive strength f_{ccp} (MPa)	20
Critical strain in compression, ε_{ccr}^{-} (mm/mm)	5.0×10^{-3}
Tensile strength at crack initiation, f_{ctc} (MPa)	1.33
Residual tensile strength, f_{ctr} (MPa)	αf_{ctc}
Tensile strain at crack initiation, ε_{ctc} (mm/mm)	4.59×10^{-5}
Tensile strain corresponding to start of residual tensile strength zone, ε_{ctr} (mm/mm)	$\beta\varepsilon_{ctc}$
Ultimate tensile strain, ε_{ctu} (mm/mm)	2.0×10^{-3}

Figure 3.9 (a) and (b) illustrate a specific set of $\nu-\mu$ curves for varying α and β respectively, for constant ω (equal to 0.4). The sets of Figure 3.9 (a) and (b) can be described by $\omega 0.4\alpha j\beta 30$ and $\omega 0.4\alpha 0.5\beta k$, respectively. Changing the value of β does not alter the curves, while α has a favourable effect on μ when μ ranges between 0 and its maximum value. For the simulations corresponding to this interval of values for μ and υ, some layers of the section were in tension, which justify the contribution of the residual tensile strength of FRC. In fact, since an increase in α represent higher post-cracking tensile strength, it results in higher resisting bending moment for the section section, if the section had certain layers in tension during moment calculation. This effect is more pronounced in case the number of layers in tension increases during moment calculation. As Figure 3.3 evidences, the larger the β parameter the higher the post-cracking residual strength between crack initiation and ε_{ctr}. However, up to β=30 (available experimental research shows that this is a quite high value) this increase has negligible influence of the resisting bending moment of the section.

Table 3.4: Values of the parameters of the steel constitutive model.

Initial Young Modulus, E_s (GPa)	200
Tangent modulus at strain hardening, E_{sh} (GPa)	6.4
Yielding strain, ε_{sy} (mm/mm)	1.74×10^{-3}
Yielding stress, f_{sy} (MPa)	348.0
Hardening strain, ε_{sh} (mm/mm)	5.0×10^{-3}
Hardening stress, f_{sh} (MPa)	348.5
Strain at the ultimate stress, ε_{su} (mm/mm)	1.0×10^{-1}
Ultimate stress, f_{su} (MPa)	349.0

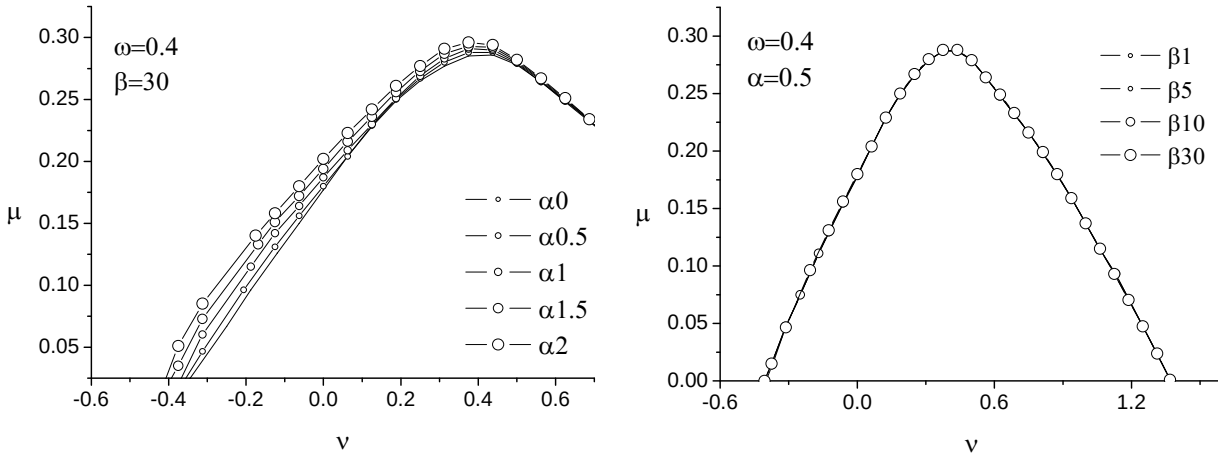

Figure 3.9: The ν-μ diagrams by varying (a) α (b) β.

Figure 3.10 shows the $\nu-\mu$ curves for varying ω (filled symbols) from 0 to 1 with $\alpha=2$ and $\beta=10$ representing strain hardening concrete, and compared to the graphs of equivalent conventional concrete represented by $\alpha=0$ and $\beta=1$ (with empty symbols). With increase of the reinforcement level the bending and load carrying capacity of a section increases, which has been discussed in various design codes. Hence from

design perspective, the favourable variation in diagrams is possible by varying either α or ω.

In order to better observe the favourable effect of concrete tensile parameters, a three dimensional representation of the curves are executed assuming for the axis the parameters ν, μ and β. The $\nu - \mu$ curves generated are illustrated in Figure 3.11 and Figure 3.12. To emphasize the effect of α for certain reinforcement ratios, Figure 3.12 only represents the portion of $\nu - \mu$ for $\nu < 0.7$, since for $\nu > 0.7$ the failure of section is governed by the compressive parameters, hence the effect of α is found to be insignificant.

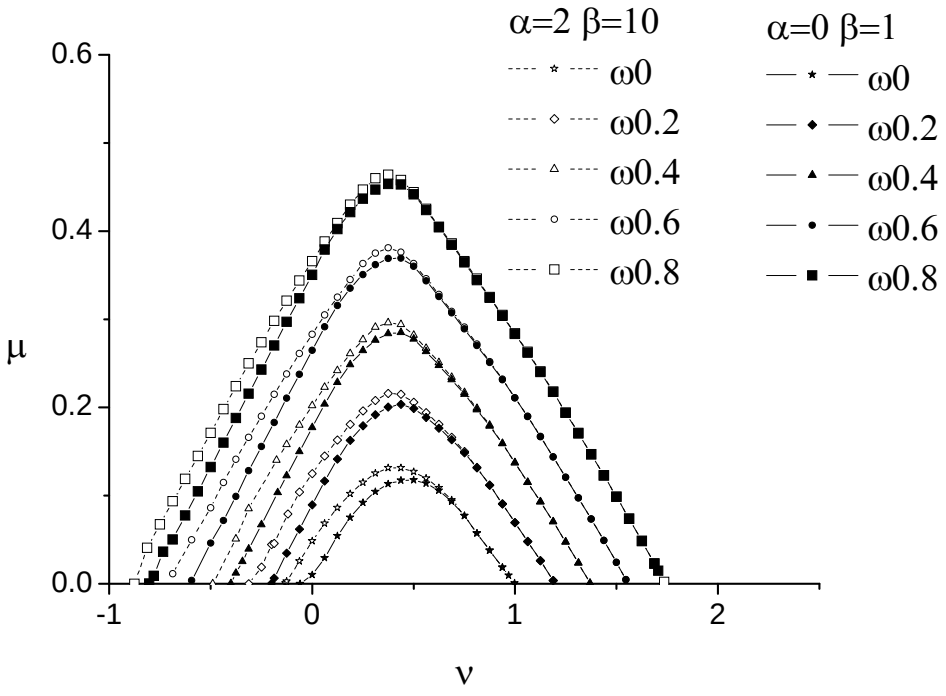

Figure 3.10: The $\nu - \mu$ diagrams by varying ω

In Figure 3.11 and Figure 3.12 the size of the markers in the curves for each β is proportional to the α value. It is observed that for a definite β and ω, the flexural capacity increases with α. The favourable effect of α is more pronounced with the decrease of ν and ω.

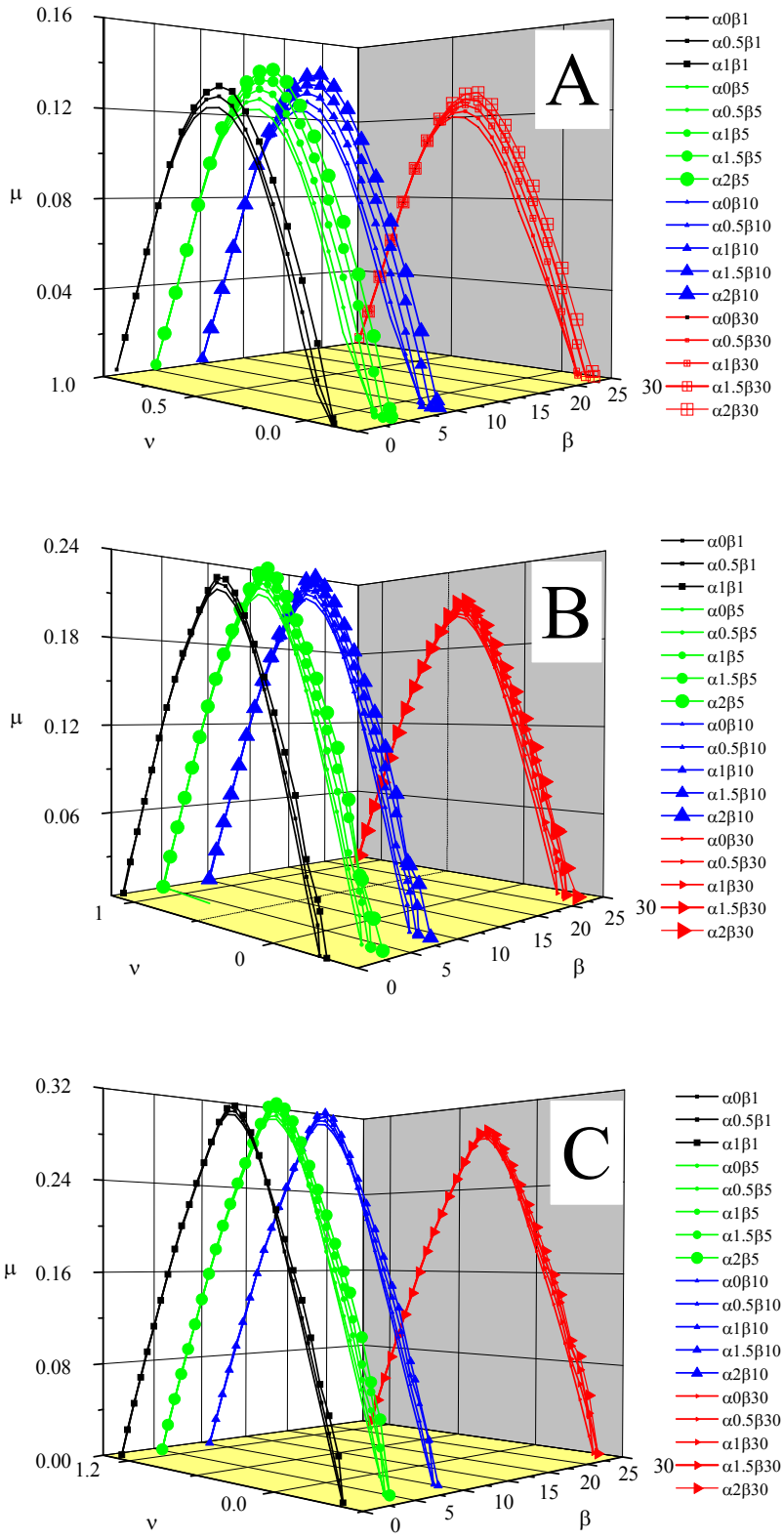

Figure 3.11: Figures showing the characteristic diagrams for (A) ω =0 (B) ω =0.2 (C) ω=0.4

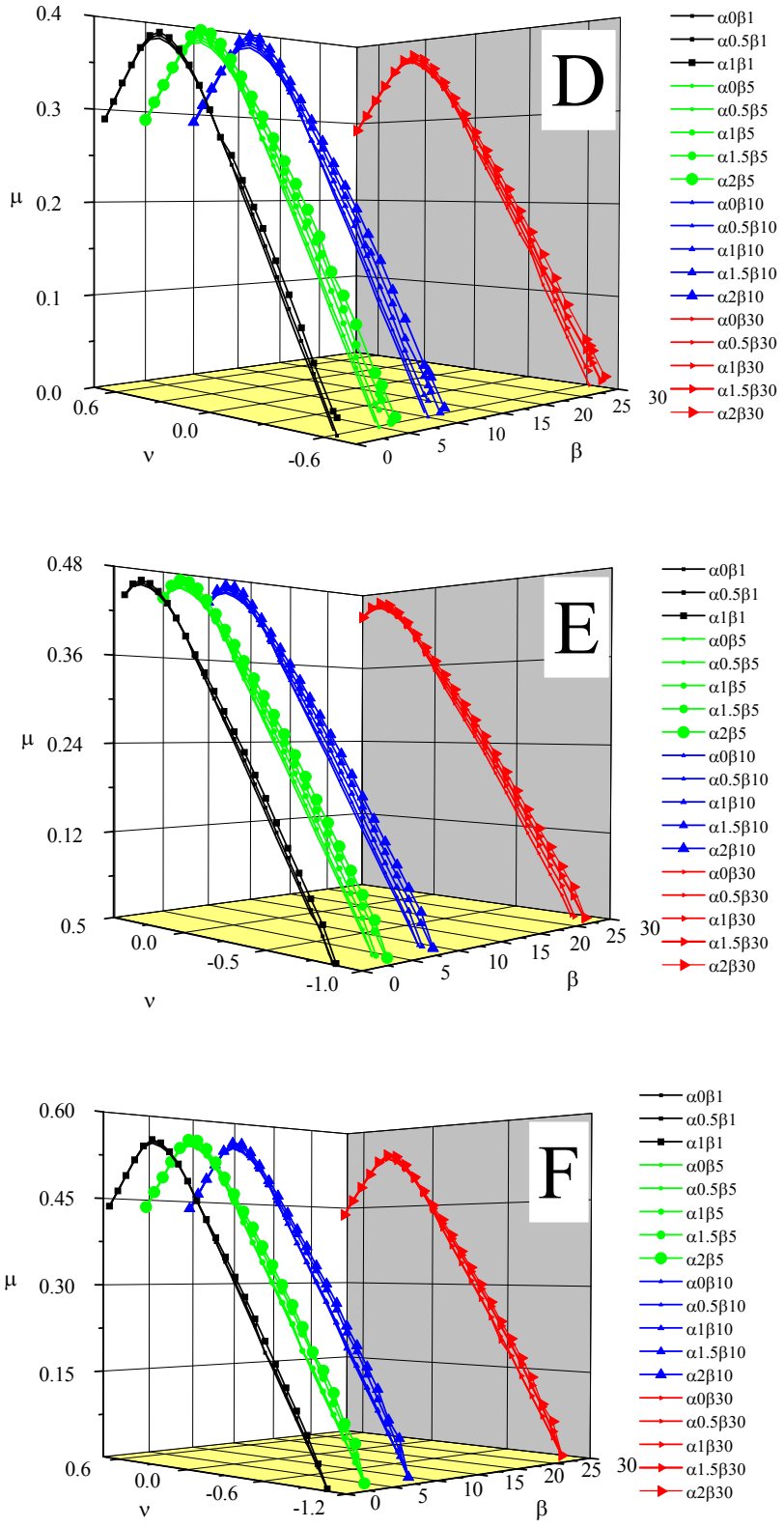

Figure 3.12 Figures showing the characteristic diagrams for (D) ω =0.6 (E) ω =0.8 (F) ω=1.0

As the ω decreases, the moment carrying capacity of section decreases, however the *relative effect* of concrete layers becomes more predominant in calculation of moment curvature relationship. Even a small change in moment in case of small ω, will relatively look significant due to diminishing effect of steel. Hence for lower values of ω the percentage increase in moment will be much higher compared to higher values of ω. The same effect can also be observed from Figure 3.13.

To illustrate the effect of α on the relative flexural resistance of the cross section, the relationship $\Delta\mu \times 100 / \mu_{RC}$ versus ν is plotted in Figure 3.13, where differential dimensionless moment ($\Delta\mu$) is defined as:

$$\Delta\mu = \mu_{FRC} - \mu_{RC} \tag{3.13}$$

being μ_{FRC} and μ_{RC} the dimensionless moment calculated for FRC and the corresponding plain concrete section. To simulate the plain concrete it was assumed $\alpha = 0$ and $\beta = 1$. This situation can be assumed similar to the plain concrete behaviour, for all ω.

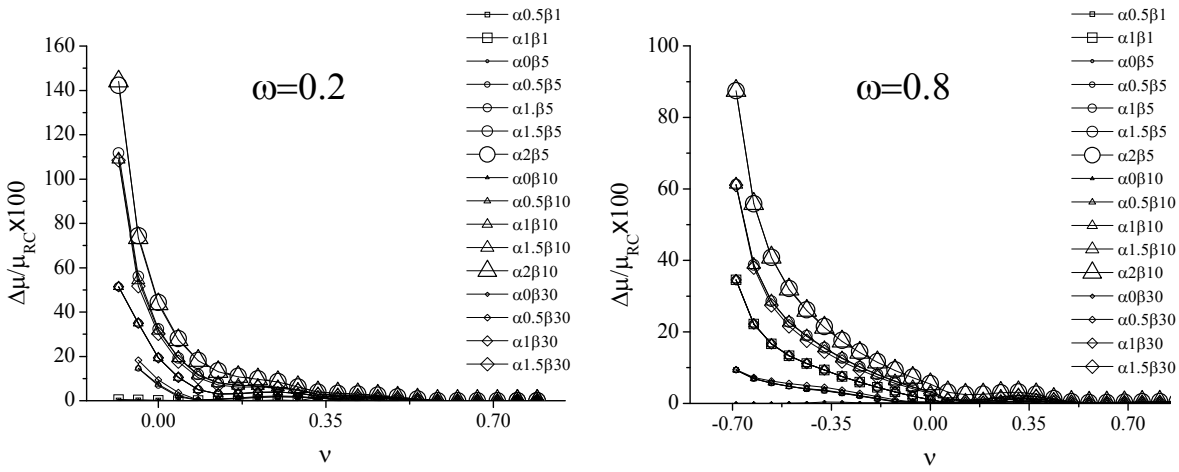

(a) (b)

Figure 3.13: Percentage increase in dimensionless moment for (a) ω=0.2 (b) ω=0.8.

It should be noted that $\Delta\mu \times 100 / \mu_{RC}$ increases with the decrease of ν (from compression to tension), which is attributed to the fact that by decreasing ν, the M is calculated with increasing number of layers in tension, being much more pronounced the favourable effect of the post-cracking tensile strength of FRC. In fact this figure shows the

favourable effect of both α and β parameters on the flexural capacity of a cross section submitted to axial and bending moments. This reinforces that plain concrete when replaced by FRC, can increase the flexural capacity of cross-sections subjected to axial and bending moments, mainly when axial compression force is small, and specially when in tension. This figure also shows that for the same ν, $\Delta\mu \times 100 / \mu_{RC}$ increases with α, while β has a marginal influence.

3.5 DESIGN EXAMPLES

A surface represented in Figure 3.14 (a) is generated by connecting a set of $\nu - \mu$ design curves by varying β and keeping ω and α constant. This representation shows clearly the benefits of α and β (specially the former one) on the flexural capacity of a cross section, but its use for design purposes is not simple. The design surface can be simplified by creating their contour map on a 2D $\nu - \mu$ representation, as shown in Figure 3.14 (b), where design curves for $\omega = 0$ and $\omega = 0.2$ are plotted. Assuming a designer perspective, the graphic of Figure 3.14 (b) is used to perform some design examples.

EXAMPLE 1: Consider a cross section of 400 mm × 400 mm, with a reinforcement ratio of 0.2 and clear cover of 20 mm. For this section made of plain concrete, the hypothetical design load is 380 kN ($\nu =$ 0.125) in compression and design moments will be evaluated depending on the concrete tensile performance. Assuming same reinforcement ratio and compressive load, the section is designed by FRC and the possible increase in moment capacity is discussed. From Figure 3.14 (b) the moment is found as 164.04 kN·m ($\mu =$ 0.142) for $\alpha 0 \beta 1$ (plain concrete) curve and illustrated by boxed **X**. The maximum moment of $\omega = 0.2$ series is represented by boxed **Y** ($\mu =$ 0.167, see Figure 3.14 (b)) and found to be 193.78 kN·m, which corresponds to $\alpha 2 \beta 5$, providing an increase of approximately 18%. The moments for the other cases lie in between the boxed **X** and **Y**, (see in Figure 3.14 (b)) and are presented in Table 3.5 with percentage increment with respect to plain concrete case ($\omega 0.2 \alpha 0 \beta 1$). In case of SSFRC, the moment increase is insignificant, since the post-cracking strength is almost exhausted before the cross section attains the curvature corresponding to its plastic moment. However, for deflections corresponding to service limit states, a SHFRC can increase significantly the flexural

capacity of RC elements, even statically determinate ones (Taheri et al. 2012). When plain concrete is completely replaced by SHFRC the increment in moment was, however, significant.

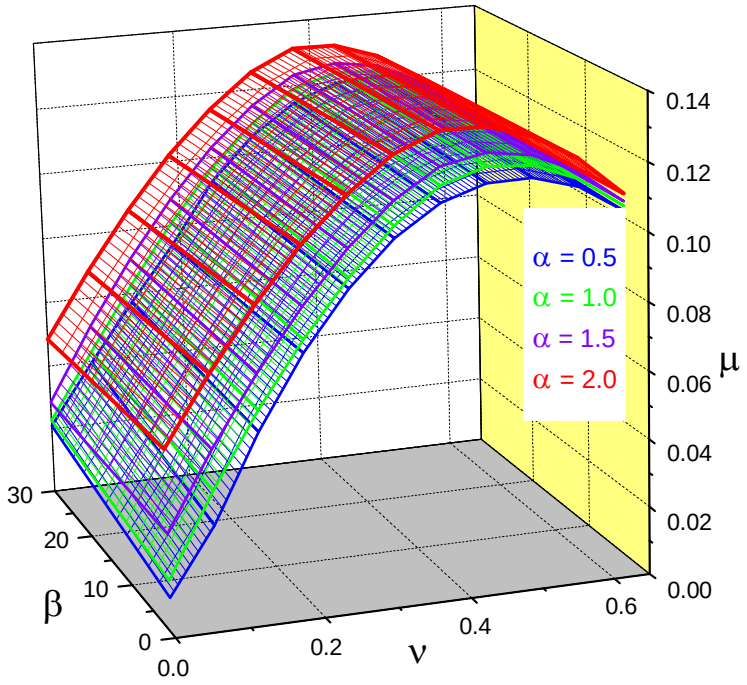

(a)

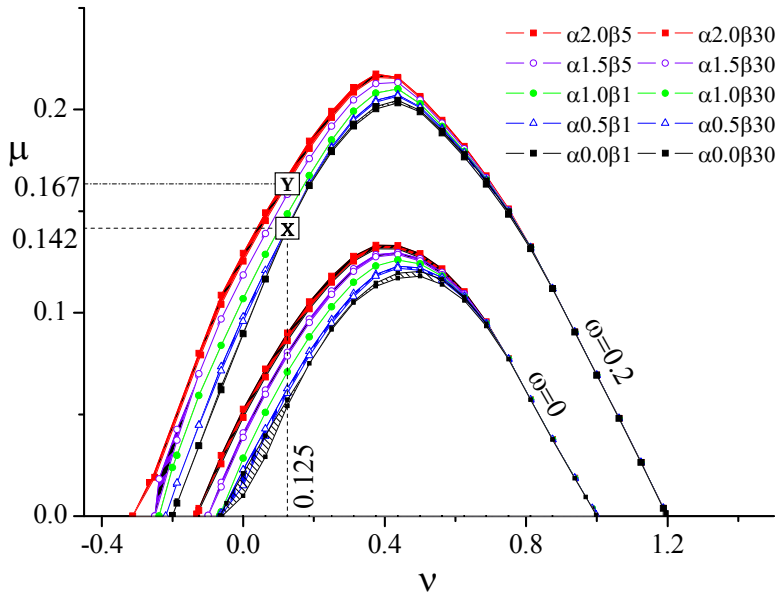

(b)

Figure 3.14 (a) Design surfaces for ω=0; and (b) Design curves for ω=0 and ω=0.2.

Table 3.5: Increase in moment for strain hardening and strain softening FRC.

Strain softening material	Moment (kN·m)	Increase in Moment (%)	Strain hardening material	Moment (kN·m)	Increase in Moment (%)
$\alpha 0 \beta 5$	164.04	0.00	$\alpha 1 \beta \mathbf{j}$*	172.20	4.97
$\alpha 0 \beta 10$	164.04	0.00	$\alpha 1.5 \beta 5$	183.45	11.83
$\alpha 0 \beta 30$	164.14	0.06	$\alpha 1.5 \beta 10$	182.69	11.37
$\alpha 0.5 \beta 1$	164.40	0.22	$\alpha 1.5 \beta 30$	181.18	10.45
$\alpha 0.5 \beta 5$	164.40	0.22	$\alpha 2 \beta 5$	193.78	18.13
$\alpha 0.5 \beta 10$	164.43	0.24	$\alpha 2 \beta 10$	193.68	18.07
$\alpha 0.5 \beta 30$	164.52	0.30	$\alpha 2 \beta 30$	189.34	15.47

* **j** = 1, 5, 10, 30

EXAMPLE 2: Consider a design situation, where a section of size of 400 mm × 400 mm with clear cover of 20 mm is subjected to a design compressive load of 570 kN and a design bending moment of 155.7 kN·m. For this section it will be obtained distinct possible arrangements of conventional reinforcement ratios and requisites for the post-cracking behaviour of FRC. This methodology can be used to optimize the reinforcement solution if direct and indirect costs are known for these solutions. Using Eqn. (3.11) and Eqn. (3.12) the ν and μ are found as 0.1875 and 0.1348, respectively, represented in Figure 3.15 by box **A**. The hypothetical design curves for this point (box **A**) lie in between the contours (see Figure 3.15) for $\omega = 0$ and $\omega = 0.2$. The points corresponding to ν =0.1875 on design curve (for plain concrete, $\alpha 0 \beta 1$) for $\omega = 0$ and $\omega = 0.2$ contours are represented by box **B** (ν =0.1875, μ =0.16257) and box **C** (ν =0.1875, μ =0.0751), respectively. Using the boxes **B** and **C,** the ω for the section is interpolated, having been obtained a value of 0.1366 that corresponds to a cross section steel area of 1256 mm^2; If for the same v=0.1875 is considered the FRC that provide the higest μ for $\omega = 0$ and $\omega = 0.2$, which is $\alpha 2 \beta 5$ for both situations, the corresponding points are represented by box **D** (μ = 0.105) and box **E** (μ = 0.184), respectively. In the extrapolation purposes it can be assumed that the point **B** and **C** has become point **D** and **E**, respectively. The same

problem can be stated as if **D** ($\mu = 0.105,\ \omega = 0$) and **E** ($\mu = 0.184,\ \omega = 0.2$) are known, the ω need to calculated for a point whose μ =0.16257. By linear interpolation, the ω can be calculated, which corresponds to the steel area of 683.34 mm^2.

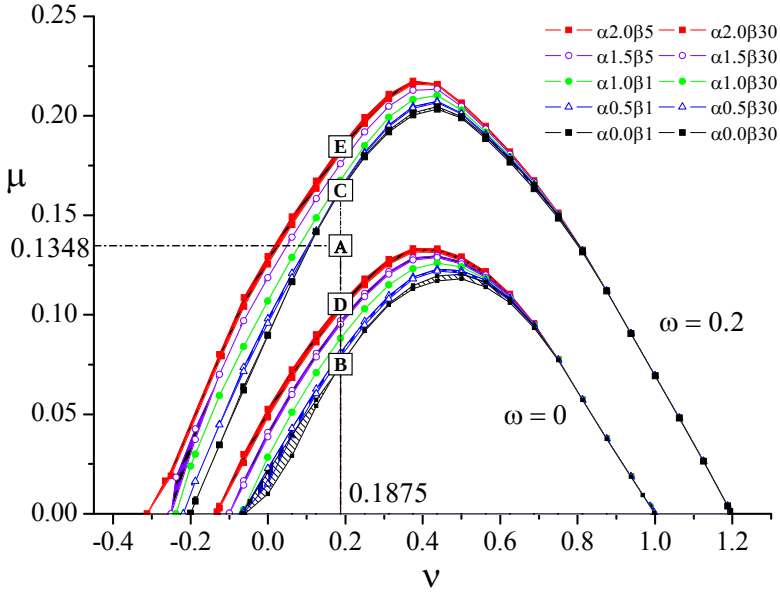

(a)

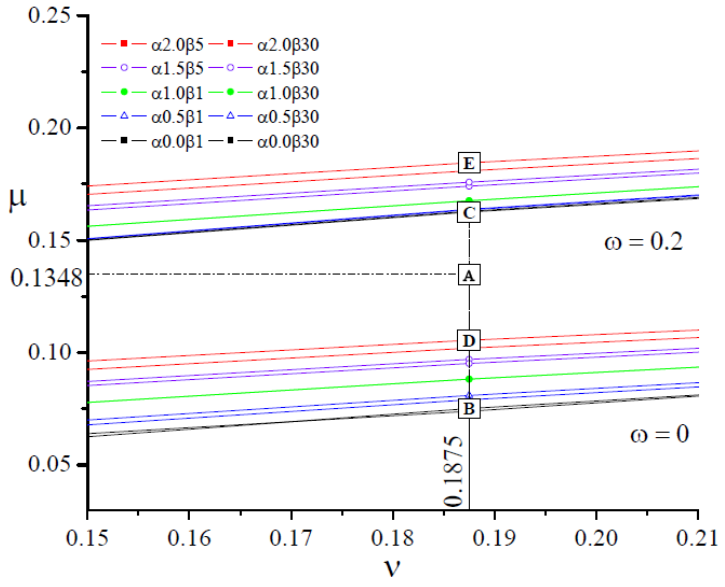

(b)

Figure 3.15: (a) Design envelopes and (b) Zoomed diagram used for interpolation of steel ratios.

Similarly, interpolation can be carried out for other homologous curves of FRC corresponding to $\omega = 0$ and $\omega = 0.2$. The area of steel reinforcement required for the FRC sections and their corresponding percentage decrease with respect to plain concrete are summarised in Table 3.6. In Table 3.6, if plain concrete of the section is assumed to be replaced by SHFRC and SSFRC, a decrease of approximately 45.60 to 13.98% and 4.75 to 0.1% respectively, is possible for steel reinforcement.

Table 3.6: Steel reinforcement ratio for strain softening and strain hardening material.

Strain softening material	Steel Area (mm^2)	Decrease in steel area (%)	Strain hardening material	Steel Area (mm^2)	Decrease in steel area (%)
$\alpha 0 \beta 5$	1255.95	0.01	$\alpha 1 \beta \mathbf{j}$*	1080.51	13.98
$\alpha 0 \beta 10$	1254.96	0.09	$\alpha 1.5 \beta 5$	882.82	29.72
$\alpha 0 \beta 30$	1248.77	0.58	$\alpha 1.5 \beta 10$	889.07	29.22
$\alpha 0.5 \beta 1$	1214.56	3.31	$\alpha 1.5 \beta 30$	924.44	26.40
$\alpha 0.5 \beta 5$	1213.63	3.38	$\alpha 2 \beta 5$	683.34	45.60
$\alpha 0.5 \beta 10$	1211.56	3.55	$\alpha 2 \beta 10$	698.28	44.41
$\alpha 0.5 \beta 30$	1196.46	4.75	$\alpha 2 \beta 30$	765.73	39.04

* **j** = 1, 5, 10, 30

EXAMPLE 3: Consider another hypothetical example of a conventionally reinforced continuous shallow beam with three supports and spans of 5000 mm each in length, as represented in Figure 3.16. The geometry, support and reinforcement details of RC beam are illustrated in this figure. The designed beam is simplified, and assumed to be composed of two types of cross-sections. The 1400 mm length on each side of middle support is described by $S_2 - S_2'$ section and the rest of beam is described by $S_1 - S_1'$ section. According to the ACI 318 (2004), the admissible deflection (δ) of the beam is *L*/480 (*L*=5000 mm is the span length of the beam). The beam has flexural longitudinal reinforcement ratio (ρ) of 0.68% and 0.79% for sections $S_1 - S_1'$ and $S_2 - S_2'$, respectively, where

$$\rho = 100A_s / bh \tag{3.14}$$

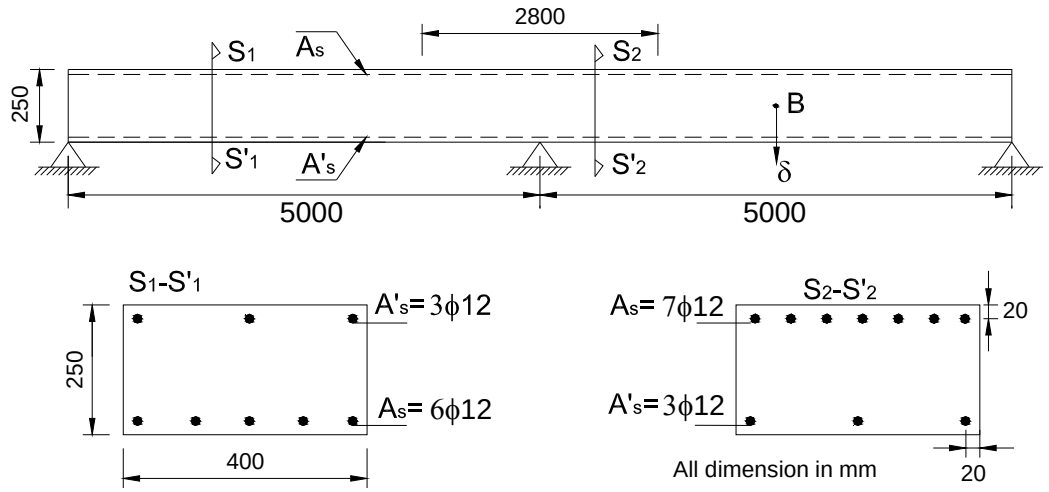

Figure 3.16: Beam and cross-sectional dimensions

The beam was analysed for ultimate load carrying capacity by FEMIX. The analysis used fibre model (described in Chapter 5), in which the beam was divided in 22 Timoshenko beam elements of equal length, along the longitudinal direction. The cross section was divided in 40 concrete fibres, and each steel bar is assumed as an additional fibre. The design values of concrete and steel are described in Table 3.3 and Table 3.4, respectively. After applying dead load of 2.5 kN/m^2, uniform distributed live load was applied until the displacement reached more than two times the admissible deflection. The force-deflection graphs are illustrated in Figure 3.17, where force corresponds to total uniformly distributed load on each span, and deflection corresponds to mid-point of span (see point B in Figure 3.16).

From Figure 3.17, it can be seen that there was a substantial increment in load carrying capacity of beam when the post-cracking strength increases. Table 3.7 presents the increment in terms of load percent for two deflection levels, δ and 2δ, for five different levels of post-cracking performance of FRC.

Moreover for a certain α, the effect of increase in ultimate strain can increase the flexural capacity tremendously.It can be concluded that the benefits in terms of load

carrying capacity provided by a certain post-cracking performance of a FRC is higher than those at the cross section level. The benefits in term of load carrying capacity for serviceability and ultimate limit states increase with the degree of the statically indeterminacy of the structure.

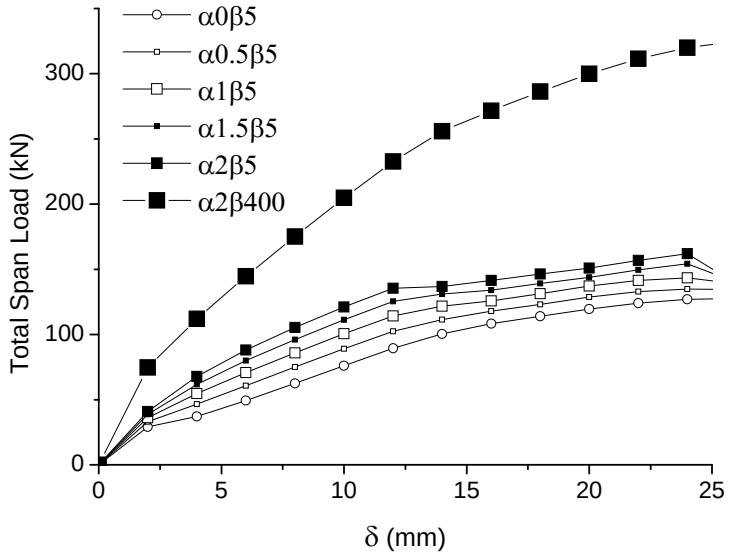

Figure 3.17: Force-deflection relationship of the continuous beam

Table 3.7: Increase in Span-Load for FRC continuous beams

FRC material	For δ deflection, increase in span-load (%)	For 2δ deflection, increase in span-load (%)
$\alpha 0.5\beta 5$	16.62	7.50
$\alpha 1\beta 5$	31.58	14.58
$\alpha 1.5\beta 5$	45.36	20.14
$\alpha 2\beta 5$	58.21	25.95
$\alpha 2\beta 400$†	175.64	161.65

† The ε_{ctu} was assumed to be 2% for this case.

3.6 SUMMARY

This chapter aims to develop numerical tools capable of determining the moment-curvature relationship ($M-\chi$) of cross sections (DOCROS software), and using this relationship estimate the force-deflection response of simply supported beams/slabs failing in flexure (DefDocros software). The DefDocros software is easy to use and consume significantly less time to predict the force deflection relation with acceptable accuracy for design purposes, when compared to FEM.

In this chapter a methodology was described to develop design-curves of strain softening and strain hardening fibre reinforced concrete elements subjected to axial load and bending moments. For the optimal and economical solution, the future design improvements are possible by exploiting the material properties of concrete, like in this chapter discussed for FRC.

The effect of α is more noteworthy compared to β, when the increase in moment carrying capacity is focus of observation. As α and β are the parameters related to tension costitutive law of concrete, the effect of them was visible when axial load applied was of tensile in nature. For any $\nu-\mu$ curve with constant ω, as ν decreased, the number of layers in tension increased simulataneously during the calculation of maximum moment. With this increase of layer in tension, the effect of α became obvious.

The design examples strengthen the fact that the FRC can be used as a partially replaceable material for reinforcement. The ductility parameter has insignificant effect on the maximum moment, but at the same time the maximum crack openning governs the servicibility criteria, which are upto certain extent dependent on ductility limits.

The shape of interaction curve depends on mechanical properties of concrete and steel, position of bars, reinforcement ratio and shape of the section. These design curves are limited in use and further design curves can be developed for other cases, similar to the approach followed in this chapter.

CHAPTER 4

Modelling of confined concrete with CFRP sheets

4.1 INTRODUCTION

The use of Carbon Fibre Reinforced Polymer (CFRP) materials has significantly increased, being the confinement of concrete columns one of the important applications of this composite. In fact, circular concrete columns fully or partially wrapped with wet lay-up CFRP sheets can significantly increase the load carrying and the energy dissipation capacities. The magnitude of these structural improvements depends on several parameters, such as: concrete strength; CFRP percentage; geometric confinement arrangement; column aspect ratio; arrangement and percentage of existing steel reinforcement. The remarkable properties of CFRP sheets, like the low weight, high strength and easy installation, make them highly suitable for the confinement of reinforced concrete (RC) columns. However, the elastic behaviour up to the abrupt rupture of these materials should be taken into account, due to the brittle failure mode and its consequence in terms of the ductility performance of CFRP-based confined columns.

Several experimental studies (Saadatmanesh *et al.* 1994, Nanni and Bradford 1995, Picher *et al.* 1996, Spolelstra and Monti 1999, Lam and Teng 2003, Barros and Ferreira 2008) have been carried out to understand the role of CFRP sheets as a confining material, and to derive enough data that can be used for the development and appraisal of constitutive models. Most of the studies have been limited to the monotonic compressive loading, except few ones (Shao *et al*. 2006, Lam *et al*. 2006) that have investigated the influence of the cyclic loading on the behaviour of FRP-based confined concrete elements. The CFRP-based confinement effectiveness on plain concrete cylinder specimens of small dimensions

was investigated by Shao *et al.* (2006) and Lam *et al.* (2006), while Ferreira (2007) explored the CFRP-based confinement effectiveness on column elements of concrete strength range representative of the concrete structures requiring strengthening intervention.

In past, some researchers (Saadatmanesh *et al.* 1994, Seible *et al.* 1995) modified the uniaxial stress-strain model proposed by Mander *et al.* (1998) for concrete columns confined with steel hoops to take into account the assumption of constant confining pressure exerted by the steel hoops, which can not be assumed for FRP materials due to the linear elastic behaviour of these composites up to their brittle failure. In the present Chapter, a new model is proposed to simulate the behaviour of CFRP-based fully and partially confined RC columns subjected to cyclic loading. The considered monotonic stress-strain relationship (envelope of the cyclic curve, as proved in a previous work – Ferreira 2007) is supported on the principles proposed by Harajli *et al.* (2006), while the hysteretic stress-strain cycles were derived using an approach similar to the analytical model of Chang and Mander (1994), and evaluating relevant parameters of this model from the available experimental data (Ferreira, 2007).

With the purpose of developing a constitutive model for CFRP-based confined circular concrete columns subjected to monotonic and cyclic loadings, the present Chapter starts with presenting the relevant results of the experimental program carried out at the University of Minho by Ferreira (2007). The constitutive model is then described and the values of crucial parameters are determined from the experimental results. Finally, the performance of the developed constitutive model, which was implemented into the FEMIX computer program for the material nonlinear analysis of concrete structures, was appraised using the experimental results.

4.2 EXPERIMENTAL CAMPAIGN CARRIED AT MINHO UNIVERSITY

4.2.1 Specimen properties and nomenclature

The experimental program deals with monotonic and cyclic axial compression tests on concrete cylinders of 200 mm diameter (D) and 600 mm height (H), divided in the G3, G1 and G2 groups, whose characteristics are indicated in Table 4.1 to Table 4.3, respectively.

In these tables $f_{co,UPC}$ and $\varepsilon_{co,UPC}$ are the concrete compressive strength of unconfined plain concrete (UPC here after) specimens and its corresponding axial strain, respectively. A total of 54 RC specimens were tested to evaluate the effectiveness of full and distinct partial confinement CFRP arrangements. The experimental program was planned to assess the influence of the following parameters on the concrete confinement effectiveness: concrete strength class; stiffness and percentage of CFRP; concrete free space between CFRP strips; number of CFRP layers per each strip. Each specimen is designated as **W***i***S***j***L***k***F***l*_*c/m*, where **W***i* represents the strip width in mm, **S***j* is the number of strips along the height of the cylinder, **L***k* represents the number of CFRP layers per each strip, and **F***l* represents the diameter of the longitudinal steel bars, in mm. To distinguish cyclic from monotonic tests, the *c* character was attributed to the cyclic tests, while the *m* letter was used to designate monotonic tests (see Figure 4.1).

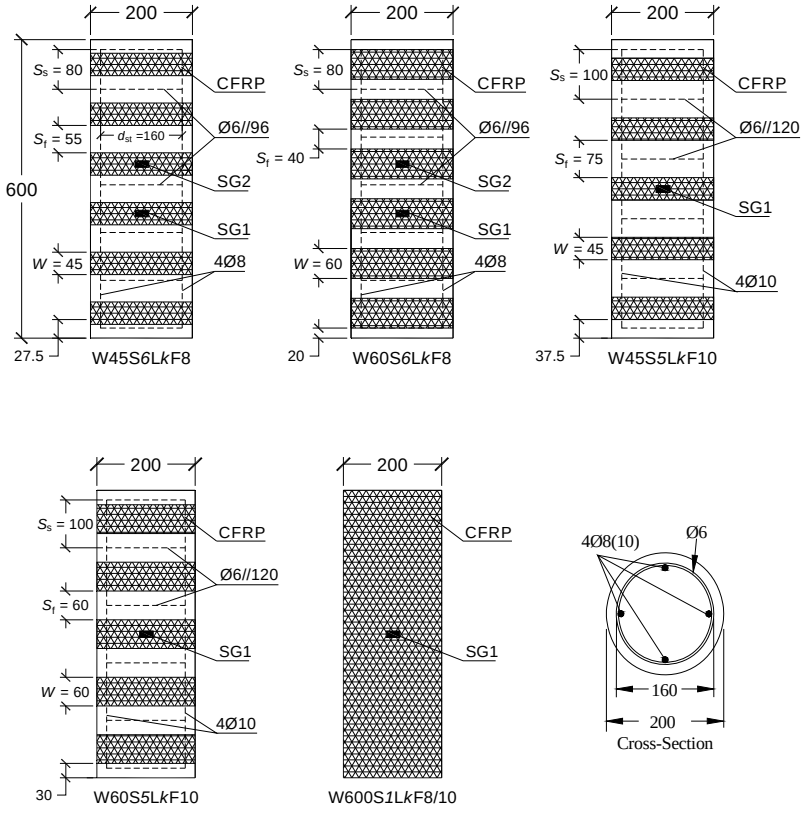

Figure 4.1: Confinement arrangements of the tested specimens and corresponding cross-section. Note: all dimensions are in mm.

Figure 4.1 represents the characteristics of the typical specimens, where s_s is the spacing between steel hoops and s_f is the clear spacing between consecutive CFRP strips (for full wrapping s_f = 0). The diameter of the steel hoops (d_{st}, see Figure 4.1) is 160 mm, while the diameter of its cross-section is 6 mm.

In Table 4.1 to Table 4.3 f_{cu} and ε_{cu} (see Figure 4.5) are the ultimate concrete compressive strength of CFRP confined concrete specimen and its corresponding axial strain, respectively, t_f is the thickness of the CFRP sheet, and ρ_f is the CFRP volumetric ratio given by Eq (4.1).

$$\rho_f = 4\frac{W\ L\ S\ t_f}{D\ H} \tag{4.1}$$

where the values of *W*, *L* and *S* can be derived from the specimen designation, as described above. CFRP confined cylinders and UPC cylinders of each series were prepared from the same concrete batch. Two cylinders were tested for each confinement arrangement, as well as for UPC. More details about the preparation of the specimens can be found elsewhere (Ferreira, 2007).

Table 4.1: G3 group of tests ($f_{co,UPC}$ = 26.47 MPa, $\varepsilon_{co,UPC}$ =0.30%)

Specimen name	t_f [mm]	ρ_f	$\varepsilon_{cu}/\varepsilon_{co,UPC}$	$f_{cu}/f_{co,UPC}$
W45S6L3F8_m[a]	0.113	0.0031	6.00	1.49
W45S6L5F8_m		0.0051	8.00	1.97
W60S6L3F8_m		0.0041	6.33	1.89
W60S6L5F8_m[a]		0.0068	6.67	2.42
W600S1L3F8_m		0.0068	8.33	2.11
W45S6L3F8_c[a,b]		0.0031	5.00	1.62
W45S6L5F8_c		0.0051	8.33	1.85
W60S6L3F8_c		0.0041	6.33	1.78
W60S6L5F8_c[a]		0.0068	9.33	2.03
W600S1L3F8_c		0.0068	4.67	2.69

[a] Used in Figure 4.3 for representation

[b] Used for numerical simulation

Table 4.2: G1 group of tests ($f_{co,UPC}$ = 13.87 MPa, $\varepsilon_{co,UPC}$ =0.27%)

Specimen name	t_f [mm]	ρ_f	$\varepsilon_{cu}/\varepsilon_{co,UPC}$	$f_{cu}/f_{co,UPC}$
W45S6L3F8_m	0.113	0.0031	5.82	1.99
W45S6L5F8_m		0.0051	9.09	2.56
W60S6L3F8_m		0.0041	6.36	2.48
W60S6L5F8_m		0.0068	10.30	3.14
W600S1L3F8_m		0.0068	9.39	3.45
W600S1L5F8_m[b]		0.0113	12.12	4.47
W45S6L3F8_m	0.176	0.0048	10.00	2.60
W45S6L5F8_m		0.0079	13.94	3.30
W60S6L3F8_m		0.0063	11.18	3.33
W60S6L5F8_m		0.0106	17.58	4.68
W600S1L3F8_m		0.0106	10.00	3.76
W600S1L5F8_m		0.0176	14.85	5.42
W45S5L3F10_m	0.113	0.0025	6.09	1.95
W45S5L5F10_m[b]		0.0042	9.60	2.37
W60S5L3F10_m		0.0034	7.91	2.37
W60S5L5F10_m		0.0057	12.27	3.16
W600S1L3F10_m		0.0068	8.98	3.38
W600S1L5F10_m		0.0113	10.41	4.06
W45S5L3F10_m	0.176	0.0040	8.60	2.23
W45S5L5F10_m		0.0066	12.12	2.76
W60S5L3F10_m		0.0053	9.78	2.66
W60S5L5F10_m		0.0088	12.22	3.34
W600S1L3F10_m		0.0106	12.87	4.52
W600S1L5F10_m		0.0176	14.55	5.42

[b] Used for numerical simulation

Table 4.3: G2 group of tests ($f_{co,UPC}$ = 30.31 MPa, $\varepsilon_{co,UPC}$ =0.31%)

Specimen name	t_f [mm]	ρ_f	$\varepsilon_{cu}/\varepsilon_{co,UPC}$	$f_{cu}/f_{co,UPC}$
W45S6L3F8_m	0.113	0.0031	3.07	1.48
W45S6L5F8_m		0.0051	4.63	1.83
W60S6L3F8_m[b]		0.0041	4.57	1.79
W60S6L5F8_m		0.0068	5.97	2.21
W600S1L3F8_m[b]		0.0068	6.03	2.35
W600S1L5F8_m		0.0113	4.67	2.36
W45S6L3F8_m	0.176	0.0048	4.40	1.74
W45S6L5F8_m		0.0079	6.17	2.00
W60S6L3F8_m		0.0063	6.17	2.10
W60S6L5F8_m		0.0106	7.50	2.57
W600S1L3F8_m		0.0106	5.60	3.09
W600S1L5F8_m		0.0176	4.03	3.83
W45S5L3F10_m	0.113	0.0025	2.28	1.43
W45S5L5F10_m		0.0042	2.81	1.62
W60S5L3F10_m		0.0034	2.68	1.58
W60S5L5F10_m		0.0057	3.50	1.69
W600S1L3F10_m		0.0068	4.17	2.36
W600S1L5F10_m		0.0113	2.66	3.31
W45S5L3F10_m	0.176	0.0040	3.18	1.52
W45S5L5F10_m		0.0066	4.13	1.79
W60S5L3F10_m		0.0053	3.50	1.85
W60S5L5F10_m		0.0088	5.03	2.12
W600S1L3F10_m		0.0106	2.91	3.17
W600S1L5F10_m		0.0176	3.05	3.67

[b] Used for numerical simulation

4.2.2 Test procedure

Three Linear Variable Displacement Transducers (LVDTs) were placed at 120° from each other around the cylindrical specimen to measure the displacements between the steel load plates of the equipment (see Figure 4.2). From the values recorded in these three LVDTs

the specimen axial displacement is determined, from which the axial strain is calculated dividing this value by the specimen initial height. This monitoring arrangement avoids that the deformation of the equipment has been added to the values recorded by the LVDTs.

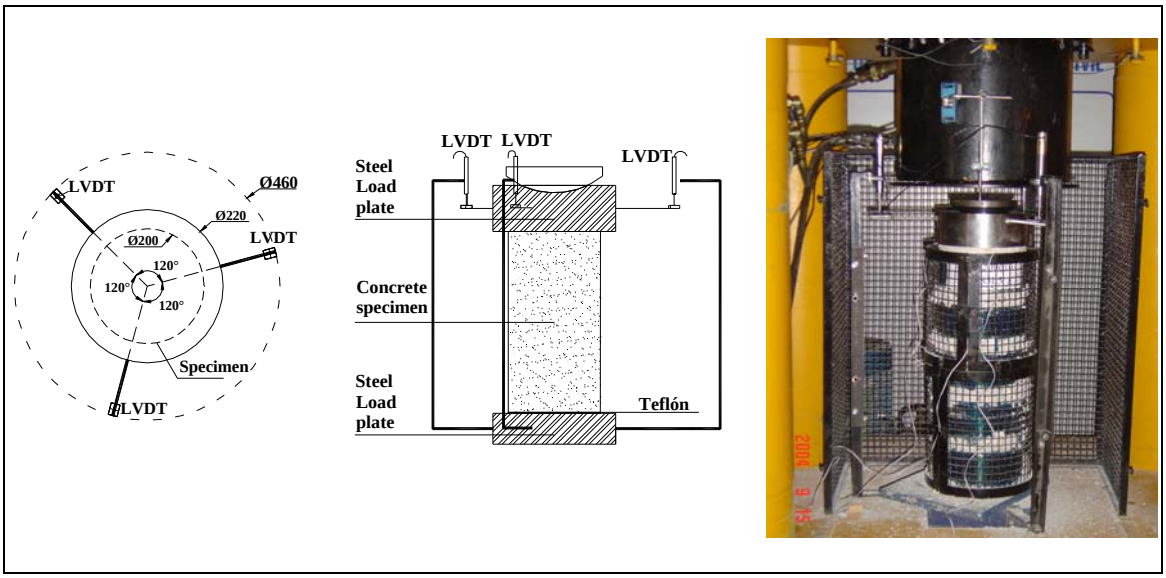

Figure 4.2: Position of the LVDTs and test apparatus (Ferreira, 2007).

4.2.3 Material properties

Two types of CFRP sheets were used in the experimental program, one with the trade name of CF120 (200 g/m^2 of fibres) and the other designated as CF130 (300 g/m^2 of fibres). The mechanical properties of the sheets were determined by experimental tests on five samples for each type of sheet. The tests were conducted according to ISO recommendations (2003). The CF130 sheets had a thickness (t_f) of 0.176 mm, an elasticity modulus (E_f), an ultimate strain (ε_{fu}) and a tensile strength (f_{fu}) in the fibre direction of 230 GPa, 1.33 % and 3070 MPa, respectively. In the tests with CF120 sheets the following values were obtained: t_f = 0.113 mm; E_f = 232 GPa; ε_{fu} = 1.52 %; f_{fu} = 3535 MPa. The values of the mechanical properties of longitudinal and transversal steel bars are included in Table 4.4. In this table, f_{sy}, f_{sh} and f_{su} represent the tensile yield stress, hardening stress and tensile strength, respectively, ε_{sh} and ε_{su} are the steel strains corresponding to f_{sh} and f_{su}, and E_s and E_{sh} are the elasticity modulus and the tangent modulus at the initial of the hardening phase, respectively.

Table 4.4: Data used in the numerical analysis to simulate the behaviour of the steel bars.

Parameter	Φ6	Φ8	Φ10
Initial Young Modulus, E_s (GPa)	212.2	199.8	200.0
Tangent modulus at strain hardening, E_{sh} (GPa)	6.4	6.4	6.4
Yielding stress, f_{sy} (MPa)	468.3	517.2	421.2
Hardening strain, ε_{sh} (mm/mm)	7.5×10^{-3}	7.5×10^{-3}	7.5×10^{-3}
Hardening stress, f_{sh} (MPa)	468.3	517.0	421.2
Strain at the ultimate stress, ε_{su} (mm/mm)	8.0×10^{-1}	1.1×10^{-1}	1.4×10^{-1}
Ultimate stress, f_{su} (MPa)	616.2	607.9	539.3

4.2.4 Results and discussions

Typical stress-strain curves of monotonic tests and cyclic tests are compared in Figure 4.4 (see also Table 4.1 to Table 4.3). The stress-strain curves of all tested specimens are available in Ferreira (2007). Figure 4.3 (a) and (b) illustrates the typical correlation between $\varepsilon_{cu}/\varepsilon_{co,UPC}$ *versus* ρ_f and $f_{cu}/f_{co,UPC}$ *versus* ρ_f, respectively. It is evident from Table 4.1 to Table 4.3 and Figure 4.3 (b) that the load carrying capacity of the specimens increased with the increase of ρ_f. Regardless the loading type, a tendency of $\varepsilon_{cu}/\varepsilon_{co,UPC}$ and $f_{cu}/f_{co,UPC}$ to increase with the increase of ρ_f is observed. However, a high dispersion in terms of $\varepsilon_{cu}/\varepsilon_{co,UPC} - \rho_f$ relationship was registered (see Figure 4.3 (a)). Due to the accumulation of the concrete compressive plastic strain, mainly in between CFRP strips in subsequent loading cycles, values of the $\varepsilon_{cu}/\varepsilon_{co,UPC}$ ratio were larger in the specimens subjected to cyclic loading than in the specimens under monotonic loading. Comparing the results of specimens of equal ρ_f, it can be concluded that, regardless of the loading type, full-wrapping was more effective than discrete confinement arrangements as

it was expected, but it should be noted that, in comparison with the full wrapping confinement systems, the partial confinement arrangements are easier and faster to apply (Barros and Ferreira 2005b, Ferreira 2007).

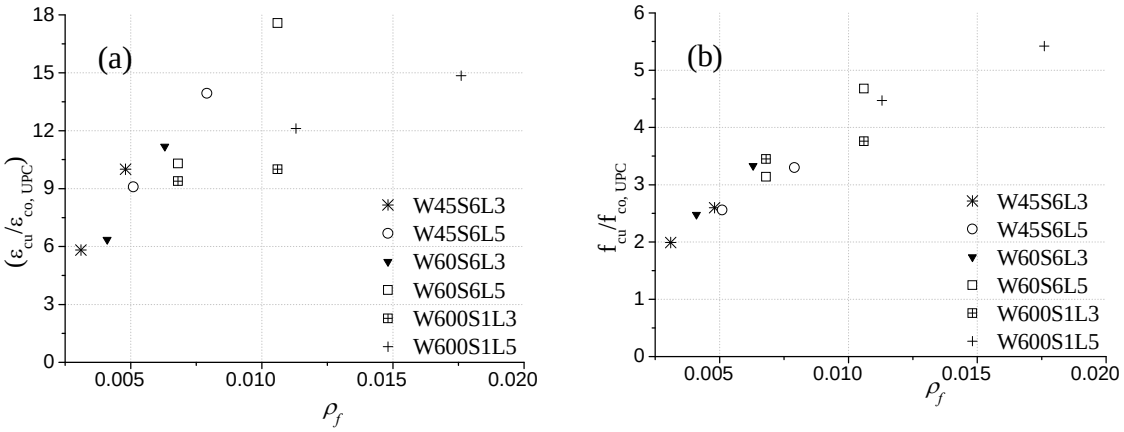

Figure 4.3: (a) $\varepsilon_{cu}/\varepsilon_{co,UPC}$ *vs.* ρ_f (b) $f_{cu}/f_{co,UPC}$ *vs.* ρ_f for the specimens with longitudinal reinforcement of 8mm (Table 4.2).

From the analysis of Figure 4.4 it is observed that a good fit exist between the envelope of the cyclic stress-strain curve and the stress-strain curve of the corresponding monotonic test. The envelope curve can be idealized as composed by three branches. The first one, of an almost linear trend with a slope that depends basically on the RC properties, is followed by a transition branch of pronounced non-linearity, which ends in another almost linear branch of a slope that depends, mainly, on the CFRP confinement properties. This slope has a tendency to increase with the increase of ρ_f. In each series of load cycles, the concrete axial strain increased from the first to the third cycle. This increase can be justified by the concrete dilation, mainly at the zones in-between CFRP strips. Due to the increase of tensile strains in the CFRP in subsequent load cycles of each series of load cycles, an increase of confinement pressure is introduced into concrete by the CFRP system, hence the reloading branch of the last cycle of each series of load cycles (the returning to the monotonic phase) has exceeded the load carrying capacity of the homologous monotonic specimen. As expected, this behaviour was more pronounced in the full-wrapped specimens.

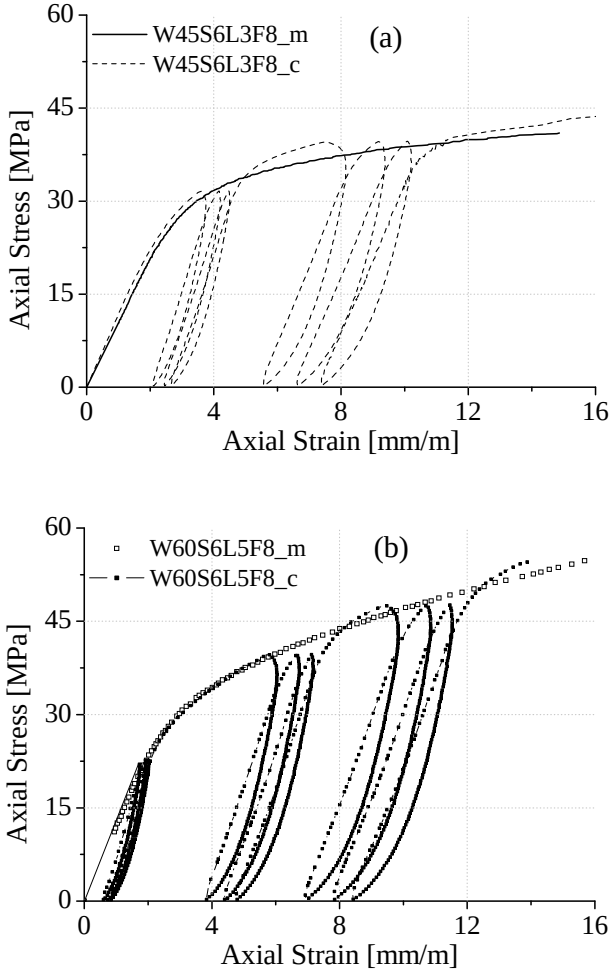

Figure 4.4: Cyclic and monotonic stress-strain curves for (a)W45S6L3F8_m/c and (b)W60S6L5F8_m/c specimens.

It is also verified that the unloading branch is eminently nonlinear, while the reloading branch is composed by nonlinear segments of reduced amplitude at its extremities, connected by a linear part. Considering the shape of the unloading and reloading branches, it is not possible to adopt a polynomial equation for their simulation. Therefore, transition type equations (described in Appendix A) are adopted to provide the required curvature to the nonlinear parts of the unloading and reloading branches. Another prominent feature, which is visible in Figure 4.4, is the asymptotic nature of the reloading branch in the vicinity of the envelope curve. Assuming that Figure 4.5(a-b) represents the fundamental features of CFRP confined concrete and, comparing Figure 4.4 with Figure 4.6, it is observed that the non-linearity of the reloading branch is more pronounced near the

envelope curve than in the starting part of this branch (at point N in Figure 4.5). In consequence, two transition type equations are required to model a reloading branch up to the envelope curve.

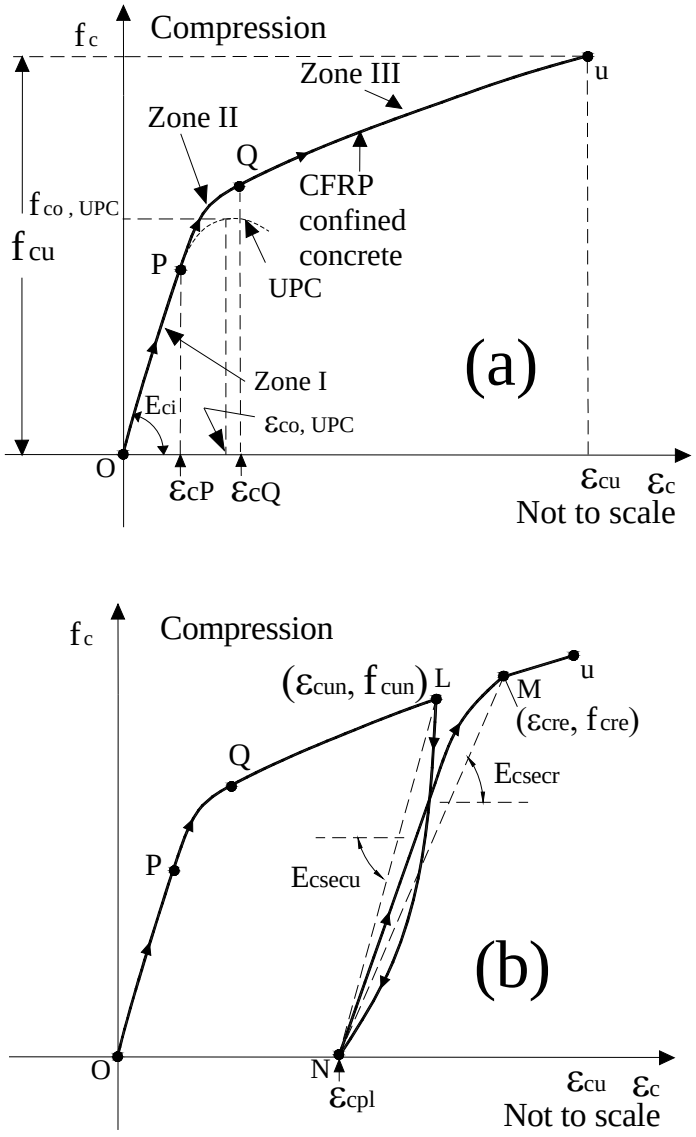

Figure 4.5: Schematic illustration of the FRP-confined concrete (a) envelope curve (b) cyclic curve.

The unloading secant stiffness (E_{csecu}), see Figure 4.5(b), is neither equal to the initial Young's modulus (E_{ci}) nor to the reloading secant stiffness (E_{csecr}). The E_{csecu} is always greater than the corresponding E_{csecr}. This implies that in a full unloading-reloading cycle,

the reloading strain (ε_{cre}, point M in Figure 4.5(b)) on the envelope is always greater than the unloading strain on the envelope (ε_{cun}, point L in Figure 4.5(b)).

The plastic strain, ε_{cpl}, is one of the most crucial features of the cyclic tests. Shao *et al.* (2006) considered that during a hysteretic phase, the plastic strain is kept constant, regardless of being a full or a partial unloading. However, Figure 4.3 does not support this assumption.

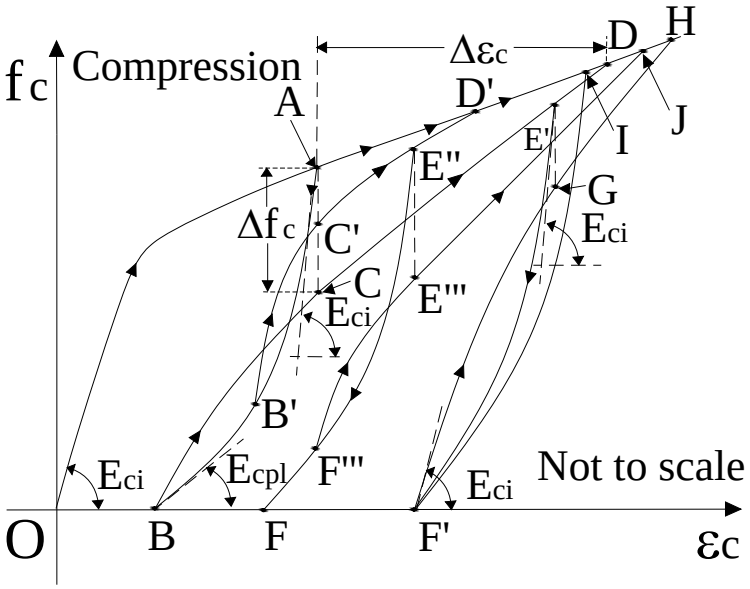

Figure 4.6: Schematic illustration of the FRP-confined concrete hysteretic model.

In the successive series of load cycles, a tendency for the decrease in stiffness of unloading and reloading branches was observed in all tested specimens. The decrease in the stiffness of these branches diminished with the increase of the specimen axial deformation. The stiffness of the unloading and reloading branches seems to approach of a constant value (residual stiffness) with the increase of the specimen axial deformation.

4.3 MODEL FOR THE CYCLIC COMPRESSION BEHAVIOUR OF CFRP CONFINED CONCRETE

4.3.1 Monotonic envelope

The monotonic compression stress-strain envelope curve is composed of a linear branch (indicated as zone I in Figure 4.5(a)), followed by a transition nonlinear branch (zone II) and ends with another nonlinear branch (zone III). In zone I (branch $\overline{OP}$) the CFRP has marginal influence, while zone III (branch $\overline{Qu}$) is significantly influenced by the effective lateral pressure provided by the CRFP confinement arrangements. Zone II (branch $\overline{PQ}$) is markedly nonlinear, connecting the branches that simulate the zones I and III. This nonlinearity is a result of the concrete nonlinear behaviour due to its crack initiation (near point P in Figure 4.5(a)) and propagation up to a strain level corresponding to the initiation of the UPC softening phase (point Q in Figure 4.5(a)). According to this approach, the zone I (for $0 \le \varepsilon_c \le \varepsilon_{cP}$) is simulated using the Eqn (4.2) to (4.4):

$$f_c(\varepsilon_c) = E_{ci}\varepsilon_c \tag{4.2}$$

$$E_c(\varepsilon_c) = E_{ci} \tag{4.3}$$

$$\varepsilon_{cP} = \beta_c \varepsilon_{co,UPC} \tag{4.4}$$

where E_{ci} is the concrete initial Young's modulus calculated according to the recommendations of CEB-FIB Model Code (1993) for UPC, or evaluated experimentally. The parameter β_c represents the percentage of $\varepsilon_{co,UPC}$ up to which UPC has linear and elastic behaviour. The available experimental research shows that β_c has a tendency to increase with the increase of the concrete compressive strength. For the concrete used in the present work, a β_c = 0.4 was assumed. The transition curve that simulates the zone II, starts from an already well-known point $(\varepsilon_{ca}, f_{ca})$ (a subscript *a* is used to designate starting point) with corresponding slope (E_{ca}), and ends at a target point $(\varepsilon_{cb}, f_{cb})$ (a subscript *b* is used to designate ending point) with a slope (E_{cb}). In Figure 4.5(a) the start

and target points of zone II correspond to points P and Q, respectively. The transition curve (for $\varepsilon_{cP} \le \varepsilon_c \le \varepsilon_{cQ}$) is simulated using the following Eq (4.5) to (4.7):

$$f_c(\varepsilon_c) = f_{ca} + (\varepsilon_c - \varepsilon_{ca})[E_{ca} + A\left|\varepsilon_c - \varepsilon_{ca}\right|^R] \tag{4.5}$$

$$E_c(\varepsilon_c) = E_{ca} + A(R+1)\left|\varepsilon_c - \varepsilon_{ca}\right|^R \tag{4.6}$$

where,

$$R = \frac{E_{ca} - E_{c\sec}}{E_{c\sec} - E_{cb}} \tag{4.7a}$$

$$A = \frac{E_{c\sec} - E_{ca}}{\left|\varepsilon_{cb} - \varepsilon_{ca}\right|^R} \tag{4.7b}$$

$$E_{\sec} = \frac{f_{cb} - f_{ca}}{\varepsilon_{cb} - \varepsilon_{ca}} \tag{4.7c}$$

Table 4.5: Parameters for the transition curves

Parameters	Zone II $P \to Q$	$A \to B$	$B \to C$	$C \to D$	$B' \to C'$	$C' \to D'$	$E' \to F'$
ε_{ca}	ε_{cP}	ε_{cun}	ε_{cpl}	ε_{cun}	ε_{cro}	ε_{cun}	$\varepsilon_{ce'}$
f_{ca}	f_{cP}	f_{cun}	0	f_{cnew}	f_{cro}	f^*_{cnew}	$f_{ce'}$
E_{ca}	E_{cP}	E_{ci}	E_{ci}	E_{cnew}	E_{ci}	E^*_{cnew}	E_{ci}
ε_{cb}	ε_{cQ}	ε_{cpl}	ε_{cun}	ε_{cre}	ε_{cun}	ε^*_{cre}	ε^*_{cpl}
f_{cb}	f_{cQ}	0	f_{cnew}	f_{cre}	f^*_{cnew}	f^*_{cre}	0
E_{cb}	E_{cQ}	E_{cpl}	E_{cnew}	E_{cre}	E^*_{cnew}	E^*_{cre}	E^*_{cpl}

In Table 4.5 E_{cP} and f_{cP} represent the tangential modulus and the stress calculated at ε_{cP} from Eq. (4.2) to (4.4) on zone I, and E_{cQ} and f_{cQ} represent the tangential modulus and the stress calculated at ε_{cQ} on zone III, according to the procedures to be described in next steps. In the present approach it is adopted that:

$$\varepsilon_{cQ} = \gamma \varepsilon_{co,UPC} \tag{4.8}$$

From the available research (Ferreira 2007) it seems reasonable to assume that the lateral confining pressure provided by CFRP systems becomes significant (a maximum tensile strain in the CFRP of about 2‰) at an axial compressive strain around $1.5\varepsilon_{co,UPC}$, resulting a value of 1.5 for the γ parameter.

If ε_{cu} represents the ultimate axial compressive strain of CFRP confined concrete, considering the high dispersion for the $\varepsilon_{cu} / \varepsilon_{co,UPC}$ values, an upper bound for the $\varepsilon_{cu} / \varepsilon_{co,UPC} - \rho_f$ relationship was considered, resulting:

$$\varepsilon_{cu} = (800\rho_f + 6)\varepsilon_{co,UPC} \text{ for } 0.0025 \le \rho_f \le 0.0176 \tag{4.9}$$

The stress-strain relationship for zone III ($\varepsilon_{cQ} \le \varepsilon_c \le \varepsilon_{cu}$) is defined from the Eq. (4.10) to (4.12) (Harajli *et al*. 2006):

$$f_c = f_{co,UPC} + k_1 f_l \tag{4.10}$$

$$\varepsilon_c = \varepsilon_{co,UPC}\left[1 + k_2\left(\frac{f_c}{f_{co,UPC}} - 1\right)\right] \tag{4.11}$$

$$f_l = f_{fl} + f_{sl}\frac{A_{cc}}{A_g} \tag{4.12}$$

where f_l is the effective lateral confinement pressure, k_1 and k_2 are confinement effectiveness coefficients derived from the experimental results, A_{cc} is the area of concrete core confined by steel hoops, measured from the centre line of the steel hoop, and A_g is the area of the specimen cross section. In Eq. (4.12), f_{fl} and f_{sl} represent the effective lateral confining pressure exerted by CFRP and steel hoops, respectively, and they can be determined from the Eqs. (4.13) and (4.14):

$$f_{fl} = \frac{\alpha_{fe}\,\alpha_{fv}\,\rho_f\,E_f}{2}\varepsilon_f \tag{4.13}$$

$$f_{sl} = \frac{\alpha_{se}\,\alpha_{sv}\,\rho_{st}}{2} f_{syt} \tag{4.14}$$

where ε_f is the lateral strain in CFRP confinement strips, ρ_{st} is the volumetric ratio of steel hoops (Mander *et al.* 1988), f_{syt} is the yield stress of steel hoops, α_{fe} and α_{fv} are the coefficients that account for the effectiveness of the FRP systems in confining the concrete along the plane of the specimen cross section, and the concrete between FRP strips, respectively (Mander *et al.* 1988). The coefficients α_{se} and α_{sv} account for the effectiveness of the steel hoops in confining the concrete along the plane of the specimen cross section, and the concrete between steel hoops, respectively (Mander *et al.* 1988). The confinement is considered to be most effective in case of circular columns, where $\alpha_{fe} = \alpha_{se} = 1$, while for the remaining cases these coefficients are evaluated from:

$$\alpha_{fv} = \frac{\left(1 - \frac{s_f}{2\,D}\right)^2}{1 - \frac{A_{sl}}{A_g}} \tag{4.15}$$

$$\alpha_{sv} = \frac{\left(1 - \frac{s_s}{2\,d_{st}}\right)^2}{1 - \frac{A_{sl}}{A_g}} \tag{4.16}$$

where A_{sl} is the cross section area of the longitudinal steel bars. The relationship between the obtained experimental values of $k_1 = (f_c - f_{co,UPC}) / f_l$ and $f_l / f_{co,UPC}$ is plotted in Figure 4.7 in order to derive an analytical relationship for k_1. This relationship can be divided in two parts. In fact, Figure 4.7 shows that for all specimens k_1 has a tendency to increase sharply up to a peak value and then decreases exponentially. To represent the influence of the ρ_f on the k_1 - $f_l / f_{co,UPC}$ relationship, markers of a size that increase with the increase of ρ_f were used to distinguish the curves of Figure 4.7. Comparing Figure 4.7 (a) and (b) it can be observed that, for the same ρ_f, k_1 is as high as larger is the concrete compressive strength. However, for same concrete strength class, k_1 decreases with the

increase of ρ_f. Various equations for k_1 depending on the $f_l / f_{co,UPC}$ were initially generated, and was later merged by mathematical tools to form a unique equation. Based on the results of Figure 4.7, the following equations for k_1 were obtained (see Eq. (4.17) to (4.19)):

$$k_1 = m\, f_l / f_{co,UPC} \text{ for } f_l / f_{co,UPC} \le \left(0.12 - 0.0025 f_{co,UPC}\right) \tag{4.17}$$

$$k_1 = \left(4.4 - 0.05 f_{co,UPC}\right)\left(f_l / f_{co,UPC}\right)^C \text{ for } f_l / f_{co,UPC} > \left(0.12 - 0.0025 f_{co,UPC}\right) \tag{4.18}$$

$$C = \frac{\log\left(\dfrac{A_{k1}}{4.4 - 0.05 f_{co,UPC}}\right)}{\log\left(0.12 - 0.0025 f_{co,UPC}\right)};\ m = \frac{A_{k1}}{\left(0.12 - 0.0025 f_{co,UPC}\right)};$$
$$A_{k1} = (0.92 f_{co,UPC} + 0.96)\frac{\rho_f^{-1/3}}{16} \tag{4.19}$$

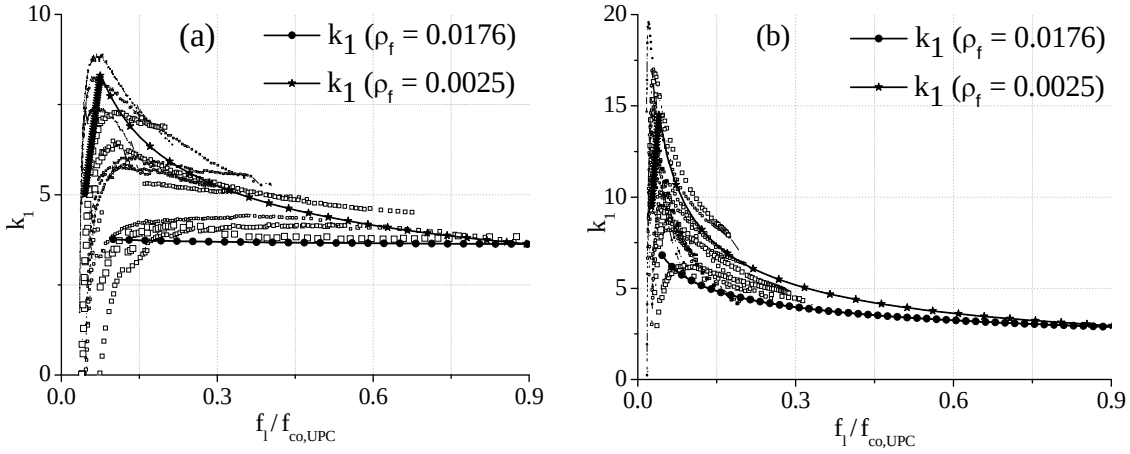

Figure 4.7: Variation of k_1 with $f_l / f_{co,UPC}$ for (a) G1 and (b) G2 group of tests. Note: all the square points are obtained from the experimental results.

The variation of k_2 with ε_f, derived from the experimental results using Eq. (4.11), $k_2 = (\varepsilon_c / \varepsilon_{co,UPC} - 1)/(f_c / f_{co,UPC} - 1)$, is represented in Figure 4.8. This figure shows that k_2 has an exponential increase with the increase of ε_f. A tendency for an increase of k_2 with the decrease of the concrete compressive strength is also apparent. Adopting the strategy of attributing markers of a size proportional to ρ_f, this figure shows that, regardless the

concrete strength class, k_2 is as high as low is ρ_f. The variation of k_2 was calculated for each figure, depending on $f_{co,UPC}$ and ρ_f, and later merged using mathematical tools. Based on the obtained results, the equations (4.20) and (4.21) were obtained:

$$k_2 = D_{k_2}(\varepsilon_l)^{E_{k_2}} \tag{4.20}$$

$$D_{k_2} = \frac{\left(7.2 - 0.05 f_{co,UPC}\right)}{16\rho_f},\ E_{k_2} = \left(0.49 - 0.0025 f_{co,UPC}\right)\rho_f^{-1.3} \tag{4.21}$$

The concrete tangential modulus, $E_c(\varepsilon_c)$, is derived from the chain derivative rule (see Eq. (4.22)):

$$E_c(\varepsilon_c) = \frac{\partial f_c}{\partial \varepsilon_f}\frac{\partial \varepsilon_f}{\partial \varepsilon_c} \text{ for } \varepsilon_{cQ} \le \varepsilon_c \le \varepsilon_{cu} \text{ (zone III)} \tag{4.22}$$

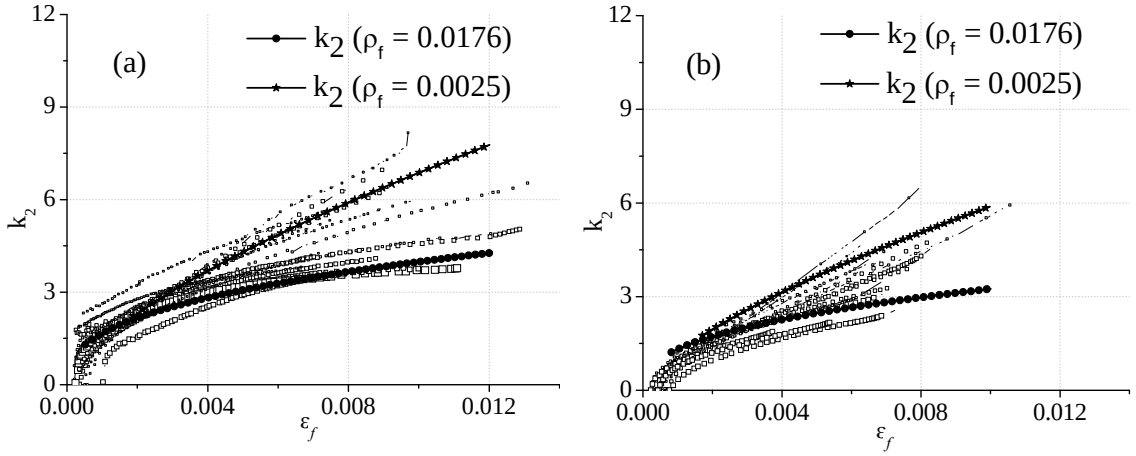

Figure 4.8: Variation of k_2 with ε_l for (a) G1 and (b) G2 group of tests. Note: all the square points are obtained from the experimental results.

4.3.2 Hysteretic scheme

The proposed compressive hysteretic scheme is shown in Figure 4.6: (i) complete unloading ($A \to B$); (ii) complete reloading ($B \to C \to D$); (iii) partial unloading with complete reloading ($A \to B' \to C' \to D'$); (iv) complete unloading with partial reloading ($A \to B \to E'$); and, (v) random loading ($A \to B' \to E'' \to F''' \to E''' \to J$). Complete unloading here refers to unloading from the envelope curve until zero stress; similarly,

complete reloading refers to reloading up to the envelope curve and; partial unloading/reloading refers to all the other possible unloading/reloading cycles that do not fall into the above categories. In chapter 2, it was verified that the parameters required for modelling of cyclic curves are plastic strain, shift in strain and stress, and secant stiffness. In this section all this parameters are calculated using the experimental data. If ε_{cun} is the unloading strain and f_{cun} its corresponding unloading stress on the envelope curve (Figure 4.9), then unloading from this point (ε_{cun}, f_{cun}), with reversal slope E_{cun} (= E_{ci}, point A in Figure 4.9), will target the point B (ε_{cpl}, 0), with target slope E_{cpl} (point B in Figure 4.9), where ε_{cpl} is the plastic strain and E_{cpl} is the tangential modulus of unloading curve at ε_{cpl} that can be determined from Chang and Mander [14]:

$$E_{\text{cpl}}=0.1E_{ci}\exp\left(-2\left|\frac{\varepsilon_{cun}}{\varepsilon_{co,UPC}}\right|\right) \tag{4.23}$$

In the CFRP-based confined specimens, the degradation of the stiffness of the unloading branches (E_{csecu}), during the axial deformation of the specimen, was not so pronounced than in UPC specimens, since CFRP confinement arrangements avoid concrete spalling and the buckling of the longitudinal bars. Normalized unloading secant (E_{csecu}/E_{ci}) *versus* normalized unloading strain ($\varepsilon_{cun}/\varepsilon_{cu}$) is plotted in Figure 4.10 using the obtained experimental data. The following equation for E_{csecu} was determined, considering the lower bound of the analyzed data:

$$\begin{aligned} &E_{\text{csecu}}=E_{ci} \text{ for } 0\le\varepsilon_{cun}\le 0.032\varepsilon_{cu} \\ &E_{\text{csecu}}=0.38E_{ci}\left(\frac{\varepsilon_{cun}}{\varepsilon_{cu}}\right)^{-0.28} \text{ for } \varepsilon_{cun}>0.032\varepsilon_{cu} \end{aligned} \tag{4.24}$$

and the plastic strain is determined from Eq (4.25) (see Figure 4.5):

$$\varepsilon_{cpl}=\varepsilon_{cun}-\frac{f_{cun}}{E_{c\text{sec}u}} \tag{4.25}$$

The equations of the transition curve (see Appendix A) are used to join the initial point *A* and the target point *B* (see Table 4.5)**.** The initial point (x_o, y_o) with slope E_o of Appendix A is equivalent to $(\varepsilon_{ca}, f_{ca})$ with slope E_{ca} (see Table 4.5), respectively. Likewise, (x_f, y_f) and E_f of Appendix A are identical to $(\varepsilon_{cb}, f_{cb})$ and E_{cb}, respectively.

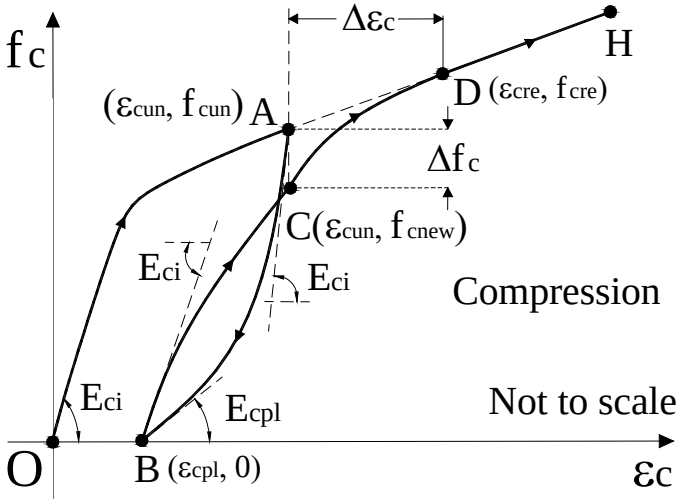

Figure 4.9: Schematic illustration of complete unloading and reloading.

One of the most commonly observed behaviour of confined concrete under a complete cycle is the shift in the strain and stress, represented in Figure 4.9 as $\Delta\varepsilon_c$ and Δf_c, respectively. It is to be noted that for the unloading strain (ε_{cun}), the reloading curve predicts new stress on reloading curve (point C, f_{cnew}), giving rise to Δf_c. Due to the difference in unloading and reloading stiffness, the reloading branch always joins the envelope curve at higher strain compared to the unloading strain on the envelope curve, giving rise to a strain shift, $\Delta\varepsilon_c$. A linear dependency between $\Delta\varepsilon_c$ and ε_{cun}, with a regression coefficient of 0.96, was obtained and described by Eq. (4.26):

$$\Delta\varepsilon_c = 0.19\ \varepsilon_{cun} \tag{4.26}$$

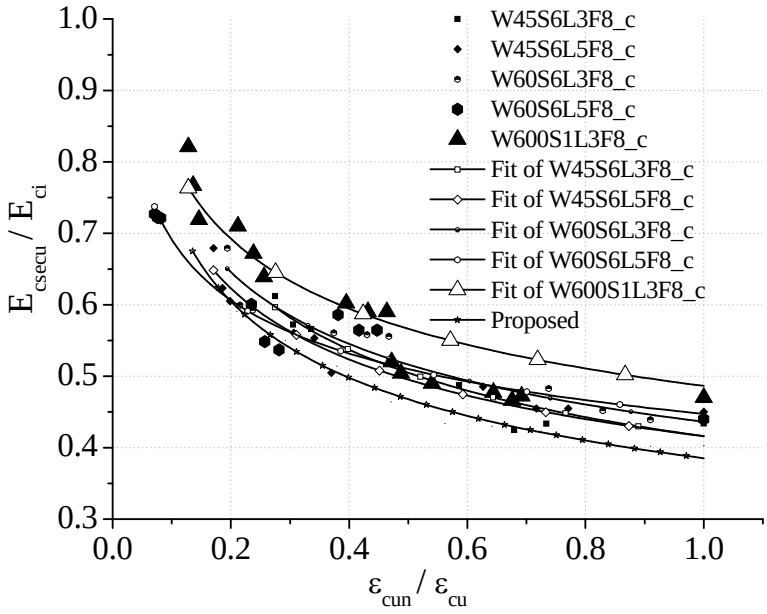

Figure 4.10: Variation of normalized secant with normalized axial strain.

Unlike to what happens in unconfined RC column elements subjected to cyclic loading, where the shift in stress, Δf_c, depends on the unloading strain of the envelope curve, Figure 4.11 shows that in CFRP confined concrete, Δf_c depends on the latest unloading strain, $\varepsilon_{cun,g}$. It should be noted that this unloading strain can lie on the envelope curve (the strain at point A for the $B'C'E''$ reloading branch, in Figure 4.6) or on a cyclic reloading branch (the strain at point E'' for the $F'''E'''J$ reloading branch, in Figure 4.6). If $f_{cun,g}$ represents a general unloading stress on either the envelope curve (corresponding to point A in Figure 4.6) or on partial reloading branch (corresponding to point E'' in Figure 4.6), and $\varepsilon_{cun,g}$ its corresponding strain on the respective branch, Figure 4.11 represents the relationship between the normalized stress shift ($\Delta f_c / f_{cun,g}$) and the normalized axial unloading strain ($\varepsilon_{cun,g} / \varepsilon_{cu}$), which can be simulated by the Eq. (4.27):

$$\Delta f_c = 0.14 f_{cun,g} \left(\left| \frac{\varepsilon_{cun,g}}{\varepsilon_{cu}} \right| \right)^{0.15} \tag{4.27}$$

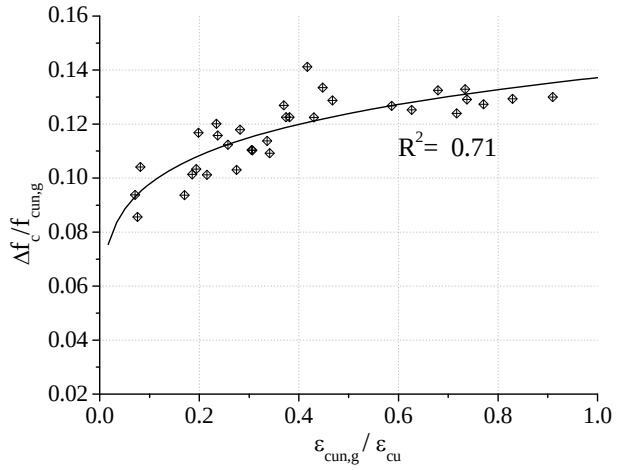

Figure 4.11: Variation of $\Delta f_c / f_{cun,g}$ with $\varepsilon_{cun,g} / \varepsilon_{cu}$.

The complete reloading curve is defined by three points and two connecting transition curves: the initial *B*, intermediate *C* and target *D* points (see Figure 4.9). The first transition curve connects point *B* (ε_{cpl}, 0), with a starting slope E_{ci}, to an intermediate point *C* ($\varepsilon_{cun}, f_{cnew}$) with slope E_{cnew} (see Table 4.5), where f_{cnew} and E_{cnew} are the stress on the reloading branch and its tangential Young's modulus, respectively, determined from:

$$f_{cnew} = f_{cun} - \Delta f_c \tag{4.28}$$

$$E_{cnew} = \frac{f_{cnew}}{\varepsilon_{cun} - \varepsilon_{cpl}} \tag{4.29}$$

Similarly, the second transition curve connects intermediate point *C* (ε_{cun}, f_{cnew}), with a slope E_{cnew}, to the return point *D* (ε_{cre}, f_{cre}), with a target slope E_{cre} (see Table 4.5), where f_{cre} and E_{cre} are the stress corresponding to the returning strain (ε_{cre}) and its tangential Young's modulus calculated on the envelope curve, respectively. The parameters required for the complete reloading are calculated from:

$$\varepsilon_{cre} = \varepsilon_{cun} + \Delta\varepsilon_c \tag{4.30}$$

$$E_{cre} = E_c\left(\varepsilon_{cre}\right) \tag{4.31}$$

$$f_{cre} = f_c\left(\varepsilon_{cre}\right) \tag{4.32}$$

After a partial unloading ($A \to B'$) a partial or a complete reloading can occur. Irrespective of being a partial or a complete reloading, a modified intermediate point $C'(\varepsilon_{cun}, f^*_{cnew})$ and a returning point $D'(\varepsilon^*_{cre}, f^*_{cre})$ is calculated, based on the history of partial unloading (see Figure 4.12). The modified reloading strain (ε^*_{cre}) is assumed to exist between the envelope unloading strain (ε_{cun}) and the envelope reloading strain (ε_{cre}) for the complete unloading ($A \to B$) and complete reloading ($B \to D$) branches. Similarly, a modified intermediate stress (f^*_{cre}) is assumed to exist between the envelope unloading stress (f_{cun}) and the intermediate stress (f_{cnew}) for complete unloading and complete reloading branches.

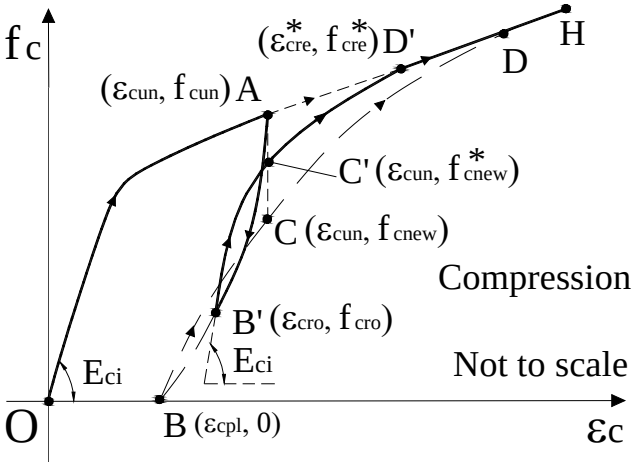

Figure 4.12: Schematic illustration of partial unloading and reloading.

Linear interpolation is used for the determination of the ε^*_{cre} and f^*_{cnew},

$$f^*_{cnew} = f_{cun} - \Delta f_c \frac{\varepsilon_{cun} - \varepsilon_{cro}}{\varepsilon_{cun} - \varepsilon_{cpl}} \tag{4.33}$$

$$E^{*}_{cnew} = \frac{f^{*}_{cnew} - f_{cro}}{\varepsilon_{cun} - \varepsilon_{cro}} \tag{4.34}$$

$$\varepsilon^{*}_{cre} = \varepsilon_{cun} + \Delta\varepsilon_{c} \frac{\varepsilon_{cun} - \varepsilon_{cro}}{\varepsilon_{cun} - \varepsilon_{cpl}} \tag{4.35}$$

$$E^{*}_{cre} = E_{c}\left(\varepsilon^{*}_{cre}\right) \tag{4.36}$$

where ($\varepsilon_{cro}, f_{cro}$) refers to the reversal point B' (see Figure 4.12) located on the unloading curve, and f^{*}_{cre} and E^{*}_{cre} are calculated on the envelope curve. The transition curves are used to join B' to C', and C' to D' (see Table 4.5). In case of the loading path $A \rightarrow B \rightarrow E' \rightarrow F'$, a partial reloading ($B \rightarrow E'$) is followed by an unloading ($E' \rightarrow F'$) branch. It should be noted that the plastic strain (ε_{cpl}) and its corresponding plastic modulus (E_{cpl}) are dependent only on the unloading strain of the envelope curve (Eqs (4.23) to (4.25)). From the experimental investigation it was found that for partial reloading ($B \rightarrow C \rightarrow E'$), the unloading branch $E' \rightarrow F'$ does not target the previous plastic strain (strain at point *B*). Hence, an imaginary unloading strain is assumed to exist between the previous envelope unloading strain (ε_{cun}, corresponding to point A) and the envelope reloading strain (ε_{cre}, corresponding to point D). A new unloading strain, ε^{*}_{cun}, is defined on the envelope curve (see point I, Figure 4.13) adopting a linear interpolation, which becomes the representative of the unloading strain (on envelope curve) for future responses, and is determined from Eq (4.37):

$$\varepsilon^{*}_{cun} = \varepsilon_{cun} + \left(\frac{\varepsilon_{ce'} - \varepsilon_{cun}}{\varepsilon_{cre} - \varepsilon_{cpl}}\right)\left(\varepsilon_{cre} - \varepsilon_{cun}\right) \tag{4.37}$$

where $\varepsilon_{ce'}$ is the strain corresponding to E' on the reloading branch ($B \rightarrow E'$). The newly calculated unloading strain on the envelope curve (ε^{*}_{cun}, corresponding to point I) is used to calculate the new plastic strain ε^{*}_{cpl} (point F') and the new plastic modulus E^{*}_{cpl} using Eqs (4.23) to (4.25). The transition curve is used to connect the points E' and F' (see Table 4.5), where $f_{ce'}$ is the stress corresponding to $\varepsilon_{ce'}$ on the reloading branch ($B \rightarrow E'$).

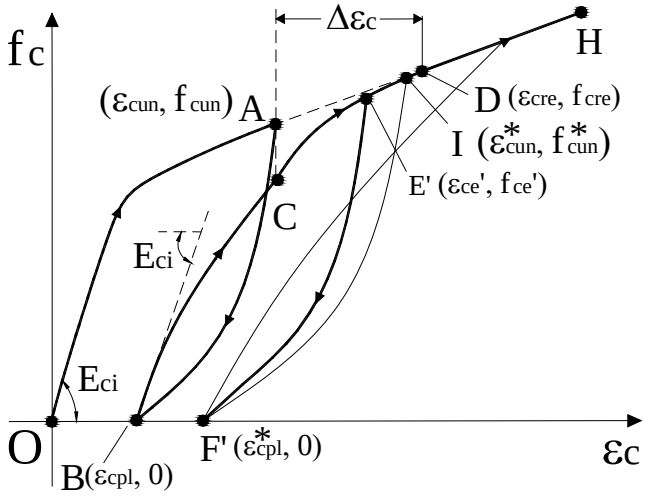

Figure 4.13: Schematic illustration of partial loops.

Once the unloading branch $E' \rightarrow F'$ is initiated, the previous unloading strain (ε_{cun}) on the envelope curve is replaced by the newly calculated unloading strain on the envelope curve (ε^{*}_{cun}).

For a general loading path, illustrated by $A \rightarrow B' \rightarrow E'' \rightarrow F''' \rightarrow E''' \rightarrow J$ (see Figure 4.6), once first reloading starts, the modified envelope reloading strain (ε^{*}_{cre}, corresponding to point D') is calculated for the branch $B' \rightarrow E''$ (same path as $B' \rightarrow D'$) using Eq. (4.35). The calculated reloading strain (ε^{*}_{cre}) on the envelope curve is used to decide the subsequent unloading paths ($E'' \rightarrow F'''$ or $E'' \rightarrow F$), until a new reloading branch ($F''' \rightarrow E'''$) is initiated. For the branch $E'' \rightarrow F'''$, an unloading strain is calculated on the envelope curve using Eq. (4.37). In this equation the previously calculated modified reloading strain is used. A transition curve similar to $E' \rightarrow F'$ is used to simulate the branch that connects the points E'' and F'''. For the reloading branch $F''' \rightarrow E'''$, it should be noted that the intermediate point E''' is calculated using Eq. (4.27), and the considered unloading stress and strain correspond to point E''. The branch $F''' \rightarrow E'''$ is similar to branch $B' \rightarrow C'$, except the calculation of the intermediate point. When the reloading branch $F''' \rightarrow E'''$ is extended up to the returning point J on envelope curve, point J is calculated using previously calculated (modified) unloading strain on the envelope curve (from Eq. (4.37)).

4.4 MODEL APPRAISAL

4.4.1 Simulation of experimental program at Minho University

A fibre model (described in Chapter 5) with the cyclic constitutive laws for CFRP confined concrete described in the previous section was implemented into FEMIX computer program, which is based on the finite element method (FEM). The constitutive model developed by Chang and Mander (1994) for the simulation of the cyclic behaviour of steel bars was also implemented into FEMIX.

4.4.1.1 Monotonic loading tests

The cylindrical RC column elements tested by Barros *et*. al (2007b) were numerically simulated using the values of the material properties included in Table 4.2 and Table 4.3 (see also Figure 4.1). The constitutive model of the steel bars was defined using the values included in Table 4.4. Along its longitudinal direction, a column is discretized with three FE of three nodes each, and two Gauss integration points per element were considered for the evaluation of the stiffness matrix and internal forces. In its longitudinal direction the three FE were discretized in 48 concrete fibres and 4 steel fibres. The cross section of a fibre was represented by eight nodded quadrilateral finite element. A 2×2 Gauss integration scheme was used for the calculation of the stiffness and internal equivalent nodal forces at the level of fibre cross section. The steel bars were assumed to be perfectly bonded and embedded into the confined concrete. The diameter of the steel hoops (d_{st}, see Figure 4.1) was 160 mm. The confinement provided by steel hoops was not explicitly considered in the FE model, but was indirectly considered in the constitutive model by Eqs. (4.12), (4.14) and (4.16). Figure 4.14 (a) and (b) shows that the implemented model was able to simulate, with high accuracy, the RC column elements subjected to monotonic loading.

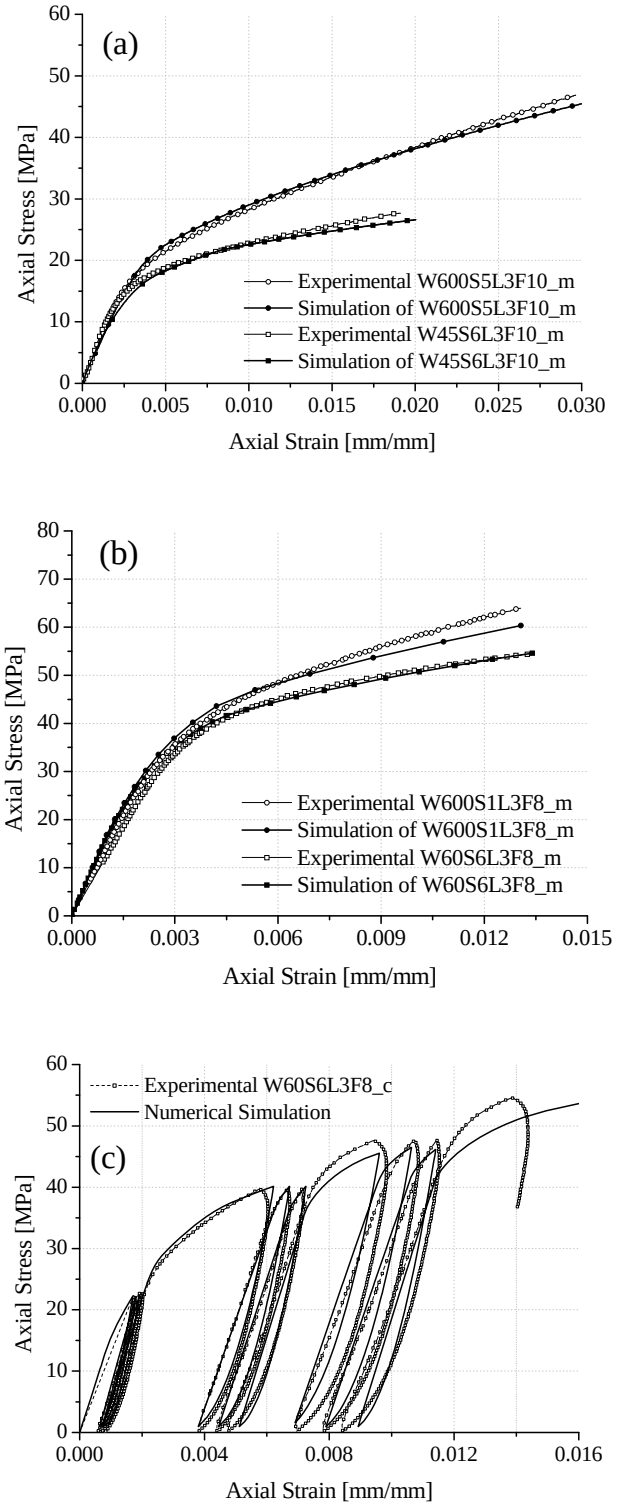

Figure 4.14: Numerical and experimental results for specimens from groups: (a) G1, (b) G2 and (c) G3.

4.4.1.2 Cyclic loading tests

The values of the model parameters used for the simulation of W60S6L3F8_c column are included in Table 4.1, Table 4.4 and Table 4.5. This column was discretized in exactly the same manner as in the case of the simulations of the monotonic loading tests. Figure 4.14(c) shows that the model used for the prediction of the hysteretic behaviour of CFRP-based confined RC columns is capable to simulate satisfactorily the deformational behaviour experimentally recorded.

4.4.2 Simulations of tests carried out by other researchers

An independent monotonic series (Li *et al.* 2003) and two cyclic series (Lam *et al.* 2006) were considered to appraise the model performance. Li *et al.* (2003) considered circular specimen of 300 mm high and 150 mm diameter. The data corresponding to the specimen is illustrated in Table 4.6. The cylindrical specimen was discretized in three 100 mm length of three nodded finite elements, each one was divided in 48 fibres in its longitudinal direction. For the calculation of the stiffness and internal forces, a 2×2 Gauss integration scheme was used for each fibre cross-section, and 2 Gauss points were used for the finite element in its longitudinal direction. The compressive cyclic loading tests performed by Lam *et al.* (2003) were also simulated by the developed constitutive model. The data available in the work of Lam *et al.* (2006), included in Table 4.6, was used in the performed numerical simulations. The discretization and the integration scheme used in case of monotonic simulations were also adopted for the specimens subject to cyclic loading. The simulations were carried out up to the end of the measured experimental strain.

Table 4.6: Experimental data used in the numerical simulation

Specimen name	W [mm]	L [mm]	S [mm]	t_f [mm]	D [mm]	H [mm]	E_f [GPa]	ρ_f	$f_{co,UPC}$ [MPa]	$\varepsilon_{co,\ UPC}$ [mm/m]
Li et al. (A)	300	1	1	0.138	150	300	232	0.0073	17.2	2.00
Lam et al. (A)	305	1	1	0.165	152	305	250	0.0043	41.1	2.56
Lam et al. (B)	305	2	1	0.165	152	305	250	0.0087	38.9	2.50

(a)

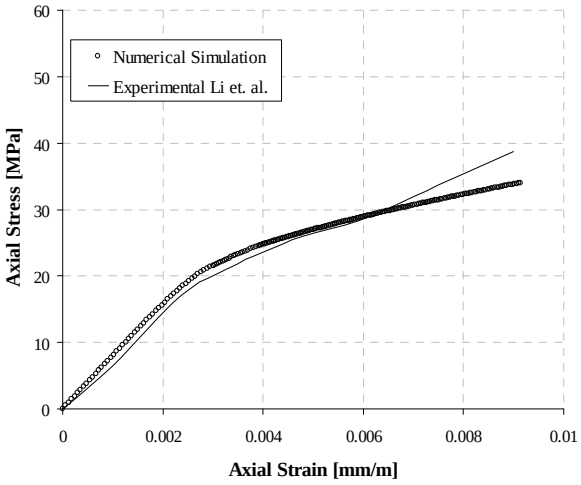

(b)

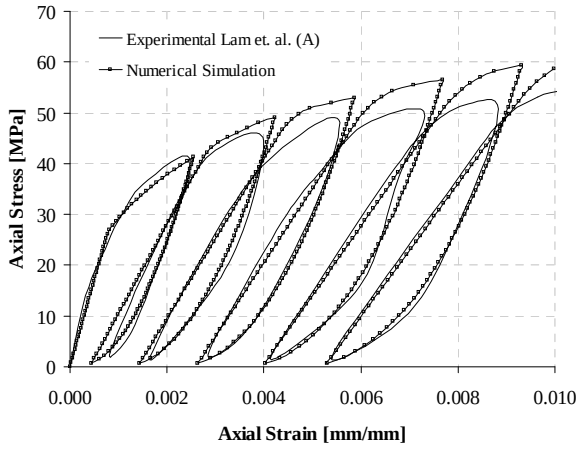

(c)

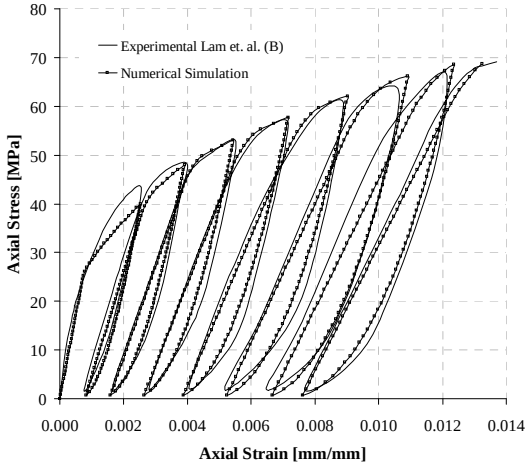

Figure 4.15: Numerical and experimental results for (a) Li *et al.* (b) Lam *et al.* (A), and (c) Lam *et al.* (B).

The numerical and experimental stress–strain curves for monotonic and cyclic analysis are compared in Figure 4.12, from which it can be concluded that the model is able to predict the response with a very good agreement.

4.5 SUMMARY

In the present chapter a constitutive model to simulate the monotonic and the cyclic behaviour of CFRP-based RC columns submitted to axial compressive loading was developed. The concrete columns can be totally or partially wrapped with wet lay-up CFRP sheets. The carried out tests showed that the stress-strain curves of the monotonic loading tests can be regarded as the envelope of the stress-strain curves of the homologous cyclic loading tests. The monotonic stress-strain curve was composed of three branches. The first one having a linear relationship between strain and stress is governed by the characteristics of the concrete and conventional reinforcement. The third branch, with a smooth nonlinearity of the stress-strain relationship, is governed by the characteristics of the CFRP confinement arrangement. Finally, the second branch, which assures a continuous connection between the former and the later branches, has a pronounced nonlinearity and is affected by the properties of the concrete, conventional reinforcement and CFRP confinement arrangement. The model herein proposed is capable to predict the stress-strain response of any arbitrary loading path. In fact, the deterioration in terms of load carrying capacity and stiffness caused by the unloading/reloading cycles was simulated adequately, taking into account relevant data derived from the experimental tests. A stress-strain nonlinear relationship was used to simulate both the unloading and reloading branches, in agreement to the results observed in the experimental tests. The model was able to simulate, with high accuracy, the tests carried out by distinct researchers.

CHAPTER 5

Fibre model

5.1 INTRODUCTION

The response of RC structures to earthquake motion depends on combination of factors, such as soil type, structure and earthquake characteristics. The structure may behave elastically for small magnitude earthquakes, but in case of regions of high seismic risk, during the occurrence of moderate or strong ground motion the structures may not respond elastically. Hence to predict the response of a structure to earthquake, accurate determination of material and structural properties of a RC element is the foremost step. Researchers have proposed tests to characterise the basic materials or tests at scale models for the RC structures. A complex interaction between the components (like beams, columns, slabs, etc.) of a structure exists; hence the failure of a structure due to dynamic loading cannot be numerically predicted reliably by tests on components of scale models only (Taucer *et* al. 1991, Spacone *et* al. 1992). At the same time such tests are expensive and are time consuming. To minimize such costs, the components of a structure are tested under monotonic and cyclic loadings, which are later used in calibration and development of models that permit the application of the limited test data to other similar types of structures (Fillipou and Issa 1998). Based on the level of load application and decomposition of structure (mesh refinement and topology), the available FE models can be categorized in three categories namely: global models, discrete member models and microscopic finite element models.

In case of global models, mostly, the aim is to predict approximate force deformation response, hence the some of the degree of freedoms are neglected and the response of the

structure is assumed to be derived from selected degree of freedom. For example, to estimate the inter-storey drifts for multi-storey frame, each floor is assigned only one lateral degree of freedom located at centroid of each floor and the rest of degree of freedom are neglected into analysis. Hence the accurate prediction of internal forces of beam or columns elements located in frame is not possible. However in discrete finite element models the structure is assumed to be an assembly of finite elements like frame element, plane stress element, etc. These finite elements behave non-linearly at their level by imposition of constitutive nonlinearity at element level or at section level. For example to analyse the same example described above by discrete method, each floors is analysed by plane stress element and extra degrees of freedom are assigned for the analyses. Moreover column and beams are also assigned degree of freedom similar to a independent frame element. The complexity of model increases in this case compared to global models. However in case of microscopic models the sections of frame elements are further discretized and assigned extra degrees of freedom at level of cross-section. These types of analysis are helpful to predict the bond deterioration, crack propagation and other types of physical nonlinearities. A brief resume of the evolution of fibre element approach from discrete models is described, before describing in detail the fibre model implemented in the ambit of present thesis.

The initial approaches of modelling nonlinear dynamic behaviour of frame elements assumed formation of zero length plastic hinges located at the member ends. Theses plastic hinges were represented by several nonlinear springs connected in series or in parallel. Clough and Johnston (1967) formulated the beam element by two parallel springs, one elastic-perfectly plastic and other perfectly plastic to generate a bilinear moment rotation relation. The stiffness matrix for the member is the sum of the stiffness of these components. Giberson (1967) introduced a model based on series of springs, consisting of one linear elastic spring and one nonlinear rotational spring attached at each end of the element. The inelastic deformations were *lumped* at the end using these springs, hence these models are also known as lumped plasticity models (see Figure 5.1). This model was superior compared to Clough and Johnston (1967), as it was able to characterise hysteretic behaviour by using the appropriate rotational springs. Later, several researchers have proposed models based on lumped plasticity, to emphasize critical effects like cyclic stiffness degradation (Takeda *et* al. 1970, Brancaleoni *et* al. 1983), pinching (Banon *et* al.

1981) and bar pull-out at beam-column joint interface (Filippou and Issa 1988). But most of these models were not generic in nature; they were mostly suitable for only limited types of problems.

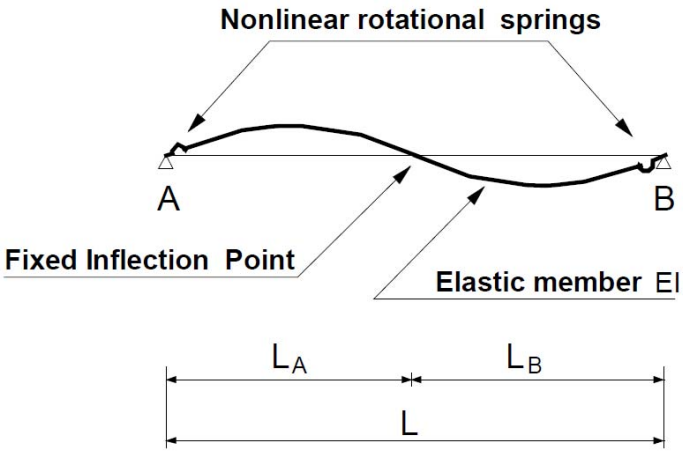

Figure 5.1:Simple lumped plasticity model (adapted from Giberson 1967)

Principally, as the structure is loaded beyond elastic deformations, the non-linear behaviour spreads gradually from high stress region to low stress region; however after induction of certain level of damage at critical sections, the damage starts accumulating at this regions and partially releasing the stresses of other zones. But in lumped models, the cause of inelastic behaviour is assumed to be concentrated for the purpose of simplification. Because of their over simplification of certain aspects of hysteretic behaviour, they find limited application. Later, Taucer *et* al. (1991) proposed the flexibility based finite element formulation for frame element using fibre approach. More recently various researchers (Chang and Mander 1994, Spacone *et* al. 1996a-b, Legeron and Paultre 2005) have applied the same fibre model, based on different solvers and various constitutive models, for seismic analysis.

In the next section implementation of fibre element method is described. The uniaxial constitutive laws described in chapter 2 are used and the performance of the fibre element will be appraised by suitable examples.

5.2 IMPLEMENTATION OF FIBRE ELEMENT IN FEMIX

The implemented model will serve as a base for estimation of the behaviour of frame elements using Timoshenko theory. A displacement based finite element approach is followed due to its easy implementation in FEMIX, contrary to the force based or hybrid methods. Fibre approach is derived from the fact that, if constituted by distinct material types, the cross-section is divided in fibres. These fibres need not be of equal area or same shape.

5.2.1 Fibre element concepts

The implementation of fibre model in the existing Timoshenko beam in the FEMIX can be divided in two major steps, namely calculation of stiffness matrix and calculation of equivalent internal nodal forces (Sena-Cruz 2005). The Timoshenko beam element for linear elastic material is described elsewhere (Ventura-Gouveia 2000, Varma *et* al. 2007), however only nonlinear analysis of frame element under Timoshenko frame work is discussed here. The detailed description of nonlinear finite element methods can be found elsewhere (Zienkiewicz and Taylor 1991, Bathe 1996).

The displacement based formulation of the finite element method leads to (Zienkiewicz and Taylor 1989):

$$\underline{K}\,\underline{a} = \underline{F} \tag{5.1}$$

where $\underline{K}$ is the stiffness matrix, $\underline{a}$ is the vector of the nodal displacements and $\underline{F}$ is the vector of the nodal forces that are equivalent to the loads acting on the finite element. The stiffness matrix is estimated as:

$$\underline{K} = \int_V \underline{B}^T \underline{D}\underline{B} dV \tag{5.2}$$

where, $\underline{D}$ is the constitutive matrix, $\underline{B}$ is a matrix that depends on the finite element type and respective shape functions, and V is the volume of the finite element. In finite element programs the Gaussian and Newton-Cotes integration schemes are adopted to evaluate the integral function of (5.2) in predefined integration points.

In the context of nonlinear analysis, the stiffness matrix depends on the values of the displacements, $\underline{a}$. In this case the load is applied in small steps and the solution is achieved by solving the system of nonlinear equations, using Newton-Raphson method. A detailed description of the method available in FEMIX can be found elsewhere (Sena-Cruz 2005)

When RC frame structure is analyzed by Timoshenko theory, the cross section can be constituted by distinct cement based and epoxy based materials, and can include steel and FRP reinforcements. For this simulation, the cross section of each element is discretized with 4-noded quadrilateral elements representing each a longitudinal fibre (see Figure 5.2). The geometry of the cross section of each fibre can vary along the beam element. The material model may vary from fibre to fibre thus allowing for the consideration of non constant concrete properties in the cross section (e.g., unconfined and confined concrete).

The stiffness matrix of the element, $K^{(e)}$, is the sum of the stiffness of all the fibres (e.g., the concrete fibres and steel fibres) composing the beam element. The stiffness contribution of theses fibres depends on the mechanical behaviour and, indirectly, on the location of fibre in the cross-section. The stiffness matrices for the fibres are composed of the tangential stiffness derived from the corresponding nonlinear constitutive laws. For the same constitutive material law, the strain in each fibre will be different based on their position, so the contribution to the element stiffness matrix will also depend on the geometric position of the fibre.

Figure 5.2 (a) represents a generic three dimensional frame element, whose size of cross section is varied and twisted along its longitudinal axis. The same frame element is discretized in three nodded finite element, and the cross-section is further divided in fibres. In Figure 5.2(a), the local axis of the frame element is represented by l_1, which is tangential to the axis of beam, while l_2 and l_3 represent the other perpendicular axis in the cross-section plane. In Figure 5.2(a)-(b) the focus is to illustrate the rotation of cross-section and variation in its size with respect to Global Coordinate System (GCS). The forces and moments acting on the section are represented by, axial force, N_1^l, shear forces, V_2^l and V_2^l, torsion, M_1^l and bending moments, M_2^l and M_3^l. In Figure 5.2(b), the generic force vector is represented in GCS, where F_i^g and M_i^g are force and moment in *i*

direction (i =1, 2, 3). Schematic diagram of the Timoshenko frame element is represented in Figure 5.2(c) with the LCS (local coordinate system) for the calculation of stiffness and internal equivalent nodal forces. The discretization of the cross-section is represented in Figure 5.2(d) and is also used to evaluate the stiffness and internal equivalent nodal forces in the LCS.

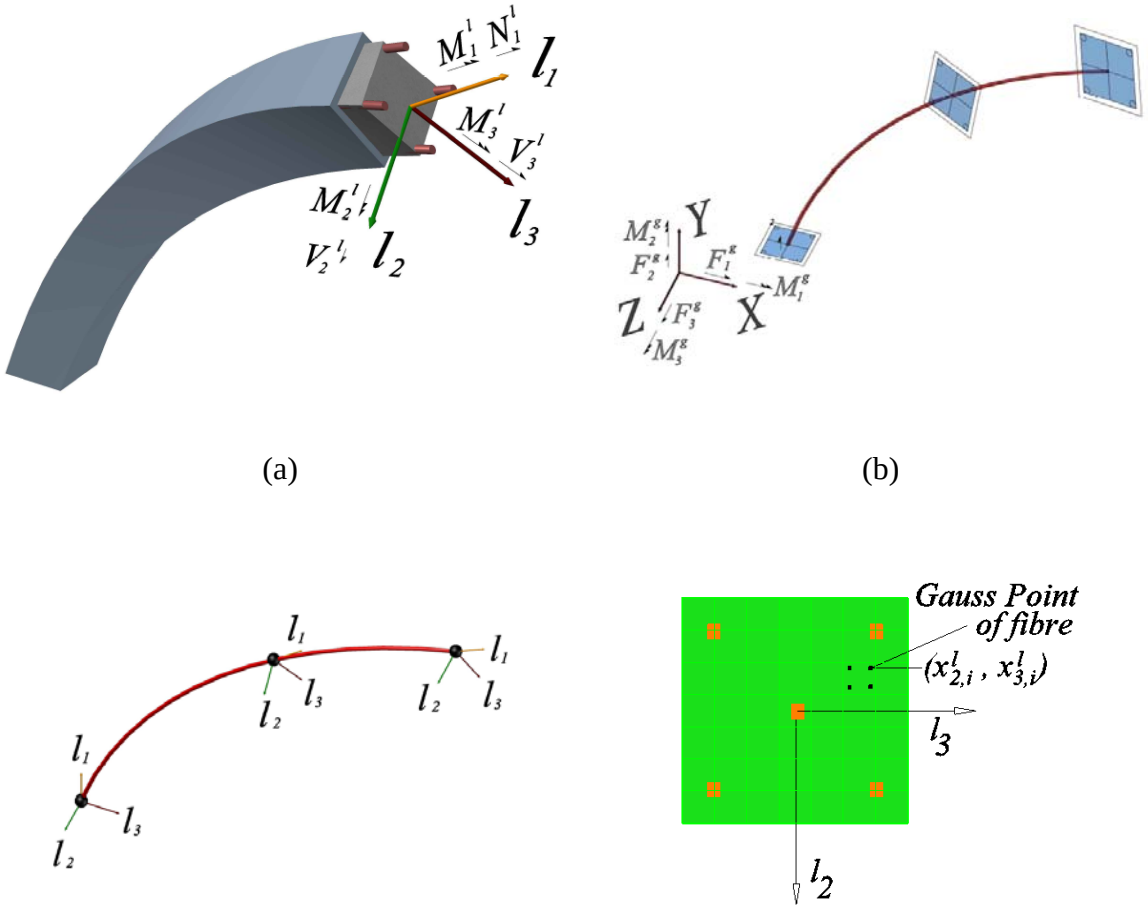

Figure 5.2: (a) Twisted frame element (b) 3D Timoshenko element in global coordinate system (GCS) with rotating cross-sections along the axis of beam (c) 3D Timoshenko frame element in local coordinate system (LCS) (d) Discretization of cross section into longitudinal fibres.

5.2.2 Stiffness matrix

For the fibres represented in Figure 5.2(d), the incremental stress-strain ($\Delta\underline{\sigma} - \Delta\underline{\varepsilon}$) can be described as:

$$\Delta\underline{\sigma} = \underline{D}_T \Delta\underline{\varepsilon} \tag{5.3}$$

where $\underline{D}_T$ corresponds to the tangent constitutive matrix that describes the behaviour of the material along its deformational process.

The calculation of the stiffness matrix is schematically described in Figure 5.3 and summarized in the following steps:

- Evaluation of the displacements ($\underline{U}$) at the integration points (sampling points) of the 3D element from extrapolating the nodal displacements;
- Calculation of the strains ($\underline{\varepsilon} = (\varepsilon_a \quad \underline{\varepsilon}_s \quad \varepsilon_t \quad \underline{\varepsilon}_b)^T$) at each sampling point of the fibre, where ε_a, $\underline{\varepsilon}_s$, ε_t, $\underline{\varepsilon}_b$ represent the axial, shear, torsion and strain components (it is to be noted that the sampling point of frame element is different from sampling points of the section fibres);
- Calculation of the tangent constitutive matrix ($\underline{D}_T$) at the level of each sampling point of the section, using the constitutive law of the fibre;
- Calculation of the stiffness matrix for the element (e) by assembling the contribution of the stiffness of each fibre of the section.

Taking into account the complete fibre discretization (see Figure 5.2), the element tangent stiffness matrix, $\underline{K}_T^{(e)}$, can be obtained from the sub-matrices associated to the axial deformations, $\underline{K}_a^{(e)}$, axial-bending and bending-axial deformations, $\underline{K}_{ab}^{(e)}$ and $\underline{K}_{ba}^{(e)}$, bending deformations, $\underline{K}_b^{(e)}$, torsion deformations, $\underline{K}_t^{(e)}$, shear deformations, $\underline{K}_s^{(e)}$, and shear-torsion and torsion-shear deformations, $\underline{K}_{st}^{(e)}$ and $\underline{K}_{ts}^{(e)}$. The matrices are described briefly in the following sections with an emphasis to the application of concrete and steel fibres. These two types of materials are highlighted since concrete fibres have stiffness components corresponding to shear-torsion and torsion-shear, however steel fibres don't have these stiffness components.

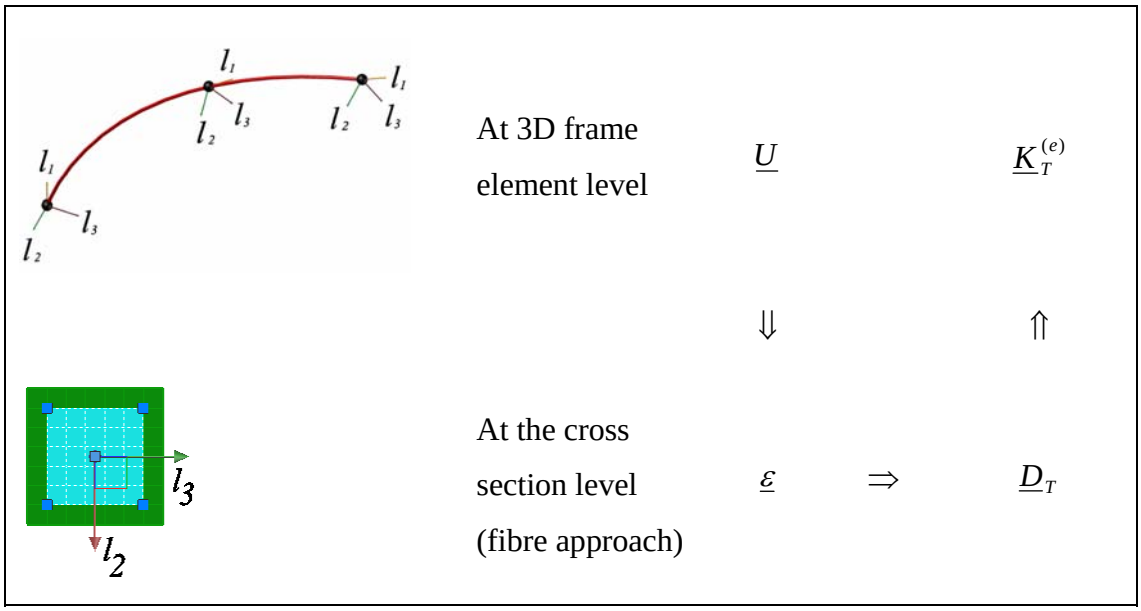

Figure 5.3: Scheme to obtain the tangent stiffness matrix of a 3D Timoshenko element.

5.2.2.1 Contribution of the concrete for the stiffness matrix

When material behaviour is not symmetric at the cross section level, the axial deformability can generate axial forces and bending moments and, curvature can generate bending moments and axial forces (see Figure 5.4(a)); for similar reasons shear deformations can generate shear forces and torsional moments and torsion can generate torsional moments and shear forces (see Figure 5.4(b)). In the Figure 5.4(a), a general fibre has axial deformation, $(\varepsilon_x)_i$, and due to this bending moments (M_y and M_z) and axial force (F_x) is generated, a similar case exist for curvature too. In the Figure 5.4(b), the same fibre is provided shear deformation in both directions ($(\gamma_{xz})_i$ and $(\gamma_{xy})_i$), which in turn contribute to torsional moment (M_x) and shear forces in both direction (F_y and F_z). Hence during nonlinear analysis, to take into account the effect, extra sub-stiffness matrix are evaluated for terms related to axial-bending, bending-axial, shear-torsion and torsion-shear interaction. These stiffness contributions are described in Eqs. (5.4) to (5.7). The equations are described in context of steel and concrete fibres, in later section.

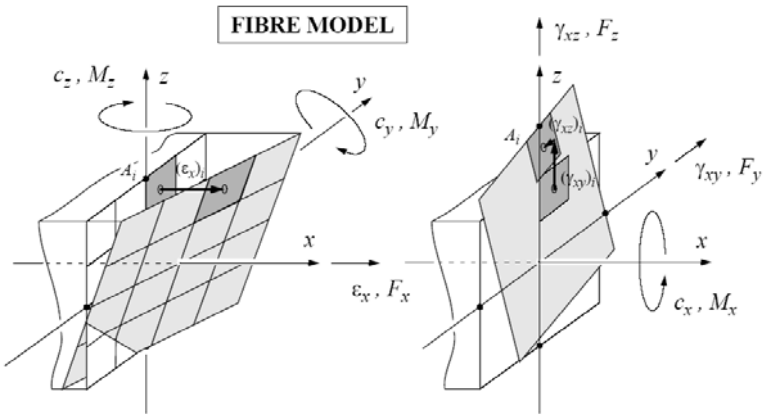

(a) (b)

Figure 5.4: (a) Axial- bending interaction (b) Shear-torsion interaction (adapted from Miranda-Guedes, 1997).

$$\underline{K}_{ab}^{(e)} = \int_{L^{(e)}} \underline{T}_a^{\lg} \underline{B}_a^T \hat{\underline{D}}_{ab} \underline{B}_b \left[\underline{T}_b^{\lg}\right]^T dL \tag{5.4}$$

$$\underline{K}_{ba}^{(e)} = \int_{L^{(e)}} \underline{T}_b^{\lg} \underline{B}_b^T \hat{\underline{D}}_{ba} \underline{B}_a \left[\underline{T}_a^{\lg}\right]^T dL \tag{5.5}$$

$$\underline{K}_{st}^{(e)} = \int_{L^{(e)}} \underline{T}_s^{\lg} \underline{B}_s^T \hat{\underline{D}}_{st} \underline{B}_t \left[\underline{T}_t^{\lg}\right]^T dL \tag{5.6}$$

$$\underline{K}_{ts}^{(e)} = \int_{L^{(e)}} \underline{T}_t^{\lg} \underline{B}_t^T \hat{\underline{D}}_{ts} \underline{B}_s \left[\underline{T}_s^{\lg}\right]^T dL \tag{5.7}$$

where, the subscripts *a*, *b*, *s* and *t* represent axial, bending, shear and torsion components, $L^{(e)}$ represents the length of element, while $\hat{\underline{D}}_{ij}$ (*i* and *j* is equal to either of *a*, *b*, *t*, *s*) represent the constitutive matrix for *i* and *j* interaction. $\underline{B}_i$ matrix is used to calculate the strain fields at sampling points from the corresponding displacements. $\underline{T}_i^{\lg}$ is transformation

matrix to convert entities from local to global coordinates and are described in detail elsewhere (Ventura-Gouveia 2000, Varma *et* al. 2007).

By applying the numerical integration method of Gauss-Legendre, the sub-matrices for stiffness can be found as shown below:

- *Sub-matrix associated to the axial deformation* ($\underline{K}_a^{\,c}$)

$$\underline{K}_a^{\,c} = \sum_{p=1}^{N_{s1}^{ab}} \left(\underline{T}_a^{\,\lg} \underline{B}_a^{\,T} \hat{\underline{D}}_a^{\,c} \underline{B}_a \left[\underline{T}_a^{\,\lg} \right]^T J \right)_{s_1^p} W_p \tag{5.8a}$$

$$\hat{\underline{D}}_a^c = \sum_{i=1}^{NG_{sec\,t}} D_{ab,i}^c A_{GP,i} \tag{5.8b}$$

where superscript *c* stands for parameters related to concrete; $NG_{sec\,t}$ represents the total number of sampling points in the section generated due to all fibres; $A_{GP,i}$ is the area at i^{th} sampling point. The number of sampling points located on Timoshenko frame element in l_1 direction, associated to the integration of the sub-matrices of axial, bending, axial-bending and bending-axial are same and equal to $N_{s_1}^{ab}$. $D_{ab,i}^c$ is the longitudinal tangential elasticity modulus at the level of i^{th} sampling point; *J* is the Jacobian matrix and W_p is the weight of p^{th} sampling point located on l_1 axis. The subscript s_1^p is used to represent the entities corresponding to p^{th} sampling point at the Timoshenko element level.

- *Sub-matrix associated to the bending deformation* ($\underline{K}_b^{\,c}$)

$$\underline{K}_b^{\,c} = \sum_{p=1}^{N_{s1}^{ab}} \left(\underline{T}_b^{\,\lg} \underline{B}_b^{\,T} \hat{\underline{D}}_b^{\,c} \underline{B}_b \left[\underline{T}_b^{\,\lg} \right]^T J \right)_{s_1^p} W_p \tag{5.9a}$$

$$\hat{\underline{D}}_b^c = \begin{bmatrix} \hat{\underline{D}}_{b,11}^c & \hat{\underline{D}}_{b,12}^c \\ \hat{\underline{D}}_{b,21}^c & \hat{\underline{D}}_{b,22}^c \end{bmatrix} = \sum_{i=1}^{NG_{sec\,t}} \begin{bmatrix} \underline{D}_{ab,i}^c (x_{3,i}^l)^2 A_{GP,i} & -\underline{D}_{ab,i}^c x_{2,i}^l x_{3,i}^l A_{GP,i} \\ -\underline{D}_{ab,i}^c x_{2,i}^l x_{3,i}^l A_{GP,i} & \underline{D}_{ab,i}^c (x_{2,i}^l)^2 A_{GP,i} \end{bmatrix} \tag{5.9b}$$

where $x_{2,i}^{l}$ and $x_{3,i}^{l}$ (see Figure 5.2(d)) are the local coordinates of the sampling point of the fibre with respect to the centroid of the section.

- *Sub-matrix associated to the axial-bending interaction* ($\underline{K}_{ab}{}^{c}$)

$$\underline{K}_{ab}{}^{c} = \sum_{p=1}^{N_{s1}{}^{ab}} \left(\underline{T}_{a}{}^{\lg} \underline{B}_{a}{}^{T} \hat{\underline{D}}_{ab}{}^{c} \underline{B}_{b} \left[\underline{T}_{b}{}^{\lg} \right]^{T} J \right)_{s_1^p} W_p \tag{5.10a}$$

$$\hat{\underline{D}}_{ab}^{c} = \left[\hat{\underline{D}}_{ab,11}^{c} \quad \hat{\underline{D}}_{ab,21}^{c} \right] = \sum_{i=1}^{NG_{sect}} \left[\hat{\underline{D}}_{ab,i}^{c} x_{3,i}^{l} A_{GP,i} \quad -\hat{\underline{D}}_{ab,i}^{c} x_{2,i}^{l} A_{GP,i} \right] \tag{5.10b}$$

- *Sub-matrix associated to the bending- axial interrelation* ($\underline{K}_{ba}{}^{c}$)

$$\underline{K}_{ba}{}^{c} = \sum_{p=1}^{N_{s1}{}^{ab}} \left(\underline{T}_{b}{}^{\lg} \underline{B}_{b}{}^{T} \hat{\underline{D}}_{ba}{}^{c} \underline{B}_{a} \left[\underline{T}_{a}{}^{\lg} \right]^{T} J \right)_{s_1^p} W_p \tag{5.11a}$$

$$\hat{\underline{D}}_{ba}^{c} = \begin{bmatrix} \hat{\underline{D}}_{ba,11}^{c} \\ \hat{\underline{D}}_{ba,21}^{c} \end{bmatrix} = \sum_{i=1}^{NG_{sect}} \begin{bmatrix} \hat{\underline{D}}_{ab,i}^{c} x_{3,i}^{l} A_{GP,i} \\ -\hat{\underline{D}}_{ab,i}^{c} x_{2,i}^{l} A_{GP,i} \end{bmatrix} \tag{5.11b}$$

It can be seen from Eq. (5.10b) that a fibre located at ($x_{2,i}^{l}$, $x_{3,i}^{l}$) with respect to centroid, generate bending moment, and hence these stiffness term are added to take into account this condition. Similarly, the curvature of a fibre located at ($x_{2,i}^{l}$, $x_{3,i}^{l}$), contribute to axial load, which can be taken into account by adding stiffness term for axial load by Eq. (5.11b). The same facts can be corroborated from Figure 5.4 (a).

- *Sub-matrix associated to the shear deformation* ($\underline{K}_{s}{}^{c}$)

$$\underline{K}_{s}{}^{c} = \sum_{p=1}^{N_{s1}{}^{st}} \left(\underline{T}_{s}{}^{\lg} \underline{B}_{s}{}^{T} \hat{\underline{D}}_{s}{}^{c} \underline{B}_{s} \left[\underline{T}_{s}{}^{\lg} \right]^{T} J \right)_{s_1^p} W_p \tag{5.12a}$$

$$\underline{\hat{D}}_s^c = \begin{bmatrix} \underline{\hat{D}}_{s,11}^c & \underline{\hat{D}}_{s,12}^c \\ \underline{\hat{D}}_{s,21}^c & \underline{\hat{D}}_{s,22}^c \end{bmatrix} = \sum_{i=1}^{NG_{sec\,t}} \begin{bmatrix} \underline{\hat{D}}_{st,i}^c A^*_{GP,i} & 0 \\ 0 & \underline{\hat{D}}_{st,i}^c A^*_{GP,i} \end{bmatrix} \tag{5.12b}$$

where, $D_{st,i}^c$ is the shear modulus of the concrete and $A_{GP,i}^* (=(5/6)A_{GP,i})$ is the reduced area of i^{th} sampling-point located on cross-section, while $N_{s1}{}^{st}$ is total number of sampling point located on l_1 axis for calculation of stiffness sub-matrices of shear, torsion, shear-torsion and torsion-shear components.

- *Sub-matrix associated to the torsional deformation* ($\underline{K}_t{}^c$)

$$\underline{K}_t{}^c = \sum_{p=1}^{N_{s1}{}^{st}} \left(\underline{T}_t{}^{\lg} \underline{B}_t{}^T \underline{\hat{D}}_t{}^c \underline{B}_t \left[\underline{T}_t{}^{\lg} \right]^T J \right)_{s_1^p} W_p \tag{5.13a}$$

$$\underline{\hat{D}}_t^c = \sum_{i=1}^{NG_{sec\,t}} D^c{}_{st,i} \left[(x_{3,i}^l)^2 + (x_{2,i}^l)^2 \right] A_{GP,i} \tag{5.13b}$$

- *Sub-matrix associated to the shear- torsion interrelation* ($\underline{K}_{st}{}^c$)

$$\underline{K}_{st}{}^c = \sum_{p=1}^{N_{s1}{}^{st}} \left(\underline{T}_s{}^{\lg} \underline{B}_s{}^T \underline{\hat{D}}_{st}{}^c \underline{B}_t \left[\underline{T}_t{}^{\lg} \right]^T J \right)_{s_1^p} W_p \tag{5.14a}$$

$$\underline{\hat{D}}_{st}^c = \begin{bmatrix} \underline{\hat{D}}_{st,11}^c \\ \underline{\hat{D}}_{st,21}^c \end{bmatrix} = \sum_{i=1}^{NG_{sec\,t}} \begin{bmatrix} -\underline{\hat{D}}_{st,i}^c x_{3,i}^l A_{GP,i} \\ \underline{\hat{D}}_{st,i}^c x_{2,i}^l A_{GP,i} \end{bmatrix} \tag{5.14b}$$

- *Sub-matrix associated to the torsion-shear interrelation* ($\underline{K}_{ts}{}^c$)

$$\underline{K}_{ts}{}^c = \sum_{p=1}^{N_{s1}{}^{st}} \left(\underline{T}_t{}^{\lg} \underline{B}_t{}^T \underline{\hat{D}}_{ts}{}^c \underline{B}s_s \left[\underline{T}_s{}^{\lg} \right]^T J \right)_{s_1^p} W_p \tag{5.15a}$$

$$\underline{\hat{D}}_{ts}^{c} = \left[\underline{\hat{D}}_{ts,11}^{c} \quad \underline{\hat{D}}_{ts,21}^{c} \right] = \sum_{i=1}^{NG_{sec\,t}} \left[-\underline{\hat{D}}_{ts,i}^{c} x_{3,i}^{l} A_{GP,i} \quad \underline{\hat{D}}_{ts,i}^{c} x_{2,i}^{l} A_{GP,i} \right] \tag{5.15b}$$

For the case of torsion-shear and shear-torsion interaction, (5.14b) and (5.15b) are used to generate extra stiffness term, which contribute for generated torsion and shear (see Figure 5.4(b)).

5.2.2.2 Contribution of the steel for the stiffness matrix

The sub-matrices for the steel fibres derived are similar to the concrete sub-matrices, except the number of sampling point assumed per fibre, which is one. The point to be noted is that the number of sampling points used at the level of frame element for calculation of stiffness matrix of concrete, ($\underline{K}^{c}$), should be same as used for calculation of stiffness matrix of steel, ($\underline{K}^{st}$). By knowing the location and the number of the steel fibres, and using the Gauss-Legendre integration technique the following sub-matrices can be found for the case of steel (or FRP) bars:

- *Sub-matrix associated to the axial deformation* ($\underline{K}_{a}^{st}$)

$$\underline{K}_{a}^{st} = \sum_{p=1}^{N_{s1}^{ab}} \left(\underline{T}_{a}^{\lg} \underline{B}_{a}^{T} \underline{\hat{D}}_{a}^{st} \underline{B}_{a} \left[\underline{T}_{a}^{\lg} \right]^{T} J \right)_{s_1^p} W_p \tag{5.16a}$$

$$\underline{\hat{D}}_{a}^{st} = \sum_{i=1}^{NS} D_{ab,n}^{st} A_{st,n} \tag{5.16b}$$

where NS is the number of steel fibres in the section, $A_{st,n}$ is the area associated with n^{th} steel fibre and $D^{st}{}_{ab,n}$ is tangential modulus of elasticity for the n^{th} steel fibre. It is to be noted that only axial deformation and its corresponding axial stress exist for the steel and FRP bars.

- *Sub-matrix associated to the bending deformation* ($\underline{K}_{b}^{st}$)

$$\underline{K}_b^{\,st} = \sum_{p=1}^{N_{s1}^{ab}} \left(\underline{T}_b^{\,\lg} \underline{B}_b^{\,T} \hat{\underline{D}}_b^{\,st} \underline{B}_b \left[\underline{T}_b^{\,\lg} \right]^T J \right)_{s_1^p} W_p \tag{5.17a}$$

$$\hat{\underline{D}}_b^{st} = \begin{bmatrix} \hat{\underline{D}}_{b,11}^{st} & \hat{\underline{D}}_{b,12}^{st} \\ \hat{\underline{D}}_{b,21}^{st} & \hat{\underline{D}}_{b,22}^{st} \end{bmatrix} = \sum_{i=1}^{NG_{sect}} \begin{bmatrix} \underline{D}_{ab,n}^{st} (x_{3,n}^l)^2 A_{st,n} & -\underline{D}_{ab,n}^{st} x_{2,n}^l x_{3,n}^l A_{st,n} \\ -\underline{D}_{ab,n}^{st} x_{2,n}^l x_{3,i}^l A_{st,n} & \underline{D}_{ab,n}^{st} (x_{2,n}^l)^2 A_{st,n} \end{bmatrix} \tag{5.17b}$$

where $x_{2,n}^l$ and $x_{3,n}^l$ are the local coordinates of the steel fibre in l_2 and l_3 direction, respectively, assuming the origin at the centroid.

- *Sub-matrix associated to the axial-bending interaction* ($\underline{K}_{ab}^{\,st}$)

$$\underline{K}_{ab}^{\,st} = \sum_{p=1}^{N_{s1}^{ab}} \left(\underline{T}_a^{\,\lg} \underline{B}_a^{\,T} \hat{\underline{D}}_{ab}^{\,st} \underline{B}_b \left[\underline{T}_b^{\,\lg} \right]^T J \right)_{s_1^p} W_p \tag{5.18a}$$

$$\hat{\underline{D}}_{ab}^{s} = \left[\hat{\underline{D}}_{ab,11} \quad \hat{\underline{D}}_{ab,21} \right] = \sum_{i=1}^{NS} \left[\hat{\underline{D}}_{ab,n} x_{3,n}^l A_{s,n} \quad -\hat{\underline{D}}_{ab,n} x_{2,n}^l A_{s,n} \right] \tag{5.18b}$$

- *Sub-matrix associated to the bending-axial interaction* ($\underline{K}_{ba}^{\,st}$)

$$\underline{K}_{ba}^{\,st} = \sum_{p=1}^{N_{s1}^{ab}} \left(\underline{T}_b^{\,\lg} \underline{B}_b^{\,T} \hat{\underline{D}}_{ba}^{\,st} \underline{B}_a \left[\underline{T}_a^{\,\lg} \right]^T J \right)_{s_1^p} W_p \tag{5.19a}$$

$$\hat{\underline{D}}_{ba}^{st} = \begin{bmatrix} \hat{\underline{D}}_{ba,11}^{st} \\ \hat{\underline{D}}_{ba,21}^{st} \end{bmatrix} = \sum_{i=1}^{NS} \begin{bmatrix} \hat{\underline{D}}_{ab,n}^{st} x_{3,n}^l A_{st,n} \\ -\hat{\underline{D}}_{ab,n}^{st} x_{2,n}^l A_{st,n} \end{bmatrix} \tag{5.19b}$$

5.2.3 Internal equivalent nodal forces

The internal equivalent nodal forces (Owen and Hinton 1980) are evaluated from the stresses in the fibres and have to be calculated from the constitutive stress-strain relations. The procedure is identical to the calculation of the stiffness matrix. The internal forces in

the element ($\underline{f}_{\text{int}}^{(e)}$) are the result of the contribution from stresses of steel fibres $\underline{f}_{\text{int}}^{st}$ and stresses in the concrete fibres $\underline{f}_{\text{int}}^{c}$.

For the calculation of these internal forces in each element, the following procedure (see Figure 5.5) can be used effectively:

- Evaluation of the generalized displacements ($\underline{U}$), at the sampling points for the 3D frame element;
- Calculation of the deformations ($\underline{\varepsilon}$) at each sampling points of the fibres of the discretized section;
- Calculation of the stresses ($\underline{\sigma}$) at the level of each sampling point of the corresponding fibre, using the constitutive relations of the material;
- Integration throughout the section will result in the resultant forces ($\underline{F} = \left[N_1^l \quad V_2^l \quad V_3^l \quad M_1^l \quad M_2^l \quad M_3^l \right]$) acting on the section;
- Calculation of the internal forces ($\underline{f}_{\text{int}}^{(e)}$) of each 3D element (due to steel fibres, $\underline{f}_{\text{int}}^{st}$, and due to concrete fibres, $\underline{f}_{\text{int}}^{c}$).

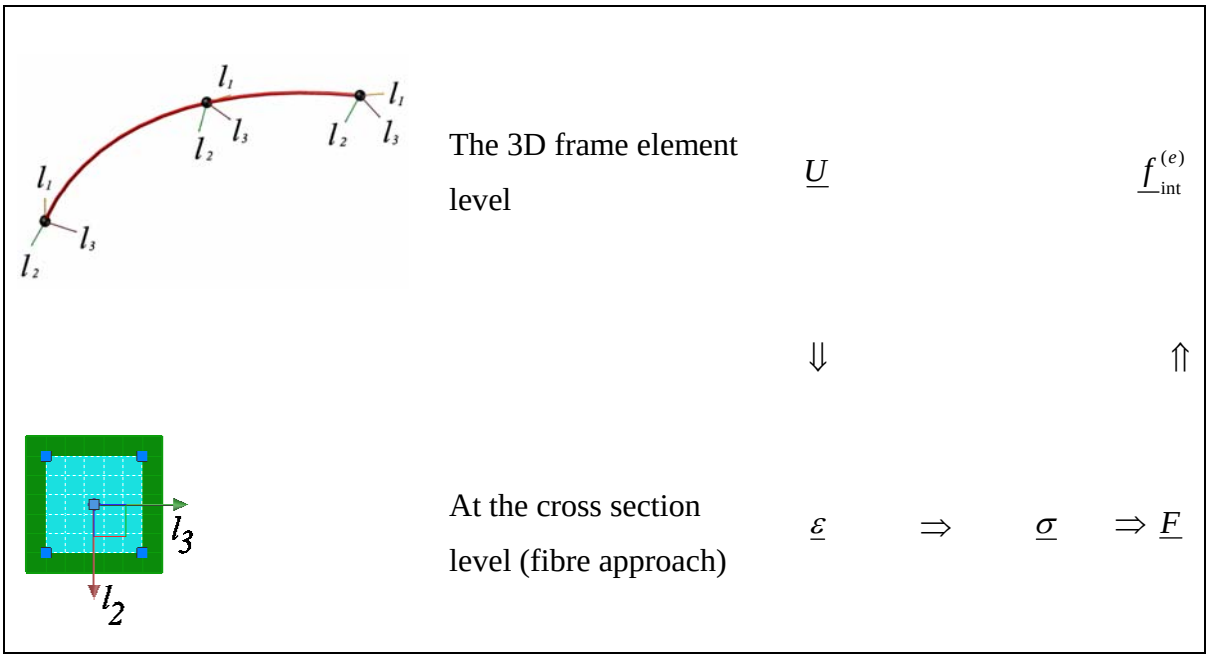

Figure 5.5: Systematic way for getting the internal forces

5.2.3.1 Contribution of concrete for the equivalent internal forces

The contribution to nodal forces due to concrete can be calculated by the Gauss-Legendre integration technique by integrating over the section. The general equations used are described in the following steps.

- *Nodal forces ($\underline{f}^{c}_{\text{int},a}$) corresponding to axial deformation for the frame elements, are equivalent to the summation of axial stresses in the fibres.*

$$\underline{f}^{c}_{\text{int},a} = \sum_{p=1}^{N_{s1}^{ab}} \left(\underline{T}_a \, {}^{\lg}B_a^{\,T} N_c J \right)_{s_1^p} W_p \tag{5.20a}$$

where,

$$N_c = \sum_{i=1}^{NG_{\text{sec}t}} \sigma^{c}_{ab,i} A_{GP,i} \tag{5.20b}$$

where $\sigma^{c}_{ab,i}$ is the normal stress in the concrete at the i^{th} sampling point of the section and N_c is the axial force.

- *Bending component of nodal forces ($\underline{f}^{c}_{\text{int},b}$) for the frame element, is equivalent to summation of bending stresses in the fibres.*

$$\underline{f}^{c}_{\text{int},b} = \sum_{p=1}^{N_{s1}^{ab}} \left(\underline{T}_b \, {}^{\lg}B_b^{\,T} \underline{M}_c J \right)_{s_1^p} W_p \tag{5.21a}$$

where,

$$\underline{M}_c = \sum_{i=1}^{NG_{\text{sec}t}} \begin{Bmatrix} \sigma^{c}_{ab,i} x^{l}_{3,i} A_{GP,i} \\ -\sigma^{c}_{ab,i} x^{l}_{2,i} A_{GP,i} \end{Bmatrix} = \begin{bmatrix} M_c^{l2} \\ M_c^{l3} \end{bmatrix} \tag{5.21b}$$

- *Shear component of the nodal forces ($\underline{f}^{c}_{\text{int},s}$) for the frame element, is equivalent to summation of shear stresses in the fibres.*

$$\underline{f}^{c}_{\text{int},s} = \sum_{p=1}^{N_{s1}^{ab}} \left(\underline{T}_s \, {}^{\lg}B_s^{\,T} \underline{Q}_c J \right)_{s_1^p} W_p \tag{5.22a}$$

where,

$$\underline{Q}_c = \sum_{i=1}^{NG_{sec\,t}} \begin{Bmatrix} \tau_{12,i}^c A^*_{GP,i} \\ \tau_{12,i}^c A^*_{GP,i} \end{Bmatrix} = \begin{bmatrix} V_c^{l2} \\ V_c^{l3} \end{bmatrix} \tag{5.22b}$$

where $\tau_{12,i}^c$ and $\tau_{13,i}^c$ are the shear stress in the concrete at the i^{th} sampling point of the section in the $l_1 l_2$ and $l_1 l_3$ plane, respectively.

- *Nodal forces ($\underline{f}_{\text{int},t}^{\,c}$) corresponding to torsional deformation of the frame element is equivalent to the summation of torsional stresses in the fibres.*

$$\underline{f}_{\text{int},t}^{\,c} = \sum_{p=1}^{N_{s1}^{ab}} \left(\underline{T}_t^{\,\text{lg}} B_t^{\,T} T_c J \right)_{s_1^p} W_p \tag{5.23a}$$

where,

$$T_c = \sum_{i=1}^{NG_{sec\,t}} -\tau_{12,i}^c x_{3,i}^l A_{GP,i} + \tau_{13,i}^c x_{2,i}^l A_{GP,i} \tag{5.23b}$$

5.2.3.2 Contribution of steel for the internal equivalent nodal forces

The contribution of nodal forces from steel fibres to element nodal force vector ($\underline{f}_{\text{int}}^{(e)}$) can be calculated as described in the following.

- *Nodal forces ($\underline{f}_{\text{int},a}^{\,st}$) corresponding to axial deformation is equivalent to summation of normal stress in the steel fibre.*

$$\underline{f}_{\text{int},a}^{\,st} = \sum_{p=1}^{N_{s1}^{ab}} \left(\underline{T}_a^{\,\text{lg}} B_a^{\,T} N_s J \right)_{s_1^p} W_p \tag{5.24a}$$

where,

$$N_{st} = \sum_{i=1}^{NS} \sigma_{ab,n}^{st} A_{st,n} \tag{5.24b}$$

where $\sigma_{ab,n}^{st}$ is the normal stress in the n^{th} steel fibre.

- *Nodal forces ($\underline{f}_{\text{int},b}^{st}$) corresponding to bending is derived from fibre axial stresses as:*

$$\underline{f}_{\text{int},b}^{st} = \sum_{p=1}^{N_{s1}^{ab}} \left(\underline{T}_f^{\text{lg}} B_f^T \underline{M}_s J \right)_{s_1^p} W_p \tag{5.25a}$$

where,

$$\underline{M}_{st} = \sum_{i=1}^{NS} \begin{Bmatrix} \sigma_{ab,n}^{st} x_{3,n}^l A_{st,n} \\ -\sigma_{ab,n}^{st} x_{2,n}^l A_{st,n} \end{Bmatrix} = \begin{bmatrix} M_{st}^{l2} \\ M_{st}^{l3} \end{bmatrix} \tag{5.25b}$$

5.3 THREE-DIMENSIONAL CABLE AND INTERFACE ELEMENTS

The three-dimensional cable element (3D Cable hereafter designated) and three-dimensional interface element (3D interface hereafter designated) are similar to their two-dimensional counterparts, except that they have extra degrees of freedom perpendicular to the longitudinal axis. The 2-dimensional models are described in detail by Sena-Cruz (2004). Here only the 3D interface element is described briefly and similar modification can be assumed for formulation of 3D Cable element. Figure 5.6 represent the 3D interface in LCS defined by $\left(x_1^l, x_2^l, x_3^l\right)$, and represented along the centre line. The axis of the 3D element is defined along x_1^l axis and the other axes are defined by x_2^l and x_3^l. The generic displacement field is represented by Eq. (5.26) and (5.27).

$$\underline{U}^l = \begin{bmatrix} u_1^l & u_2^l & u_3^l \end{bmatrix}^T \tag{5.26}$$

$$\underline{U}^g = \begin{bmatrix} u_1^{\text{g}} & u_2^g & u_3^g \end{bmatrix}^T \tag{5.27}$$

where u_i^l and u_i^g are the local and global translation displacements of the 3D interface element in x_i-direction (i=1, 2, 3).

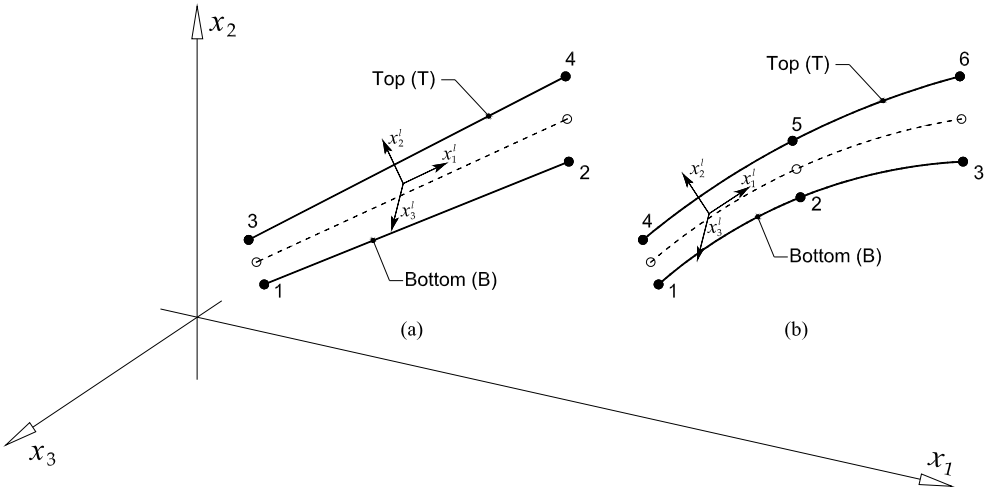

Figure 5.6: 3D line interface elements: (a) linear 4-node; (b) quadratic 6-node.

The nodal displacement vector for the element with four nodes in the local coordinate system is represented as:

$$\underline{a}^l = \begin{bmatrix} a_{11}^l & a_{12}^l & a_{13}^l & a_{21}^l & a_{22}^l & a_{23}^l & a_{31}^l & a_{32}^l & a_{33}^l & a_{41}^l & a_{42}^l & a_{43}^l \end{bmatrix} \tag{5.28}$$

where a_{ij}^l is the displacement of node i in the x_j^l direction. The displacement field is obtained from the element nodal displacements using the shape function matrix, $\underline{N}$ (Bathe 2006).

$$\underline{U}^l = \underline{N}\underline{a}^l \tag{5.29a}$$

$$\begin{bmatrix} u_{B1}^l \\ u_{B2}^l \\ u_{B3}^l \\ u_{T1}^l \\ u_{T2}^l \\ u_{T3}^l \end{bmatrix} = \begin{bmatrix} N_1 & 0 & 0 & N_1 & 0 & 0 & 0 & 0 & 0 & 0 & 0 & 0 \\ 0 & N_1 & 0 & 0 & N_1 & 0 & 0 & 0 & 0 & 0 & 0 & 0 \\ 0 & 0 & N_1 & 0 & 0 & N_1 & 0 & 0 & 0 & 0 & 0 & 0 \\ 0 & 0 & 0 & 0 & 0 & 0 & N_2 & 0 & 0 & N_2 & 0 & 0 \\ 0 & 0 & 0 & 0 & 0 & 0 & 0 & N_2 & 0 & 0 & N_2 & 0 \\ 0 & 0 & 0 & 0 & 0 & 0 & 0 & 0 & N_2 & 0 & 0 & N_2 \end{bmatrix} \underline{a}^l \tag{5.29b}$$

The deformation vector is calculated as difference in displacement along the axis of the element:

$$\Delta \underline{u}^{l} = \begin{bmatrix} \Delta u_1^l \\ \Delta u_2^l \\ \Delta u_3^l \end{bmatrix} = \begin{bmatrix} u_{T1}^l - u_{B1}^l \\ u_{T2}^l - u_{B2}^l \\ u_{T3}^l - u_{B3}^l \end{bmatrix} \tag{5.30a}$$

$$\Delta \underline{u}^{l} = \begin{bmatrix} -1 & 0 & 0 & 1 & 0 & 0 \\ 0 & -1 & 0 & 0 & 1 & 0 \\ 0 & 0 & -1 & 0 & 0 & 1 \end{bmatrix} \begin{bmatrix} u_{B1}^l \\ u_{B2}^l \\ u_{B3}^l \\ u_{T1}^l \\ u_{T2}^l \\ u_{T3}^l \end{bmatrix} \tag{5.30b}$$

$$\Delta \underline{u}^{l} = \underline{L}\underline{U}^{l} \tag{5.30c}$$

where Δu_i^l is the difference in displacement of homologous nodes for i^{th} direction, where $\underline{L}$ is the differential operator. The Eqn. (5.30c) can also be written in terms of nodal displacement as

$$\begin{aligned} \Delta \underline{u}^{l} &= \underline{L}\underline{N}\underline{a}^{l} \\ &= \underline{B}\underline{a}^{l} \end{aligned} \tag{5.31}$$

where $\underline{B}$ matrix is the product of differential operator and shape function matrix as described below

$$\underline{B} = \begin{bmatrix} -N_1 & 0 & 0 & -N_2 & 0 & 0 & N_1 & 0 & 0 & N_2 & 0 & 0 \\ 0 & -N_1 & 0 & 0 & -N_2 & 0 & 0 & N_1 & 0 & 0 & N_2 & 0 \\ 0 & 0 & -N_1 & 0 & 0 & -N_2 & 0 & 0 & N_1 & 0 & 0 & N_2 \end{bmatrix} \tag{5.32}$$

The constitutive behaviour of the interface element is simulated by using nonlinear models implemented in FEMIX, which can be described as

$$\underline{\sigma}^{l} = \underline{D}\Delta\underline{u}^{l} \tag{5.33}$$

where

$$\underline{D} = \begin{bmatrix} D_1 & 0 & 0 \\ 0 & D_2 & 0 \\ 0 & 0 & D_3 \end{bmatrix} \text{ and } \underline{\sigma}^{l} = \begin{bmatrix} \sigma_1^l \\ \sigma_2^l \\ \sigma_3^l \end{bmatrix} \tag{5.34}$$

σ_i^l and D_i are stresses and the tangential stiffness in the i^{th} direction in LCS.

The uniaxial nonlinear interface laws described in Chapter 2 are assumed for the calculation of stresses and corresponding stiffness in x_1^l direction, while for the other directions (x_2^l and x_3^l) linear elastic laws with high stiffness ($= D_2 = D_3 >> D_1$) is assumed to follow. Applying the principle of virtual work:

$$W_{\text{int}} = \int_S \delta(\Delta\underline{u}^{l})^T \underline{\sigma}^{l} dS \tag{5.35}$$

where $\delta(\Delta\underline{u}^{l})^T$ is the virtual relative displacement vector. The element nodal displacements in GCS and LCS are related as:

$$\underline{a}^{l} = \underline{T}\underline{a}^{g} \tag{5.36}$$

where $\underline{a}^{g}$ is the displacement vector in GCS and $\underline{T}$ is the transformation matrix. From Eqn. (5.36) and (5.31)

$$\Delta\underline{u}^{l} = \underline{B}\underline{a}^{l} = \underline{B}\underline{T}\underline{a}^{g} \tag{5.37}$$

Using the Eqn. (5.37) in Eqn. (5.33), yields

$$\underline{\sigma}^{l} = \underline{D}\,\underline{B}\,\underline{T}\,\underline{a}^{g} \tag{5.38}$$

Using Eqn. (5.37)and (5.38) in (5.35) yields:

$$W_{\text{int}} = \int_{S} \delta(\underline{B}\,\underline{T}\,\underline{a}^{g})^{T}\, \underline{D}\,\underline{B}\,\underline{T}\,\underline{a}^{g}\, dS \tag{5.39}$$

$$W_{\text{int}} = \int_{S} (\delta \underline{a}^{g})^{T}\, \underline{T}^{T}\, \underline{B}^{T}\, \underline{D}\,\underline{B}\,\underline{T}\,\underline{a}^{g}\, dS \tag{5.40}$$

The virtual work due to external forces is obtained from:

$$W_{ext} = \delta(\Delta \underline{a}^{l})^{T}\, \underline{F}^{l} \tag{5.41}$$

Using the force and displacement transformation Eq. (5.41) can be written as:

$$\begin{aligned} W_{ext} &= \delta(\underline{a}^{g})^{T}\, \underline{T}^{T}\, \underline{T}\,\underline{F}^{g} \\ &= \delta(\underline{a}^{g})^{T}\, \underline{F}^{g} \end{aligned} \tag{5.42}$$

From the principle of virtual work Eqs. (5.35) and (5.42) should be equated, which leads to

$$\int_{S} \underline{T}^{T}\, \underline{B}^{T}\, \underline{D}\,\underline{B}\,\underline{T}\,\underline{a}^{g}\, dS = \underline{F}^{g} \tag{5.43}$$

or

$$\underline{K}^{g}\, \underline{a}^{g} = \underline{F}^{g} \tag{5.44}$$

where $\underline{F}^{g}$ is force vector and, $\underline{K}^{g}$ is stiffness matrix given by

$$\underline{K}^{g} = \int_{S} \underline{T}^{T}\, \underline{B}^{T}\, \underline{D}\,\underline{B}\,\underline{T}\, dS \tag{5.45}$$

5.4 MODEL APPRAISAL

The performance of the developed fibre model was verified by predicting the behaviour using different examples existing in the literature. The examples that show the application of the fibre model are published by the author in Barros *et.* al (2008b) and Varma *et.* al (2010), while some other examples are described below. The examples selected constitute numerical modelling at structural element level, and later also on full scale for a seven storey building.

5.4.1 Cyclic test by Gomes

The performance of the model developed was evaluated by comparing the numerical results with column tested under cyclic alternating loads (Gomes 1992). Gomes studied column section of a building, subjected to an axial load of 400 kN and alternately increasing curvature. An auxiliary frame element was assumed with load and support conditions as represented in Figure 5.7. As the experimental results derived involve only the moment curvature relationship for section, an auxiliary element was proposed to simulate the moment curvature relationship numerically (Figure 5.7). The curvature χ to this element was applied at the ends through rotation $\theta(=\chi/2)$. The history of rotations, as described in Figure 5.8, was applied keeping constant the compressive axial load of 400 kN.

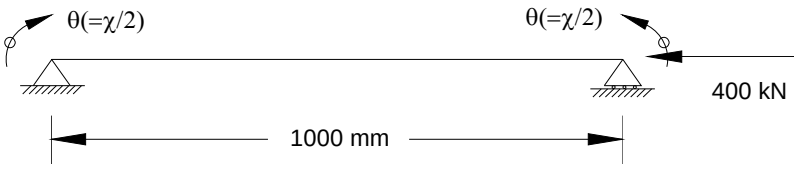

Figure 5.7: Beam configuration.

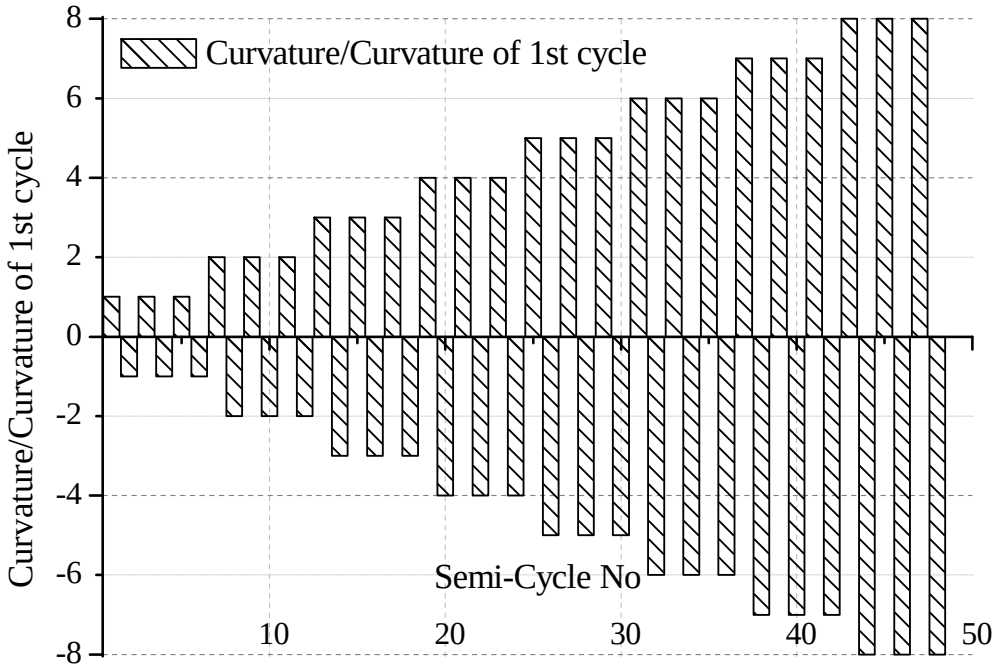

Figure 5.8: Beam curvature history.

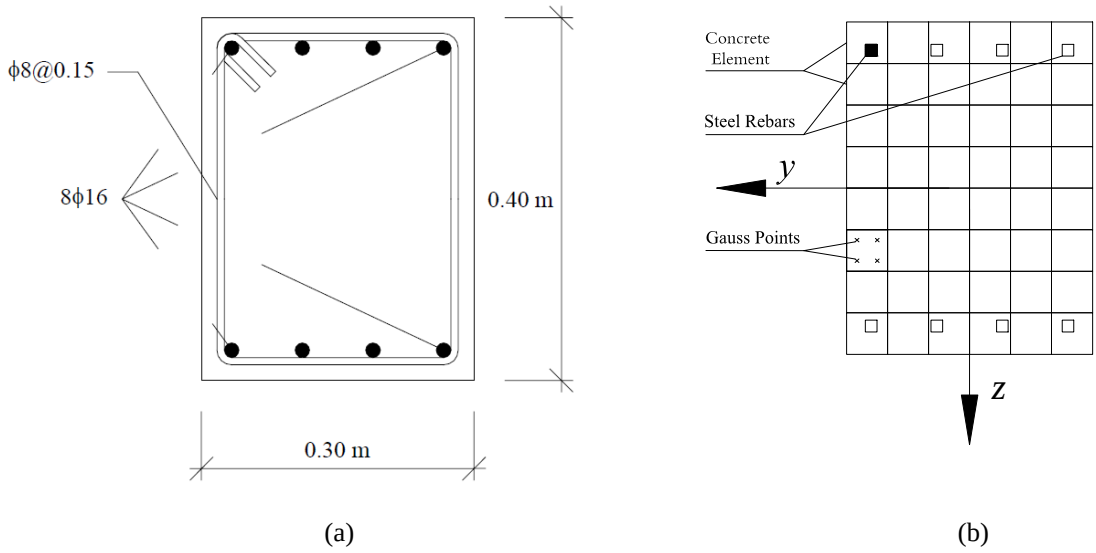

(a) (b)

Figure 5.9: (a) Section-details and (b) corresponding section mesh.

Table 5.1: Values of the mechanical properties of the steel used in constitutive model (adapted from Gomes, 1992).

Initial Young modulus, E_s (GPa)	200
Tangent modulus at strain hardening, E_{sh} (GPa)	6.4
Yielding strain, ε_{sy} (mm/mm)	2.0×10^{-3}
Yielding stress, f_{sy} (MPa)	400.0
Hardening strain, ε_{sh} (mm/mm)	2.3×10^{-3}
Hardening stress, f_{sh} (MPa)	401.0
Strain at the ultimate stress, ε_{su} (mm/mm)	2.2×10^{-2}
Ultimate stress, f_{su} (MPa)	600

The longitudinal steel reinforcement was constituted by 8 bars of 16 mm diameter (see Figure 5.9a), with symmetrical distribution about the axis of bending, *y*, and their corresponding mechanical properties are listed in Table 5.1. The transverse steel reinforcement is composed by stirrups of $\Phi 8$ at 150 mm. The values for the mechanical properties of the concrete used in the numerical simulation are included in Table 5.2. The tensile strength of concrete was negligible (Sena-Cruz 1998). However, during cyclic analysis for the constitutive laws for hysteretic scheme to be valid, the internal parameters need minimum value of tensile strength as 0.1 MPa.

The beam (see Figure 5.7) was discretized in three elements of three nodded each and numerical integration was carried with two sampling points each for stiffness and internal nodal equivalent force calculations. The cross section was divided into 48 fibres of concrete and 8 fibres of steel (see Figure 5.9b). The numerical and experimental moment-curvature curves of the cyclic test are compared in Figure 5.10, from which it can be concluded that the model is able to predict the response with a very good agreement. The model not only predicted correctly the peak strength but also the cycles with appreciable accuracy.

Table 5.2: Values of the mechanical properties of the concrete used in constitutive model (adapted from Gomes, 1992).

Initial Young Modulus, E_c (GPa)	25
Peak compressive strength of confined concrete, f_{cc} (MPa)	26.77
Peak compressive strain, ε_{cc} (mm/mm)	2.14×10^{-3}
Non-dimensional critical strain on the compression envelope, ε_{ccr}^{-} (mm/mm)	3.2×10^{-3}
Peak tensile strength, f_{ct} (MPa)	0.10
Peak tensile strain, ε_{ct} (mm/mm)	8×10^{-6}
Non-dimensional critical strain on the tension envelope, ε_{ccr}^{+} (mm/mm)	1.2×10^{-5}

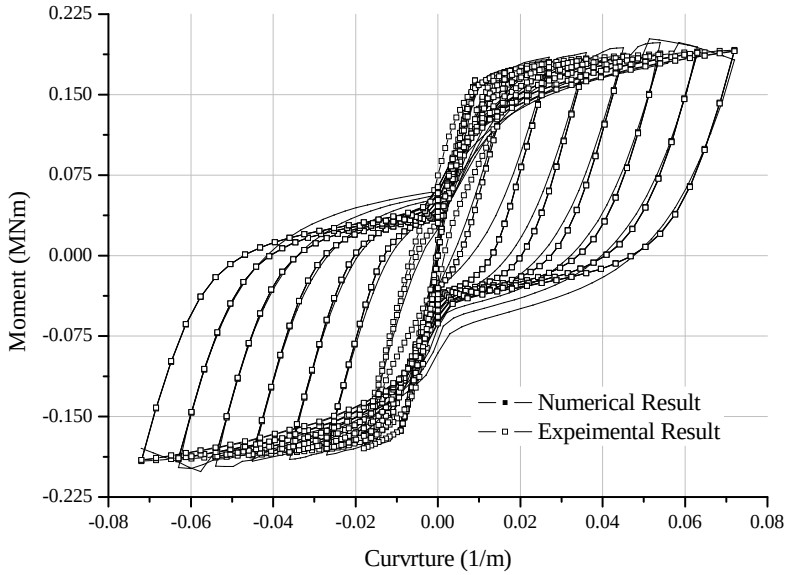

Figure 5.10: Moment-curvature response obtained by fibre model and by experimental result (Gomes 1992).

The pinching of the cycles is also predicted in this case which is one of the critical features of this simulation. For this simulation, the shift in strain for concrete, ε_{co} (see Chapter 2 for detail) was reduced to negligible value, which led to this refinement of the result. The pinching in the last few cycles predicted by FEMIX does not match exactly experimental results, since concrete cracking and spalling occurred experimentally, yielded to the sliding between steel rebars and concrete, contrary to the assumption of the perfect bond assumption on the numerical model.

5.4.2 Pushover analysis by N2 method

One of the emerging analysis trends in nonlinear static procedure (NSP) is *pushover analysis* as described by FEMA-273 guidelines, which has almost become a standard procedure for seismic analysis of multi-storey buildings. The performance of fibre model for analysis of pushover has been validated by various researchers (Cosenza et al. 2006, Monteiro *et* al. 2008). The pushover method can be easily extended for the analysis of frame, as structural components have been successfully validated by the author elsewhere (Barros *et* al. 2008b). In this NSP, the structure is subjected to a set of monotonically increasing lateral forces until a target displacement is reached. The method followed here is described as N2 by Fajfar (2000). The method involves conversion of a multi-degree-of-freedom (MDOF) model to an equivalent single-degree-of-freedom (SDOF) system. The response spectrum analysis of SDOF is used, based on the acceleration-displacement format, which offers easy interpretation of the basic quantities governing the seismic response. The results derived from SDOF are again converted to MDOF, for performance evaluation of the structure. One of the main assumptions of N2 method is that the response of a structure is assumed to be in one of the predominant mode of vibration. The flowchart of the method is described in Appendix C. The steps deemed necessary for fibre model are described here and the detailed description of the N2 method can be found elsewhere (Fajfar 1999, Fajfar 2000). An example of a seven-storey reinforced concrete frame (see Figure 5.11) subjected to the predominant mode of vibration is analysed by this method. During the analysis the Appendix C is followed and reader is requested to consult it as benchmark, while steps are referred. The existing building was found to be deficiently designed and made with low grade concrete (see Table 5.3), which is shown by the

following analysis. The proposal also analyse the strengthened building by the same push over method.

The building is analysed as plane frame and the height of each storey is 3000 mm. The uniform distributed load applied at each beam, storey including the dead load and live load was found to be equal to 41.77 N/mm (=Q, see Figure 5.11). As the mass of each floor (m_i) was the same, hence m_i = 72053 kg (i= 1 to 7 is storey number). A realistic acceleration response spectrum *versus* time period of linear SDOF system graph (S_{ae}-T) derived from EN 1998-1 is assumed and illustrated in Figure 5.12(a) (Step 1). The stiffness of MDOF was found to be 12837.49 N/mm (Barros *et* al. 2009) and the time period of building according to Fajfar (2000) was found to be 1.24 s. The time period of 1.24 s is also represented in the Figure 5.12(a). The SDOF elastic spectrum can be converted to an inelastic SDOF acceleration (S_a) *versus* the displacement spectrum (S_d), determined according to (Vidic *et* al. 1994, Step 2).

The displacement shape used to generate the SDOF from the MDOF is described by:

$$\underline{\Phi}^T = [0.143 \quad 0.286 \quad 0.429 \quad 0.571 \quad 0.714 \quad 0.857 \quad 1]$$

The coefficients of the displacement shape function are determined as ratio of height of each storey to total height of the building (e.g., Φ_1=0.143=3000/21000) (Step 3). The mass vector corresponding to the MDOF is described by $\underline{M}^T$ as:

$$\underline{M}^T = [m_1 \quad m_2 \quad m_3 \quad m_4 \quad m_5 \quad m_6 \quad m_7]$$

The equivalent mass of SDOF was calculated as $\underline{M}\underline{\Phi}^T = 288213\,\text{Kg}$. The coefficient for transformation (Γ) of quantities from MDOF to SDOF was found to be 0.714(Appendix C, Step 5).

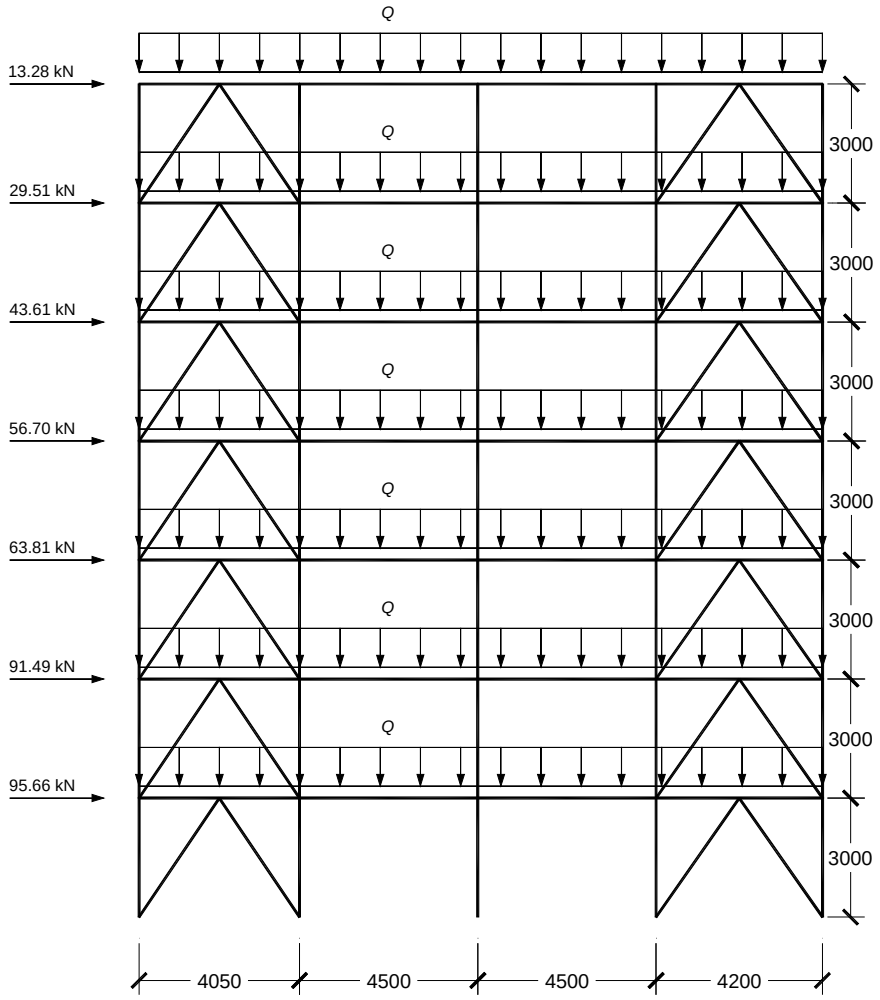

Figure 5.11: Load configuration of multi-storey building (all dimensions are in mm).

A bilinear elasto-plastic curve (capacity diagram, Step 6) is required to calculate the seismic demand of the SDOF. It is to be noted that the capacity curve of SDOF is generated from push over curve of MDOF. Assuming that the pushover curve for MDOF is already known (derived below, Step 4), the base shear and top displacement of the MDOF system is transformed using Γ (Step 7, Appendix C). The capacity curve and inelastic spectrum are illustrated in Figure 5.12(b) (Step 8). From the intersection of curves, the seismic demand for SDOF system is found to be 39.88 cm, and for the multi-storey building is estimated to be 28.49 cm (=39.88/Γ). It is to be noted that the seismic demand can change depending on the load configuration and displacement shape assumed. The top of multi-storey frame needs to be displaced in multiples of this displacement for various combinations of load cases. However here the push over analysis (Step 9) is performed for

load case described in Figure 5.11, and the same curve is used in the calculation of capacity curve (Step 4 to 7).

The columns and beams were discretized in three nodded Timoshenko frame elements and, for the calculation of stiffness matrix and internal equivalent nodal forces two Gauss points per element were used. The mesh topology of the frame is represented in Appendix D. The section details of the frame are described in Figure 5.13. The cross sections were decomposed in concrete and steel fibres, using the approach used in previous example, and are described in Appendix D. The unstrengthened sections (without steel plates) were used in this analysis. The mechanical properties of concrete and steel (rebars and plates) are described in Table 5.3 and Table 5.4, respectively. The properties described in these tables are derived from tests reported in Barros *et* al. (2009). A 2x2 gauss integration scheme was used for all fibres in the cross section plane. The horizontal loads were applied on the frame to each storey at floor level and are in Figure 5.11.

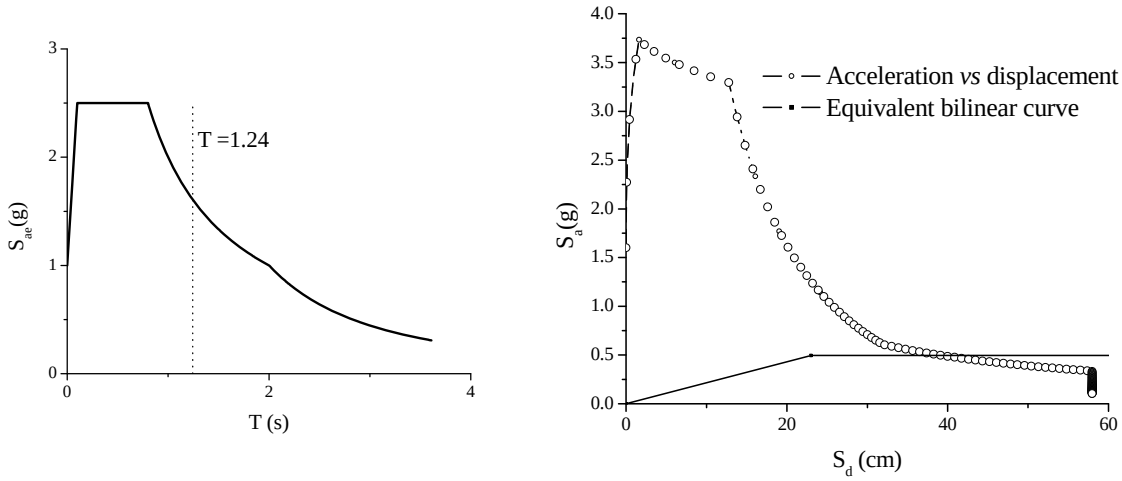

(a) (b)

Figure 5.12: (a) Elastic spectra and (b) Inelastic demand spectra from time period of structure.

Table 5.3: Mechanical properties of the concrete used in constitutive model for frame.

Parameter	Section S1, S2, S3 and S6	Section S4 and S5
Initial Young Modulus, E_c (GPa)	16.06	16.00
Peak compressive strength of confined concrete, f_{cc} (MPa)	5.5	13.9
Peak compressive strain, ε_{cc} (mm/mm)	2.5×10^{-3}	2.5×10^{-3}
Non-dimensional critical strain on the compression envelope, ε_{ccr}^{-} (mm/mm)	4.0×10^{-3}	4.0×10^{-3}
Peak tensile strength, f_{ct} (MPa)	0.10	0.45
Peak tensile strain, ε_{ct} (mm/mm)	1.5×10^{-4}	1.5×10^{-4}
Non-dimensional critical strain on the tension envelope, ε_{ccr}^{+} (mm/mm)	2.4×10^{-4}	2.4×10^{-4}

It is assumed that floor is rigid and hence the axial displacements of the beams positioned in same floor level are equal. The frame was analysed in two dimension hence all the out of plane degrees of freedom were frozen. The pushover curve, a plot of base shear and horizontal displacement at the top of the building, is illustrated in Figure 5.14 (Step 9). The load carrying capacity of the frame estimated from characteristic and minimum concrete strength is described by 592.44 kN and 394.96 kN (see Figure 5.14), respectively (Barros *et* al. 2009). However once the minimum displacement is found, the push-over is repeated by displacing top of the frame by specific displacements. In this case the frame is displaced until the frame failed, which in this case is described by yielding of left side columns in tension and consequently, sudden drop of load carrying capacity. The frame can be analysed for displacement in multiple of 28.49 cm. It can be seen from Figure 5.14, that the load carrying capacity of the frame is lesser than the minimum load carrying capacity (=394.96 kN). Moreover for twice the displacement value of 28.94 cm, the frame has base shear more than minimum base shear required. The frame need to be strengthened to

satisfy both the seismic demand and should be checked for other load cases. The analysis of columns and beams is not described here, which is required for the detailed investigation of such frames.

Table 5.4: Values of the mechanical properties of the steel used in constitutive model.

Mechanical properties	Steel rebars	Steel plates
Initial Young modulus, E_s (GPa)	200	200
Tangent modulus at strain hardening, E_{sh} (GPa)	6.4	6.4
Yielding strain, ε_{sy} (mm/mm)	2.0×10^{-3}	2.0×10^{-3}
Yielding stress, f_{sy} (MPa)	204.0	400.0
Hardening strain, ε_{sh} (mm/mm)	1.02×10^{-3}	3.5×10^{-3}
Hardening stress, f_{sh} (MPa)	210.0	410.0
Strain at the ultimate stress, ε_{su} (mm/mm)	3.0×10^{-2}	3.0×10^{-2}
Ultimate stress, f_{su} (MPa)	220	420

As the frame is deficiently designed, hence retrofitting solutions need to be adopted. Following that, steel plates were applied on the sides of sections S3 and S6. This retrofitting strategy is described in detail elsewhere (Barros *et* al. 2009). The load configuration similar to the one applied to the deficient frame was also adapted to this strengthened frame, and Pushover procedure was repeated, until the estimated base shear had shown sudden loss. The results are represented in Figure 5.14, and shows that the strengthened frame was able to withstand higher load for prescribed seismic displacement and without yielding. The load carrying capacity derived from push over curve is well above the required limit derived as minimum base shear (=394.96 kN), and capacity derived from characteristic values of concrete, for the seismic demands. The detailed investigation of column and beams can also be performed from the results obtained by

fibre model. In these cases the stresses of various critical elements can be verified based on standards.

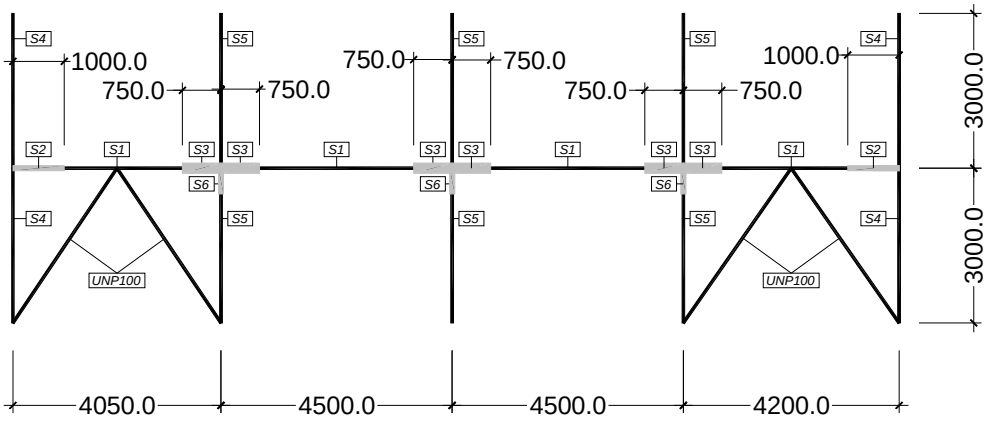

(a)

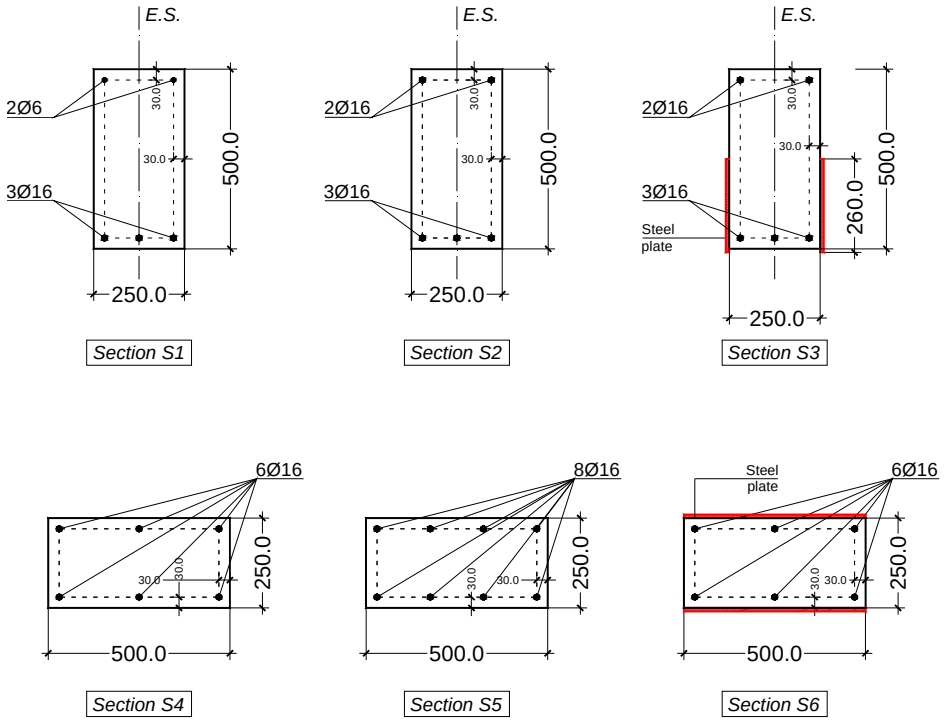

(b)

Figure 5.13: (a) Frame storey with sections and (b) section details. (all units in mm)

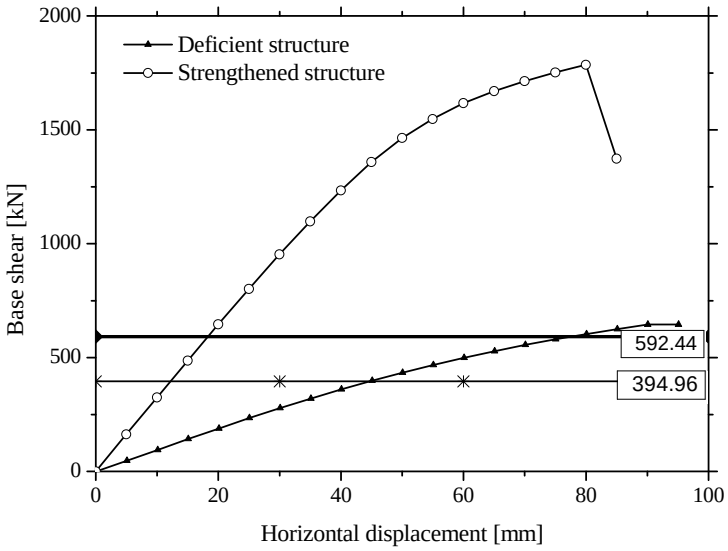

Figure 5.14: Pushover result of deficient and strengthened frame.

The example herein described shows the possibility of fibre model for seismic analysis of frames. This example shows that the performance of any existing frame and retrofitted frame can be evaluated successfully by fibre model.

5.4.3 Simulation of columns under cyclic loading

A series of RC columns monolithically connected to a RC footing were tested by Barros *et* al. (2008) with the aim of evaluating the influence of concrete compressive strength, and reinforcement ratio of longitudinal steel bars on the effectiveness of a CFRP-based strengthening intervention for this type of elements when submitted to cyclic loading. Figure 5.15 shows the typical specimen of the experimental program. The columns were cast in a second phase, 3 days after the corresponding footing has been cast, in order to reproduce the real practice as much as possible. With the same purpose, starter longitudinal steel bars were used to connect the reinforcement system of the column to the corresponding foot (see Figure 5.15(a)). The lap splice of the starter bars had a length of 260 mm. The columns were identified with the denomination as F**10**, F**12** and F**16**, where **10**, **12** and **16** represents the diameter of the longitudinal steel bars in mm.

A constant vertical load of approximately 120 kN was applied to the column, inducing an axial compressive stress of 1.92 N/mm^2. A history of horizontal displacements was

imposed at 150 mm from top of column, which included eight load cycles between ±2.5 mm and ±20.0 mm, in increments of ±2.5 mm, with a displacement rate of 50 μm/s for the first set of cycles, 75 μm/s for the second set of cycles, and 100 μm/s for the remaining set of cycles. The detailed experimental program can be found elsewhere (Perrone 2008).

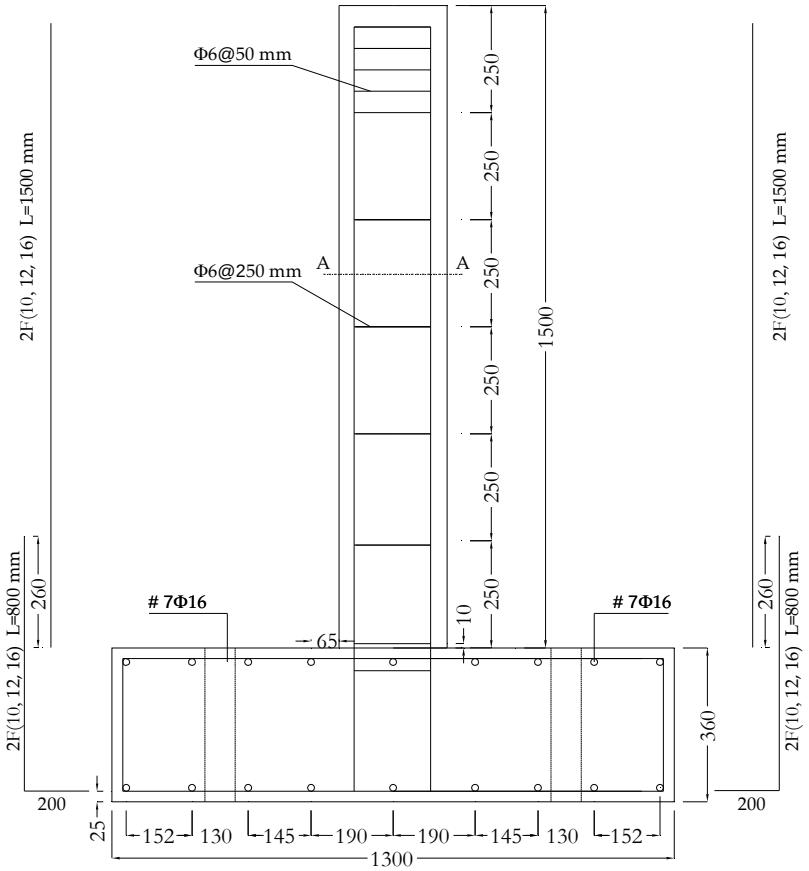

(a)

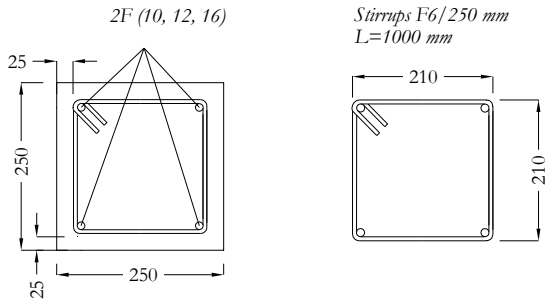

(b)

Figure 5.15: (a) Geometry of the specimens and (b) transverse section (all dimensions are in mm).

As the concrete strength was quite low, during the experiments, large discrete cracks were observed at column base shearing through the column axis almost perpendicular to it, which must have led to bar slip. In this analysis the columns are simulated with perfect bond between concrete and steel using the described fibre model. Later, the same experimental results are simulated assuming the bond-slip behaviour between concrete and steel bars. Spacone and Limkatanyu (2000) have derived a formulation based on fibre approach to simulate bond-slip behaviour of rebars, but it was not possible to implement it in FEMIX. Hence an interface based model (described later), in combination with fibre model is used to simulate the experimental tests. Only two columns, F10 and F16 are simulated here.

Uniaxial tensile tests were conducted on the steel bar according to NP-EN 10 002-1, and the values obtained for the mechanical properties are presented in Table 5.5. The values for the concrete properties derived from compressive tests on concrete cylinders are indicated in Table 5.6. The tensile strength was calculated according to CEB-FIB (1993).

Table 5.5: Values of the mechanical properties of the steel bars used in the constitutive model.

Parameter	Φ10	Φ16
Initial Young modulus, E_s (GPa)	204.5	210
Tangent modulus at strain hardening, E_{sh} (GPa)	6.4	6.4
Yielding strain, ε_{sy} (mm/m)	2.2	2.2
Yielding stress, f_{sy} (MPa)	445	450
Hardening strain, ε_{sh} (mm/m)	3.5	3.5
Hardening stress, f_{sh} (MPa)	460	455
Strain at the ultimate stress, ε_{su} (mm/m)	168	268
Ultimate stress, f_{su} (MPa)	564	580.5

Table 5.6: Values of the mechanical properties of the concrete used in constitutive model.

Initial Young modulus, E_c (GPa)	20
Peak compressive strength of confined concrete, f_{cc} (MPa)	8.0
Peak compressive strain, ε_{cc} (mm/mm)	3.0×10^{-3}
Non-dimensional critical strain on the compression envelope, ε_{ccr}^{-} (mm/mm)	5.0×10^{-3}
Peak tensile strength, f_{ct} (MPa)	0.5
Peak tensile strain, ε_{ct} (mm/mm)	2.0×10^{-4}
Non-dimensional critical strain on the tension envelope, ε_{ccr}^{+} (mm/mm)	3.5×10^{-4}

5.4.3.1 Perfect bond

For perfect bond simulation, the columns were discretized with six isoparametric Timoshenko beam elements with three nodes each. According to the developed approach, at the cross section level each fibre is discretized with a quadrilateral finite element. These fibres are represented by 4-noded finite elements with a 2x2 Gauss-Legendre integration rule, thus simulating the concrete core, concrete cover and steel bars. The concrete part of the cross section was discretized with sixteen quadrilateral elements. Each longitudinal bar was simulated with an additional quadrilateral element. However, only the column was simulated with all the degree of freedoms fixed at bottom with stiff footing. Figure 5.17 shows the comparison between the experimental and numerical envelope curves for F**10** and F**12** columns. It can be concluded that the implemented numerical model was not able to capture the main phenomena observed in the experimental tests. The fibre model failed to predict the peak strength of each cycle and pinching observed during cycles. Even after a displacement of just 2.5 mm in each direction, the concrete was cracked and steel rebars governed the cycles, which led to almost no pinching and simultaneously predicted high capacity for the columns, numerically. As the percentage of longitudinal steel is higher in

F**16** compared to F**10**, the numerical simulation of Figure 5.17 (b) represent more pronounced increase in peak strength. Moreover as concrete was of low grade, the force deformation cycles were like replication of the steel behaviour. Hence the next paragraph is dedicated to the estimation of cyclic behaviour of these columns by considering the bond-slip behaviour.

5.4.3.2 Bond-slip

During simulation assuming bond-slip, the concrete and steel rebars were separated through interface. The Figure 5.16 (a) illustrates the schematic model of footing, column axis, steel bars and stiff transversal cables The concrete column was simulated by fibre mesh, as described above. In Figure 5.16 (a), the cross section of column (green plane) is represented at nodes, the bars are assumed to be passing through this plane. The interface elements with zero width were positioned at steel rebars (see Figure 5.16 (b)). To calculate the slip between the nodes of interface element, displacement generate due to in-plane deformation of concrete and steel bar need to be calculated. To calculate the deformation at interface due to axis of column, stiff cables were attached to axis of the column at one end and to interface element node at other end (see Figure 5.16 (b)). In the same figure, the finite element model of concrete column (represented by axis), interface element, stiff transversal cables and steel rebars is described. The elements used can be summarized as: Timoshenko fibre element to simulate the concrete of column, stiff cable for calculation of displacement at the bar end due to movement of column axis, cable elements to simulate the reinforcements, three dimensional line interface elements to model the interface between the reinforcement and concrete, and solid element to simulate the footing. The longitudinal bars were assumed to be penetrating inside the footing. The footing was rigidly connected to the base and all the degree of freedom were frozen at bottom of it. The mechanical parameters used in constitutive models of bond-slip are shown in Table 5.7 where the bond-slip parameters were calculated according to the Verderame *et* al. (2009a-b). As the concrete was of low strength, the longitudinal rebars can be assumed to be sliding smoothly, hence the bond-slip parameters were calculated assuming equivalent to plain rebars.

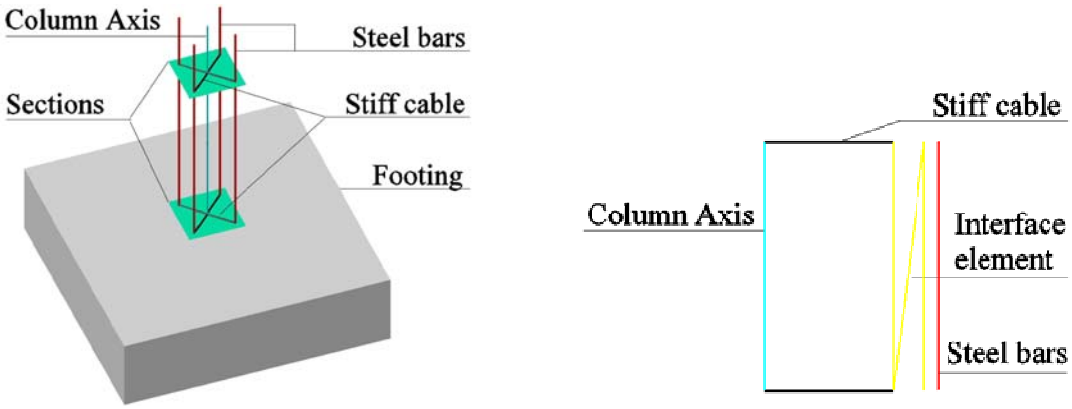

(a) (b)

Figure 5.16: (a) FE modelling of column and (b) View of column axis (Timoshenko beam) in context of stiff cable, interface element and longitudinal steel bars.

Table 5.7: Values of the mechanical properties of bond model.

Parameter	Value
Exponential factor, α	0.5
Slip at peak stress, s_{bp} (mm)	0.1
Slip at end of plateau, s_{bl} (mm)	0.21
Peak stress, τ_{bp} (MPa)	0.42
Frictional stress, τ_{bf} (MPa)	0.13
Clear distance between lugs, s_{bf} (mm)	1.5
Tangential bond stiffness, E_b (MPa/mm)	125
Normal bond stiffness l_2 direction (MPa/mm)	500

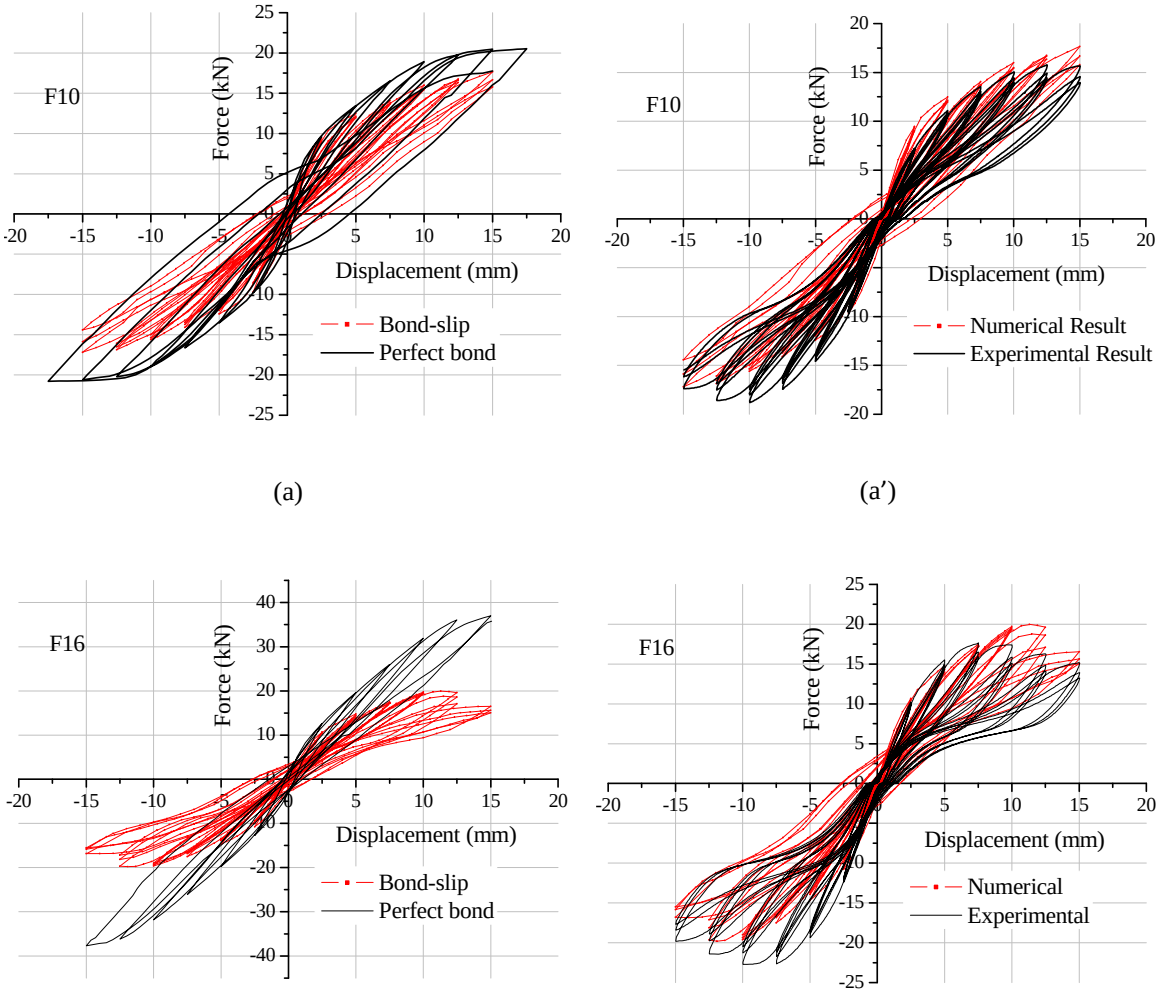

Figure 5.17: Experimental and numerical results of column with (a-b) perfect bond; and (a'-b') bond-slip.

The concrete column (without reinforcing bar) was simulated with two nodded nine Timoshenko beam elements and the cross-section was discretized in similar fashion as in perfect bond condition. The footing was simulated with 8 node 144 solid elements. For the calculation of stiffness and internal equivalent nodal force, the solid elements were performed by using 2×2×2 integration scheme and the footing was assumed behaving as linear elastic with modulus of elasticity of 30 GPa. The longitudinal steel reinforcements were simulated by 3D cable elements and stiff transverse cables were simulated with 2-node frame elements with two Gauss-Legendre integration points. Each longitudinal bar

was discretized in 9 finite elements. To calculate the displacement at the location of steel bar nodes due to the displacement of column axis, the area of the stiff cables was assumed to be of 1000 mm^2 and modulus of elasticity of 200 GPa. The area of stiff cable was found from iteration, which should be unique for all the columns and can simulate the envelope of these cyclic loading tests successfully. The steel-concrete interface is simulated by 4-node interface elements with two Gauss-Lobatto integration points.

Figure 5.17 (a′) and (b′) compares the experimental and numerical results obtained assuming the slip of rebar. It can be observed that the simulation improved significantly in term of pinching, peak strength. Moreover, the estimated cyclic loops have shown the degradation during cycles with much higher precision compared to the perfect bond examples. The numerical simulations estimate pinching and peak resistance in acceptable limits, contrary to the case when perfect bond condition was assumed. However, it can be observed that the maximum force reached in either direction is same (see Figure 5.17 (a′) and (b′)), while in the experimental results a significant difference was registered. The shift of the experimental curve towards negative ordinate could have been due to sliding of footing, and hence the force calculated in negative direction is higher compared to the other.

5.5 SUMMARY

With the aim of simulating the behaviour of RC columns and seismic analysis (e.g., by pushover), a fibre model with cyclic constitutive laws for concrete and steel bars was implemented in a computational code based on finite element technique. This computational model can simulate the cyclic behaviour in compression and in tension, of unconfined. The numerical model has reproduced, with good agreement, the behaviour observed in the experiments, being a useful tool for the analysis of this type of structures. The fibre model provides reliable and acceptable new generation of design and analysis solution. It can be a very effective tool in investigating alternative retrofit schemes, or for the evaluation of seismic performance of seismically-designed and non seismically designed existing structures. It can also model effectively the sub-assemblies like beams, columns, joints etc.

The numerical model was improved to consider the slip of reinforcing bars, and the three dimensional interface elements have realistically captured various aspects of the behaviour of the column, when subjected to reversed load cycles. The interface element was used in combination with stiff transverse cables, which were primarily deployed to transfer the in-plane displacement of column axis. This technique has very well simulated the bond-slip phenomenon. Simulating debond has also improved the results in terms of pinching and load carrying capacity, compared to the perfect bond condition of fibre model.

CHAPTER 6

Material nonlinear behaviour of laminar RC structures subjected to cyclic loading

6.1 INTRODUCTION

In case of multi-axial stress, the strength capacity of a concrete element subjected to a multi-axial stress field, a suitable failure criterion is required to define the failure of concrete, e.g. Mohr-Columb, Drucker Prager etc. The present chapter is dedicated to the modelling of laminar concrete structures like walls that can be considered as a plane stress problem, or 3D plane shells assumed as the assemblage of layers in plane stress state.

Some of the important aspects of the plane stress simulation are to address the following issues: the strength of concrete subjected to various combinations of biaxial stresses; deviation in material properties before and after cracking; concrete cracking and, the crack propagation. As all these behaviours were not addressed in fibre element models, hence these issues will be investigated by the implemented formulation. A short resume of these problems faced by researchers is discussed here.

More than four decades ago, the first time FEM was applied by Ngo and Scordelis (1967) to reinforced concrete beams to predict the principal stresses in concrete and stresses in steel bars, and by assuming the steel and concrete as linear elastic materials. Cervenka and Gerstle (1971) modelled the compressive behaviour of concrete, and steel was assumed as having elasto-plastic behaviour. However, concrete in tension was assumed to have an elastic-brittle behaviour. The cracking was modelled by separation of nodes and hence, redefinition of structural topology was done. As re-meshing is a cumbersome and time consuming process, Rashid (1968) proposed the concrete as an orthotropic material. The orthotropic nature of concrete is one of the important characteristic to model the crack.

Among various available models of concrete, the orthotropic models developed based on the concept of "*equivalent uni-axial strain*" provides a balance between accuracy and computing time. Some of the researchers (Blakely and Park 1973, Aktan *et* al. 1973) used uniaxial constitutive models in orthotropic directions to represent the concrete, while performing the cyclic analysis in biaxial stress conditions. Some of the early models, which reproduced the expereimental results, were proposed by Liu *et* al. (1972a and 1972b) and Kupfer and Gerstle (1973). A layered rectangular plate element with axial and bending stiffness interaction was developed by Rajagopal (1976) to analyse RC beam, and the concrete was modelled as an orthotropic material. Later several researchers (Rots *et* al. 1985, Barzegar and Schnobrich 1986, Kwak 1990) have performed tests and validated the orthotropic nature of concrete on slabs and beams.

The initial numerical biaxial models based on uni-axial concrete model assumed that once the crack is formed the stiffness perpendicular to the crack and shear stiffness along the crack is zero. The use of uni-axial behaviour to represent the cracked concrete may not be completely realistic as the cracked concrete of a reinforced concrete element can still carry some tensile stress in the direction normal to crack. To take into account this effect, tension stiffening was introduced by Scanlon (1971). It has been found that tension stiffening is necessary to simulate the experimental behaviour. The tension stiffening can be considered equivalent to retaining shear stiffness after cracking as reported by Hand *et* al. (1973).

A biaxial model based on orthotropic nature of concrete is implemented in FEMIX under plane stress condition. The same model is also extended to laminar structures simulated by Mindlin Shell theory (Ventura Gouveia, 2011). The purpose of implementation of these models in FEMIX is to analyse the whole class of structure which are in plane stress condition e.g. beams, and shear-walls, and then extend the formulation for shell structures that can be modelled by Reissner-Mindlin type shell finite elements . As the uniaxial constitutive model of concrete proposed by Chang and Mander (1994) has predicted the behaviour of concrete satisfactorily, the same laws are used as in describing the equivalent uniaxial stress-strain relation of concrete.

The material model matches the existing experimental evidence for the behaviour of reinforced concrete under monotonic and cyclic loading. The model is simple to synthesize and yet robust to estimate the experimental behaviour with a satisfactory accuracy. The

implemented model does simulate the strength increase of concrete when submitted to biaxial compression, and the strength decrease when submitted to tension-compression and tension-tension, as was evidenced by experimental research, and modelled through failure functions [add references].

In a cracked plane, when the tensile strain of concrete exceeds ultimate tensile strain the tensile forces are taken up by steel. However, between adjacent cracks, still bond forces exist that are responsible for transfer of tensile forces from steel to surrounding concrete. The contribution of the concrete may be considered to increase the stiffness of the tensile reinforcement. Hence, in case of structural member if the tension stiffening is ignored, under-estimation of stiffness is observed. The tensile behaviour of the implemented model can simulate tension stiffening too.

6.1.1 Plane stress element and Laminar structures – general formulation

The Reissner-Mindlin theory (Reissner 1945, Mindlin 1951) is one of the most widely used to estimate the behaviour of laminar structures. While both plane stress and Mindlin shell uses same type of finite elements (four or eight nodded quadrilaterals), the laminar structures can be composed of several layers with distinct material characteristics. The behaviour of each layer is estimated independently for the membrane, bending and out-of-plane shear nonlinear behaviour. Several researchers (Huang 1989, Barros 1989, Barros 1995, Oñate 1995) have implemented the layered approach of laminar structures in finite element codes. This section will describe important characteristics of general multi-layer element approach, and plane stress element formulation will be described in detail in next section.

The Figure 6.1 represents the basic features of Reissner-Mindlin shell decomposed in layers. Any generic layer is represented by k with its thickness as h_k along x_3-axis. The bottom, mid and top of the k^{th} layer is represented by $x_{3,k}^{b}$, $x_{3,k}^{m}$ and $x_{3,k}^{t}$, respectively. The height of the shell element is assumed to be h, which can vary along nodes. It is assumed that the degree of freedom (u_1 and u_2) of each node allows in plane deformation and, the stress in direction x_3 is negligible compared to the other stress components. The section normal to the middle surface of the shell may not remain perpendicular to the middle

surface during deformation. This assumption is similar to the Timoshenko beam theory, where the plane sections perpendicular to the axis of beam need not be perpendicular to axis after deformation.

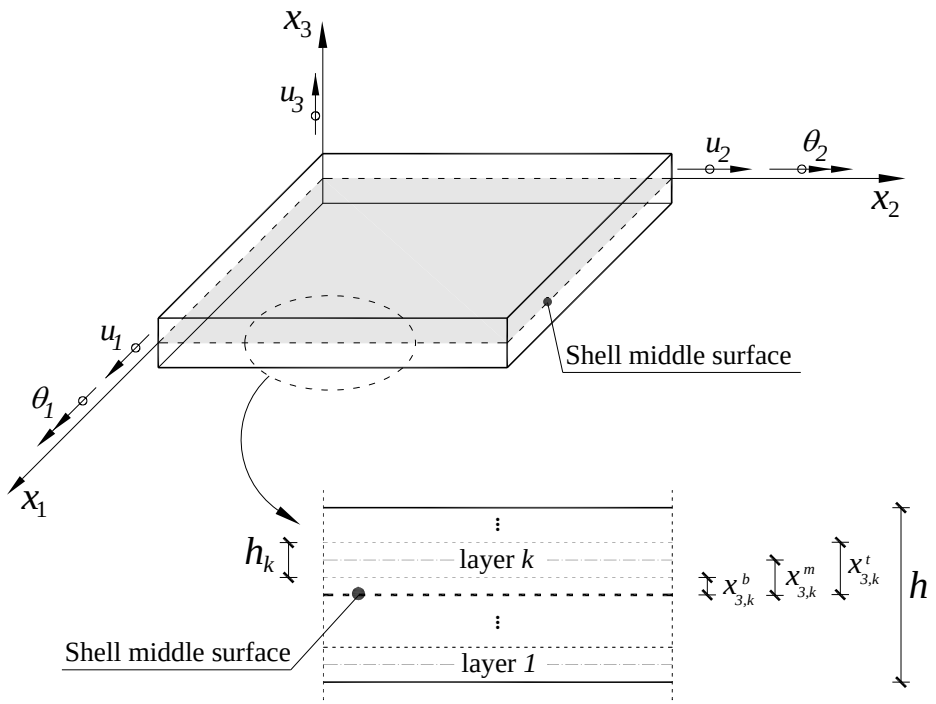

Figure 6.1: Multi-layer plane shell: displacements, rotations and *k* layer geometry definition (adapted from Ventura-Gouveia, 2011).

When the 3D shell finite element (see Figure 6.1 and Figure 6.3) is divided into layers through the thickness, the layers can be assumed of distinct thickness and material properties. The constitutive stress-strain relation of each layer is applied at middle surface of that layer.

As the in-plane strains along the thickness of the shell does not remain same as the middle surface, the strain in each layer differs, so does the stress state. Hence the contribution of stress and stiffness of each layer varies, depending on the position from the mid-surface, even if the material characteristics of different layers may be same.

Constitutive relation described in the Chapter 2 in combination with supplementary information described in later section is implemented at the finite element sampling point level for the calculation of internal equivalent nodal forces and stiffness. The algorithm

followed for the calculation of stiffness matrix and internal equivalent nodal forces for element level from its constituent layers is described in Figure 6.2. Once the displacement field at finite nodes is known, using shape functions it is converted to displacement ($\underline{a}$) at the sampling points. The strains ($\underline{\varepsilon}$) are calculated at the mid-surface of each layer by derivative operators. Once the strains are calculated at sampling point of each layer, the tangent constitutive matrix or corresponding stresses can be calculated by constitutive relation of the material for each layer. The calculated quantities are then assembled at finite element level for tangent stiffness matrix ($\underline{K}_T^e$) or internal equivalent nodal force vector ($\underline{f}_{\text{int}}^e$).

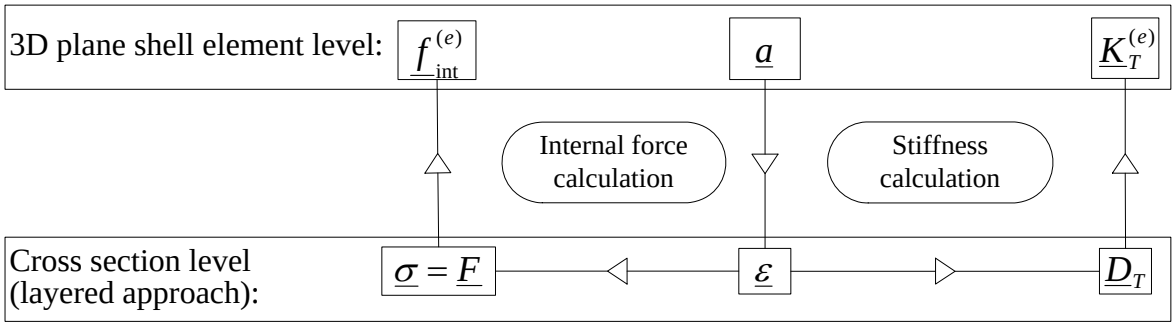

Figure 6.2: Scheme to obtain the tangent stiffness matrix and internal equivalent nodal forces of an element.

The stiffness matrix, $\underline{K}_T^{(e)}$, can be obtained from the sub-matrices associated to the membrane deformations ($\underline{K}_m^{(e)}$), membrane-bending and bending-membrane deformations, $\underline{K}_{mb}^{(e)}$ and $\underline{K}_{bm}^{(e)}$, bending deformations, $\underline{K}_b^{(e)}$, and out-of-plane shear deformations, $\underline{K}_s^{(e)}$. The matrices are represented in Appendix E, and are described in detail elsewhere (Ventura-Gouveia, 2011). The internal equivalent nodal forces generated by stresses of the layer in the structure should be equal to the equivalent externally applied loads at nodes. These internal equivalent nodal forces, represented by $\underline{f}_{\text{int}}$, are generated by the stresses developed in the distinct layers. The Figure 6.2 illustrates schematically the calculation procedure of internal forces, and the same is also described in Appendix E in detail.

(a) Plane shell element

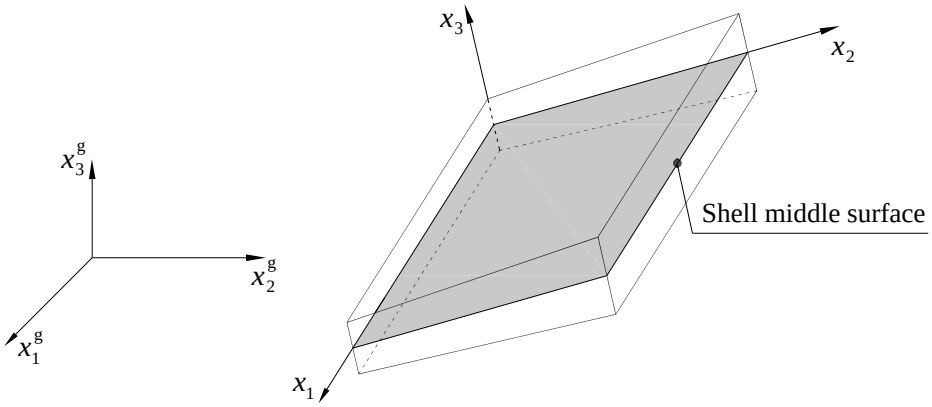

(b) Mindlin shell (3D) finite element idealization

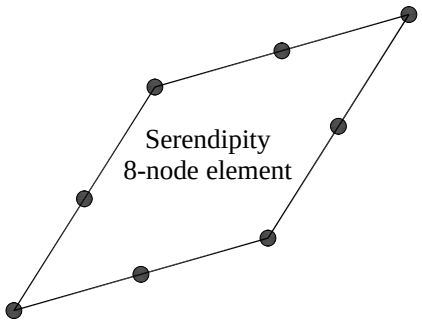

(c) Cross section multi-layer approach

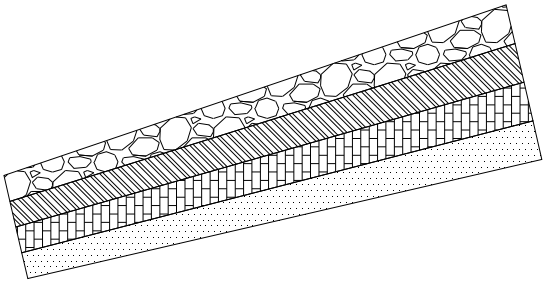

(Layers with different material properties)

Figure 6.3: Example of a finite element idealization of a plane shell element according to

the multi-layer (adapted from Ventura-Gouveia, 2011).

6.1.2 Smeared crack model

During biaxial loading, when the principal tensile stress at any point inside an element attains the maximum tensile strength, a crack is considered to form. The crack evolution can be simulated in two ways: a) Discrete crack approach, and b) Smeared or distributed crack approach.

The model developed by Hillerborg and co-workers (1976) is one of the first successful attempts to analyze the concrete fracture by a discrete crack approach. When this method was implemented, it was based on the fact that the direction of discrete cracks is predefined, while later researchers proposed the algorithms for unbiased approach of determining the crack direction, still maintaining the formation of crack along the common sides of any two adjacent concrete elements. Figure 6.4(b) shows an individual discrete crack that it is introduced between two concrete elements at their boundaries. Even though the method is more general compared to the predefined crack location, still it lacked generality, because the cracks were not allowed to form inside the element. Moreover it produced a stiffer response. Later some researchers (Gupta and Maestrini 1989, Miguel 1990) introduced the modifications, in which new elements were allowed to form and, new nodes were added along the direction perpendicular to the direction of maximum principal tensile stress. When there are only few dominant cracks and the micro level behaviour is to be of interest, the discrete crack approach is better suited. As mostly is the case, the cracks can form with unknown orientation in advance, may be significant in number, and then from computational point of view it becomes difficult to redefine the mesh and introduce new degrees of freedom. Both approaches, discrete and smeared, have their advantages and disadvantages, in case when there are very few cracks that govern the response of structure, the discrete crack approach is the possible option, but in case when the reinforcement is dense or a strain hardening cement material is used, diffuse crack patterns can be formed, which is favourable to the use of a smeared crack approach (see Figure 6.4).

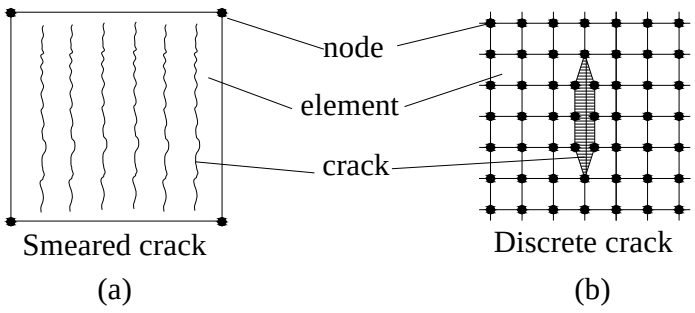

Figure 6.4: (a) Smeared and (b) discrete crack formed by nodal separation on element boundaries.

The smeared crack approach is more popular also due to three reasons:

- The crack is allowed to form in any direction;
- When the overall behaviour of the structure is important compared to the localized zones;
- During the calculation, only the stiffness matrix at integration point is changed compared to the finite element topology.

The smeared crack approach can be divided in two categories: a) fixed b) rotating crack. As soon as the maximum tensile stress at any integration point reaches the peak tensile strength for the first time, a crack is introduced at that point. The material behaviour at that point in the direction parallel to the crack and orthogonal to it, can be treated differently based on stress state induced anisotropy, directionally dependent, as opposed to isotropy (CEB-FIB 1996). It is to be noted that at the instant of crack formation, the direction of principal stress coincides with the direction of principal strain. The crack can be assumed in local coordinate system (hereafter crack coordinate system), defined by ***ns***-coordinate system, where ***n*** and ***s***-axes represent the direction normal and tangential to crack, respectively. In fixed crack approach, the direction of ***n***-axis (normal to the crack) is fixed, as one of the orthotropic direction for the rest of analysis/response. This permanent allocation of damage is the main characteristic of fixed crack approach. During subsequent loading the ***n*** and ***s*** coordinate axis may not remain the new principal directions of stress and strain. If a new principal stress is calculated, then it may exceed the tensile strength, and should be a criterion for another crack.

But as the direction of ***n*** and ***s*** axes are fixed and the condition of cracking is checked for only ***s***-direction and not any direction in between these axes. Hence, a new crack can form only in the ***n***-direction. This results in much stiffer response, and can be avoided by assuming non-orthogonal cracks (Rots and Blaauwendraad 1989, Crisfield and Wills 1989, Barzegar 1989) to form. de Borst and Nauta (1985) proposed a strategy in which if the angle between previously calculated principal stress and newly calculated principal stress exceeds the empirically defined threshold angle, then a new crack is recorded. Cervenka (1985) has also investigated the non-orthogonal fixed crack approach but assumed no threshold angle concept, which is found to have no discontinuity as also discussed by Chrisfield and Wills (1989). These models assume either secant or elastic unloading. Some algorithms retain the crack closing in memory, while some assume the crack to become inactive and new cracks are formed. Moreover it is to be noted that fracture energy (Barros 1995) available to new cracks keep decreasing as some part of it is utilized in the previous cracks formed at that gauss point. The fixed crack approach produces stiffer than actual response, with overestimated ultimate load. The rotating crack proposed by (Gupta and Akbar, 1983) is capable to resolve this up to some extent as investigated by other researchers (Balakrishnan and Murray 1988, Hu and Schronobrich 1990, Vecchio and Collins 1982). In this approach the direction of principal stresses are calculated for every load increment; all over again, without retaining the previous principal stress orientation. As the principal stress orientation is calculated for each increment of load combination; the direction of crack keeps rotating. The newly formed crack is a symbolic representation and may not be a physical phenomenon; still it follows most predominant or active crack at that point. The total stress and strains are (Gupta and Akbar, 1983) calculated in global coordinates from the principal values by appropriate transformation matrix.

It has been reported that rotating crack approach produces less stiff response than the non-orthogonal fixed crack model (CEB FIB: State of art, 1996). However, smeared crack approach has a drawback of stress-locking in the vicinity of dominant discrete crack, still it is less severe in case of rotating crack approach. In smeared crack approach, when a crack is formed in any element, it results in softening of that element; if further strain increment happens for that element, because of displacement continuity, the neighbouring un-cracked element are forced to follow it, a spurious increase in the stress of un-cracked element is observed. This is contrary to the strain localization and undesirable.

6.2 GENESIS OF BIAXIAL CONCRETE CONSTITUTIVE LAWS USING UNI-AXIAL CONCRETE LAWS

The concrete can be assumed to follow linear elastic isotropic behaviour until cracking. In global ***xy*** coordinate system, based on the total strain approach, the constitutive relationship is described as:

$$\underline{\sigma}_{xy} = \underline{D}_{xy}\,\underline{\varepsilon}_{xy} \tag{6.1a}$$

$$\begin{bmatrix} \sigma_x \\ \sigma_y \\ \sigma_{xy} \end{bmatrix} = \frac{E}{1-\nu^2}\begin{bmatrix} 1 & \nu & 0 \\ \nu & 1 & 0 \\ 0 & 0 & (1-\nu)/2 \end{bmatrix}\begin{bmatrix} \varepsilon_x \\ \varepsilon_y \\ \gamma_{xy} \end{bmatrix} \tag{6.1b}$$

where E and ν are the elasticity modulus and the Poisson's ratio of concrete, respectively; σ_x and σ_y are normal stresses in ***x*** and ***y*** direction, and ε_x and ε_y are the corresponding normal strains; τ_{xy} is the shear stress in ***xy*** plane corresponding to shear strain γ_{xy}.

Once the concrete is cracked, it can be assumed to follow orthotropic behaviour. The direction of orthotropy can coincide with the direction of principal stresses as proposed by Elwi and Murray (1979).

Assuming that the stresses are not coupled in the crack local coordinate system, Eq. (6.1(a-b)) will be replaced by:

$$\underline{\sigma}_{ns} = \underline{D}_{ns}\,\underline{\varepsilon}_{ns} \tag{6.2a}$$

$$\begin{bmatrix} \sigma_n \\ \sigma_s \\ \tau_{ns} \end{bmatrix} = \begin{bmatrix} E_n & 0 & 0 \\ 0 & E_s & 0 \\ 0 & 0 & G_{ns} \end{bmatrix}\begin{bmatrix} \varepsilon_n \\ \varepsilon_s \\ \gamma_{ns} \end{bmatrix} \tag{6.2b}$$

where σ_n and σ_s are normal stresses corresponding to ε_n and ε_s, respectively; τ_{ns} is the shear stress corresponding to γ_{ns}, shear strain in ***ns*** plane; E_n and E_s are tangential moduli in ***n*** and ***s*** direction, respectively, while G_{ns} is the shear modulus in ***ns*** plane. It is

to be noted that the local shear stress component τ_{ns} of the stress vector $\underline{\sigma}_{ns}$ is always zero according to the definition of the rotating crack model.

Consider the situation of plane stress, where initial co-axiality between principal stress, strain and material orthotropy is already established. From Mohr's strain circle, it can be established that a small increment of γ_{ns} causes the direction of principal strains to rotate by an angle (θ_{γ}) as illustrated by:

$$\tan(2\theta_{\gamma})=\frac{\Delta\gamma_{ns}}{2(\varepsilon_n-\varepsilon_s)} \tag{6.3}$$

Similarly, from Mohr's stress circle, it can be established that a small increment of τ_{ns} causes the direction of principal stresses to rotate by an angle (θ_{τ}) as illustrated by:

$$\tan(2\theta_{\tau})=\frac{\Delta\tau_{ns}}{2(\sigma_n-\sigma_s)} \tag{6.4}$$

To maintain the co-axiality between principal stress and strain, it requires that $\theta_{\gamma}=\theta_{\tau}$. From Eq. (6.3) and (6.4), this condition can only be fulfilled if the tangential shear modulus G_{ns} is described by Eq (6.5).

$$G_{ns}=\frac{(\sigma_n-\sigma_s)}{2(\varepsilon_n-\varepsilon_s)} \tag{6.5}$$

The local strains of ***ns*** coordinate system are derived from global strain vector by Eq. (6.6).

$$\underline{\varepsilon}_{ns}=\overline{\underline{T}}_{ns}(\theta)\underline{\varepsilon}_{xy} \tag{6.6}$$

where $\overline{\underline{T}}_{ns}(\theta)$ is the strain transformation matrix, to convert entities from global ***xy*** coordinate system to ***ns*** coordinate system, and the angle between ***x***-axis and ***n***-axis is represented by θ. Being it a rotating crack approach, the crack keeps rotating, consequently, θ keeps changing. Similarly, the stresses and the constitutive matrix ($\underline{\sigma}_{xy}$; $\overline{\underline{D}}_{xy}$) in global coordinate system can be calculated from those in the crack local coordinate system by:

$$\underline{\sigma}_{xy} = \overline{\underline{T}}^{T}_{ns}(\theta)\underline{\sigma}_{ns} \tag{6.7}$$

$$\overline{\underline{D}}_{xy} = \overline{\underline{T}}^{T}_{ns}(\theta)\overline{\underline{D}}_{ns}\overline{\underline{T}}_{ns}(\theta) \tag{6.8}$$

He *et* al. (2008) have assumed the effect of Poisson's ratio as described by Eq. (6.9) during post-cracking.

$$\begin{bmatrix} \varepsilon_n^* \\ \varepsilon_s^* \end{bmatrix} = \frac{1}{1-\nu^2}\begin{bmatrix} 1 & \nu \\ \nu & 1 \end{bmatrix}\begin{bmatrix} \varepsilon_n \\ \varepsilon_s \end{bmatrix} \tag{6.9}$$

where ε_n^* and ε_s^* are equivalent strains in ***ns*** coordinate system. It is to be noted that ε_n^* and ε_s^* does not represent exact principal strains, but they represent modified principal strains in the principal directions. The stresses in ***ns*** coordinate system are evaluated from the equivalent strain using uni-axial stress strain constitutive models as presented in Chapter 2. Hence from hereafter, the ε_n^* and ε_s^* will be represented by common symbol, ε_c.

One of the important assumptions in the formulation is based on realistic condition is that the principal strain (ε_i) at any sampling point in *i*-direction (*i*=*n, s*) is the sum of an elastic (ε_i^{el}) and a cracked concrete (ε_i^{cr}) component. The assumptions of the modifications are: principal strains are assumed independent to each other in calculation; only elastic part of principal strain is used to calculate the Poisson's effect, for one direction to other direction of ***ns*** co-ordinate system.

$$\varepsilon_i = \varepsilon_i^{el} + \varepsilon_i^{cr} \tag{6.10}$$

The Eq. (6.9) can be modified to take into account this effect as:

$$\begin{bmatrix} \varepsilon_n^* \\ \varepsilon_s^* \end{bmatrix} = \frac{1}{1-\nu^2}\begin{bmatrix} 1 & \nu \\ \nu & 1 \end{bmatrix}\begin{bmatrix} \varepsilon_n^{el} \\ \varepsilon_s^{el} \end{bmatrix} + \begin{bmatrix} \varepsilon_n^{cr} \\ \varepsilon_s^{cr} \end{bmatrix} \tag{6.11}$$

Consider a biaxial loading situation of a single finite element, and the principal strain in ***n***-direction and ***s***-direction are calculated as ε_n and ε_s, respectively. The incremental strain

can be tensile or compressive in nature. For the first time, if the condition of tensile maximum strength is violated *only* in ***n***-direction, then the Poisson effect, see Eq.(6.9)) from ***n***-direction to ***s***-direction will cease from this moment onwards. But it should be noted that the contribution of strain to ***s***-direction will still be there due to elastic strain component only (ε_s^{el}, using Eq. (6.11)). As the strain in ***s***-direction has not violated the maximum strength criteria, no cracks will form in this direction and hence it will still act as a continuum of concrete. Moreover, concrete in this direction will be able to contribute to strain in ***n***-direction.

6.2.1 Concrete constitutive model

The uniaxial model of concrete in compression and hysteretic scheme (compression and tension both) described in Chapter 2 is used for ***ns*** directions, while only tension envelope is assumed to be a tri-linear curve as it is different from the one described in Chapter 2; however the entities will be in similar format.

The tension envelope is simulated by linear elastic behaviour until cracking and, by tri-linear branches for post cracking behaviour, as represented in Figure 6.5. The stress-strain relationship for tension envelope until cracking is illustrated by Eq (6.12):

$$f_c^+ = E_c\ \varepsilon_c \ \text{ for } 0 \le \varepsilon_c \le \varepsilon_c^{cr} \tag{6.12}$$

where E_c is the Young's modulus and ε_c^{cr} is the initial cracking strain derived as

$$\varepsilon_c^{cr} = f_c^{cr} \Big/ E_c \tag{6.13}$$

where f_c^{cr} is the concrete tensile strength.

The ultimate cracking strain (ε_c^u) is calculated from fracture energy (G_f), trilinear stress-strain parameters ($\alpha_1, \alpha_2, \beta_1, \beta_2$) and crack band width ($l_b$). The ε_c^u, is calculated by Eqn (6.14) as described by (Barros 1995, Sena-Cruz 2005). One of the drawbacks of this type of softening approach is the dependence of the results on the mesh refinement, which means that if no corrective steps are taken, the results are dependent up on mesh size used in the simulation. To assure mesh objectivity the crack band width can be assumed to be

square root of the area of sampling point under consideration, as proposed by researchers (Rots 1988).

$$\varepsilon_c^u = \left(\frac{2}{\beta_1 + \alpha_1\beta_2 - \alpha_2\beta_1 + \varepsilon\alpha_2} \right) \frac{G_f}{f_c^{cr} l_b} \tag{6.14}$$

Once the ultimate cracking strain is calculated, the strains and stresses at the end of first and second branches can be calculated (see Figure 6.5). The stress-strain relations for post-cracking behaviour can be described as:

$$f_{ct} = f_c^{cr} + (\varepsilon_{ct} - \beta_1\varepsilon_c^u) \frac{f_c^{cr}(1-\alpha_1)}{\varepsilon_c^{cr} - \beta_1\varepsilon_c^u} \text{ for } \varepsilon_c^{cr} \le \varepsilon_{ct} \le \beta_1\varepsilon_c^u \tag{6.15a}$$

$$f_{ct} = \alpha_2 f_c^{cr} + (\varepsilon_{ct} - \beta_2\varepsilon_c^u) \frac{f_c^{cr}(\alpha_1 - \alpha_2)}{\varepsilon_c^u(\beta_1 - \beta_2)} \text{ for } \beta_1\varepsilon_c^u \le \varepsilon_{ct} \le \beta_2\varepsilon_c^u \tag{6.15b}$$

$$f_{ct} = (\varepsilon_{ct} - \varepsilon_c^u) \frac{f_c^{cr}\alpha_2}{\varepsilon_c^u(\beta_2 - 1)} \text{ for } \beta_2\varepsilon_c^u \le \varepsilon_{ct} \le \varepsilon_c^u \tag{6.15c}$$

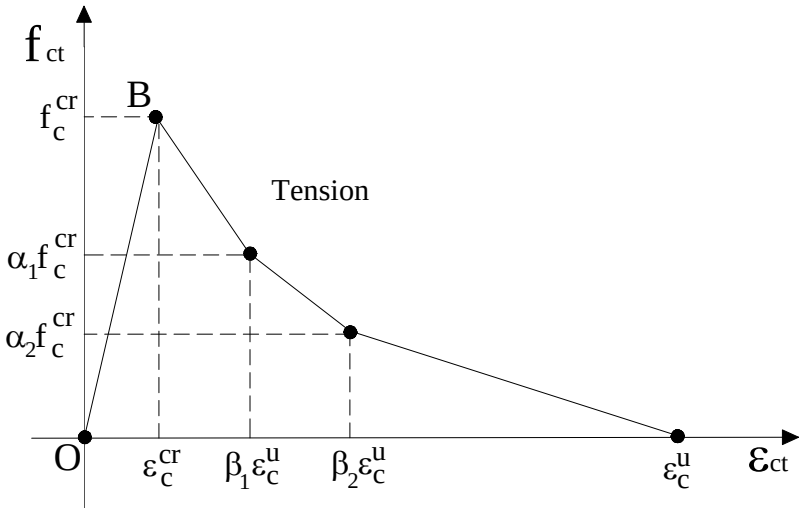

Figure 6.5: Tensile envelope curve used in constitutive models.

6.2.2 Modelling of steel

The steel reinforcement can be modelled in three ways, namely, smeared reinforcement, embedded cable and discrete steel models (ASCE Task Committee, 1982, Chapter 3). FEMIX already has two types of model, embedded cable and discrete cable element. The smeared reinforcement model was implemented in FEMIX, under the framework of laminar structures.

In the context of smeared reinforcement formulation, the reinforcing steel is assumed to be distributed uniformly over concrete element at a certain angle of orientation. From the point of view of finite element, the stiffness and internal stresses of this element is assumed along the angle of orientation only. The cyclic constitutive model described in Chapter 2, was adopted in the direction of orientation. The implementation procedure of smeared reinforcement is described elsewhere (Vechhio and Collins, 1986). One of the drawbacks of the smeared reinforcement model is that it cannot simulate bond-slip, hence discrete reinforcement models need to be adopted in such cases.

6.3 MODEL APPRAISAL

In order to validate the implemented rotating crack model and address the important characteristics of it, experimental data (Oesterle *et* al. 1976, Barros and Dias 2006) and hypothetical data (Rots 1988) by independent group of researchers have been selected. The simulated examples were distinct in nature based on structural form and load combination.

6.3.1 Tension-Shear model problem

The hypothetical test example carried out by Willam *et* al. (1987) represent the tension shear model problem, which is assumed to be a benchmark, as the response of it has been discussed by various researchers in perspective of comparing different kinds of cracking models, for example fixed cracks *versus* rotating cracks, orthogonal cracks *versus* non-orthogonal cracks. In this section, results obtained by Rots (1988) are compared to the proposed implemented model. Rots (1988) simulated the result with *pure* rotating crack model.

A quadrilateral element of unit length is assumed as shown in Figure 6.6. The material properties used are represented in Table 6.1. The post peak behaviour of concrete is assumed to be linear and the ultimate strain is 3×10^{-4} mm/mm. The problem assumes tensile loading of a specimen in the ***x***-direction in combination with Poisson contraction in ***y***-direction until a vertical crack initiates (see Figure 6.6(a)), the incremental strain pattern considered is described as:

$$\Delta\varepsilon_{xx} : \Delta\varepsilon_{yy} : \Delta\gamma_{xy} = 1 : -\nu : 0 \tag{6.16}$$

As soon as the crack appears, the specimen loading is switched to biaxial tension and shear (see Figure 6.6(b)). The second combination of loading is described as:

$$\Delta\varepsilon_{xx} : \Delta\varepsilon_{yy} : \Delta\gamma_{xy} = 0.5 : 0.75 : 1 \tag{6.17}$$

It causes the principal stress directions to rotate, consequently *rotation of crack* starts. However the smeared crack model proposed by Rots (1988) and in this study is slightly different; some of the details are investigated in perspective of *pure* rotating crack model of Rots (1988).

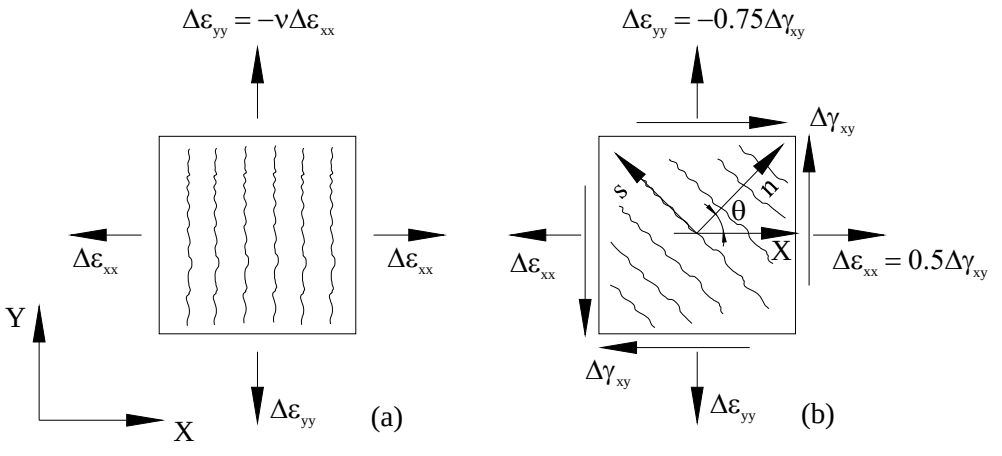

Figure 6.6: Tension-shear model with load combinations (a) tension up to cracking (b) Biaxial tension-compression with shear stress.

The rotating angle of principal stress (θ, see Figure 6.6) obtained from FEMIX is plotted on the normal strain in ***y***-direction and compared to results of Rots (see Figure 6.7), which show complete match.

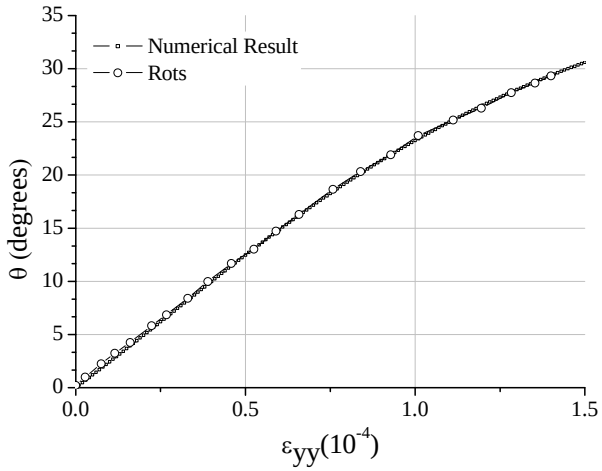

Figure 6.7: Rotation of principal tensile stress axis with respect to global ***x***-axis.

The first crack is registered after the end of loading condition described by Eq. (6.16), at the principal strains coincide the global strains in ***x*** and ***y*** direction, respectively. When the switch is made to loading condition described by Eq. (6.17), the principal strains are calculated from global strains ($\begin{bmatrix}\varepsilon_x & \varepsilon_y & \gamma_{xy}\end{bmatrix}^T$). These principal strains ($\begin{bmatrix}\varepsilon_n & \varepsilon_s\end{bmatrix}^T$) are then modified according to Eq. (6.11) to obtain $\begin{bmatrix}\varepsilon_n^* & \varepsilon_s^*\end{bmatrix}^T$. The normal stresses is found from these strain according to constitutive law.

As can be seen from Figure 6.8, where the normal stress in ***x***-direction is plotted with respect to normal strain in the ***x***-direction, difference in calculation of normal stress is found in post cracking behaviour. The strain exceeds the cracking strain only in ***n***-direction and hence only the elastic strain component (ε_n^{el}) of ***n***-direction will contribute to ***s***-direction (using Eq. (6.11)). The other component of ***n***-direction, i.e. ε_n^{cr} will not contribute to strain in ***s***-direction, as described by Eq. (6.11). As ***s***-direction does not have any crack, hence it has only elastic component (ε_s^{el}) and it will contribute to ***n***-direction due to Poisson effect (Eq. (6.11)). Due to these assumptions, the model is not able to estimate

exact principal stresses, which are later converted to global stresses. The estimated normal stresses in ***x*** and ***y***-direction (see Figure 6.8 and Figure 6.9) show little difference.

Table 6.1: Values of the mechanical properties of the concrete used in tension-shear problem

Initial Young Modulus, E_c (GPa)	10.0
Poisson's ratio, ν	0.2
Peak compressive strength of confined concrete, f_{cc} (MPa)	10.0
Peak compressive strain, ε_{cc} (mm/mm)	3.7×10^{-3}
Non-dimensional critical strain on the compression envelope, $\bar{\varepsilon}_{ccr}$ (mm/mm)	5.0×10^{-3}
Peak tensile strength, f_{ct} (MPa)	1.0
Peak tensile strain, ε_{ct} (mm/mm)	1.0×10^{-4}
Fracture Energy, G_f (N/mm^2)	1.5×10^{-4}
Ratio between the strain at the first post-peak point and ultimate strain, α_1	0.4
Ratio between the stress at the first post-peak point and peak tensile strength, β_1	0.9
Ratio between the strain at the second post-peak point and ultimate strain, α_2	0.5
Ratio between the stress at the first post-peak point and peak tensile strength, β_2	0.75
Crack band width, l_b (mm)	1.0

One of the critical features of the rotating crack approach is to introduce implicit shear softening and shear-normal stress coupling, without the need to model shear, which is

necessary in fixed crack modelling. The Figure 6.10 illustrates that the shear stress increases to a certain maximum value and then decreases to zero, which is characteristic behaviour of rotating crack models and cannot be simulated by fixed crack models. However as explained earlier that the principal stresses does not match the principal stresses estimated by Rots (1988). And the global stresses in this approach are derived from principal stresses, which in turn are not derived from exact principal strains. Hence the shear stress in global co-ordinate system (see Figure 6.10) is underestimated in this case.

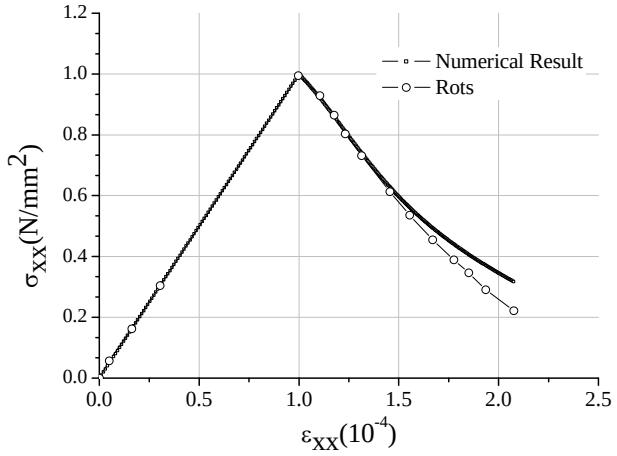

Figure 6.8: Normal stress-strain response in x direction.

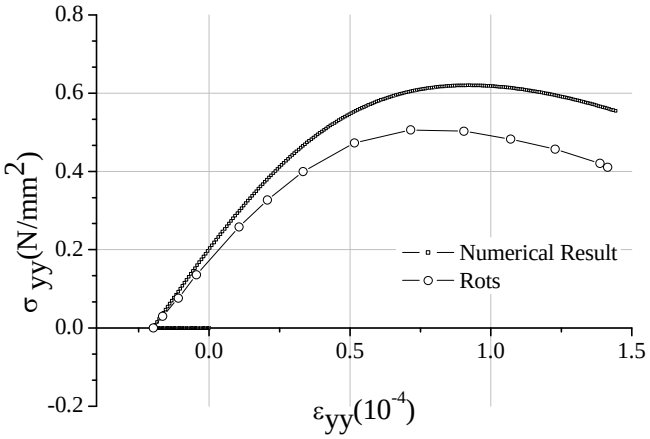

Figure 6.9: Normal stress-strain response in y direction.

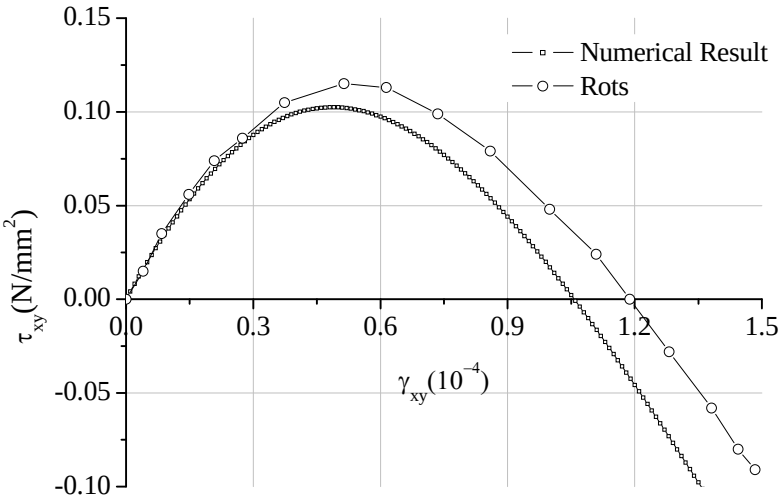

Figure 6.10: Shear stress-strain response in ***xy*** plane.

6.3.2 Monotonic loading tests

An experimental program of four-point bending tests was carried out with reinforced concrete beams failing in shear by Barros and Dias (2006). The experimental program is composed of beams without any shear reinforcement and reinforced with steel stirrups. The beams which are simulated by FEMIX belong to A10 and A12 series. Figure 6.11 shows the geometry, loading and support conditions of the tested beams. Each series is made up of beams without any shear reinforcement (A10, A12) and beam reinforced with steel stirrups of $\phi 6$ (A10_S, A12_S). Beams A10 and A12 have a cross section of 150×300 mm^2 and a span length of 1500 mm. The A10 and A12 had $4\phi 10$ and $4\phi 12$ steel bars at beam bottom tensile surface, respectively. At the top surface all the beams were reinforced with $2\phi 6$ steel bars. The concrete clear cover for the top, bottom and lateral faces of the beams was 15 mm. A more complete and extensive description of experimental program is described by Barros and Dias (2006).

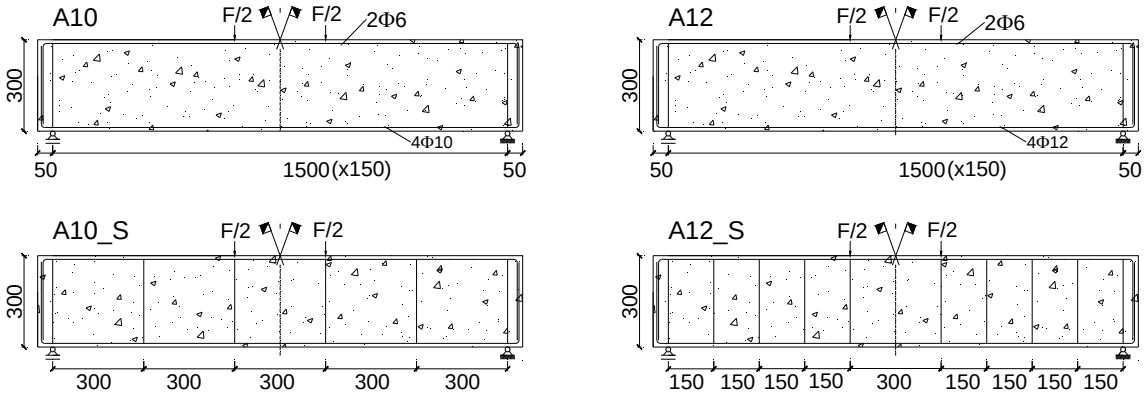

Figure 6.11: The geometry and loading configuration of the beams for A10 and A12 series. Note: all the dimensions are in mm.

Due to symmetry, only half of the beam is considered for the simulations, using the mesh topology as described in Figure 6.12. The beam was divided in 112 quadrilateral finite elements. The steel bars were assumed to be perfectly bonded and embedded into the confined concrete. Hence, the longitudinal and transverse steel reinforcements are simulated with 3-node two dimensional embedded cable elements, and concrete is simulated by 8-node plane stress quadrilateral elements. Two Gauss-Legendre integration points along the longitudinal axis of embedded cable, and 3×3 Gauss-Legendre integration points for the plane stress element were used for the calculation of the stiffness and internal equivalent nodal forces.

The post-cracking behaviour of reinforced concrete is simulated by tri-linear stress-strain tension diagram. Two types of post-cracking diagrams were used: tension–softening and tension–stiffening. The tension–softening and tension–stiffening regions are represented by ABCDA and BEFCA (see Figure 6.12), respectively. It can be expected that the cracks will form on tensile surface of beam. At the cracked planes where tensile strain is more than ultimate strain of concrete, the stress bore by steel bars is higher compared to other section along the bar. Hence tension stiffening law is introduced for ABCDA region, and the post cracking parameters of the concrete were modified as depicted in Table 6.4. The compressive strength was determined from experimental tests, however other parameters were suitably adjusted according to described elsewhere (Sena-Cruz 2005). The parameters

described in Table 6.2 and Table 6.3 are used for the constitutive modelling of steel and evaluated experimentally by Barros and Dias (2006).

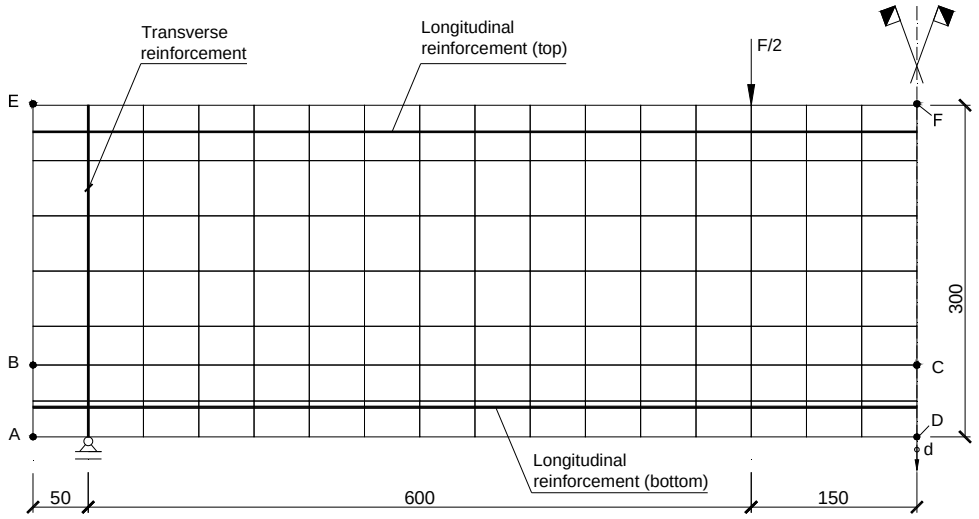

Figure 6.12: The finite element mesh topology for the beams for A10 and A12 series (adapted from Sena-Cruz 2005).

Figure 6.14(a-b) and Figure 6.15(a-b) shows that the implemented model was able to simulate, with enough accuracy, the RC beams subjected to monotonic loading. However, in simulation of A10 and A12, sudden loss of strength is predicted, which might have been due loss of strength generated due to crack close to support and due to opening of spurious cracks. From the numerical crack pattern shown for A10 at 1.55 mm and 1.85 mm displacement, (see Figure 6.13(a) and (b)) and, it is revealed that the already formed vertical cracks kept opening and start spreading near the bottom reinforcement towards support. The numerical crack pattern for A10 and A12 reveals that the cracks are formed near the bottom reinforcement. The appearance of vertical cracks seems to be spurious in nature (see Figure 6.14(c) and Figure 6.15(c)). This spurious cracking in not observed in case of A10_S and A12_S (see Figure 6.14(d) and Figure 6.15(d)). In rotating crack model, shear is modelled implicitly as a consequence of principal stress. The crack pattern observed experimentally in A10 and A12 (see Figure 6.14(e) and Figure 6.15(e)) shows that the cracks are more discrete in nature when compared with the counterpart A10_S and A12_S (see Figure 6.14(f) and Figure 6.15(f)), correspondingly, where the cracks are more smeared. Similarly the numerical crack pattern observed for the beams A10_S and A12_S

show smeared cracking, which is because of available shear reinforcement. Due to continuous shear reinforcement, the large and discrete cracks are not formed, a characteristic of high reinforcement. As the reinforcement is increased and spread uniformly, diffused and smeared cracks are formed. Moreover when A10_S and A12_S are compared (see Figure 6.14(d) and Figure 6.15(d)), it can be observed that the shear reinforcement was higher in A12_S, and, due to this the cracks are even more uniform and smeared in A12_S.

Table 6.2: Data used in A_10 series for the behaviour of the steel bars.

Parameter	$\Phi 6^T$	$\Phi 6^L$	$\Phi 10^L$
Initial Young Modulus, E_s (GPa)	200	200	200
Tangent modulus at strain hardening, E_{sh} (GPa)	6.4	6.4	6.4
Yielding strain, ε_{sy} (mm/mm)	2.7×10^{-3}	3.11×10^{-3}	2.32×10^{-3}
Yielding stress, f_{sy} (MPa)	540.0	622.0	464.0
Hardening strain, ε_{sh} (mm/mm)	1.0×10^{-2}	1.0×10^{-2}	1.0×10^{-2}
Hardening stress, f_{sh} (MPa)	545.0	645.0	465.0
Strain at the ultimate stress, ε_{su} (mm/mm)	1.8×10^{-2}	1.8×10^{-2}	1.8×10^{-2}
Ultimate stress, f_{su} (MPa)	548.0	648.0	468.0

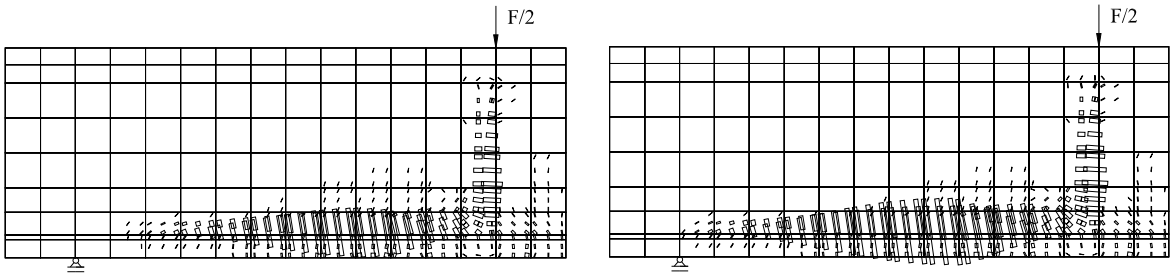

(a) (b)

Figure 6.13: Crack pattern predicted from FEMIX at (a) 1.55mm and (b) 1.85mm (cracks with open, opening, completely open status is shown)

Table 6.3: Data used in A_12 series for the behaviour of the steel bars.

Parameter	$\Phi 6^T$	$\Phi 6^L$	$\Phi 12^L$
Initial Young Modulus, E_s (GPa)	200	200	200
Tangent modulus at strain hardening, E_{sh} (GPa)	6.4	6.4	6.4
Yielding strain, ε_{sy} (mm/mm)	2.7×10^{-3}	3.09×10^{-3}	2.85×10^{-3}
Yielding stress, f_{sy} (MPa)	540.0	618.0	571.0
Hardening strain, ε_{sh} (mm/mm)	1.0×10^{-2}	1.0×10^{-2}	1.0×10^{-2}
Hardening stress, f_{sh} (MPa)	545.0	691.0	670.0
Strain at the ultimate stress, ε_{su} (mm/mm)	1.8×10^{-2}	1.8×10^{-2}	1.8×10^{-2}
Ultimate stress, f_{su} (MPa)	548.0	695.0	673.0

^{T} = Transverse reinforcement; ^{L} = Longitudinal reinforcement

Table 6.4: Data used in A_10 and A_12 series to simulate the concrete behaviour.

Parameter	A10	A10_S	A12	A12_S
Poison's ratio, ν	0.2	0.2	0.2	0.2
Initial Young Modulus, E_c (GPa)	32.7	32.7	38.0	38.0
Peak compressive strength of concrete, f_{cc} (MPa)	49.2	49.2	56.2	56.2
Peak compressive strain, ε_{cc} (mm/m)	2.5	2.5	2.5	2.5
Non-dimensional critical strain on the compression envelope, ε^{-}_{ccr} (mm/m)	3.0	3.0	5.0	5.0
Peak tensile strength, f_{ct} (MPa)	2.85	2.85	3.1	3.1
Peak tensile strain, ε_{ct} (mm/m)	0.078	0.078	0.0815	0.0815
Fracture energy, G_f (N/mm^2)	0.12	0.12	0.15	0.15
Tension softening diagram, (α_1, β_1, α_2, β_2)	α_1=0.10; β_1=0.50; α_2=0.30; β_2=0.20	α_1=0.10; β_1=0.50; α_2=0.30; β_2=0.20	α_1=0.12; β_1=0.52; α_2=0.75; β_2=0.32	α_1=0.12; β_1=0.52; α_2=0.75; β_2=0.32
Tension stiffening diagram, (α_1, β_1, α_2, β_2)	α_1=0.05; β_1=0.55; α_2=0.85; β_2=0.13	α_1=0.05; β_1=0.55; α_2=0.85; β_2=0.13	α_1=0.05; β_1=0.30; α_2=0.40; β_2=0.10	α_1=0.05; β_1=0.30; α_2=0.40; β_2=0.10
Crack band width, l_b	SQRT_IP	SQRT_IP	SQRT_IP	SQRT_IP

where SQRT_IP = square root of area of the integration point.

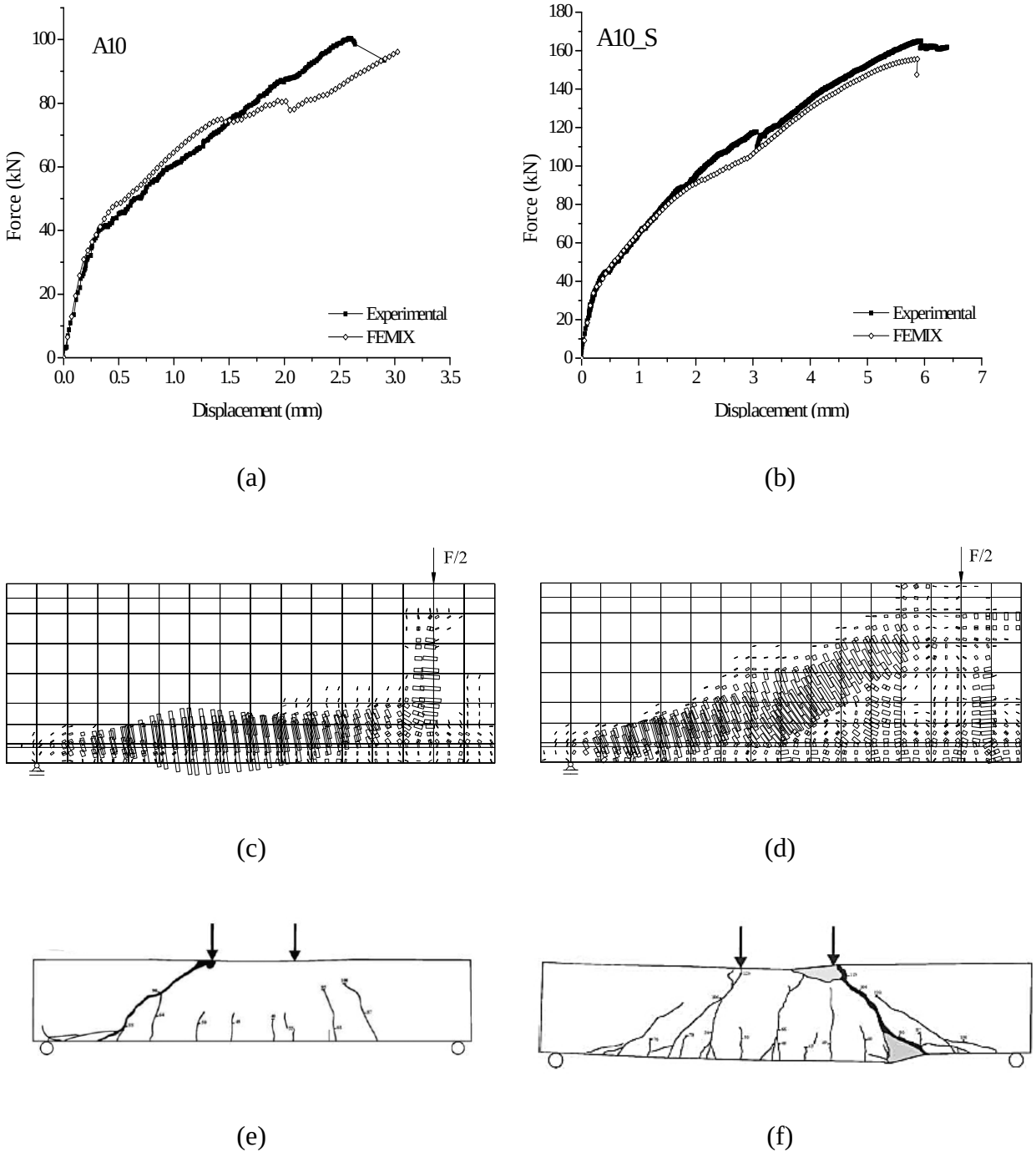

Figure 6.14: (a)-(b) Load *vs* deflection at mid-span obtained experimentally and numerically; (c)-(d) crack pattern predicted from FEMIX (cracks with open, opening, completely open or closing status is shown) and; (e)-(f) experimental crack pattern observed for the beams A10 and A10_S (Barros and Dias 2006)

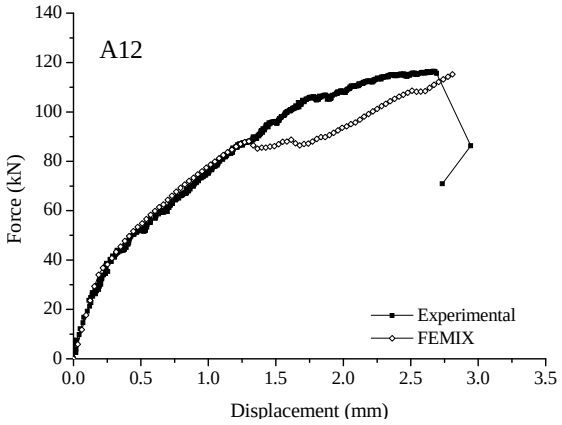

(a)

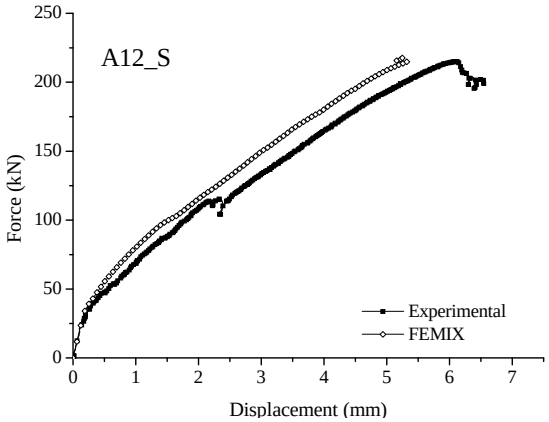

(b)

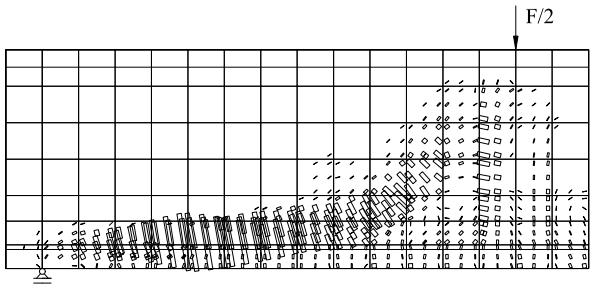

(c)

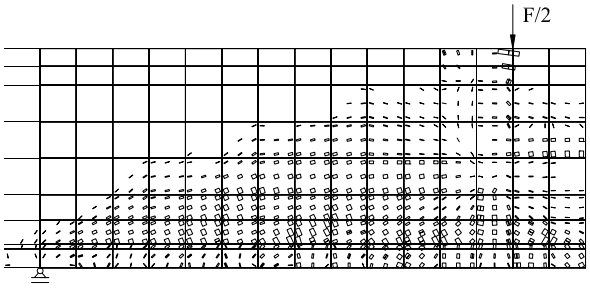

(d)

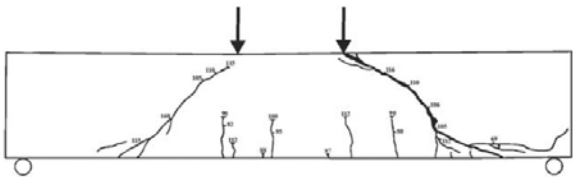

(e)

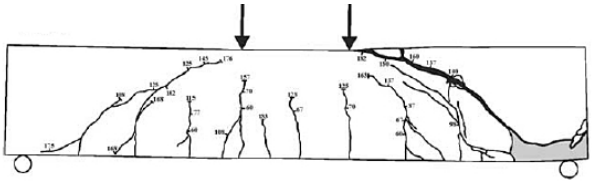

(f)

Figure 6.15: (a)-(b) Load *vs.* deflection at mid-span obtained experimentally and numerically; (c)-(d) crack pattern predicted from FEMIX (cracks with open, opening, completely open or closing status is shown) and; (e)-(f) experimental crack pattern observed for the beams A12 and A12_S (Barros and Dias 2006)

6.3.3 Cyclic loading test

To validate the cyclic laws a barbell-shaped shear wall B2, which was tested by Oesterle *et* al. (1976) at the Portland Cement Association, was used for the numerical analysis. The isolated shear wall B2 (hereafter shear wall) was approximately 1/3-scale models of full size walls, and was composed of wall web and boundary elements (see Figure 6.16(a)), which were sandwiched between stiff base block and stiff top slab. The wall was tested like a vertical cantilever with reversing horizontal displacements applied through the top slab. The boundary element was 4570 mm (high) × 305 mm (long) × 305 mm (thick) and the vertical reinforcement in it amounted to 3.67% ($12\phi 20$). The wall web was 4570 mm (high) × 1910 mm (long) × 102 mm (thick), and was reinforced with 0.28% ($12\phi 6$) in the vertical direction. The horizontal reinforcement of $\phi 6$ was placed uniformly throughout the wall web at 203 mm distance and, was extended inside the boundary elements. In boundary elements the horizontal ties (see Figure 6.16(b)) were placed simultaneously with web ties.

The stiff top slab of shear wall was subjected to cyclic horizontal displacement as illustrated in Figure 6.17(a), where every displacement cycle was repeated two times, before the extreme displacement of the next cycle was incremented by 25 mm in each direction.

The shear wall can be divided in three zones to reflect the change in cross section and discretizing in mesh, namely side walls, wall web and top slab. The side walls were divided in 40, the wall web in 200 and the top slab in 18; four-node quadrilateral elements, of uniform shape in their respective zone (see Figure 6.16 (b)). All the elements were discretized in 11 layers, namely layer pattern. All the zones followed the same layer pattern. Each element can be considered to be composed of three layers of steel (two horizontal and one vertical), two concrete cover layers and six layers of confined concrete. For the concrete cover and confined concrete it was assumed the same constitutive model, and the properties of the concrete are represented in Table 6.5. The steel bars were modelled smeared in this analysis and the properties of horizontal and longitudinal steel reinforcement is described according to the rebar type in Table 6.6. The concrete tensile properties were derived according to He *et* al. (2008), however the compressive properties

of concrete and mechanical properties of steel reinforcement is derived from Oesterle *et* al. (1976). All the layers assumed 2×2 Gauss-Legendre integration scheme for the Mindlin shell element in the calculation of the stiffness and internal equivalent nodal forces. The displacements of the side wall and wall web were constraint at bottom to replicate the displacement of base block.

Table 6.5: Data used in constitutive model of concrete for simulation of shear wall B2.

Poisson's ratio, ν	0.2
Initial Young Modulus, E_c (GPa)	32.7
Peak compressive strength of concrete, f_{cc} (MPa)	53.7
Peak compressive strain, ε_{cc} (mm/mm)	2.5×10^{-3}
Non-dimensional critical strain on the compression envelope, $\bar{\varepsilon}_{ccr}$ (mm/mm)	2.55×10^{-3}
Peak tensile strength, f_{ct} (MPa)	4.29
Peak tensile strain, ε_{ct} (mm/mm)	7.8×10^{-5}
Fracture energy, G_f (N/mm^2)	0.20
Ratio between the strain at the first post-peak point and ultimate strain, α_1	0.10
Ratio between the stress at the first post-peak point and peak tensile strength, β_1	0.65
Ratio between the strain at the second post-peak point and ultimate strain, α_2	0.45
Ratio between the stress at the first post-peak point and peak tensile strength (β_2)	0.26
Crack band width, l_b	SQRT_IP

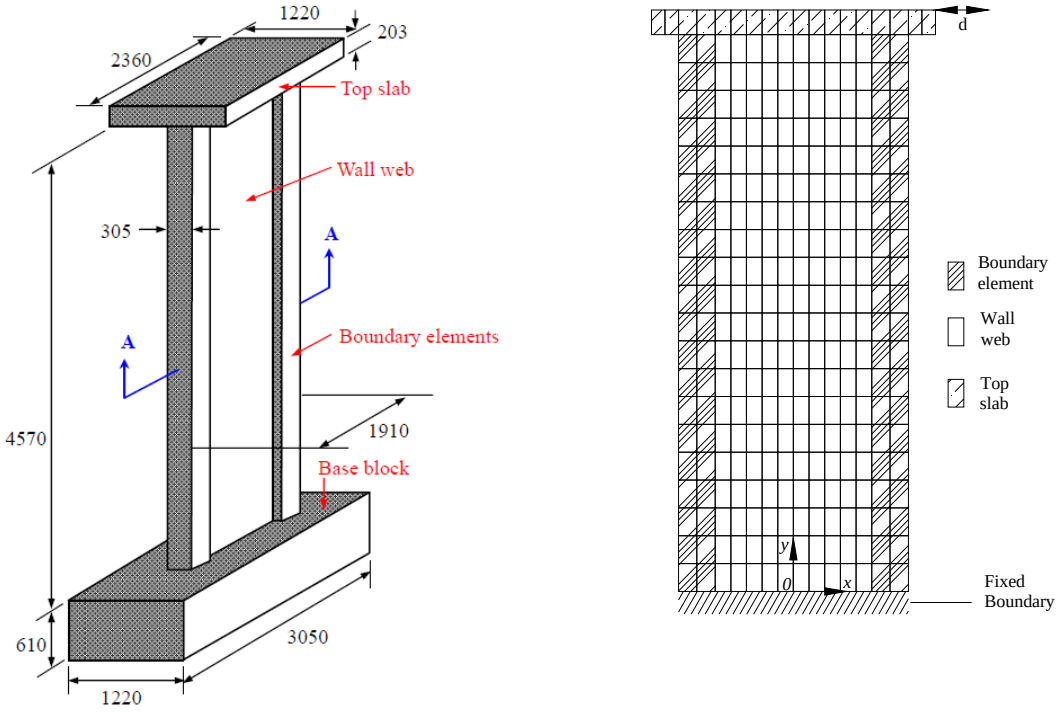

(a) (b)

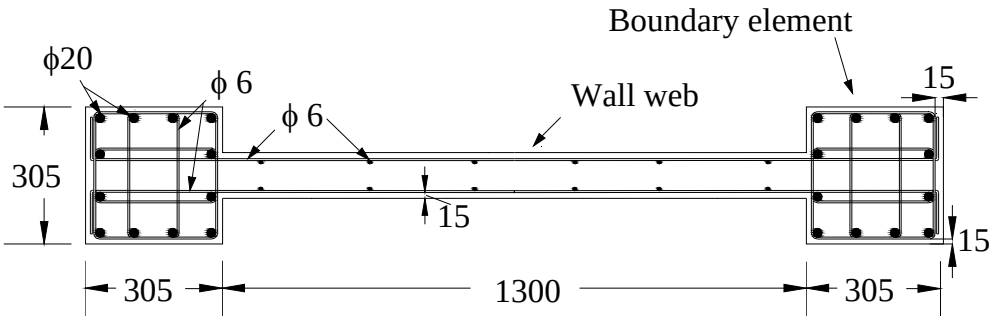

(c)

Figure 6.16: (a) Nominal dimension (adapted from He *et*. al 2008) (b) Finite element mesh and (c) cross-sectional details of shear-wall B2.

Table 6.6: Data used in simulation of shear wall B2 for the behaviour of the smeared reinforcement.

Parameters	H^w, H^b, V^w	V^b
Initial Young Modulus, E_s (GPa)	200	200
Tangent modulus at strain hardening, E_{sh} (GPa)	6.4	6.4
Yielding strain, ε_{sy} (mm/mm)	2.7×10^{-3}	3.11×10^{-3}
Yielding stress, f_{sy} (MPa)	532.4	410.3
Hardening strain, ε_{sh} (mm/mm)	1.5×10^{-2}	1.5×10^{-2}
Hardening stress, f_{sh} (MPa)	544.0	425.0
Strain at the ultimate stress, ε_{su} (mm/mm)	1.68×10^{-2}	1.8×10^{-2}
Ultimate stress, f_{su} (MPa)	548.0	435

[b] = Boundary element; [w] = Wall element, H = Horizontal reinforcement, V = vertical reinforcement.

The response obtained from FEMIX is compared with the experimental response and is illustrated in the Figure 6.17. The numerical response predicted satisfactory the important characteristics of the cyclic loading, including the strength degradation in consecutive cycles, degradation of stiffness during reloading. The unloading path of simulated cycles closely follow the experimental path, while during reloading the experimental cycles predict lower stiffness in last few cycles. In the cycles with maximum displacement it was found that the concrete was almost crushed in compression, as also reported in experiment. The used numerical model did not allow neither bar buckling nor slip between concrete and steel. The bar-slip or buckling becomes almost certain in such cases, where the concrete cover is completely crushed or removed during loading. Oesterle *et* al. (1976) has reported that the steel ties were visible in lower part of shear wall during last cycles, which led to ultimate failure of the shear wall. The experimental response show a high load carrying capacity, compared to numerical simulation. This might have caused due to

slightly higher strength of the reinforcing bars in boundary elements compared to the tested specimen of reinforcing bars.

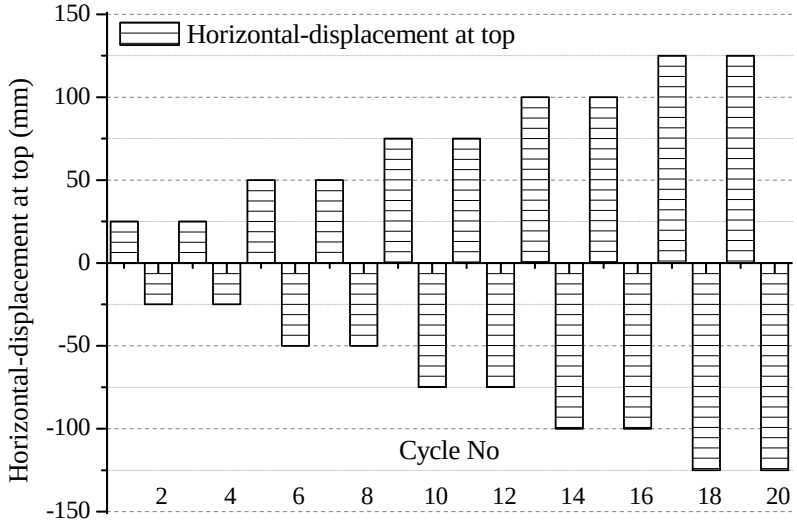

(a)

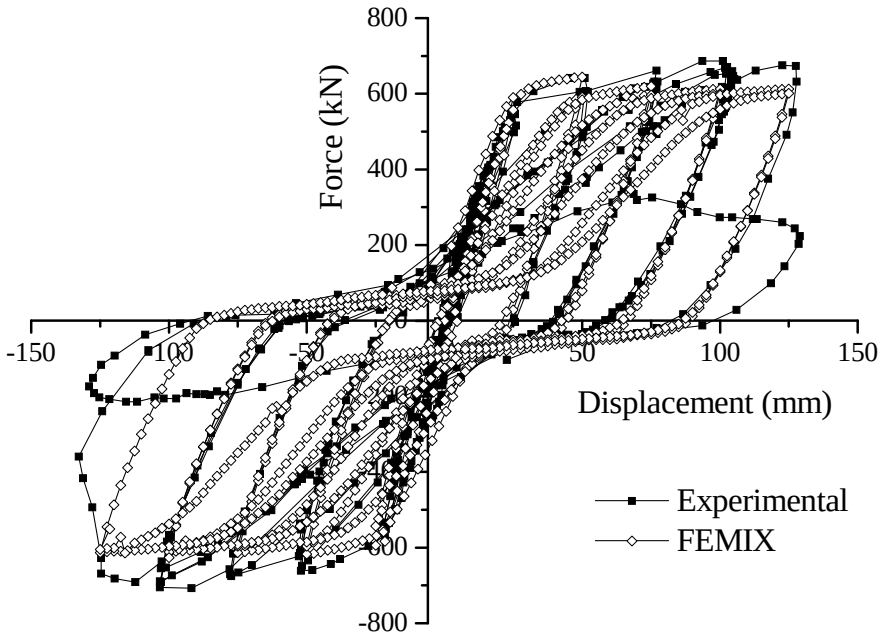

(b)

Figure 6.17: (a) Displacement loading history for shear wall B2 (b) comparison of Force *versus* displacement graphs observed from experiment and estimated by FEMIX.

The crack pattern obtained for the maximum displacement of 125 mm is represented in the Figure 6.18(a). The experimental crack pattern observed for the wall up to approximately 1800 mm is presented in Figure 6.18(b). It can be observed by comparing the figures that the cracks observed by FEMIX are similar in term of orientation. The concrete was completely crushed on outer side of web and on other side almost sheared through the web. As the concrete cover was lost on both sides due to reversed cycles during experiments has led to bar slippage (Oesterle *et* al. (1976).

From the experiment result (see Figure 6.18(b)) it was found that the cracks formed in negative direction and positive direction formed a criss-cross pattern. Moreover as the shear wall was displaced from negative side to positive side, the cracks of negative side got closed and only positive side were visible. The numerical pattern observed (see Figure 6.18(a)) also reveal that on displacing the wall to positive extreme the cracks formed on negative extreme were completely closed.

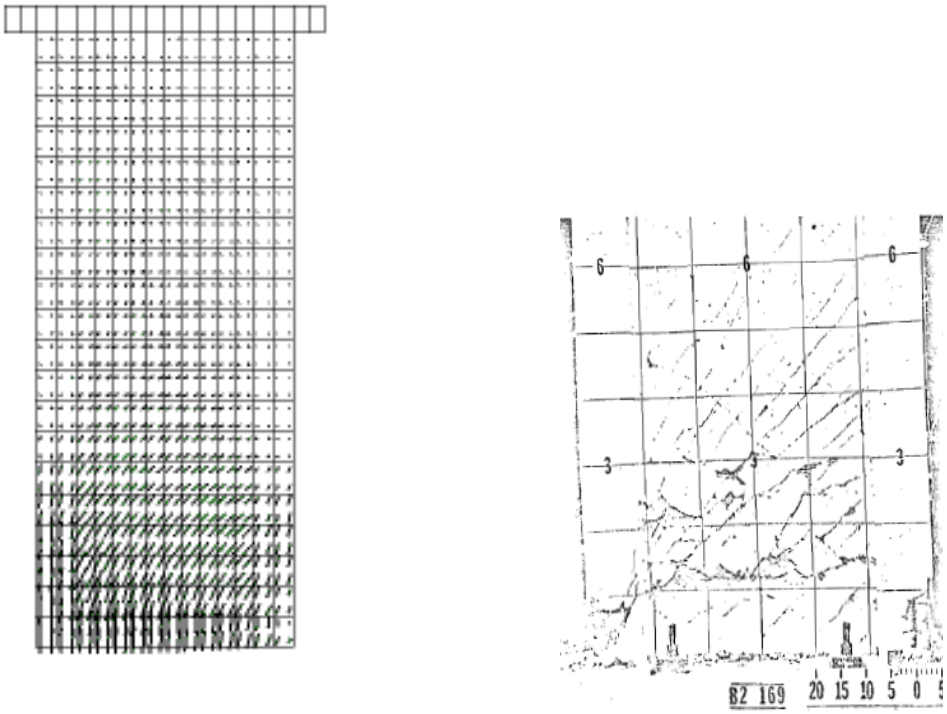

Figure 6.18: (a) Crack pattern obtained from FEMIX; and (b) experimental crack pattern of the shear wall B2 at 125 mm horizontal displacement up to the height of 1800 mm

6.4 SUMMARY

The chapter describes a model developed for the analysis of reinforced concrete beams, shear-walls and plane shells that are submitted to monotonic and cyclic loads. For the same purpose, a biaxial constitutive model for concrete was implemented based on smeared crack approach. During post-cracking, the concrete model is based on condition that the effect of Poisson's ratio to other direction will cease as soon as the maximum strength condition is violated for this direction. However the elastic strain will still continue to contribute to other direction. The implemented model estimate the rotating smeared crack formation based on principal strain and principal stress. The principal stress and strain are assumed to be coaxial. Similarly, a steel model was also implemented to simulate smeared reinforcement.

The concrete and steel uni-axial constitutive models were derived from Chapter 2 assuming them as benchmark, except the tensile envelope of concrete. The implemented envelope curve for tension follows a tri-linear post cracking behaviour, which can simulate the tension stiffening and softening depending on the fracture energy and by using parameters α_1, β_1, α_2 and β_2.

The model is compared and validated with benchmark problems at material level and structural level by experimental results. The implemented model is able to predict the response of RC structures under hysteretic loading with acceptable accuracy.

CHAPTER 7

Conclusions and possible future work

1.1 SUMMARY OF RESULTS

The present thesis had been devoted, mainly, to the improvement and development of constitutive models for concrete, steel and FRP materials, and its implementation into FEMIX and DOCROS computational tools for the simulation of RC structures under different loading conditions. This section describes the summary of chapters, sequentially.

The Chapter one was dedicated to the establishment of the thesis by highlighting the importance and objective of the study.

The Chapter 2 served as foundation for material modelling, with special emphasis on the cyclic constitutive laws for concrete and steel those are described in detail. The uniaxial constitutive envelope of confined and unconfined concrete, in tension and compression follow the Tsai's equation. This equation is relatively simple, as it required very few parameters and is able to predict the monotonic behaviour very successfully for confined and unconfined concrete. The cyclic constitutive laws for concrete and steel were derived from Chang and Mander (1994). The behaviour of CFRP materials and the interface behaviour between concrete and steel are also established in detail. A numbering rule based approach is used in constitutive laws, which can take into account the partial unloading and reloading, effectively.

The Chapter 3 was based on the use of constitutive model for the estimation of moment-curvature (M-χ) relationship, by implementing the constitutive models described in chapter 2 into DOCROS that is developed for the design of cross sections of RC elements failing in

bending. The software can estimate the M-χ relationship for sections of irregular shape composed of distinct materials, under prestressing or axial load application. A parametric study was conducted based on section composed of different types of FRC, i.e. presenting strain-hardening or strain-softening character. For this purpose a tensile constitutive model representing the generic condition of softening and hardening was implemented in DOCROS. Design graphs were proposed and suitable examples were used to evidence the favourable effect of the post-cracking strength and deformability of FRC. To determine the force-deflection relationship of concrete beams failing in bending, by using the M-χ response generated by Docros, a software was developed, designated as DefDocros, which uses the tangent or secant flexural stiffness from M-χ with the matrix displacement method. In spite of its simplicity, this approach was capable of simulating the deformational response of RC beams failing in bending with reasonable accuracy.

The Chapter 4 was dedicated to development of cyclic constitutive modelling of CFRP confined concrete. Most of researches have been devoted to monotonic compressive loading of column, except very few researchers that have explored the cyclic behaviour of confined columns. The monotonic envelope was composed of three branches and assumed to be based on the principles proposed by Harajli *et* al. (2006). In order to adjust the model to the specificities of the simulated structural elements, empirical relations were derived for internal parameters from extensive experimental data. The salient features of the experimental tests were discussed to justify the evolution of parameters considered necessary for the formulation of the constitutive law. The parameters defining the cyclic scheme were obtained from regression analysis of experimental data from Ferreira (2007). The developed confinement model is able to estimate the behaviour of cyclic compression tests carried out by other researchers for columns, for partial unloading and reloading cycles with high accuracy, which is critical for reliable estimation of behaviour.

The detailed finite element formulation for fibre element model was described in Chapter 5 that was based on 3D Timoshenko beam theory. The frame element is discretized in fibres along its longitudinal direction, and a distinct constitutive model can be assigned to each fibre. This approach allows the constitutive laws of the individual sub-element to be simpler, while the member still exhibits a complex hysteretic behaviour through the interaction of the different sub-elements. The constitutive laws used were already

described in Chapter 2 and Chapter 4. The results estimated from fibre model shown good correlation with experimental data. An example proving the capability of fibre element for seismic analysis of frame structures is also presented. The fibre model failed to predict pinching observed in cyclic tests on columns, which is a characteristic of column or joint tests where high stress gets concentrated in the joints. To simulate it, a formulation for 3D interface finite element was implemented. The interface element was installed with stiff cables to transfer the in plane displacement due to frame element axis at sliding points.

The main goal of Chapter 6 was to implement the constitutive models described in Chapter 2 in a plane stress formulation in order to simulate beams and shear walls. These constitutive models were also implemented in a 3D plane shell formulation (Reissner-Mindlin theory) in order to simulate shell type structures. For the shell type formulation, a finite element is decomposed in layers that can have distinct constitutive models. Combining the fibres model with the 3D plane shell formulation, an entire 3D reinforced concrete building can be simulated under monotonic or cyclic loading, where columns and beams can be modelled with 3D Timoshenko finite elements through fibres model, and the floors by the shell type elements. The cyclic constitutive model for concrete was implemented in the framework of fracture mechanics supported by smeared rotating crack approach. The rotating crack model is an efficient method, as the shear modelling is not required to be explicitly simulated, which makes the formulation easier to implement. A smeared reinforcement model for steel bars was also implemented, which can be helpful in case of uniform and large number of rebars. When compared with the experimental data from tests of other researchers, the developed numerical model provided acceptable estimation for the entire load-deformation response of tests over a wide range of effects. The crack pattern estimated by the proposed model matched the experimental crack pattern with acceptable accuracy.

1.2 FUTURE OUTLOOK

The work carried out during this PhD program can be extended or developed for further research, in spite of all the goals of the PhD were fulfilled.

In case when the concrete cover is damaged completely, the longitudinal steel reinforcement in compression can lead to buckling, as observed by Gomes and Appleton

(1997). The buckling has been found to have significantly reduced the strength of RC structure. The steel laws can be implemented with extended parameter, based on empirical data, to inherently derive the relation for buckling.

The bond-slip law introduces reduction is steel stress during the cycles, which if implemented implicitly into steel hysteretic scheme can yield desired result. For such cases, parametric studies should be carried out by the experimental data of steel rebars, and corresponding changes can be added to the model.

A characteristic of displacement based finite element, in case of fibre approach, is inability to predict the softening in force *versus* displacement curve; this can be avoided by selecting force based finite element or hybrid finite element method. The displacement based finite element at *section level* can be replaced by hybrid approach inside FEMIX as proposed by various researchers.

When a strengthening system is applied in a RC structure, a certain strain and stress field was already installed in the concrete substrate. This strain and stress fields are dependent on the acting loads in the moment when the strengthening intervention is applied. If strengthening systems are not applied with post-tension, strains are introduced in these systems for the external loads that are applied only after the strengthening intervention. To simulate the gap of strains between concrete substrate and strengthening systems, when these last ones are applied, the construction phase concept should be implemented in FEMIX for the fibrous and layer models. In case of fibre model, each fibre can have each own phase, which allows the possibility of activating the participation of the strengthening systems when a certain level of damage is already installed in the other fibre.

In multi-layered concept of shell analysis, the implementation of embedded/discrete reinforcement should be implemented, which can be useful in case of unsymmetrical reinforcement.

As the uniaxial constitutive laws were extended to biaxial case of laminar structure, the same should be done for tri-axial loading of solid elements. That type of formulation is important from the point of view of simulating volumetric type structures, like some foundations.

References

ACI Committee (2008). "Building code requirements for structural concrete (ACI 318-08) and commentary." American Concrete Institute.

ACI Committee 318 (2004). "Building code requirements for structural concrete and Commentary (ACI 318-04)." Reported by committee 318, American Concrete Institute, Detroit, 351 pp.

Al-Noury, S.I., and Chen, W. (1982). "Behavior and design of reinforced and composite concrete sections." Journal Struct Div, ASCE, 108 (6), 1266-84.

ASCE. (1982). "State-of-the-art report on finite element analysis of reinforced concrete." 978-0872623071, ASCE, New York.

Aveston, J., Cooper, G.A., and Kelly, A. (1971). "Single and multiple fracture." in Properties of Fiber Composites, Proceedings of Conference of the National Physical Laboratory, Guildford, U.K., IPC Science and Technology Press, 15-26.

Ayoub, A., and Filippou, F.C. (1998). "Nonlinear Finite-element analysis of RC shear panels and walls." Journal of Structural Engineering, ASCE , Vol 124 No. 3, 298-308.

Badawi, M., and Soudki, K. (2009). "Flexural strengthening of RC beams with prestressed NSM CFRP rods – experimental and analytical investigation." Construction and Building Materials, Vol. 23, 3292–3300.

Bahn, B.Y., Hsu, C.T. (1998). "Stress-strain behavior of concrete under cyclic loading." ACI Materials Journal 95(2), 178–93.

Balakrishnan, S., and Murray, D.W. (1988). "Concrete constitutive model for NLFE analysis of structures." Journal of Structural Engineering, ASCE, Vol. 114, No. 7, 1449-1466.

Banon, H., Biggs, J., and Irvine, M. (1981). "Seismic damage in reinforced concrete frames." Journal of Structural Engineering, ASCE, 107(ST9), 1713-1729.

Barros, J.A.O. (1989). "Modelos de análise de estruturas laminares e de compósitos laminados (Models for the analysis of laminar structures and laminate composites)." MSc Thesis, Civil Eng. Dept., Faculty of Engineering, University of Porto, Portugal [in Portuguese].

Barros, J.A.O. (1995). "Comportamento do betão reforçado com fibras. Análise experimental e simulação numérica. Behavior of fiber reinforced concrete. Experimental analysis and numerical simulation." PhD Thesis, Faculty of Engineering, University of Porto, Portugal. [in Portuguese]

Barros, J.A.O., and Dias, S.J.E. (2006.) "Near surface mounted CFRP laminates for shear strengthening of concrete beams." Cement and Concrete Composites Journal, 28(3), 276-292.

Barros, J.A.O., and Ferreira, D.R.S.M. (2005a). "An efficient confinement strategy with CFRP sheets to increase the energy absorption capacity of concrete columns." 1st US-Portugal International Workshop – Grand challenges in earthquake engineering, Portugal 13.1-13.8.

Barros, J.A.O., and Ferreira, D.R.S.M. (2005b). "Partial versus full wrapping confinement systems for concrete columns." International Conference on Concrete Repair, Rehabilitation and Retrofitting, South Africa, 1123-1129.

Barros, J.A.O., and Ferreira, D.R.S.M. (2008). "Assessing the efficiency of CFRP discrete confinement systems for concrete column elements." Journal of Composites for Construction, ASCE, Vol. 12 Issue 2, 134-148.

Barros, J.A.O., and Fortes, A.S. (2005). "Flexural strengthening of concrete beams with CFRP laminates bonded into slits." Cement and Concrete Composites, Vol. 27, No. 4, 471-80.

Barros, J.A.O., Dias, S.J.E., Lima, J.L.T. (2007a). "Efficacy of CFRP-based techniques for the flexural and shear strengthening of concrete beams." Cement and Concrete Composites Journal, 29(3), 203-217.

Barros, J.A.O., Ferreira, D.R.S.M., and Varma, R.K. (2007). "CFRP confined reinforced concrete elements submitted to direct cyclic compressive loading." Special Publication "Seismic Strengthening of Concrete Buildings using FRP Composites" Paper SP-06 ACI, 85-104.

Barros, J.A.O., Perrone, M., and Aprile, A. (2008a). "Hybrid CFRP-based strengthening technique to increase the flexural resistance and concrete confinement of RC columns submitted to axial and lateral loading." Proceedings of CCC 2008 - Challenges for Civil Construction. Marques, T. (ed.). FEUP, 146-147.

Barros, J.A.O., Sena-Cruz, J.M., Azenha, M., Lourenço, L. (2009) "Structural strengthening of Panoramico building." Report no. 09-DEC/E-11, Department of Civil Engineering, University of Minho, Guimarães, 70 pp.[Confidential Report]

Barros, J.A.O., Sena-Cruz, J.M., Ferreira, D.R.S.M., Lourenço, P.J.B. (2001). "Análise Experimental de Pilares de Betão Armado Reforçados com Laminados de Carbono sob Acções Cíclicas (Experimental analysis of RC columns strengthened by CFRP laminates submitted to cyclic loads)." 5th National Conference of Seismology and Seismic Engineering, Civil Engineering Regional Laboratory, Ponta Delgada, Azores, 491-503. (in Portuguese)

Barros, J.A.O., Varma, R.K., Sena-Cruz, J.M., and Azevedo, A.F.M. (2008b). "Near surface mounted CFRP strips for the flexural strengthening of RC columns - experimental and numerical research." Engineering Structures Journal, 30(12), 3412-3425.

Barzegar, F. (1989). "Analysis of RC membrane elements with anisotropic reinforcement." Journal of Structural Engineering, ASCE, 115, 647-665.

Bathe, K.J. (1996) "Finite Element Procedures." Prentice Hall, New Jersey, US.

Bazant, Z.P., and Oh, B.H. (1983). "Crack band theory for fracture of concrete", Materials and Structures, RILEM, 16(93), 155-177.

Bertero, V. V., & Mahin, S. A. (1975). "An evaluation of some methods for predicting the seismic behavior of reinforced concrete buildings." Earthquake Engineering Research Center, Berkeley, University of California 360 pp.

Bertero, V., & Popov, E. (1975). “Hysteretic behavior of ductile moment resisting reinforced concrete frame components.”, Earthquake Engineering Research Center, Report No. EERC 75-16, University of California, Berkeley, 81 pp.

Brancaleoni, F., Ciampi, V., and Di Antonio, R. (1983). “Rate-type models for non linear hysteretic structural behavior.” EUROMECH Colloquium, Palermo, Italy.

CEB (1994). “Behavior and analysis of reinforced concrete structures under alternate actions inducing inelastic response.” Thomas Telford, Lausanne, Switzerland.

CEB (1996a). “RC elements under cyclic loading. state-of-art report.” Comite Euro-Internaltional du Beton, Thomas Telford Publications, London.

CEB. (1996b). “RC frames under earthquake loading. state-of-art report.” Comite Euro-Internaltional du Beton, Thomas Telford Publications, London.

CEB-FIB (1993). “CEB-FIP Model Code 1990 - Design Code.” Thomas Telford, Lausanne, Switzerland.

CEB-FIB (2008). “Practitioners' guide to finite element modelling of reinforced concrete structures State-of-art report.” Fédération Internationale du Béton, Lausanne.

CEN. (2004) EN 1998-1 Eurocode 8: Design of structures for earthquake resistance -Part 1: General rules, seismic actions and rules for buildings. Brussels, Belgium.

Cervenka, V. (1985). “Constitutive model for cracked reinforced concrete.” ACI Journal Proceedings, Vol.82, No.6, Nov-Dec., 877-882.

Cervenka, V. and Gerstle, K.H. (1971). “Inelastic analysis of reinforced concrete panels Part I: Theory.” Intl Assoc Bridge Struct Engrs Publs, 31 (11), 31-45.

Chang G.A., and Mander, J.B. (1994). “Seismic energy based fatigue damage analysis of bridge columns: Part I-Evaluation of seismic capacity.” Report No. NCEER-94-0006, 240 pp.

Chen, A.C., and Chen, W.F. (1975). “Constitutive relations for concrete.” Journal of Engrg. Mech. Div., ASCE, 101(4), 465 – 481.

Chen, W.F. (1982). “Plasticity in reinforced concrete.” McGraw-Hill, New York.

Ciampi, V., Eligehausen, R., Bertero, V.V., Popov, E.P. (1982). “Analytical model for concrete anchorages of reinforcing bars under generalized excitations.” Report No.

EERC 82-83, Earthquake Engineering Research Center, University of California, Berkeley, 121 pp.

Clough, R.W., and Johnston, S.B. (1966). "Effect of stiffness degradation on earthquake ductility requirements." 2nd Japan National Conference on Earthquake Engineering, 227-232.

Cornelissen, H.A.W., Hordijk, D.A., Reinhardt, H.W. (1985). "Experiments and theory for the application of fracture mechanics to normal and lightweight concrete." In: Wittman FH (Editor), Proc. int. conf. on fracture mechanics of concrete. Amsterdam (The Netherlands), Elsevier.

Cosenza, E., Manfredi, G., Verderame, G.M. (2006). "A fibre model for push-over analysis of underdesigned reinforced concrete frames." Computers and Structures, 84 (13-14), 904-916.

Cowell, A.D., Bertero, V.V., and Popov, E.P. (1982). "An investigation of local bond slip under variation of specimen parameters." Earthquake Engineering Research Center, Report No. UCB/EERC 82/23, University of California, Berkeley 121 pp.

Crisfield, M.A., and Wills, J. (1989). "Analysis of RC panels using different concrete models." J. of Eng. Mechanics, ASCE, 115(3), 578–597.

de Borst, R., and Nauta, P. (1985). "Non-orthogonal cracks in smeared finite element model." Engineering Computations Journal, Vol. 2, 35-46.

Desayi, P., and Krishnan, S. (1964). "Equation for the stress-strain curve of concrete." ACI Journal. , Vol. 61, 345-350.

Drucker, D.C., and Prager, W. (1952). "Soil mechanics and plastic analysis for limit design." Quarterly of Applied Mathematics, Vol. 10, No. 2, 157–165.

Elwi, A.A., and Murray, D.W. (1979). "A 3D hypoelastic concrete constitutive relationship." Journal of Engineering Mechanics Division, ASCE, 105 (4), 623-641.

Fajfar, P. (1999). "Capacity spectrum method based on inelastic demand spectra." Earthquake Engineering and Structural Dynamics, 28 (9), 979-993.

Fajfar, P. (2000). "A nonlinear analysis method for performance based seismic design." Earthquake Spectra, Vol.16, No.3, 573-592.

FEMA, 1997, NEHRP guidelines for the seismic rehabilitation of buildings, FEMA 273, and NEHRP Commentary on the guidelines for the seismic rehabilitation of buildings, FEMA 274, Federal Emergency Management Agency, Washington, D.C.

Ferreira, D.R.S.M. (2007). "CFRP-based confinement of circular concrete column elements – experimental and analytical research." PhD thesis, University of Minho. (in Portuguese).

Filippou, F.C., and Issa, A. (1988). "Nonlinear analysis of reinforced concrete frames under cyclic load reversals." EERC Report 88-12, Earthquake Engineering Research Center, Berkeley,112 pp.

Filippou, F.C., Popov, E.P., Bertero, V.V. (1983). "Effects of bond deterioration on hysteretic behavior of reinforced concrete joints." Report No. UCB/EERC 83-19, Earthquake Engineering Research Center, University of California, Berkeley, California, 184 pp.

Filippou, F.C., Popov, E.P., Bertero, V.V. (1986). "Analytical studies of hysteretic behavior of RC joints." Journal of Structural Engineering, ASCE, V. 112, No. 7, July 1605-1622.

Giberson, M. (1967). "The response of nonlinear multi-story structures subjected to earthquake excitations." Earthquake Engineering Research Laboratory, Pasadena, 232 pp.

Gomes, A.M. (1992). "Comportamento e reforço de elementos de betão armado sujeitos a acções cíclicas", Dissertação submetida para a obtenção do grau de Doutor em Engenharia Civil pela Universidade Técnica de Lisboa [in Portuguese].

Gopalaratman, V.S., Shah, S.P. (1985). "Softening response of plain concrete in direct tension." ACI Journal, 82(3), 310–23.

Goto, Y. (1971). "Cracks formed in concrete around deformed tension bars." ACI Journal, 68 (4), 244-251.

Gupta, A.K., and Akbar, H. (1983). "A finite element for the analysis of reinforced concrete structures." International Journal for Numerical Methods in Engineering, Vol. 19, 1705-1712.

Gupta, A.K., and Maestrini, S.R. (1989). “Post-cracking behavior of membrane reinforced concrete elements including tension-stiffening.” Journal of Structural Engineering, ASCE, Vol. 115 No 4, 957-976.

Harajli, M.H., Hantouche, E., and Soudki, K. (2006). “Stress-strain model for fibre-reinforced polymer jacketed concrete columns.” ACI Structural Journal, 105(5), 672-682.

Hawkins, N.M., Lin, I.J., and Jeang, F.L. (1982). “Local bond strength of concrete for cyclic reversed loadings.” Bond in Concrete (P. Bartos, ed.), Applied Science Publishers Ltd., 151-161.

He, W., Wu, Y., and Liew, K. M. (2008). “A fracture energy based constitutive model for the analysis of reinforced concrete structures under cyclic loading.” Computer Methods in Applied Mechanics and Engineering, Oct, 197(51-52), 4745-4762.

Hillerborg, A., Modeer, M., Petersson, P.E. (1976). “Analysis of crack formation and crack growth in concrete by means of fracture mechanics and finite elements.” Cement and Concrete Research 6(6), 773-782.

Hognestad, E., Hanson, N.W., McHenry D. (1955). “Concrete stress distribution in ultimate strength design.” ACI Journal, 27(4), 455–79.

Huang, Hou-Cheng. (1989). “Static and dynamic analyses of plates and shells – Theory,

ISO TC 71/SC 6 Non-conventional reinforcement of concrete-test methods-part 2: Fiber reinforced polymer (FRP) sheets, International standard (2003).

Iyengar, K., Desayi, P., and Reddy, K. (1970). “Stress-strain characteristics of concrete confined in steel binders.” Mag.Concrete Res , 22, 173-184.

Karsan I.D., Jirsa J.O. (1969). “Behavior of concrete under compressive loadings.” Struct Div ASCE, 95 (ST12), 2543–63.

Kasparkiewicsz, J. (1978). discussion, in Proceedings of RILEM Symposium on Testing and Test Methods of Fiber Cement Composites, Edited by N. Swamy, The Construction Press, England, 493−495.

Kelly, A. (1972). “Reinforcement of structural materials by long strong fibers.” Metallurgical trans., 3(9), 2313-2325.

Kelly, A., and Davis, G.J. (1965). “The principles of fiber reinforcement of metals.” Metallurgical Review, Vol. 10, No. 37, 1-77.

Kent, D.C., Park, R. (1971). “Flexural members with confined concrete.” J. Struct. Div. ST7, 97, 1969–1990.

Kotsovos, M.D. (1983). “Effect of testing techniques on the post-ultimate behaviour of concrete in compression.” Materials and Structures, Vol. 16, No. 1, 3-12.

Kwak, H.G., Kim, D.Y. (2004). “Material nonlinear analysis of RC shear walls subjected to cyclic loadings.” Engineering Structures, Vol. 26, Issue 10, 1423-1436.

Lam, L., and Teng, J.G. (2003). “Design-oriented stress-strain model for FRP-confined concrete.” Construction and building materials, Elsevier, Vol. 17, 471-489. Issue?

Lam, L., Teng, J.G., Cheung, C.H., and Xiao, Y. (2006). “FRP-confined concrete under cyclic axial compression.” Cement & Concrete Composites, 28, 949-958.

Légeron, F., Paultre, P. (2005). “Damage mechanics modelling of nonlinear seismic behaviour of concrete structures.” Journal of Structural Engineering, Vol. 131, No. 6, 946-955.

Lin, C.S., Scordelis, A. (1975). “Non linear analysis of RC shells of general forms.” J Struct Engng, ASCE, 101(ST3), 523–38.

Lutz, L.A., and Gergely, P. (1967). “Mechanics of bond and slip of deformed bars in concrete,” ACI Journal, Vol. 64, No. 11, 711-721.

Lutz, L.A., Gergely, P., and Winter G. (1966). “The mechanics of bond and slip of deformed reinforcing steel in concrete.” Structural Engineering Report No. 66/05. Cornell University.

Ma, S., Bertero, V., & and Popov, E. (1976). “Experimental and analytical studies on the hysteretic behavior of reinforced concrete rectangular and T-Beams.” Earthquake Engineering Research Center, EERC Report 76-2. Berkeley: University of California, 260 pp.

Majumdar, A.J. (1968). “Determining bond strength in fiber reinforced composites.” Magazine of Concrete Research, Vol. 20, Dec, 78–84.

Majumdar, A.J., Ryder, J.F. (1968) “Glass fiber reinforcement of cement products.” Glass Technology, Vol. 9, No. 3, June, 78−84.

Mander, J.B., Priestley, M.J.N., Park, R. (1988a). “Theoretical stress–strain model for confined concrete.” Journal of Structural Engineering, Vol. 114, Issue 8, 1804–1826.

Mander, J.B., Priestley, M.J.N., Park, R. (1998b). “Observed stress–strain behaviour of confined concrete.” Journal of Structural Engineering, 114(8) 1827–1849.

Mansour, M., and Hsu, T.T.C. (2005). “Behavior of reinforced concrete elements under 32 cyclic shear II: Theoretical model.” Journal of Structural Engineering, ASCE, 131(1), 54–65.

Mansour, M., Lee, J.Y., Hsu, T.T.C. (2001). “Cyclic stress-strain curves of concrete and steel bars in membrane elements”, Journal of Structural Engineering, ASCE, 127(12), 1402-1411.

Menegotto, M., and Pinto, P. E. (1973). “Method of analysis for cyclically loaded reinforced concrete plane frames including changes in geometry and non elastic behaviour of elements under combined normal force and bending.” IABSE Symp. on Resistance and Ultimate Ultimate Deformability of Struct. Acted on by Well-Defined Repeated Loads, Lisbon, 15-22.

Miguel, P.F. (1990). “A discrete-crack model for the analysis of concrete structures.” Computer aided analysis and design of concrete structures, Proc. 2nd Int. Conf. Zell-am-See, Apr. 897-908.

Miranda-Guedes, J.P.S.C. (1997). “Seismic behaviour of reinforced concrete bridges modelling, numerical analysis and experimental assessment.” PhD Thesis, Univerity of Porto, Portugal.

Mobasher, M. (2012). “Use of fibre reinforced concrete in support of sustainable infrastructure systems.” BEFIB2012 - 8th RILEM International Symposium on Fibre Reinforced Concrete (in eventual publication)

Monteiro, R., Ribeiro, R., Marques, M., Delgado, R., Costa, A. (2008). “Pushover analysis of RC bridges using fiber models or plastic hinges.” The 14th World Conference on Earthquake Engineering, Beijing, China, October 12-17.

Morita, S., and Kaku, T. (1973). “Local bond stress-slip relationship and repeated loading.” IABSE Symp. on Resistance and Ultimate Deformability of Structures Acted on by Well Defined Repeated Loads, Lisbon, 221-27.

Motavalli, M., & Czaderski, C. (2007). “FRP composites for retrofitting of existing civil structures in europe: state-of-the-art review.” Composites and Polycon, American Composites Manufacturers Association Tampa, FL USA, Oct. 17-19.

Naaman, A.E., and Reinhardt, H.W. (2006). “Proposed classification of frc composites based on their tensile response.” Materials and Structures, Vol. 39, 547−555.

Naaman, A.E., and Shah, S.P. (1979). “Fracture and multiple cracking of cementitious composites.” Fracture Mechanics Applied to Brittle Materials, ASTM STP 678, Part II, S.W. Frieman, (Editor), pp. 183-201.

Nanni, A., and Bradford, M.N. (1995). “FRP jacketed concrete under uniaxial compression”, Construction and building materials, Vol. 9(2), 115–124.

Neville, A. (1975). Editor, Proceedings of the RILEM International Symposium on Fiber Reinforced Cement and Concrete, London, September.

Ngo, D., and Scordelis, A.C. (1967). “Finite element analysis of reinforced concrete beams.” ACI Journal Proceedings, 64 (3), 152-163.

NP-EN 10 002-1, (1990).Metallic materials - Tensile testing. Part 1: Method of test (at ambient temperature), European Standard, CEN, Brussels, Belgium, 35 pp.

Oesterle, R.G., Fiorato, A.E., Johal, L.S., Carpenter, J.E., Russell, H.G., Corley, W.G. (1976). “Earthquake-resistant structural walls—Tests of isolated walls”, Report to the National Science Foundation, Construction Technology Laboratories, Portland Cement Association, Skokie, Illinois, November, 315 pp.

Owen, D.R.J., and Hinton, E. (1980). “Finite elements in plasticity. Theory and practice.”

Palermo, D., Vecchio, F.J. (2003). “Compression field modeling of reinforced concrete subjected to reversed loading: formulation”, ACI Structural Journal 100 (5), 616-625.

Panthanki, F.D. (1991). “Low cycle fatigue behavior of high strength and ordinary reinforcing steels.” MSc. Thesis, State University of New York, Buffalo.

Perrone M. (2008). “Cyclic behaviour of RC columns strengthened according to a CFRP-based hybrid technique”, MSc thesis, University of Ferrara.

Perrone, M., Barros, J.A.O., Aprile, A. (2009). “A CFRP-based strengthening technique to increase the flexural and energy dissipation capacities of RC columns.” ASCE, Composites for Construction Journal, Vol. 13, No. 5, 372-383.

Picher, F., Rochette, P., Labossiere, P. (1996). “Confinement of concrete cylinders with CFRP.” Proc., First Int. Conf. on Compos. Infrastructures, Tucson, Ariz., 829–841.

Pineridge Press Limited, Swansea, UK.

Popovics, S. (1970). “A review of stress-strain relationships for concrete.” ACI Journal, Vol. 67, 243-248.

Popovics, S. (1973). “A numerical approach to the complete stress-strain curves for concrete.” Cement Concr. Res., 3583–599.

Ramberg, W., and Osgood, W.R. (1943). “Description of stress-strain curves by three parameters.” Technical Note No. 902, National Advisory Committee for Aeronautics, Washington DC, 1943-07.

Rashid, Y.R. (1968). “Analysis of prestressed concrete pressure vessels.” Nuclear Engineering and Design, 7 (4), 334-344.

Rehm, G. (1958). “The fundamental law of bond.” Proceedings of the Symposium on Bond and Crack Formation in Reinforced Concrete, RILEM, Stockholm, Sweden, 491-498.

Reinhardt, H.W. (1984). “Fracture mechanics of an elastic softening material like concrete.” Heron, 29(2), Delft University of Technology, 42 pp.

Reinhardt, H.W., Cornelissen, H.A.W., Hordijk, D.A. (1986). “Tensile test and failure analysis of concrete.” J Struct Engng, 112(11), 2462–77.

Romualdi, J.P. (1969) “Two phase concrete and steel materials.” U.S. Patent No. 3,439,094, Feb. 25.

Romualdi, J.P., and Mandel, J.A. (1964). “Tensile strength of concrete affected by uniformly distributed closely spaced short length of wire reinforcement.” ACI Journal, Vol. 6, No. 6, 657-671.

Rots, J.G. (1988), "Computational modeling of concrete fracture", PhD Thesis, Delft University of Technology.

Rots, J.G., and Blaauwendraad, J. (1989). "Crack models for concrete: discrete or smeared? fixed, multi-directional or rotating?," HERON, Vol. 34, No. 1, Delft University of Technology, The Netherlands. 59 pp.

Rots, J.G., Nauta, P., Kusters, G.M., Blaauwendraad, J. (1985) "Smeared crack approach and fracture localization in concrete." Heron, 30(1), Delft University of Technology, 48 pp.

Saadatmanesh, H., Ehsani, M.R., and Li, M.W. (1994). "Strength and ductility of concrete columns externally reinforced with fiber composite straps." ACI Struct. J., 91(July–Aug.), 434–447.

Saenz, L.P., (1964). "Discussion of "Equation for the stress-strain curve of concrete." by P. Desayi and S. Krishnan, ACI Journal Proc., 61(9), 1229-1235.

Scott, B.D., Park, R., and Priestley, M.J. (1982). "Stress-strain behavior of concrete confined by overlapping hoops at low and high strain rates." ACI Journal, 79(1), 13-27.

Seible, F., Burgueno, A., Abdallah, M.G., Nuismer, R. (1995). "Advanced composites carbon shell system for bridge columns under seismic loads." In Proceedings, National Seismic Conference on Bridges and Highways: San Diego, USA.

Sena-Cruz, J. M. (1998). "comportamento cíclico de estruturas porticadas de betão armado reforçado com fibras de aço." Mater Thesis, University of Porto, Portugal [*in Portuguese*].

Sena-Cruz, J.M. (2005). "Strengthening of concrete structures with near-surface mounted CFRP laminate strips." PhD Thesis, University of Minho, Portugal.

Shah, S.P., and Ranjan, R.V. (1971). "Fiber reinforced concrete properties." ACI Journal, Vol. 68, No. 2, 126-135.

Shah, S.P., Kuder, K.G., and Mu, B. (2004). "Fiber reinforced cement-based composites: a forty year odyssey." Proceedings of the Sixth International Rilem Symposium, Varenna-Italy, 3-30.

Shao, Y., Zhu, Z., Mirmiran, A. (2006). “Cyclic modelling of FRP-confined concrete with improved ductility.” Cement & Concrete Composites, Elsevier, 28(10), 959-968.

Sheikh, S.A., and Uzumeri, S.M. (1980). “Strength and ductility of tied concrete columns.” ASCE J. Struct. Div., Vol. 106, No. 5, 1079-1102.

Shipman, J.M., and Gerstle, K.H. (1979). “Bond deterioration in concrete panels under load cycles.” ACI Journal, 67(2), 311-325.

Sinha, B.P., Gerstle, K.H. and Tulin, L.G. (1964) “Stress-strain relations for concrete under cyclic loading.” ACI Journal, 61(2), 195-210.

Smith, G.M., and Young, L.E. (1955). “Ultimate theory in flexure by exponential function.” ACI Journal, 52(11), 349-359.

software and applications”, Springer-Verlag Berlin Heidelberg.

Soranakom, C., and Mobasher, B. (2007) “Closed form solutions for flexural response of fiber reinforced concrete beams.” Journal of Engineering Mechanics, Vol. 133, No. 8, 933–941.

Spacone, E. and Limkatanyu, S. (2000). “Response of Reinforced Concrete Members Including Bond-Slip Effects.”, ACI Structural Journal, 97(6), 831-839.

Spacone, E., Ciampi, V. and Filippou, F.C. (1992). “A beam element for seismic damage analysis.” Report No. UCB/EERC-92/07. Earthquake Engineering Research Center, University of California, Berkeley 118 pp.

Spacone,E., Filippou, F., and Taucer, F. (1996) “Fiber beam-column modeling for non-linear analysis of R/C frames.” Journal of Earthquake Engineering and Structural Dynamics, 1996, 25(7), 711-725.

Spolelstra, M.R., Monti, G. (1999). “FRP-Confined concrete model.” Journal of Composites for Construction, ASCE, 3(3), 144-150.

Suidan, M.T., and Schnobrich, W.C. (1973). “Finite element analysis of reinforced concrete.” Journal of the Structural Division, ASCE, Vol. 99, No. ST10, 2109-2122.

Swamy, R.N., Editor, (1978) “Testing and test methods of fiber cement composites”, RILEM Symposium Proceedings, Sheffield, The Construction Press, England, 545 pp.

Taheri, M., Barros, J.A.O., Salehian, H.R. (2012). “A design model for strain-softening and strain-hardening fiber reinforced elements reinforced longitudinally with steel and FRP bars.” Composites - part B Journal, 42 1630-1640.

Takeda, T., Sozen, M.A., and Nielsen, N. (1970). “Reinforced concrete response to simulated earthquakes.” Journal of Structural Engineering, ASCE, 96(ST12), 2557-2573.

Tassios, T.P. (1979). “Properties of bond between concrete and steel under load cycles idealizing seismic actions.” AICAP-CEB Symposium, Structural Concrete Under Seismic Actions, Comite Euro-International du Beton, Bulletin D’Information, Vol. 1, No. 131, Rome, Italy, 67-122.

Tassios, T.P., and Yannopoulos, P.J. (1981). “Analytical studies on reinforced concrete members under cyclic loading based on bond stress-slip relationships.” ACI Journal, Vol. 78, Issue 3, 206-216.

Taucer, F.F., Spacone E. and Filippou F.C. (1991). “A fibre beam-column element for seismic response analysis of reinforced concrete structures.” Report No. UCB/EERC-91/17. Earthquake Engineering Research Center, University of California, Berkeley. 140 pp.

Teng, J., & Lam, L. (2006). “Behavior and modeling of frp-confined concrete: a state-of-the-art review.” American Concrete Institute , Special Publication (238), 327-346.

Tepfers R. (1979). “A theory of bond, applied to overlapped tensile reinforcement splices for deformed bars.” Publ. 73.2, Div. of Concrete Structures, Chalmers University, Goteborg, No. 106, 3-12.

Tilantera, T., and Rechardt T. (1977). “Bond of reinforcement in light-weight aggregate concrete.” Otanjemi, Helsinki University of Technology, Division of Structural Engineering, Publication 17 1-36.

Toutanji, H.A. (1999). “Stress-strain characteristics of concrete columns externally confined with advanced fiber composites sheets”. ACI Material Journal, 96(3), 397-404.

Tsai, W.T. (1988). “Uniaxial Compression stress-strain relation of concrete.” Journal of Structural Engineering, Vol. 114 (9), 2133-2136.

Ugural, A.C. (1981). "Stresses in plates and shells." McGraw-Hill, Inc.

Varma, R.K., Barros, J.A.O., and Sena-Cruz, J.M. (2007) "Fibrous model for the simulation of the cyclic behaviour of 3D reinforced concrete frames." Technical Report nº 07-DEC/E-04, Department of Civil Engineering of the University of Minho, 90 pp.

Varma, R.K., Barros, J.A.O., and Sena-Cruz, J.M. (2009). "Numerical model for CFRP confined concrete elements subject to monotonic and cyclic loadings." Composites Part B 40 (8), 766-775.

Vecchio, F.J. (1999). "Towards cyclic load modeling of reinforced concrete." ACI Structural Journal, 96 (2), 193-202.

Vecchio, F.J., and Collins, M.P. (1982). "Response of reinforced concrete to in-plane shear and normal stresses." Publication No. 82-03, Department of Civil Engineering, University of Toronto, 332 pp.

Vecchio, F.J., and Collins, M.P. (1986). "The modified compression field theory for reinforced concrete elements subjected to shear." ACI Journal Proceedings, 83(2), 219-231.

Ventura-Gouveia, A. (2000). "Análise Experimental e Simulação Numérica de Elementos de Barra de Pórtico Tridimensional de Betão Armado (Experimental Analysis and Numerical Simulation of Reinforced Concrete 3D Frame Elements)", MSc Thesis, Department of Civil Engineering, University of Minho, July [in Portuguese].

Verderame, G.M., Ricci, P., Carlo, G.D., and Manfredi, G. (2009a). "Cyclic bond behaviour of plain bars Part I: Experimental investigation." Construction and Building Materials, Vol. 23, Issue 12, 3499-3511.

Verderame, G.M., Ricci, P., Carlo, G.D., and Manfredi, G. (2009b). "Cyclic bond behaviour of plain bars Part II: Analytical investigation." Construction and Building Materials, Vol. 23, Issue 12, 3512-3522.

Vidic, T., Fajfar, P., and Fischinger, M. (1994). "Consistent inelastic design spectra: strength and displacement." Earthquake Engineering and Structural Dynamics, 23, 502-521.

Viwanthanatepa, S., Popov, E.P., and Bertero., V.V. (1979c). “Effects of generalized loadings on bond of reinforcing bars embedded in confined concrete blocks.” Report No. UCB/EERC-79/22, EERC, University of California, Berkeley, 316 pp.

Viwathanatepa, S., (1979a). “Bond Deterioration of Reinforce Bars Embedded in Confined Concrete Blocks.” Thesis, University of California, Berkeley.

Viwathanatepa, S., Popov E.P., and Bertero V.V. (1979b). “Seismic behavior of reinforced concrete interior beam-column sub assemblages.” Report No. UCB/EERC 79/14, EERC, University of California, Berkeley, 198 pp.

Warner, R. (1969). “Biaxial moment thrust curvature relations.” Journal of Structural Division, ASCE, No ST5, 923-940.

Watstein, D. and Mathey R.G. (1959). “Width of cracks in concrete at the surface of reinforcing steel evaluated by means of tensile bond specimens.” ACI Journal, Proceedings 56 (1) July 47-56.

Willam, K., Pramono E., and Sture, S. (1987). “Fundamental issues of smeared crack models.” Proc. SEM–RILEM International Conference on Fracture of Concrete and Rock, S.P. Shah and S.E. Swartz (Eds.), SEM, Bethel, 192–207.

Yankelevsky, D., and Reinhardt, H. (1987). “Model for cyclic compressive behaviour of concrete.” Journal of Structural Engineering, ASCE, Vol. 113, 228-240.

Young, L.E. (1960). “Simplifying ultimate flexural theory by maximizing the stress block.” AC1 Journal, 57 (5), 549-556.

Zienkiewicz, O.C., and Taylor, R.L. (1991). “The finite element method (Fourth edition) Volume 2, Solid and fluid mechnanics, dynamics and non-linearity.” McGraw-Hill, Berkshire, England.

APPENDIX A

The transition curve (see Figure A. 1) for concrete requires six known parameters to find the desired equation, three for the initial point and the other three for the final (target) point. The parameters required are the coordinates of the initial point (x_o, y_o) and corresponding slope E_o, and analogous parameters ((x_f, y_f) and E_f) are adopted for the final point.

The equation can be considered with A and B as parameters to be found:

$$y = y_o + E_o(x - x_o) + A(x - x_o)^B \tag{A.1}$$

The derivative will be,

$$y' = E_o + AB(x - x_o)^{B-1} \tag{A.2}$$

Assuming B>1, else y' ($x = x_o$) would be indeterminate,

$$y'(x_o) = E_o \tag{A.3}$$

y' at the final point, x_f, should be E_f, hence:

$$y'(x_f) = E_f = E_o + AB(x_f - x_o)^{B-1} \tag{A.4}$$

or,
$$AB(x_f - x_o)^{B-1} = E_f - E_o \tag{A.5}$$

By evaluating the equation (A.1) at x_f

$$y_f = y_o + E_o(x_f - x_o) + A(x_f - x_o)^B \tag{A.6}$$

or,
$$A(x_f - x_o)^{B-1} = \frac{y_f - y_o}{x_f - x_o} - E_o = E_{\text{sec}} - E_o \tag{A.7}$$

where,
$$E_{\text{sec}} = \frac{y_f - y_o}{x_f - x_o} \tag{A.8}$$

Using equation (A.5) and (A.7), B can be found,

$$B = \frac{E_f - E_o}{E_{\text{sec}} - E_o} \tag{A.9}$$

Finally,

$$A = \frac{E_{\text{sec}} - E_o}{(x_f - x_o)^{B-1}} \tag{A.10}$$

The final equation can be written as

$$y = y_o + (x - x_o)\left(E_o + A\left|x - x_o\right|^R\right) \text{ for } x_o \le x \le x_f \tag{A.11}$$

where,

$$R = \frac{E_f - E_{\text{sec}}}{E_{\text{sec}} - E_o} \tag{A.12}$$

And

$$A = \frac{E_{\text{sec}} - E_o}{\left|x_f - x_o\right|^R} \tag{A.13}$$

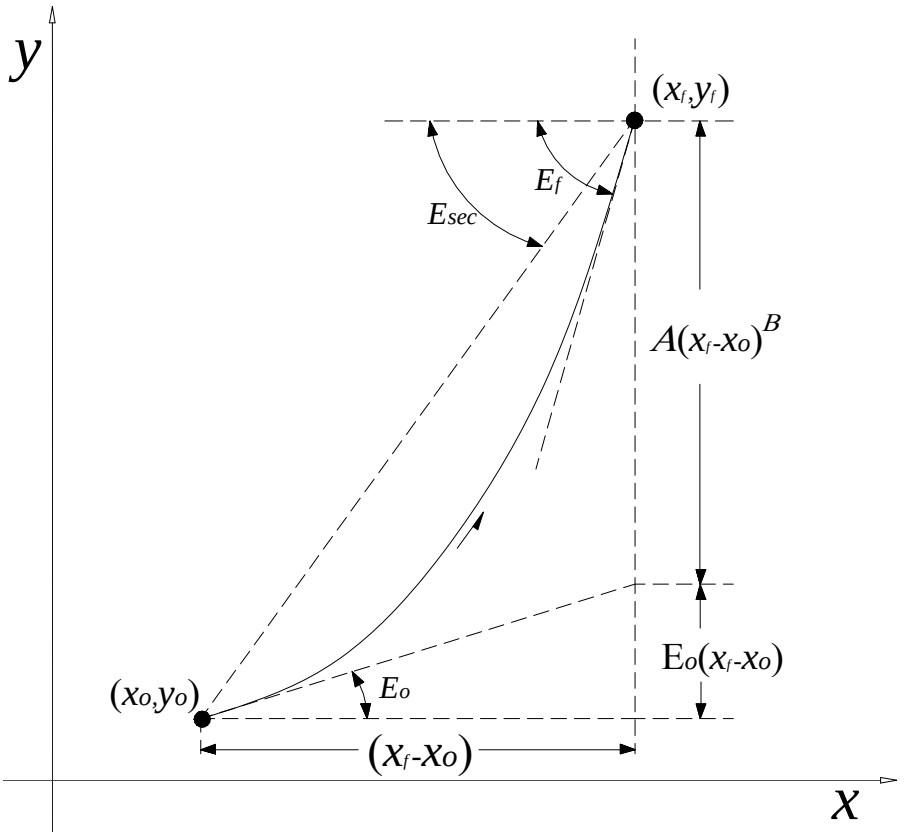

Figure A. 1: Transition Curve representation.

APPENDIX B

The Menegotto-Pinto (M-P) equation describes a curve connecting two tangents with a variable radius of curvature at the intersection point of these tangents. The M-P equation describing a curve (Fig. B.1) that joins the initial point (ε_o, f_o) and final point (ε_f, f_f) can be represented as follows:

$$f_s = f_0 + E_0(\varepsilon_s - \varepsilon_0)\left\{Q + \frac{1-Q}{\left[1+\left|E_0\,\frac{\varepsilon_s-\varepsilon_0}{f_{ch}-f_0}\right|^R\right]^{\frac{1}{R}}}\right\} \qquad \text{B.1.}$$

The tangent modulus at any point is given by:

$$E_t = \frac{\partial f_s}{\partial \varepsilon_s} = E_{\text{sec}} - \frac{E_{\text{sec}} - QE_0}{1+\left|E_0\,\frac{\varepsilon_s-\varepsilon_0}{f_{ch}-f_0}\right|^{-R}} \qquad \text{B.2.}$$

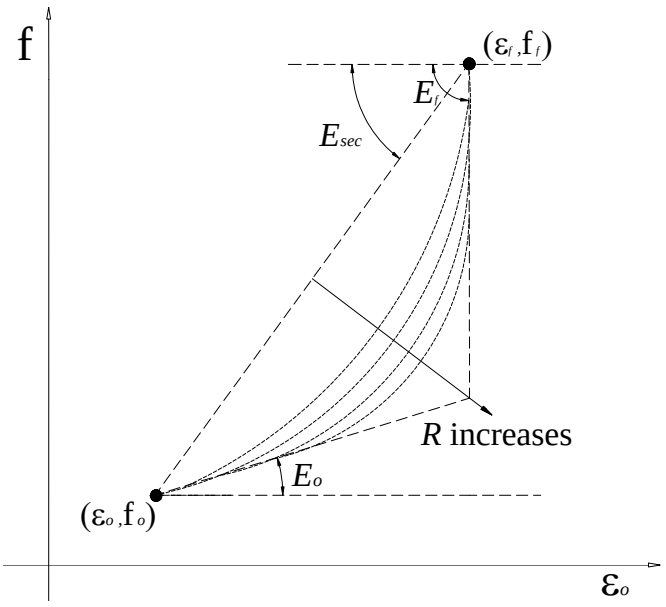

Figure B.1 Menegetto-Pinto curve representation.

where f_s = stress in steel at any strain (ε_s); f_o = stress in steel at initial point of the curve corresponding to ε_o strain; E_o = tangent modulus at initial point of the curve; E_{sec} = secant modulus or the slope of the line connecting the initial point (ε_o, f_o) and the final point (ε_f, f_f); E_f = tangent modulus at final point of the curve; and Q, f_{ch} and R are equation parameters to control the shape of the curve, and calculated as shown in Figure B.2. In Figure B.2 the initial value of R is derived from steel parameters.

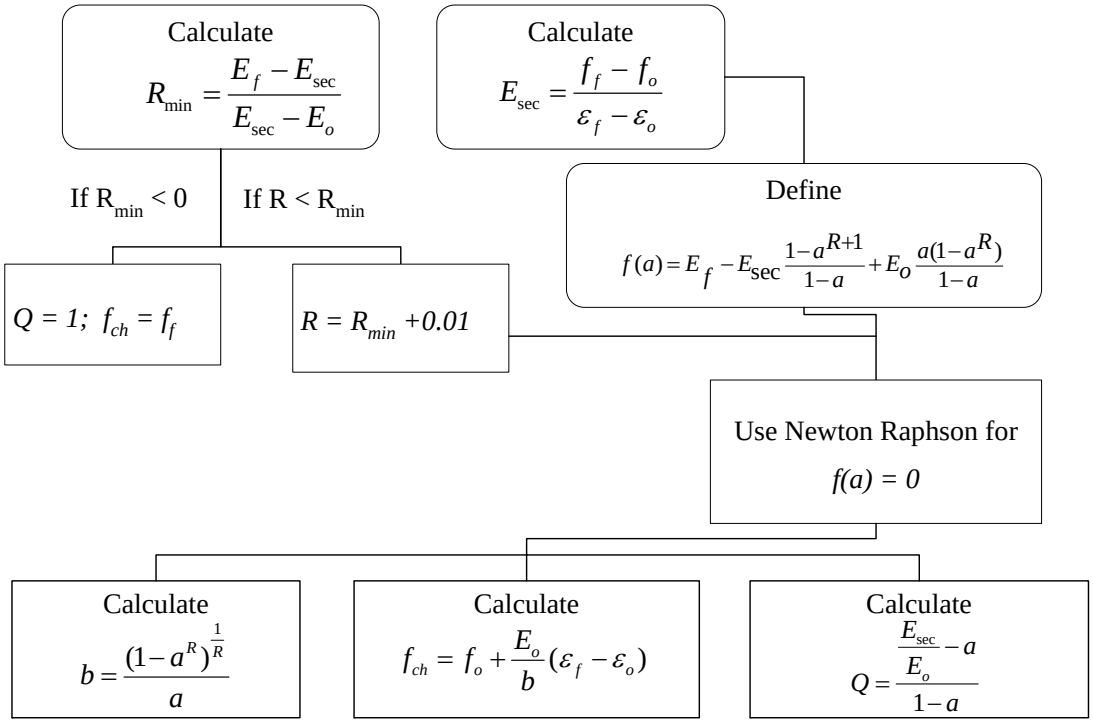

Figure B.2 Algorithm for the calculation of internal parameters of M-P equation.

Using these obtained values of initially unknown parameters b, f_{ch} ,and Q, the value of f_s corresponding to the value of ε_s can be calculated from Eq. B.1 and the value of tangent modulus E_t can be obtained from Eq. B.2.

APPENDIX C

N2 Method

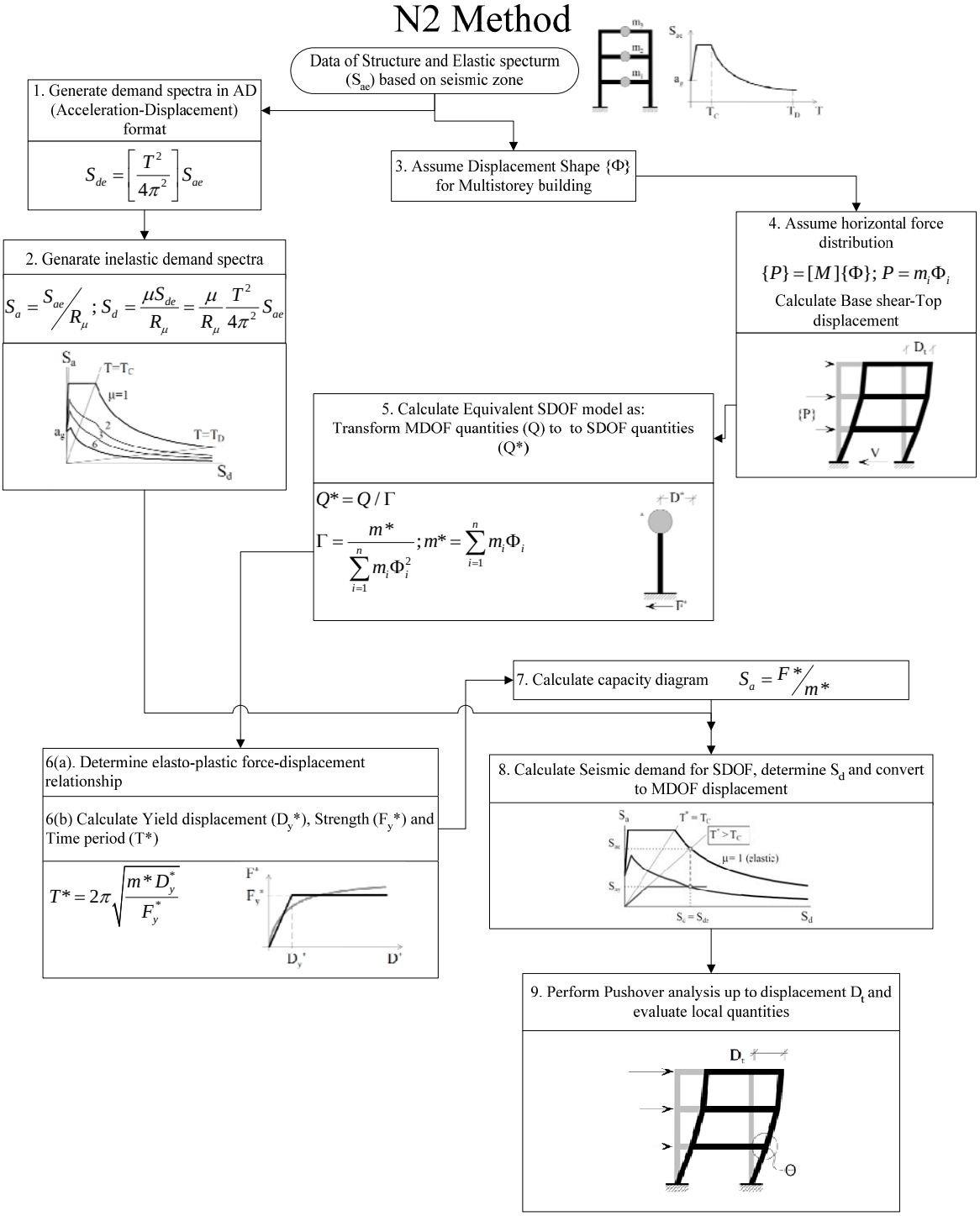

APPENDIX D

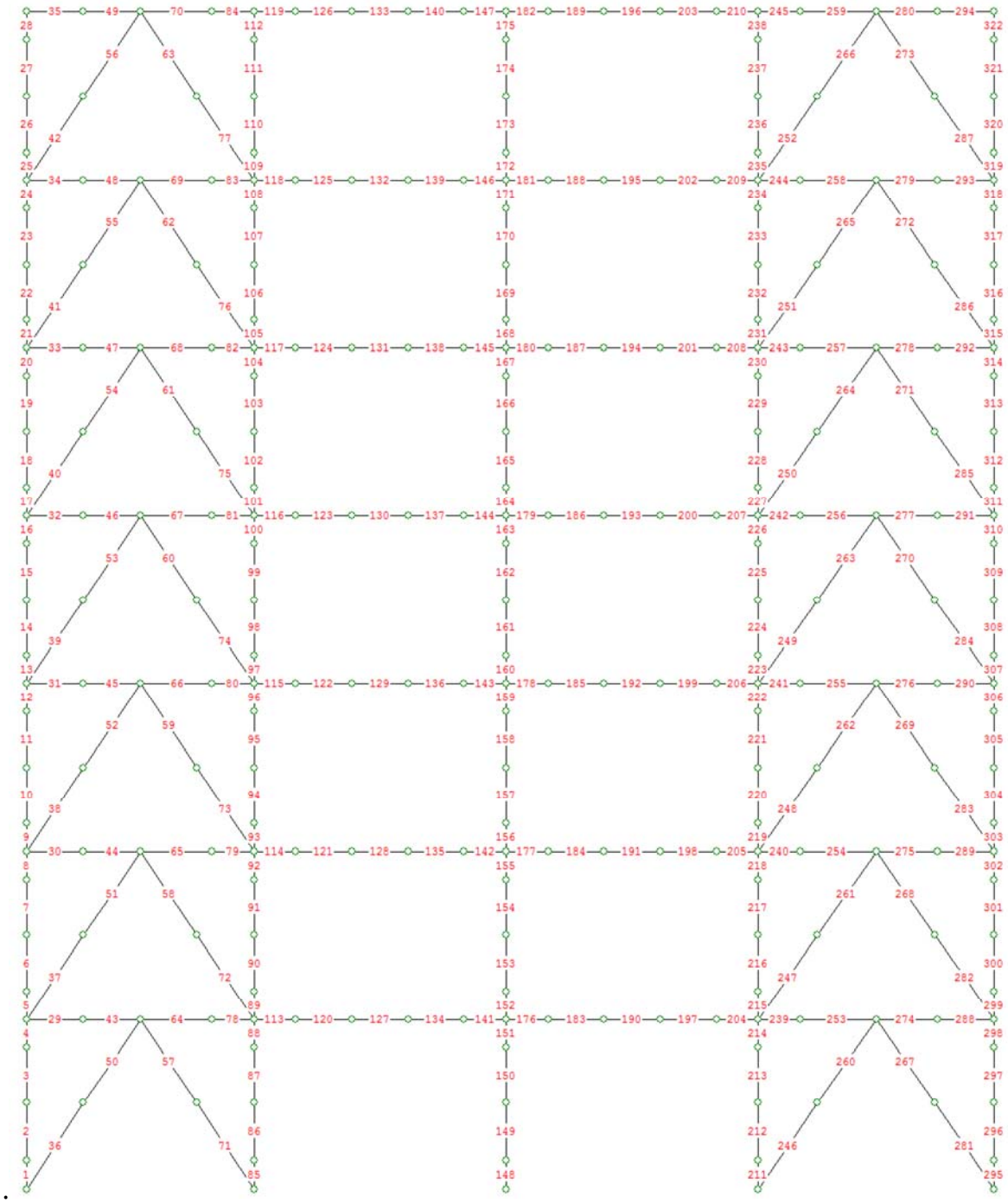

Figure D.1: Mesh topology of Multi-storey building

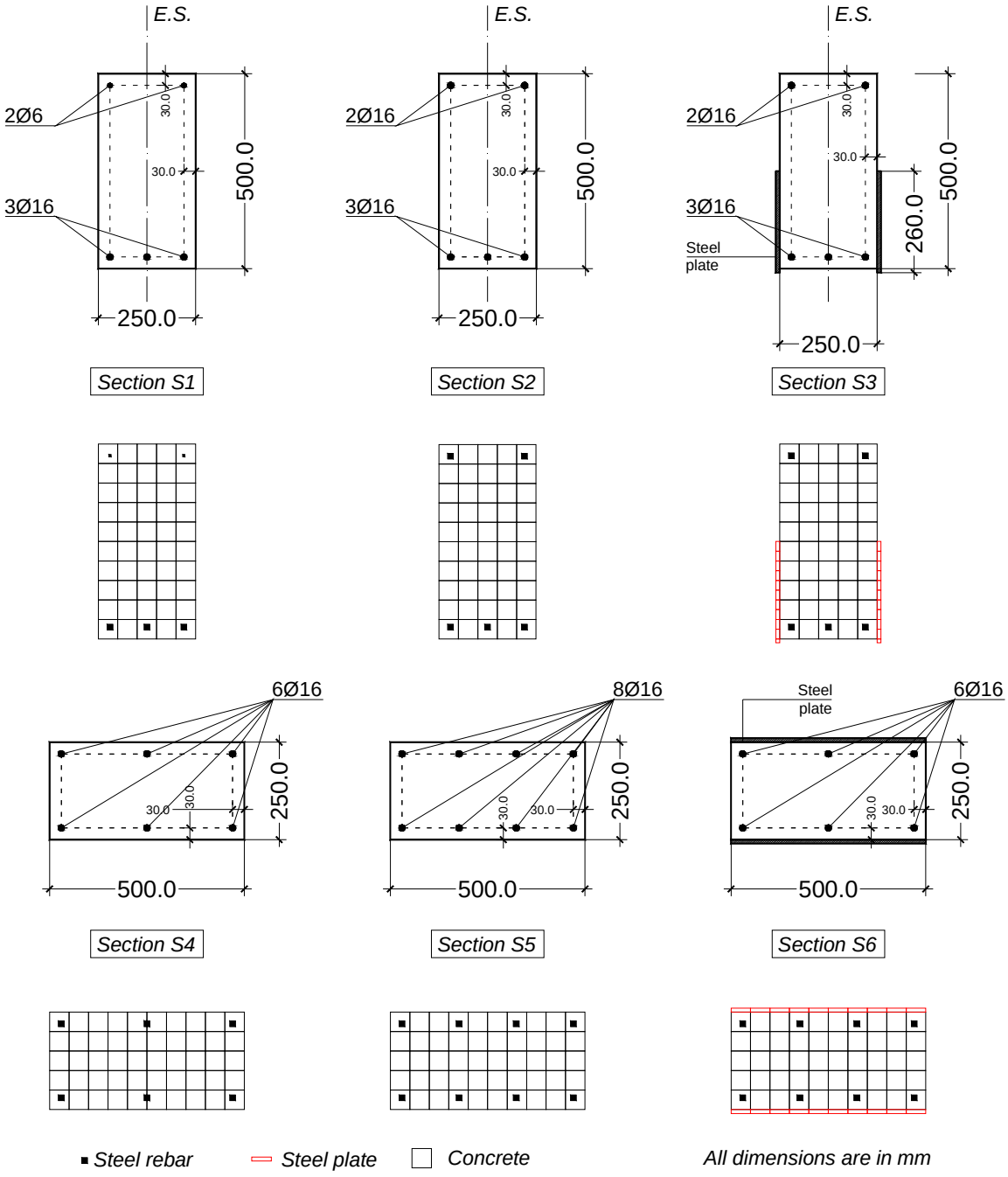

Figure D.2: Discretization of section in fibres

APPENDIX E

Stiffness Sub-matrices and Internal force for Mindlin Shells

The submatrix $\underline{K}_m^{(e)}$ is obtained from

$$\underline{K}_m^{(e)} = \int_{A^{(e)}} \underline{B}_m^T \underline{\hat{D}}_m \underline{B}_m dA \tag{E.1a}$$

where

$$\underline{\hat{D}}_m = \int_{-h/2}^{h/2} \underline{D}_{mb}\ dx_3 = \sum_{k=1}^{N_{layers}} \underline{D}_{mb,k} \left(x_{3,k}^t - x_{3,k}^b \right) \tag{E.1b}$$

In Eqn. (E.1b) h is the thickness of finite element, N_{Layers} represent total number of layers, $\underline{D}_{mb,k}$, is the constitutive matrix associated to the membrane-bending deformation of the k^{th} layer and the $\left(x_{3,k}^t - x_{3,k}^b \right)$ is the k^{th} layer thickness h_k

The submatrix $\underline{K}_{mb}^{(e)}$ is obtained from

$$\underline{K}_{mb}^{(e)} = \int_{A^{(e)}} \underline{B}_m^T \underline{\hat{D}}_{mb} \underline{B}_b dA \tag{E.2a}$$

where

$$\underline{\hat{D}}_{mb} = \int_{-h/2}^{h/2} \underline{D}_{mb}\ x_3\ dx_3 = \sum_{k=1}^{N_{layers}} \underline{D}_{mb,k}\ x_3^m \left(x_{3,k}^t - x_{3,k}^b \right) \tag{E.2b}$$

being $x_{3,k}^m$ the x_3 distance of k layer middle surface.

The submatrix $\underline{K}_b^{(e)}$ is obtained from

$$\underline{K}_b^{(e)} = \int_{A^{(e)}} \underline{B}_b^T \underline{\hat{D}}_b \underline{B}_b dA \tag{E.3a}$$

where

$$\underline{\hat{D}}_b = \int_{-h/2}^{h/2} \underline{D}_{mb} \left(x_3 \right)^2\ dx_3 = \sum_{k=1}^{N_{layers}} \underline{D}_{mb,k} \left(x_3^m \right)^2 \left(x_{3,k}^t - x_{3,k}^b \right) \tag{E.3b}$$

The submatrix $\underline{K}_s^{(e)}$ is obtained from

$$\underline{K}_s^{(e)} = \int_{A^{(e)}} \underline{B}_s^T \hat{\underline{D}}_s \underline{B}_s dA \tag{E.4a}$$

where

$$\hat{\underline{D}}_s = \int_{-h/2}^{h/2} \underline{D}_s \, dx_3 = \sum_{k=1}^{N_{layers}} \underline{D}_{s,k} \left(x_{3,k}^t - x_{3,k}^b \right) \tag{E.4b}$$

being $\underline{D}_{s,k}$ the constitutive matrix associated to the out-of-plane-shear deformation of the k layer.

To take also into account the flexural stiffness of each layer, equation (E.3b) is substituted by (Barros 1989)

$$\hat{\underline{D}}_{mb} = \int_{-h/2}^{h/2} \underline{D}_{mb} \, x_3 \, dx_3 = \sum_{k=1}^{N_{layers}} \underline{D}_{mb,k} \frac{\left(x_{3,k}^t \right)^2 - \left(x_{3,k}^b \right)^2}{2} \tag{E.5}$$

and equation (E.4b) is replaced by

$$\hat{\underline{D}}_b = \int_{-h/2}^{h/2} \underline{D}_b \left(x_3 \right)^2 dx_3 = \sum_{k=1}^{N_{layers}} \underline{D}_{mb,k} \frac{\left(x_{3,k}^t \right)^3 - \left(x_{3,k}^b \right)^3}{3} \tag{E.6}$$

The $\underline{B}_m$, $\underline{B}_b$ and $\underline{B}_s$ in equations (E.1) to (E.4) are the matrices that allow to obtain the membrane, bending and shear deformations from the corresponding degrees of freedom in the finite element. The constitutive matrix associated to the membrane-bending deformation of the k layer, $\underline{D}_{mb,k}$ used in the equations (E.2) to (E.4) and (E.6) depends on the material state or regime assigned to this layer, i.e., material linear or nonlinear behavior.

The constitutive matrix associated to the shear deformation of the k layer, $\underline{D}_{s,k}$, used in equation (E.4) depends also on the assumption of the out-of-plane shear material behavior assigned to the layer.

In a plane shell decomposed in layers, the element internal equivalent nodal forces can be obtained from the vectors associated to the membrane forces, $\underline{f}_{\text{int},m}^{(e)}$, bending moments, $\underline{f}_{\text{int},b}^{(e)}$, and out-of-plane shear forces, $\underline{f}_{\text{int},s}^{(e)}$

The vector $\underline{f}_{\text{int},m}^{(e)}$ is obtained from

$$\underline{f}_{\text{int},m}^{(e)} = \int_{A^{(e)}} \underline{B}_m^T \, \underline{\hat{N}} \, dA \tag{E.7a}$$

Where

$$\underline{\hat{N}} = \begin{bmatrix} N_1 & N_2 & N_{12} \end{bmatrix}^T = \int_{-h/2}^{h/2} \underline{\sigma}_{mb} \, dx_3 = \sum_{k=1}^{N_{layers}} \sigma_{mb,k} \left(x_{3,k}^t - x_{3,k}^b \right) \tag{E.7b}$$

are the membrane forces.

The vector $\underline{f}_{\text{int},m}^{(e)}$ is obtained from

$$\underline{f}_{\text{int},b}^{(e)} = \int_{A^{(e)}} \underline{B}_b^T \, \underline{\hat{M}} \, dA \tag{E.8a}$$

where

$$\underline{\hat{M}} = \begin{bmatrix} M_1 & M_2 & M_{12} \end{bmatrix}^T = \int_{-h/2}^{h/2} x_3 \, \underline{\sigma}_{mb} \, dx_3 = \sum_{k=1}^{N_{layers}} \sigma_{mb,k} \, x_{3,k}^m \left(x_{3,k}^t - x_{3,k}^b \right) \tag{E.8b}$$

are the bending moments.

The vector $\underline{f}_{\text{int},m}^{(e)}$ is obtained from

$$\underline{f}_{\text{int},s}^{(e)} = \int_{A^{(e)}} \underline{B}_s^T \, \underline{\hat{Q}} \, dA \tag{E.9a}$$

where

$$\underline{\hat{Q}} = \begin{bmatrix} Q_{23} & Q_{31} \end{bmatrix}^T = \int_{-h/2}^{h/2} \underline{\sigma}_s \, dx_3 = \sum_{k=1}^{N_{layers}} \sigma_{s,k} \left(x_{3,k}^t - x_{3,k}^b \right) \tag{E.9b}$$

If a particular layer has linear elastic behavior the equations (E.7b) and (E.8b) are substituted by the equations (E.10) and (E.11), respectively (Barros 1989). This is important when the thickness of the plane shell is discretized with only one layer (in the case of performing linear elastic analysis).

$$\hat{N} = \sum_{k=1}^{N_{layers}} \underline{D}_{mb,k}\ \overline{\underline{\varepsilon}}_m \left(x_{3,k}^t - x_{3,k}^b \right) + \underline{D}_{mb,k}\ \overline{\underline{\varepsilon}}_f \frac{\left(x_{3,k}^t \right)^2 - \left(x_{3,k}^b \right)^2}{2} \tag{E.10}$$

$$\hat{M} = \sum_{k=1}^{N_{layers}} \underline{D}_{mb,k}\ \overline{\underline{\varepsilon}}_m \frac{\left(x_{3,k}^t \right)^2 - \left(x_{3,k}^b \right)^2}{2} + \underline{D}_{mb,k}\ \overline{\underline{\varepsilon}}_f \frac{\left(x_{3,k}^t \right)^3 - \left(x_{3,k}^b \right)^3}{3} \tag{E.11}$$

where $\overline{\underline{\varepsilon}}_m$ and $\overline{\underline{\varepsilon}}_b$ are, respectively, the membrane and bending deformations.